University of Cyprus

DEPARTMENT OF ELECTRICAL AND COMPUTER ENGINEERING

SYNCHRONIZATION AND CONTROL METHODS FOR ADVANCING THE GRID SIDE CONVERTER OF RENEWABLE ENERGY SOURCES

DOCTOR OF PHILOSOPHY DISSERTATION

LENOS HADJIDEMETRIOU

2016

DEPARTMENT OF ELECTRICAL AND COMPUTER ENGINEERING

SYNCHRONIZATION AND CONTROL METHODS FOR ADVANCING THE GRID SIDE CONVERTER OF RENEWABLE ENERGY SOURCES

LENOS HADJIDEMETRIOU

A dissertation submitted to the University of Cyprus in partial fulfillment of the requirements for the degree of Doctor of Philosophy

February 2016

VALIDATION PAGE

Doctoral Candidate: Lenos Hadjidemetriou

Doctoral Dissertation Title: Synchronization and Control Methods for Advancing the Grid Side Converter of Renewable Energy Sources

The present Doctoral Dissertation was submitted in partial fulfillment of the requirements for the degree of Doctor of Philosophy at the ***Department of*** *Electrical and Computer Engineering and was approved on the* 8^{th} *of February 2016 by the members of the* ***Examination Committee.***

Examination Committee:

Research Supervisor: _____

(Dr. Elias Kyriakides, Associate Professor)

Committee Member: _____

(Dr. Marios Polycarpou, Professor)

Committee Member: _____

(Dr. Christos Panayiotou, Associate Professor)

Committee Member: _____

(Dr. Frede Blaabjerg, Professor)

Committee Member: _____

(Dr. Constantinos Pattichis, Professor)

DECLARATION OF DOCTORAL CANDIDATE

The present doctoral dissertation was submitted in partial fulfillment of the requirements for the degree of Doctor of Philosophy of the University of Cyprus. It is a product of original work of my own, unless otherwise mentioned through references, notes, or any other statements.

……... **[**Full name of Doctoral candidate]

……... **[**Signature]

ΠΕΡΙΛΗΨΗ

Η αύξηση στην τιμή καθώς και το περιβαλλοντικό αντίκτυπο των ορυκτών καυσίμων έχουν εγείρει το διεθνή ενδιαφέρον για τις Ανανεώσιμες Πηγές Ενέργειας (ΑΠΕ), ειδικά όσο αφορά τις ανεμογεννήτριες και τα φωτοβολταϊκά συστήματα. Η τεχνολογία κλειδί για να επιτρέψει την ιδιαίτερα υψηλή διείσδυση ΑΠΕ είναι ο αντιστροφέας (μετατροπέας ισχύος βασισμένος σε ηλεκτρονικά ισχύος), ο οποίος είναι υπεύθυνος για την ορθή διασύνδεση των ΑΠΕ με το δίκτυο ηλεκτρικής ισχύος. Επομένως, η βελτίωση της λειτουργίας του αντιστροφέα ισχύος αποτελεί απαραίτητη προϋπόθεση ώστε οι ΑΠΕ να επιτύχουν: την ορθή λειτουργία υπό οποιεσδήποτε συνθήκες λειτουργίας του δικτύου, να εναρμονιστούν με τις πρόσφατους κανονισμούς δικτύου σχετικά με την διασύνδεση ΑΠΕ, και να προσφέρουν την απαραίτητη στήριξη στο δίκτυο όποτε χρειάζεται.

Η συγκεκριμένη διδακτορική διατριβή έχει ως κύριο στόχο την ενίσχυση αντιστροφέα ισχύος όσο αναφορά την λειτουργία κατά την διάρκεια βραχυκυκλωμάτων καθώς και την ποιότητα της εγχεόμενης ισχύος. Η ενίσχυση του αντιστροφέα δύναται να επιτευχθεί βελτιώνοντας τα κύρια υποσυστήματα της μονάδας ελέγχου του. Ο ελεγκτής του αντιστροφέα βασίζεται στη μέθοδο συγχρονισμού, στον ελεγκτή ρεύματος και στον ελεγκτή ισχύος. Η απόκριση της μονάδας συγχρονισμού είναι το πιο σημαντικό μέρος του ελεγκτή αφού επηρεάζει άμεσα την λειτουργία των λοιπών υποσυστημάτων του ελεγκτή καθώς και την λειτουργία του αντιστροφέα και κατ' επέκταση την λειτουργία του συστήματος ΑΠΕ. Επομένως, η συγκεκριμένη διδακτορική διατριβή εστιάζει ιδιαιτέρως στην βελτίωση της μεθόδου συγχρονισμού και προτείνει αρκετές νέες μεθοδολογίες συγχρονισμού τόσο για μονοφασικούς όσο και για τριφασικούς αντιστροφείς. Οι προτεινόμενες μεθοδολογίες συγχρονισμού επιτυγχάνουν την ταχύτατη και υψηλής ακριβείας απόκριση υπό οποιεσδήποτε συνθήκες του δικτύου στο σημείο διασύνδεσης. Επιπλέον, ένα νέος ελεγκτής ρεύματος έχει υλοποιηθεί για την ορθή ρύθμιση των εγχεόμενων ρευμάτων του αντιστροφέα όταν η τάση στο σημείο διασύνδεσης είναι αρμονικά παραμορφωμένη ή παρουσιάζει βυθίσεις λόγω σφαλμάτων. Επίσης, προηγμένες μεθοδολογίες έχουν προταθεί για τον ελεγκτή ισχύος ώστε να επιτυγχάνεται η ορθή λειτουργία του αντιστροφέα κατά την διάρκεια βραχυκυκλωμάτων. Όλες οι προτεινόμενες μεθοδολογίες έχουν εφαρμοστεί στη μονάδα ελέγχου για την πειραματική επιβεβαίωση της ορθής τους λειτουργίας. Επομένως, έχει πειραματικά επιβεβαιωθεί ότι οι προτεινόμενες μεθοδολογίες για τον συγχρονισμό και έλεγχο του αντιστροφέα μπορούν να

βελτιώσουν σημαντικά την λειτουργία του αντιστροφέα και επομένως και του συστήματος ΑΠΕ, όσο αναφορά την ποιότητα της εγχεόμενης ισχύος καθώς και την ορθή και δυναμική απόκριση του συστήματος κατά την διάρκεια βραχυκυκλωμάτων στο δίκτυο.

Σύμφωνα με διερευνητικές μελέτες που έχουν γίνει στα πλαίσια της διδακτορικής διατριβής, καταδεικνύεται ότι η βελτίωση της λειτουργίας του αντιστροφέα ισχύος από τις προτεινόμενες μεθοδολογίες επιφέρει ευεργετικά αποτελέσματα, τόσο στο να επιτρέψει την αυξημένη διείσδυση των ΑΠΕ λόγω της προηγμένης τους λειτουργιά αλλά και στο να ενίσχυση την ευστάθεια και την ποιότητα ισχύος ολόκληρου του συστήματος ηλεκτροδότησης. Επιπλέον, στην διατριβή αυτή περιλαμβάνεται μελέτη για διαφορετικές στρατηγικές ελέγχου των ΑΠΕ (σύμφωνα με του πρόσφατους κανονισμούς για διασύνδεση ΑΠΕ) κατά την διάρκεια βραχυκυκλωμάτων στο δίκτυο. Η μελέτη καταδεικνύει κάποια προβλήματα που μπορούν να προκληθούν στην λειτουργία των ΑΠΕ κατά το βραχυκύκλωμα τα οποία μπορούν να απειλήσουν την ευστάθεια του συστήματος ηλεκτροδότησης. Επομένως, προτείνονται κάποιες μετατροπές που θα πρέπει να υιοθετηθούν από τους κανονισμούς διασύνδεσης ώστε να αποφευχθούν τέτοια φαινόμενα. Επιπλέον, στα πλαίσια της διατριβής έχει προταθεί μία μεθοδολογία ελέγχου των ΑΠΕ από το κέντρο ελέγχου του συστήματος ηλεκτροδότησης, η οποία μπορεί συνδράμει ουσιαστικά στην ενίσχυση της ευσταθείας του συστήματος ηλεκτρικής ισχύος.

Σε γενικές γραμμές, αυτή η διδακτορική διατριβή προτείνει διάφορες τεχνικές οι οποίες μπορούν να βελτιώσουν σημαντικά την λειτουργία του αντιστροφέα ισχύος για την διασύνδεση των ΑΠΕ. Η εφαρμογή των προτεινόμενων μεθοδολογιών μπορεί να επιδράσει ευεργετικά στη βελτίωση της λειτουργία ενός συστήματος ΑΠΕ, στην ενίσχυση της ευστάθειας και της ποιότητας ισχύος του συστήματος ηλεκτροδότησης, και στη δημιουργία εχεγγύων για την αύξηση της διείσδυσης των ΑΠΕ, το οποίο είναι ιδιαίτερα επωφελές για το περιβάλλον.

ABSTRACT

The increasing price and the environmental impact of fossil fuels have grown the attention to modern Renewable Energy Sources (RES), such as wind and solar systems. The key technology for enabling a high penetration of RES is the power electronic based Grid Side Converter (GSC), which is responsible for the proper injection of the produced energy into the power grid. Thus, there is a need to advance the operation of the GSC to ensure that RES will be able to meet the modern grid regulations, to operate properly under any grid conditions, and to ensure the support to the grid when needed.

The main objective of this Ph.D. dissertation is to enhance the performance of the GSC with regards to its Fault Ride Through (FRT) operation and to its power quality, through the improvement of the main units of the GSC controller. The design of the GSC controller is based on a fast and robust synchronization method, an advanced current controller, and a power controller enhanced with FRT capabilities. The most crucial aspect of the control of a grid-connected RES is the synchronization method. Thus, this Ph.D. dissertation proposes several single- and three-phase synchronization methods that can achieve a fast and accurate response under any grid conditions. Further, a current control that enables a proper operation under grid faults is proposed and some advanced methodologies for enabling the FRT operation of GSC are suggested. The proposed methodologies are directly applied to the GSC controller and it has been experimentally proved that the proposed methods for the synchronization and control of the GSC can improve the performance of RES, in terms of dynamic and FRT operation, as well as enhancing the quality of the injected currents. Investigations performed depict significant impacts from advancing the performance of the GSC. For example, the improved operation of the GSC enables a higher penetration of RES and enhances the power quality and stability of the power system under an increased penetration of RES.

In addition to the above contributions, a benchmarking study of different fault ride through strategies for RES has been performed on a dynamic test power system, where some issues have been highlighted and modifications are proposed for the current grid regulations in order to improve the system stability. Further, a centralized control methodology for RES has been suggested to enhance the voltage stability of the power system by utilizing the improved capabilities of RES.

ACKNOWLEDGMENTS

This research project was performed under the supervision of Dr. Elias Kyriakides, Associate Professor at the Department of Electrical and Computer Engineering of the University of Cyprus. First and foremost, I would like to express my deepest gratefulness to my advisor, Prof. Kyriakides, for his professional and patient guidance with his open-mindedness and kindness during the Ph.D. project period. His kind support and tremendous help, as well as his insightful comments and ideas and his enthusiasm about research were essential for overcoming any obstacle and for achieving the goals during this Ph.D. project. It was a great honor for me to work with Prof. Kyriakides and the encouragement that he gave me will be of great supportiveness for my career and throughout my whole life.

Furthermore, I would like to express my deepest gratitude and appreciation to Prof. Frede Blaabjerg from the Department of Energy Technology of Aalborg University. His kindness, support and professional supervision during my several visits to Aalborg University, his long expertise in power electronics and his insightful comments and ideas were of high importance for completing this Ph.D. dissertation. It was a great honor and privilege for me to work and cooperate with Prof. Blaabjerg.

Special thanks to Dr. Marios Polycarpou, Dr. Christos Panayiotou and Dr. Constantinos Pattichis for their participation in the committee. The time and effort that they spent to review the dissertation is really appreciated, while their comments have been really helpful for improving the quality of this dissertation.

I would also like to thank Dr. Yongheng Yang for his support and assistance during my visits to Aalborg University. The cooperation with him, the helpful discussions and his valuable comments were very useful for completing my Ph.D. dissertation.

I would like to express my sincere thanks to all my colleagues at the KIOS Research Center for the lovely environment and the endless friendship. A special thanks to all the team members of Dr. Elias Kyriakides for the very effective collaboration and the sharing of research experience during all these years.

Finally, I want to express the most important and the sincerest gratitude to my parents for their exceptional and unconditional love and their encouragement throughout my life, to my beloved brother and sister and to my fiancée for the support and understanding.

TABLE OF CONTENTS

LIST OF TABLES

LIST OF FIGURES

CHAPTER 1
INTRODUCTION

The increasing price and the environmental impact of fossil fuels have grown the international attention to Renewable Energy Sources (RES). Renewable technologies, such as Wind Power Systems (WPS) and Photovoltaic (PV) systems, are of increasing competiveness and thus, their involvement in the generation of electric power is an ideal alternative to fossil fuels.

Technical reports regarding the worldwide installation of modern RES show a continuous growing trend [1]-[4]. Fig. 1.1 represents the total installed capacity worldwide for WPS and PV systems for the last decade, where it is demonstrated that the WPS and PV reached an installed capacity of 370 GW and 177 GW respectively at 2014. More specifically at the European level, RES have recently reached 14% of the total energy generation [2]. Furthermore, according to the 2020 and 2030 frameworks of climate and energy of European commission the RES penetration should reach 20% and 27% respectively in the European Union. Such an increased penetration of RES can have a significant impact on the operation of the power system. Therefore, modern RES should be designed in a way to ensure proper operation and to support the power system under any grid conditions.

1.1 Motivation and objectives

To pave the way for an even more increased penetration of RES, the grid interconnection of RES should be enhanced. The need for advancing the RES controllers for the proper grid interconnection is demonstrated through the evolution of grid regulations. Several international standards [5]-[10] have been derived and local grid codes [11]-[27] have

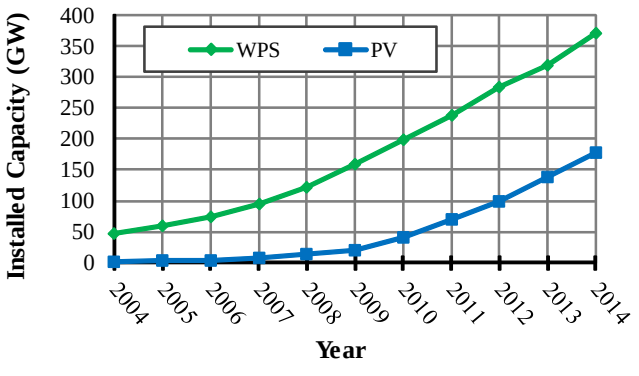

Fig. 1.1. Total installed capacity worldwide for WPS and PV systems for the last decade [1].

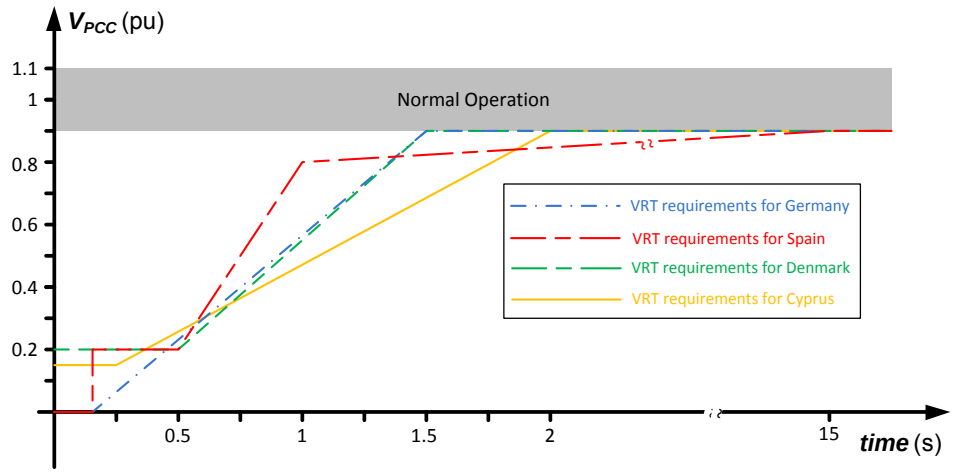

Fig. 1.2. Grid-connected RES should remain connected when the voltage at the PCC is above the line defined by the corresponding grid regulations.

been issued from each country in order to guarantee the appropriate performance of the grid-connected RES. These grid regulations determine the desired operation of RES under normal and abnormal grid conditions. An example is shown in Fig. 1.2, where grid codes regarding the Voltage Ride Through (VRT) capability of RES are demonstrated for four different countries; Germany [11], [12], Spain [13], [14], Denmark [15], [16] and Cyprus [17]. RES interconnected at the medium or high voltage level of the power system should keep their synchronization and remain grid-connected when the voltage at the Point of Common Coupling (PCC) is above the characteristic line set by the regulation of each country as presented in Fig. 1.2. It is to be noted that according to the grid codes of Germany and Spain, RES should remain interconnected for 150 ms even under zero voltage conditions. Furthermore, in the near future, similar VRT regulations will also be necessary for RES connected at the low-voltage level distribution network due to the significant amount of residential PV installations. So far, only Italy [20] and Japan [22] have issued such VRT regulations for RES connected at the low-voltage distribution network.

Moreover, when the voltage at the PCC is outside the normal operation voltage window, then the RES should inject/absorb a proper amount of reactive current (I_Q) under Low-Voltage Ride Through (LVRT)/ High-Voltage Ride Through (HVRT) conditions as shown in Fig. 1.3. The amount of reactive current should be provided by the RES within 20 ms and it is defined by the ratio k and the voltage sag $\Delta V=V_N - V_{PCC}$, where V_N is the nominal voltage and V_{PCC} is the voltage measurement at the PCC. The ratio k, which determines the VRT strategy, is defined by the grid codes as,

$$k = \frac{I_Q}{\Delta V} \tag{1.1}$$

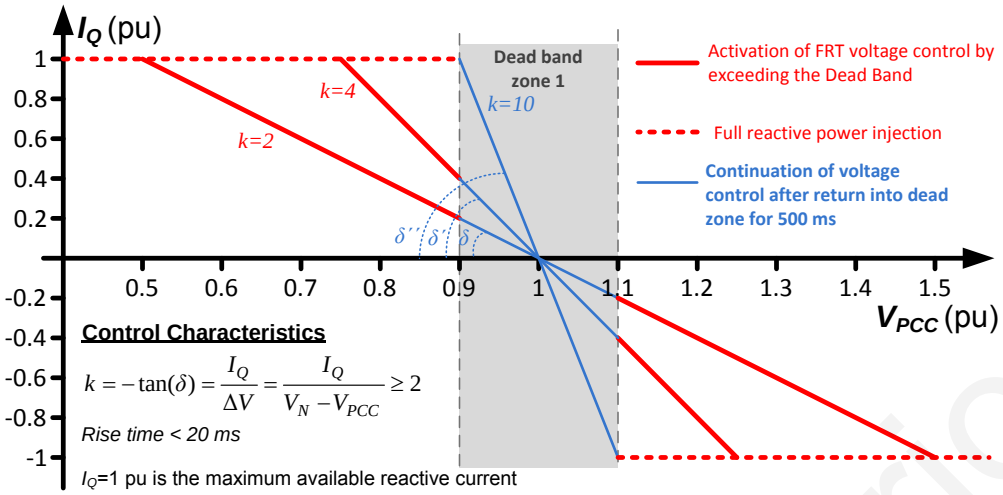

Fig. 1.3. Required reactive current support under low and high VRT according to Germany and Cyprus grid codes.

Fig. 1.3 presents the Germany and Cyprus grid codes regarding the reactive power support by RES under VRT conditions. According to these regulations, the value of k should be greater or equal to two in order to provide a sufficient voltage support under grid faults. Hence, the grid regulations specify that the grid-connected RES should keep their synchronization under grid faults and additionally should operate fast and properly in order to provide support to the power system under grid disturbances.

In summary, several requirements have been defined by the grid regulations to determine the desired operation of RES under normal and abnormal grid conditions. Thus, grid regulations determine, besides others, the desired operation of RES regarding the voltage and frequency normal operation window, the active/reactive power operation window according to grid frequency/voltage variations, the VRT capability, the reactive current support under VRT conditions, and the power quality specifications for limiting the injection of harmonic currents for the proper electromagnetic compatibility according to [9].

The Grid Side Converter (GSC) based on power electronic technology is responsible for the grid interconnection of RES; however, current techniques for controlling the GSC may fail to meet the recent grid regulations under some circumstances. An example is demonstrated in Fig. 1.4, where the controller of the three-phase GSC of a RES is designed based on existing synchronization and control techniques. In the example of Fig. 1.4, initially the grid voltage is ideal (symmetrical and harmonic free) and thus, the synchronization signals (e.g., estimated frequency f' and the voltage expressed in synchronous reference frame $\mathbf{v}_{dq}$ as explained in Appendix A.4) are very accurate and the

current injection ($\mathbf{i}_{abc}$) by the RES is of high quality (its total harmonic distortion (THD_i) is equal to 3.5%). When the grid voltage is distorted with 5% of fifth harmonic ($t > 0.5$ s) as shown in Fig. 1.4, the synchronization signals present serious inaccuracies due to the presence of harmonics and as a consequence the injected currents are also distorted. In this case the power quality of the injected currents is seriously affected (THD_i>10%) and the RES cannot meet the grid regulations, which requires that the THD_i should be less than 5% according to [9]. The injection of low quality currents by the RES, especially under a high penetration of RES, can seriously affect the power quality of the entire power system.

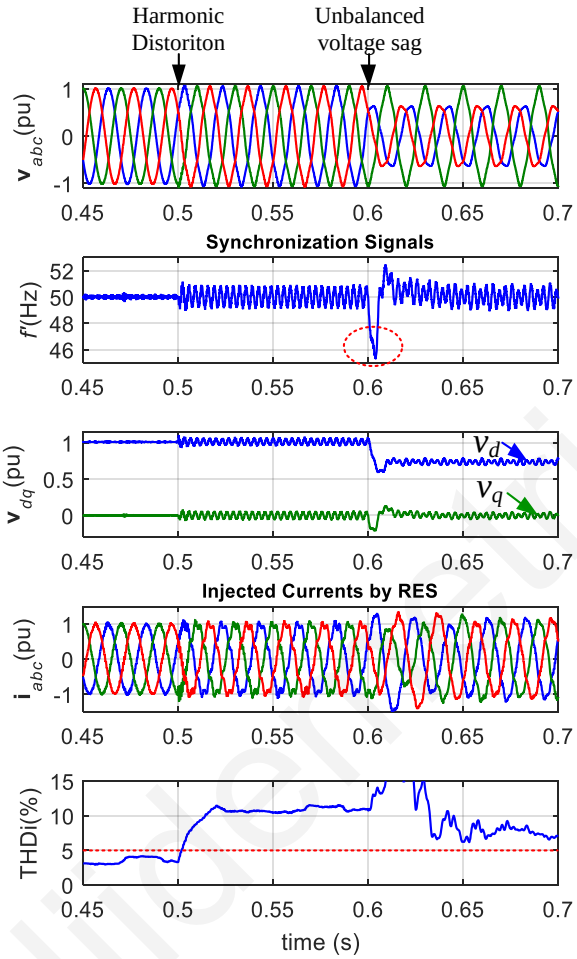

Fig. 1.4. Architecture schematic of a grid-connected RES (for WPS or PV technology system). Both systems use the same type of GSC for interconnecting with the power grid.

Furthermore, Fig. 1.4 also presents the RES operation under an unbalanced voltage sag at $t = 0.5$ s. According to the recent grid regulations the RES should not be disconnected during short voltage sags, as demonstrated in Fig. 1.2, and should provide a proper reactive support to the grid, as defined by Fig. 1.3. When the grid fault occurs, such as in the case of Fig. 1.4, the overshoot of the estimated frequency by the existing synchronization method is high and as a result the detected frequency is outside the operating frequency window (47 Hz $< f <$ 52 Hz) as defined by the local grid regulations in [17]. The violation of the frequency operating window will cause a non-expected disconnection of the RES. Moreover, in Fig. 1.4 the RES can also be disconnected due to the violation of the GSC current ratings (trip of the overcurrent protection of the GSC) after the occurrence of the fault. The violation of the current ratings (for 0.6 s $< t <$ 0.65 s) is caused due to the relatively slow response of the synchronization and control method of the GSC. Hence, in case where the RES is unexpectedly disconnected from the grid during a grid fault (e.g., a voltage sag event), the RES fails to meet the grid codes for

the Fault Ride Through (FRT) operation of RES. As a consequence, the disconnection of RES during a grid disturbance will cause a further disturbance to the power system and will not provide the required active and reactive support to the faulty power grid. Hence, cascading failures and blackouts may be caused due to the non-proper operation of RES, especially under a high penetration of RES, and the stability of the entire power system will be seriously affected.

In light of the above issues, there is a need to advance the design of RES in order to meet the new specifications set by the modern grid codes. As the penetration of RES is increased, the necessity of enhancing the operation of RES is becoming more crucial in order to ensure the stability and the power quality of the grid and to avoid cascading and blackout events in the power system. Thus, the main objectives of this Ph.D. dissertation are:

- to enhance the performance of the GSC of a grid-connected RES with regards to its FRT operation and to its power quality, through the improvement of the main units of the GSC controller;
- to improve RES capabilities in order to improve the power quality and the stability of the power system.

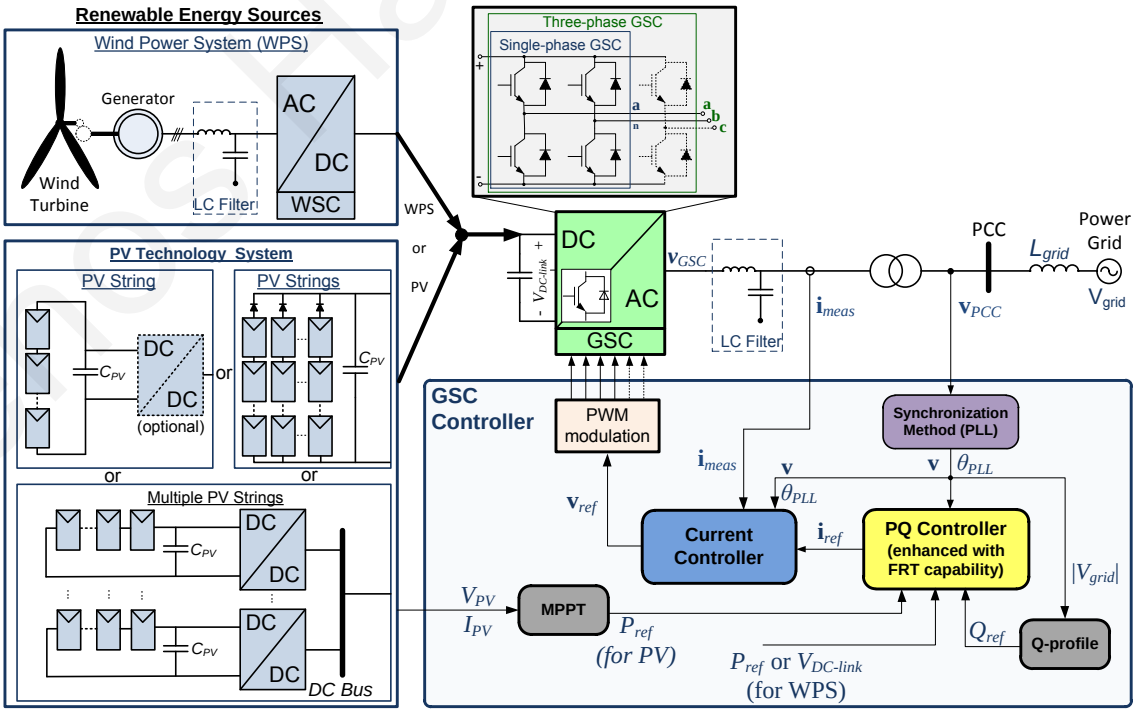

Fig. 1.5. Architecture schematic of a grid-connected RES (for WPS or PV technology system). Both systems use the same type of GSC for connecting with the power grid.

The accomplishment of the main objectives of this Ph.D. dissertation can advance the grid interconnection of RES, can ensure the power quality and the stability of the power system and can pave the way for the even increasing penetration of RES.

1.2 Contribution of this work

The key element to enhance the operation of the grid-connected RES is to improve the performance of the Grid Side Converter (GSC). The GSC usually consists of a conventional two level voltage source power electronic converter, with a full bridge topology in case of single-phase RES systems and with a six-pack topology in case of three-phase RES. A typical architecture of the GSC among with its controller is presented in Fig. 1.5. It is to be noted that the GSC of a WPS or a PV technology system is similar and thus, the suggested techniques in this Ph.D. dissertation can be straightforwardly applied to both systems. The GSC controller is based on the synchronization unit, the active and reactive power (PQ) controller, the current controller and the Pulse Width Modulation (PWM) technique as shown in Fig. 1.5. The synchronization unit is usually a Phase-Locked Loop (PLL) algorithm to estimate the phase and the amplitude of the positive sequence of the grid voltage measurement at the PCC. The synchronization method is the most crucial part for intercconecting RES and thus, it is necessary to present fast dynamic response under grid faults and accurate response under grid disturbances (e.g., voltage sag, phase change and frequency step events). Furthermore, a synchronization method should present great immunity against harmonic distortion and should be of low complexity in order to straightforwardly apply in the embedded microcontroller of the GSC. The PQ controller is responsible to generate the reference currents according to the DC-link voltage and the active power set-point ($P_{set\text{-}point}$) and according to the grid voltage amplitude ($\mathbf{v}_{PCC}$) and the reactive power set-point ($Q_{set\text{-}point}$). The current controller ensures the proper current injection under any grid conditions. Furthermore, the effect of the operation of RES interconnected with realistic and dynamic power systems are of increased interest, especially under abnormal grid conditions.

The main purpose of this Ph.D. dissertation is to advance the GSC of a RES by improving its performance regarding the dynamic response and the power quality. As a consequence, the grid interconnection of RES will be improved with beneficial effects for the whole power system. Hence, the main contributions of this work are demonstrated in Fig. 1.6 and are briefly analyzed below:

- the proposition of four new synchronization methods (the dαβ-PLL [28], [29], the adaptive dαβ-PLL [30], [31], the FPD-dαβ-PLL [31] and the adaptive FPD-dαβ-PLL [31]), which enable a faster synchronization of the GSC under balanced and unbalanced grid voltage conditions as presented in Chapter 2 and Chapter 3,

- the investigation of the effect of the faster synchronization on the RES FRT performance [31]-[33] as presented in Chapter 2 and Chapter 3,

- the proposition of two new three-phase synchronization methods (the MSHDC-PLL [34] and the DNαβ-PLL [35]), which present great dynamic performance and immunity against unbalanced grid faults and harmonic distorted conditions as proposed in Chapter 4,

- the proposition of two new single-phase PLLs; the MHDC-PLL [36]-[38], which enhance the accuracy of the synchronization under unbalanced and harmonic distorted grid without affecting its dynamic response and the frequency adaptive MHDC-PLL [39], which improves the MHDC-PLL with regards to the complexity of the algorithm and the accuracy under non-nominal frequencies. This single-phase PLLs are presented in Chapter 5,

- the investigation of the effect of an accurate synchronization (with great robustness against harmonics) on the power quality of the RES [35], [36]. This investigation take place in Chapter 4 and Chapter 5,

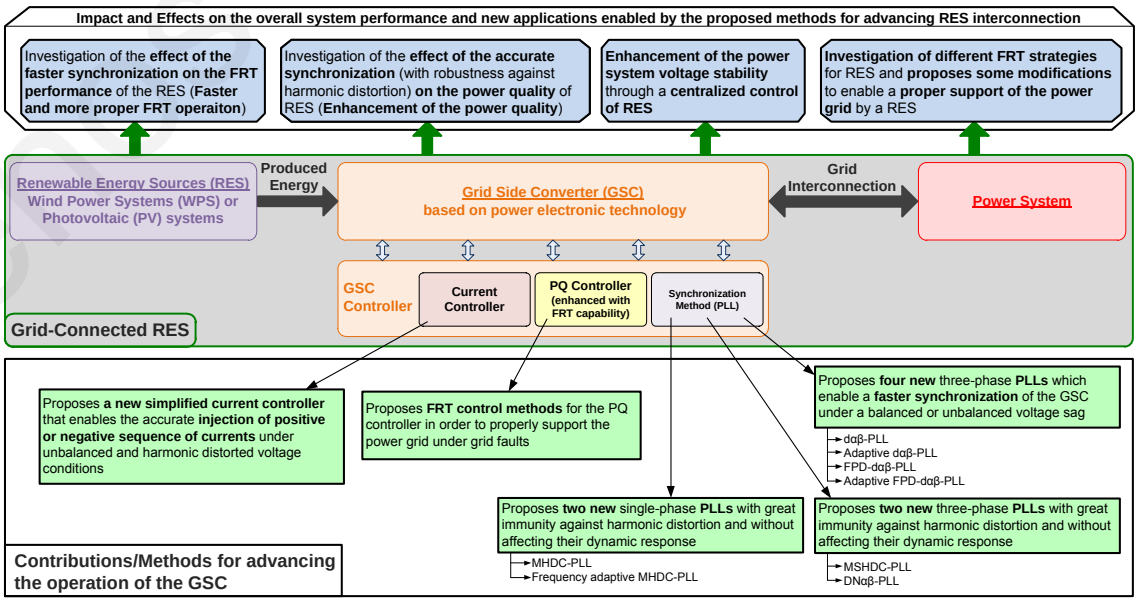

Fig. 1.6. Synopsis of the main contributions and effects of this Ph.D. dissertation.

- the proposition of a new current controller in Chapter 6 for accurate and high quality current injection under unbalanced and harmonic distorted grid conditions [40],

- FRT control methods for the PQ controller in order to properly support the power grid under grid faults [31], [33], [35] as presented in Chapter 2-Chapter 6,

- the investigation of different FRT strategies for RES [41] presented in Chapter 7,

- the enhancement of the power system voltage stability though a centralized control of RES [42] as proposed in Chapter 8.

The proposed synchronization methods, current controller, and FRT control methods for the PQ controller can be applied to the controller of the next-generation (single- or three-phase) GSC in order to advance the performance of the grid-connected RES under normal, abnormal and distorted grid conditions. The outcomes of this work can significantly improve the RES operation regarding the FRT operation and the power quality of the injected currents. Thus, such improved operation of RES can beneficially affect the quality and stability of power systems and can enable the further penetration of RES.

1.3 Dissertation outline

The work in this Ph.D. dissertation for advancing the grid interconnection of RES is organized in nine chapters. Chapter 2 begins with a benchmarking between three Phase-Locked Loop (PLL) based synchronization methods for three-phase RES. The results from the benchmarking motivate the proposition of a new hybrid PLL, named dαβ-PLL, which inherits the advantage of two other PLLs. The new dαβ-PLL presents an improved dynamic performance and it is very accurate under unbalanced grid faults. Thus, the new synchronization method can improve the dynamic performance of a RES and more specifically the FRT operation in order to provide the proper support to the power system when a grid fault occurs.

Chapter 3 proposes several adaptive tuning mechanisms that can accelerate the performance of a synchronization method. These adaptive tuning mechanisms have been applied to the structure of the dαβ-PLL in order to further improve its performance,

especially under balanced or unbalanced voltage sags. First, a novel tuning mechanism is proposed (and the adaptive dαβ-PLL is developed) to online adjust the tuning parameters of the PLL according to the type and the level of a voltage sag event in order to accelerate the synchronization response as much as possible without causing any violation of the grid codes. Then, a frequency phase decoupling method is implemented (and the FPD-dαβ-PLL is proposed), where the phase locked loop and the frequency locked loop are decoupled in the synchronization algorithm and further the integral tuning parameter is online adjusted in order to enhance the dynamic response of the synchronization. Finally, the two prior-mentioned adaptive tuning mechanisms are combined in the new adaptive FPD-dαβ-PLL, which achieves a significant improvement regarding its dynamic response under grid faults. The effect of the faster synchronization is also demonstrated in this chapter, where it is shown that a faster synchronization can accelerate the dynamic response of the GSC and consequently a more proper FRT operation can be achieved by the RES.

Two new synchronization methods for three-phase GSCs are proposed in Chapter 4, which achieve a fast dynamic response and present great immunity against harmonic distortion. First, the MSHDC-PLL is developed based on a novel decoupling network for the fast and accurate extraction of positive and negative sequences and all the existing harmonic orders. The only disadvantage of the MSHDC-PLL is the increased complexity/required processing time. Thus, a second PLL is proposed, named DNαβ-PLL, which can also achieve a fast and accurate synchronization under any grid conditions, but it requires a significantly less processing time. The fast synchronization can enable the proper dynamic FRT operation of RES while the accuracy against harmonic distortion can improve the power quality of the injected currents by the RES.

Chapter 5 proposes two new synchronization methods for single-phase GSC, which can achieve a fast response under grid disturbances and a very accurate response against voltage harmonic distortion. The first single-phase synchronization method, named MHDC-PLL, is designed based on a novel decoupling network that dynamically cancels out the effect of the low-order harmonics. The only disadvantages of the MHDC-PLL are the increased complexity and the inaccurate response under non nominal frequencies. These disadvantages are overcome in the second proposed synchronization method, named frequency adaptive MHDC-PLL. The frequency adaptive MHDC-PLL uses a frequency adaptive method for the quadrature signal generator to achieve an accurate response under any grid frequencies and a new decoupling network with decreased complexity for enabling an accurate response under harmonic distortion. The dynamic response of the proposed synchronization methods can enable a proper FRT operation of single-phase RES

while the robustness against harmonic distortion is beneficial for the power quality of the RES.

The appropriate operation of a RES requires an advanced current control methodology for enabling the accurate and high quality current injection by the GSC. Such an advanced current control technique is proposed in Chapter 6. The proposed current controller enhances the structure of the conventional current controller with an unbalanced compensation module and a harmonic compensation module in order to achieve a proper current injection under any grid conditions. Thus, the new current controller improves the overall operation of the GSC in term of accuracy under unbalanced grid faults and in terms of power quality. It is to be noted that the proposed current controller of Chapter 6 has been used on the simulation and experimental model of Chapter 2-Chapter 5 in order to investigate the effect of the advanced synchronization method on the overall performance of the GSC.

An investigation of different FRT strategies for RES is presented in Chapter 7. In this investigation, several FRT strategies according to the grid regulations has been studied based on analytic RES models that are interconnected with a realistic dynamic power system. The investigation highlights some issues on the current grid regulations that can cause undesired phenomena in the operation of the power system. Hence, some modifications of the existing grid codes are proposed in order to overcome these issues and ensure the proper operation of the grid.

Chapter 8 proposes a centralized control method for the RES in order to enhance the power stability of the power system. The control methodology is applied at the control center of the power system in order to decide the proper active and reactive power set-points for the RES for enhancing the stability of the system. The proposed methodology has been tested in a simulation model where both the RES and the power system have been integrated using fully analytic models. Finally, this Ph.D. dissertation concludes in Chapter 9, where the conclusions, the impact, and the future work are presented.

CHAPTER 2
A NEW HYBRID SYNCHRONIZATION METHOD

2.1 Introduction

The performance of a grid-connected RES is directly affected by the GSC controller, and especially by the response of the synchronization method. The synchronization method, usually a Phase-Locked Loop (PLL) algorithm, is responsible for the grid interconnection of RES with the power system. The accurate operation of the synchronization method can affect the power quality of the GSC while the fast synchronization response is directly affecting the dynamic performance of the GSC.

In the case of WPS and PV technology systems with rated power above 5 kW, a three-phase GSC is used to inject the produced energy into the power grid. This GSC is usually a two-level six-pack voltage source switching power electronic converter with six Insulated-Gate Bipolar Transistor (IGBT) components. The topology and the corresponding controller diagram for such a three-phase GSC is presented in Fig. 1.5, as it is described in the literature [27], [43]-[47]. In the case of small residential PV installations (with rated power below 5 kW) a single-phase two-level full-bridge switching power electronic converter based on four IGBTs or four Metal-Oxide-Semiconductor Field-Effect Transistors (MOSFETs) is usually used as a GSC. The topology of a single-phase GSC is also presented in Fig. 1.5 and the corresponding controller for this GSC is described in [27], [48]-[53]. Both GSC controllers for single- and three- phase systems are mainly based on a synchronization unit, a PQ controller unit and a current controller unit. These units are similar (with slight differences) for single- and three-phase GSCs according to the nature of each system. This chapter focuses on the synchronization methods for three-phase GSCs, while the single-phase synchronization methods are examined in Chapter 5.

This chapter initially presents a benchmarking of three synchronization methods for three-phase GSCs, with regards to their performance under various grid disturbances [28] (Section 2.3). The results from this benchmarking inspire the proposition of a new hybrid PLL [28], [29] (Section 2.4), named dαβ-PLL. The new dαβ-PLL inherits the advantages of two other PLLs and as a result the new PLL can achieve an improved performance with

regards to its dynamic response. The fast performance of a PLL based synchronization method is particularly desired under disturbances and grid faults in order to enable the proper dynamic and FRT operation of grid-connected RES [29], [32], [33].

2.2 Literature review

2.2.1 Conventional synchronization methods

The synchronization method is the most crucial unit of the GSC and is responsible for a proper grid interconnection of RES. A Phase-locked Loop (PLL) or Frequency-Locked Loop (FLL) algorithm can be used as a synchronization method in order to achieve the estimation of the phase angle and frequency of the fundamental grid voltage according to the voltage measurements at the PCC. The design of the GSC controller is usually based on space vector transformations in order to simplify the controller design and to enable a decoupled control of active and reactive power as explained in Appendix A. When the GSC controller is designed on a Synchronous Reference Frame (*dq*-frame) (see Appendix A.4) with Proportional-Integral (PI) controllers [27], [43], [48], then, the most important synchronization variable is the phase angle of the grid voltage and therefore, it is highly recommended to use a PLL algorithm for the synchronization. On the other hand, when the GSC is designed on the Stationary Reference Frame (*αβ*-frame) (see Appendix A.3) with Proportional-Resonant (PR) controllers [27], [43], [53], then, the frequency is the crucial synchronization variable and thus, it is intuitive to use FLL techniques. Some interesting FLL techniques are presented in [54]-[56]. This work mainly focuses on GSC controllers designed in one or multiple *dq*-frames and thus, only PLL techniques will be evaluated here. Some alternative methods for tracking the phase angle of the voltage are based on mathematical analysis approaches, such as the Discrete Fourier Transformation (DFT) based techniques [57], [58]. However, synchronization methods based on DFT present a relatively slow dynamic response and raise practical implementation issues, especially under non-nominal frequency grid operation. To overcome these practical issues, a variable sampling rate or an adaptive observation window length is required, techniques that are not always allowable in such real-time and high sampling rate applications.

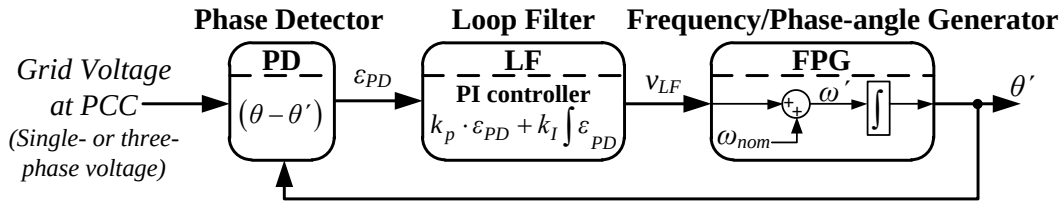

Fig. 2.1. The block diagram of an elementary PLL.

According to the aforementioned, the PLL based techniques constitute the most widely used synchronization methods for such grid-connected RES. A PLL based synchronization method is a closed-loop system and it consists of a Phase Detector (PD) unit, a Loop Filter (LF) unit which is usually a PI controller, and a Frequency/Phase-angle Generator (FPG) unit as analyzed in [27], [38]. The block diagram of an elementary PLL is presented in Fig. 2.1 , where θ is the phase angle of the grid voltage and θ' is the estimated phase by the PLL.

The dq-PLL

In the case of three-phase RES systems, a corresponding three-phase synchronization method is required in order to track the phase angle of the positive sequence of the grid voltage at the PCC. A conventional three-phase synchronization method designed in the *dq*-frame, named dq-PLL, has initially been proposed in [59] and its structure is presented in Fig. 2.2. The dq-PLL uses the transformation matrix $[T_{\theta'}]$ of (A.12) (see Appendix A.4) in order to translate the three-phase measurement voltage vector ($\mathbf{v}_{abc}$) into the *dq*-frame as $\mathbf{v}_{dq}$. Utilizing this transformation theory, the phase detector unit of the dq-PLL is given by the signal v_q as explained in (A.14) and summarized in (2.1).

$$\mathbf{v}_{dq} = \begin{bmatrix} v_d \\ v_q \end{bmatrix} = [T_{\theta'}]\mathbf{v}_{abc} = V\begin{bmatrix} \cos(\Delta\theta) \\ \sin(\Delta\theta) \end{bmatrix} \approx V\begin{bmatrix} \cos(\Delta\theta) \\ \Delta\theta \end{bmatrix} \tag{2.1}$$

where $\Delta\theta=\theta-\theta'$ is the phase difference between the grid phase angle (θ) and the estimated angle (θ'). Thus, when $\Delta\theta$ is small, v_q can operate as the phase detector unit of the dq-PLL. Further, the signal $v_d=V'$ can be used to estimate the amplitude V of the grid voltage.

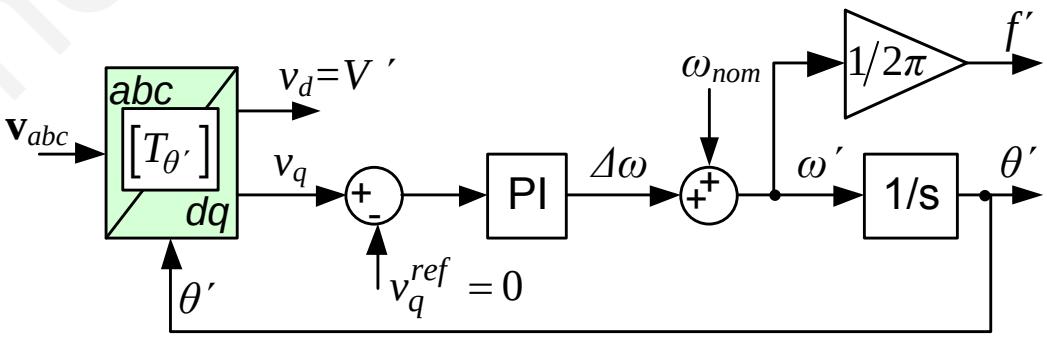

Fig. 2.2. The structure of the conventional dq-PLL.

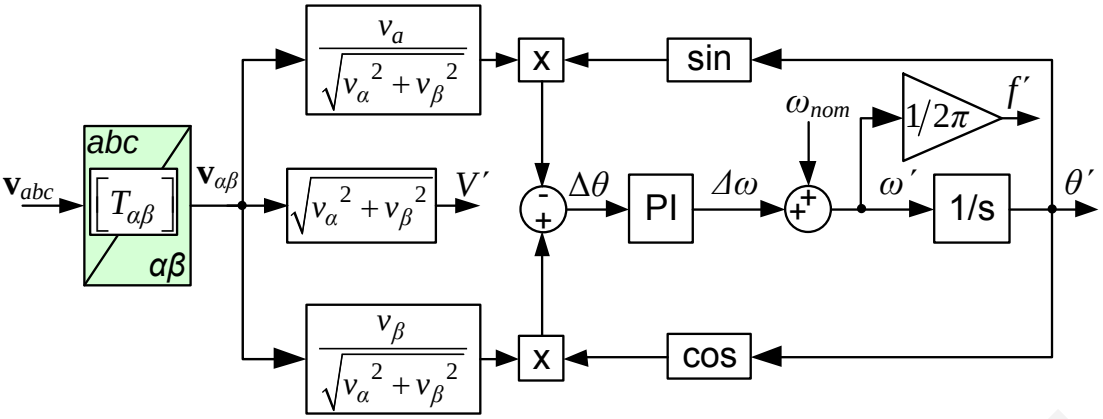

Fig. 2.3. The structure of the conventional αβ-PLL.

The αβ-PLL

Another conventional PLL technique, named αβ-PLL has been proposed in [60]-[62]. The αβ-PLL is implemented in the αβ-frame and its structure is presented in Fig. 2.3. The αβ-PLL utilizes the transformation matrix [$T_{\alpha\beta}$] of (A.5) (see Appendix A.3) in order to express the voltage vector $\mathbf{v}_{abc}$ into the $\alpha\beta$-frame as $\mathbf{v}_{\alpha\beta}$, as explained in (A.6) and shown below.

$$\mathbf{v}_{\alpha\beta} = \left[T_{\alpha\beta}\right]\mathbf{v}_{abc} = V\begin{bmatrix}\cos(\theta)\\ \sin(\theta)\end{bmatrix} \tag{2.2}$$

Thus, the phase detector unit of αβ-PLL can be developed by combining the resulted $\mathbf{v}_{\alpha\beta}$ with trigonometric identities as,

$$\Delta\theta = \theta - \theta' \approx \sin(\theta - \theta') = \sin(\theta)\cos(\theta') - \sin(\theta')\cos(\theta) \tag{2.3}$$

These conventional techniques (dq-PLL and αβ-PLL) are very simple regarding their structure and complexity. However, they can only ensure the accurate synchronization under ideal grid voltage conditions. Therefore, these PLLs are inaccurate under abnormal grid conditions, since the synchronization signals (estimated phase angle θ' and estimated angular frequency ω') are vulnerable against unbalanced conditions (negative sequence of voltage) and against voltage harmonic distortion. Hence, there is a need to advance the synchronization methods with regards to the accuracy and dynamic performance under any grid conditions. The accuracy of the synchronization method against unbalances and harmonic distortion is critical for ensuring a high quality current injection by the RES, while the fast time performance is necessary for a proper dynamic response of the RES under disturbances and FRT operation.

2.2.2 Advanced synchronization methods regarding the time performance

This chapter aims to advance the time performance of synchronization methods and to still present an accurate performance under balanced and unbalanced voltage disturbances. The study of this chapter does not consider the harmonic distortion effect and focuses only on enhancing the time performance of synchronization methods, which are accurate under balanced or unbalanced voltage sags. The fast time performance of the synchronization is critical especially under balanced and unbalanced grid faults in order to enable the proper FRT operation of an interconnected RES. As explained in Appendix A.5.2, the existence of negative sequence voltage components (under unbalanced voltage sags) can cause undesired double frequency oscillation on the synchronization signals (θ', f', $\mathbf{v}_{dq}$). Thus, these oscillations due to the unbalanced conditions (see Fig. A.3 of Appendix A.5.2), cause significant problems on the estimation of the phase angle (θ') and frequency (f') of the grid voltage and on the calculation of the positive sequence of the voltage vector in the dq-frame (v_{dq}^{+1}), which are the most useful components for the synchronization and control of GSC. Therefore, there is a need for advanced PLL algorithms that will enable a fast and accurate synchronization under balanced or unbalanced grid faults. In the literature, several methods have been proposed to mitigate these oscillations under unbalanced voltage conditions. The methods are mainly divided into two categories; the methods that apply a pre-filtering or pre-calculating stage within the phase detector unit in order to mitigate the effect of negative sequence and the methods that modify the loop filtering stage to achieve an improved response. Unfortunately, the robustness of synchronization methods against unbalanced conditions is usually compromised by an undesired deceleration of the time performance.

Methods based on a pre-filtering or a pre-calculating stage

A simple and intuitive method is presented in [63], which employs two low-pass filters (LPFs) in the closed-loop control path of the conventional dq-PLL. The LPFs are used to mitigate the double frequency oscillations on the synchronization signals (v_d, v_q) due to the unbalanced voltage conditions. However, the LPFs can critically decelerate the PLL performance.

An interesting method based on Dual Second-Order Generalized Integrator (DSOGI), named DSOGI-PLL, has been proposed in [63], [64]. The DSOGI-PLL is designed in the $\alpha\beta$-frame and uses two Second-Order Generalized Integrator (SOGI) based

quadrature signal generators in order to enable a positive-sequence voltage calculator. This method achieves an accurate operation under unbalanced conditions but its time performance is unavoidably affected as shown in the comparative analysis of [65]. The synchronization methods presented in [66]-[68] are enhanced with adaptive low-pass or notch filtering techniques in order to cancel out the undesired oscillations caused by the negative-sequence of voltage. Unfortunately, the adaptive filters used in these PLLs can also decelerate the response of the synchronization, which affects the dynamic operation of the RES. In [69], the three-phase Enhanced PLL (3E-PLL) is proposed based on four single-phase Enhanced PLLs (E-PLLs) [50], [70]-[72] and on symmetrical components theory (see Appendix A.5.1). The 3E-PLL actually uses an adaptive filtering based single-phase synchronization method (E-PLL) for each phase of the system and then combining the symmetrical components theory to estimate the phase angle of the positive-sequence of the voltage. The performance of 3E-PLL is compared with other PLLs in [65], where the 3E-PLL presents an accurate response under unbalanced grid conditions but slower dynamics compared to other PLLs.

Some other interesting synchronization solutions based on Moving Average Filters (MAFs) are proposed in [73]-[76]. These MAF based PLLs have a simplified structure and are robust against unbalanced and harmonic distorted grid conditions. However, such PLLs can present small inaccuracies when the grid frequency deviates from its nominal value due to discrete implementation restrictions. These inaccuracies can be minimized, but not completely eliminated, by adjusting the number of samples according to the operating frequency as suggested in [73]. The only way to completely eliminate these inaccuracies is to use a variable sampling period for the PLL to adapt the window length of the MAF [77], but the variable sampling rate can cause restrictions on the design of the GSC controller. Nevertheless, even if these inaccuracies are overcome, the main disadvantage of the MAF based PLLs is their slow dynamic performance.

Another synchronization solution is proposed in [65], which is based on a variable sampling period and on a sliding Goertzel transform filter. This technique shows improved dynamics and immunity to the voltage disturbances; however, the variable sampling rate on the PLL may not be always possible due to the restrictions of the GSC controller. A modified PLL has been proposed in [78] based on a non-linear adaptive approximation technique. This synchronization technique presents a higher degree of immunity to noise but unfortunately, this PLL presents very slow dynamics and thus, it is not appropriate to be used in control paths, as already mentioned in [78].

The ddsrf-PLL

A remarkable synchronization method also based on a pre-calculating/pre-filtering stage is the Decoupled Double Synchronous Reference Frame PLL (ddsrf-PLL), which has been initially proposed in [79] and its modified version is presented in [80], [81]. This method is designed in two Synchronous Reference Frames (SRF), the dq^{+1}-frame rotating with positive synchronous speed ($+\omega$) whose angular position is θ' and the dq^{-1}-frame rotating with negative synchronous speed ($-\omega$) whose angular position is $-\theta'$. Furthermore, a novel cross-feedback decoupling network is developed in [79] based on the two SRF in order to dynamically cancel out the double frequency oscillations on the positive sequence voltage due to the presence of unbalanced voltage, as shown in Fig. 2.4. The design of the coupling network of ddsrf-PLL [79] is based on the space vector transformation theory of Appendix A.

At this point, it is necessary to describe further the development of the decoupling network of ddsrf-PLL since it constitutes the cornerstone of this Ph.D. dissertation. In case of any unbalanced voltage conditions (see Appendix A.5.1) and of a three-wire

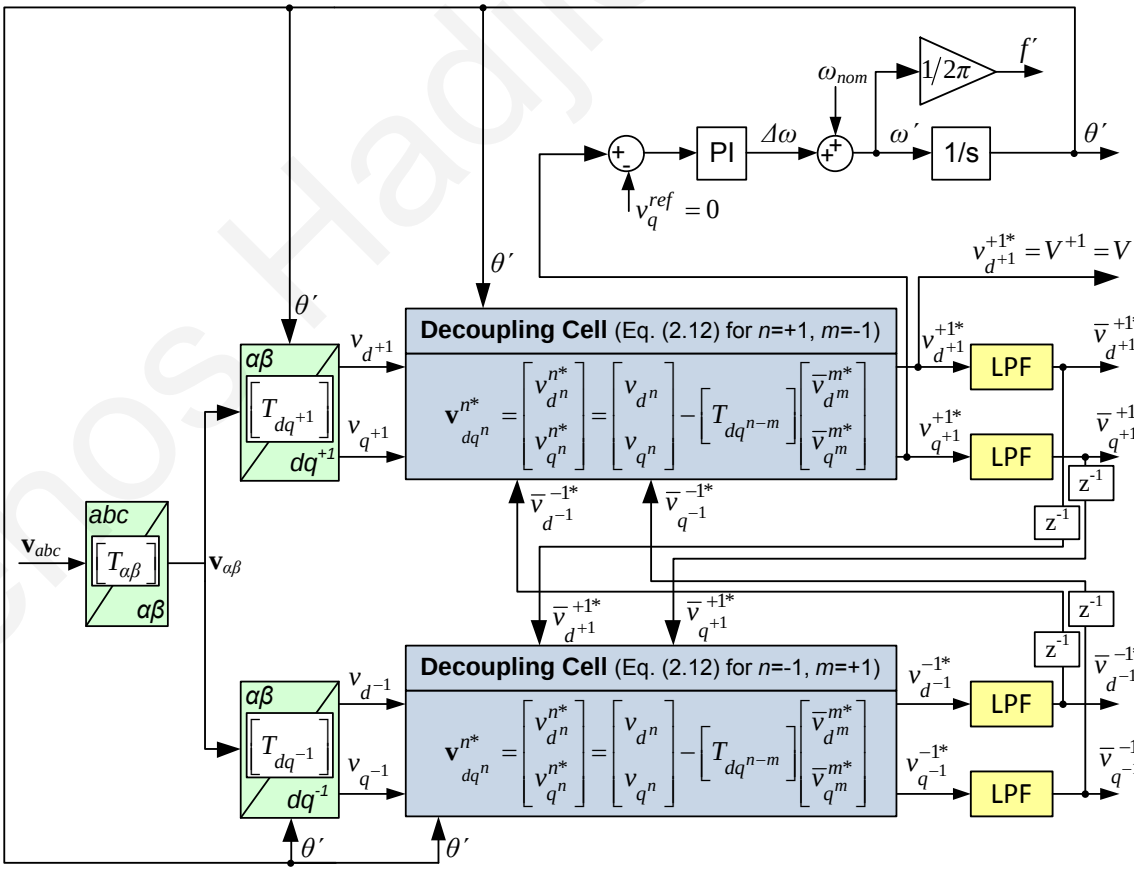

Fig. 2.4. The structure of the ddsrf-PLL.

interconnection of the GSC (eliminates the zero-sequence components), the voltage vector at the PCC can be expressed in the natural reference frame (*abc*-frame) as a summation of the positive (+1) and the negative (-1) sequence of the fundamental voltage component, as given by,

$$\mathbf{v}_{abc} = \mathbf{v}_{abc}{}^{+1} + \mathbf{v}_{abc}{}^{-1} \tag{2.4}$$

The voltage vector of (2.4) can be expressed in the stationary reference frame ($\alpha\beta$-frame), as shown in (2.5), by using the transformation matrix [$T_{\alpha\beta}$] according to Appendix A.3.

$$\begin{aligned} \mathbf{v}_{\alpha\beta} &= \left[T_{\alpha\beta}\right]\mathbf{v}_{abc} = \left[T_{\alpha\beta}\right]\left(\mathbf{v}_{abc}^{+1} + \mathbf{v}_{abc}^{-1}\right) \\ \Leftrightarrow \mathbf{v}_{\alpha\beta} &= \mathbf{v}_{\alpha\beta}^{+1} + \mathbf{v}_{\alpha\beta}^{-1} = V^{+1}\begin{bmatrix}\cos(+\omega t + \varphi^{+1})\\ \sin(+\omega t + \varphi^{+1})\end{bmatrix} + V^{-1}\begin{bmatrix}\cos(-\omega t + \varphi^{-1})\\ \sin(-\omega t + \varphi^{-1})\end{bmatrix} \end{aligned} \tag{2.5}$$

Therefore, according to the theory of Appendix A.4, the unbalanced voltage vector $\mathbf{v}_{\alpha\beta}$ of (2.5) can be re-expressed in any dq^n-SRF rotating with an angular frequency ($n\omega$) whose angular position is θ_n', by using (2.6).

$$\begin{aligned} \mathbf{v}_{dq^n} &= \left[T_{dq^n}\right]\cdot\mathbf{v}_{\alpha\beta} = \left[T_{dq^n}\right]\cdot\left(\mathbf{v}_{\alpha\beta}^{+1} + \mathbf{v}_{\alpha\beta}^{-1}\right) \\ \text{where: } \left[T_{dq^n}\right] &= \begin{bmatrix}\cos(\theta_n') & \sin(\theta_n')\\ -\sin(\theta_n') & \cos(\theta_n')\end{bmatrix} \text{ and } \theta_n' = n\omega t \end{aligned} \tag{2.6}$$

Thus, the transformation of the vector $\mathbf{v}_{\alpha\beta}$ into the positive sequence dq^{+1}-frame can be achieved by substituting n=+1 in (2.6), as presented in (2.7).

$$\begin{aligned} \mathbf{v}_{dq^{+1}} &= \left[T_{dq^n}\right]\Big|_{n=+1}\cdot\mathbf{v}_{\alpha\beta} = \left[T_{dq^{+1}}\right]\cdot\left(\mathbf{v}_{\alpha\beta}^{+1} + \mathbf{v}_{\alpha\beta}^{-1}\right) = \mathbf{v}_{dq^{+1}}^{+1} + \mathbf{v}_{dq^{+1}}^{-1} \\ \Leftrightarrow \mathbf{v}_{dq^{+1}} &= \underbrace{V^{+1}\begin{bmatrix}\cos(\varphi^{+1})\\ \sin(\varphi^{+1})\end{bmatrix}}_{\substack{\text{Oscillation-free}\\ \text{Terms}}} + \underbrace{V^{-1}\begin{bmatrix}\cos(-2\omega t + \varphi^{-1})\\ \sin(-2\omega t + \varphi^{-1})\end{bmatrix}}_{\substack{\text{Double-frequency oscilation}\\ \text{Terms}}} \\ \Leftrightarrow \mathbf{v}_{dq^{+1}} &= \mathbf{v}_{dq^{+1}}^{+1} + \left[T_{dq^{+2}}\right]\mathbf{v}_{dq^{-1}}^{-1} \\ \text{where: } \mathbf{v}_{dq^{+1}}^{+1} &= V^{+1}\begin{bmatrix}\cos(\varphi^{+1})\\ \sin(\varphi^{+1})\end{bmatrix} \quad \textit{and} \quad \mathbf{v}_{dq^{-1}}^{-1} = V^{-1}\begin{bmatrix}\cos(\varphi^{-1})\\ \sin(\varphi^{-1})\end{bmatrix} \end{aligned} \tag{2.7}$$

By using trigonometric identities, it is possible to re-write (2.7) in terms of oscillation-free terms as,

$$\mathbf{v}_{dq^{+1}} = \mathbf{v}_{dq^{+1}}^{+1} + \mathbf{v}_{dq^{+1}}^{-1} = \mathbf{v}_{dq^{+1}}^{+1} + \left[T_{dq^{+2}}\right]\mathbf{v}_{dq^{-1}}^{-1} \tag{2.8}$$

$$\text{where: } \mathbf{v}_{dq^{+1}}^{+1} = V^{+1}\begin{bmatrix}\cos(\varphi^{+1})\\ \sin(\varphi^{+1})\end{bmatrix}, \mathbf{v}_{dq^{-1}}^{-1} = V^{-1}\begin{bmatrix}\cos(\varphi^{-1})\\ \sin(\varphi^{-1})\end{bmatrix}$$

It is to be noticed that for the purposes of this Ph.D. dissertation, the annotation $\mathbf{v}_{dq^n}^{m}$ represents the *m* sequence/harmonic component of the voltage vector expressed in dq^n-frame rotating with an angular frequency $n\cdot\omega$, where ω is the fundamental angular frequency of the power grid. Thus, in (2.7), the $\mathbf{v}_{dq^{+1}}^{+1}$ represents the positive sequence of the voltage vector $\mathbf{v}^m$ (where *m*=+1) expressed in the dq^n-SRF (where *n*=+1). It is obvious that $\mathbf{v}_{dq^{+1}}^{+1}$ consists of an oscillation-free matrix with "Constants/DC" terms, which are dependent only on the amplitude (V^{+1}) and the initial phase angle (φ^{+1}) of the positive sequence voltage vector. The corresponding $\mathbf{v}_{dq^{+1}}^{-1}$ matrix of (2.7) represents the negative sequence of the voltage vector $\mathbf{v}^m$ (where *m*=-1) expressed in the dq^n-SRF (where *n*=+1). It is worth to notice that the $\mathbf{v}_{dq^{+1}}^{-1}$ consists of an oscillation matrix with terms that oscillate with a rotational speed equal to (*m*-*n*)ω.

Similarly, the unbalanced voltage vector $\mathbf{v}_{\alpha\beta}$ of (2.5) can be re-expressed in the corresponding dq^{-1}-frame rotating with an angular frequency (-ω) by substituting *n*=-1 in (2.6), as given by,

$$\mathbf{v}_{dq^{-1}} = \left[T_{dq^n}\right]\Big|_{n=-1}\cdot\mathbf{v}_{\alpha\beta} = \left[T_{dq^{-1}}\right]\cdot\left(\mathbf{v}_{\alpha\beta}^{+1} + \mathbf{v}_{\alpha\beta}^{-1}\right) = \mathbf{v}_{dq^{-1}}^{+1} + \mathbf{v}_{dq^{-1}}^{-1}$$

$$\Leftrightarrow \mathbf{v}_{dq^{-1}} = \underbrace{V^{+1}\begin{bmatrix}\cos(+2\omega t+\varphi^{+1})\\ \sin(+2\omega t+\varphi^{+1})\end{bmatrix}}_{\substack{\text{Double-frequency oscilation}\\ \text{Terms}}} + \underbrace{V^{-1}\begin{bmatrix}\cos(\varphi^{-1})\\ \sin(\varphi^{-1})\end{bmatrix}}_{\substack{\text{Oscillation-free}\\ \text{Terms}}} \tag{2.9}$$

Equation (2.9) can also be re-written in terms of oscillation-free terms as,

$$\mathbf{v}_{dq^{-1}} = \mathbf{v}_{dq^{-1}}^{+1} + \mathbf{v}_{dq^{-1}}^{-1} = \left[T_{dq^{-2}}\right]\mathbf{v}_{dq^{+1}}^{+1} + \mathbf{v}_{dq^{-1}}^{-1} \tag{2.10}$$

In this case, the $\mathbf{v}_{dq^{-1}}^{-1}$ consists of oscillation-free terms and represents the negative sequence of the voltage vector $\mathbf{v}^m$ (where *m*=-1) expressed in the corresponding dq^n-frame (where *n*=-1). The corresponding $\mathbf{v}_{dq^{+1}}^{-1}$ matrix represents the component $\mathbf{v}^m$ of the voltage vector (where *m*=-1) expressed in the dq^n-frame (where *n*=+1). The $\mathbf{v}_{dq^{-1}}^{+1}$ consists of an oscillation matrix with terms that oscillate with a rotational speed of (*m*-*n*)ω.

It is worth mentioning that these double frequency $(m\text{-}n)\omega$ oscillation terms are the reasons for the inaccuracies of synchronization methods under unbalanced conditions. The ddsrf-PLL proposed a decoupling network that dynamically cancels out these oscillations and thus, a fast and accurate synchronization is enabled under unbalanced voltage sags. As can be observed by (2.7) and (2.9), the DC terms in the dq^{+1}- and dq^{-1}-frame correspond to the amplitudes of the sinusoidal signals of $\mathbf{v}^{+1}$ and $\mathbf{v}^{-1}$ respectively. On the other hand, the double frequency oscillations on dq^{+1}-frame correspond to the $\mathbf{v}^{-1}$ vector, which rotates in the opposite direction, compared to the dq^{+1}-frame. The same coupling effect causes the double frequency oscillations on the dq^{-1}-frame due to the opposite rotation of the $\mathbf{v}^{+1}$ vector.

Therefore, the cross-feedback decoupling network of ddsrf-PLL [79] aims to estimate the DC terms in the dq^{+1}- and dq^{-1}-frames by dynamically subtracting the coupling effect between the two axes as shown in Fig. 2.4. Since the vectors $\mathbf{v}^{+1}$ and $\mathbf{v}^{-1}$ are unknown, the decoupling network initially expresses the voltage vector $\mathbf{v}=\mathbf{v}_{\alpha\beta}$ in both the dq^{+1}- and dq^{-1}-frames, and then tries to subtract the coupling effect between the two frames. To enable the subtraction of the coupling effect, the "Constant/DC" terms $\mathbf{v}_{dq^n}^{n}$ need to be estimated first. This can be done by resolving (2.8) or (2.10) in its general form in terms of the oscillation-free terms $\mathbf{v}_{dq^n}^{n}$ and $\mathbf{v}_{dq^m}^{m}$ where n =+1 and m=-1 or n =-1 and m=+1, as shown in (2.11).

$$\begin{aligned} &\mathbf{v}_{dq^n} = \left[T_{dq^n}\right]\cdot\mathbf{v}_{\alpha\beta} = \left[T_{dq^n}\right]\cdot\left(\mathbf{v}_{\alpha\beta}^{n}+\mathbf{v}_{\alpha\beta}^{m}\right) = \mathbf{v}_{dq^n}^{n}+\mathbf{v}_{dq^n}^{m} \\ &\Leftrightarrow \mathbf{v}_{dq^n}^{n} = \left[T_{dq^n}\right]\cdot\mathbf{v}_{\alpha\beta}-\mathbf{v}_{dq^n}^{m} = \mathbf{v}_{dq^n}-\left[T_{dq^{n-m}}\right]\mathbf{v}_{dq^m}^{m} \end{aligned} \tag{2.11}$$

Then, the vector $\mathbf{v}_{dq^n}^{n}$ can be approximated by the estimation vector $\mathbf{v}_{dq^n}^{n*}$ as given by (2.12), where the vector $\mathbf{v}_{dq^m}^{m}$ has been replaced by its estimated version $\bar{\mathbf{v}}_{dq^m}^{m*}$.

$$\begin{aligned} &\mathbf{v}_{dq^n}^{n*} = \left[T_{dq^n}\right]\cdot\mathbf{v}_{\alpha\beta}-\left[T_{dq^{n-m}}\right]\bar{\mathbf{v}}_{dq^m}^{m*} = \mathbf{v}_{dq^n}-\left[T_{dq^{n-m}}\right]\bar{\mathbf{v}}_{dq^m}^{m*} \\ &\Leftrightarrow \begin{bmatrix} v_{d^n}^{n*} \\ v_{q^n}^{n*} \end{bmatrix} = \begin{bmatrix} v_{d^n} \\ v_{q^n} \end{bmatrix} - \left[T_{dq^{n-m}}\right]\begin{bmatrix} \bar{v}_{d^m}^{m*} \\ \bar{v}_{q^m}^{m*} \end{bmatrix} \end{aligned} \tag{2.12}$$

Finally, the estimated vector $\bar{\mathbf{v}}_{dq^m}^{m*}$ is given by filtering the $\mathbf{v}_{dq^m}^{m*}$ through the first-order Low Pass Filter (LPF) $F(s)$ as shown in (2.13), in order to eliminate any remaining oscillations.

$$\bar{\mathbf{v}}_{dq^m}^{m*} = F(s) \cdot \mathbf{v}_{dq^m}^{m*} \tag{2.13}$$

where: $\bar{\mathbf{v}}_{dq^m}^{m*} = \begin{bmatrix} \bar{v}_{d^m}^{m*} \\ \bar{v}_{q^m}^{m*} \end{bmatrix}$, $F(s) = \frac{\omega_f}{s + \omega_f}$, and $\mathbf{v}_{dq^m}^{m*} = \begin{bmatrix} v_{d^m}^{m*} \\ v_{q^m}^{m*} \end{bmatrix}$

The cross-feedback decoupling network of ddsrf-PLL [79] is actually developed in two SRFs by employing (2.12) in each decoupling cell, once for n=+1 and m=-1 and once for n=-1 and m=-1 as shown in Fig. 2.4. It is to be noticed that a sample delay is used for the signals of the cross-feedback decoupling network in order to avoid any algebraic loops. The design parameter ω_f should be set equal to $\omega/\sqrt{2}$, where ω is the grid operating angular frequency, in order to achieve a reasonable trade-off between the time response and the oscillation damping as analyzed in [79]. Then, the ddsrf-PLL estimates the phase angle of the positive sequence of the fundamental voltage component by trying to force the estimated $v_{q^n}^{n*}$ to track zero through the dq-PLL algorithm [59], which has already been explained in Section 2.2.1. The structure of the ddsrf-PLL is analytically presented in Fig. 2.4.

It is worth to mention that the ddsrf-PLL can achieve a very fast and accurate performance under phase jumps, frequency changes, balanced or unbalanced voltage sags and thus it is considered one of the state-of-the-art synchronization methods. Ddsrf-PLL is a widely used synchronization solution, since its fast and accurate operation under unbalanced faults can enable the proper FRT operation of RES in order to meet the new grid regulations regarding the grid interconnection of RES. The only disadvantages of ddsrf-PLL are: the high overshoot on the estimation of the phase angle and frequency when a grid fault occurs and the fact that the immunity of the ddsrf-PLL against harmonic distortion is restricted, especially for low-order harmonics.

2.3 A benchmarking of three synchronization methods

The technical part of this Ph.D. dissertation begins with a benchmarking of three PLLs: the dq-PLL [59] (presented in Section 2.2.1), the αβ-PLL [60]-[62] (presented in Section 2.2.1) and the ddsrf-PLL [79] (presented in Section 2.2.2). The benchmarking of the PLLs is based on dynamic models (for the GSC among with its controller and its synchronization units) implemented in PSCAD and MATLAB/Simulink.

TABLE 2.1: PARAMETERS OF PI CONTROLLER FOR PLLS

Time Response Settings	dq-PLL		αβ-PLL		ddsrf-PLL		dαβ-PLL	
	k_p	T_i	k_p	T_i	k_p	T_i	k_p	T_i
Slow	36.8	0.0066	16.4	0.0333	36.8	0.0066	15.5	0.0376
Medium	73.6	0.0030	34.1	0.0138	78.6	0.0026	32.7	0.0150
Fast	200.0	0.0004	102.2	0.0015	184.0	0.0005	93.9	0.0180
According to German grid codes	-	-	-	-	22.44	0.0179	12.35	0.059

One of the main targets of this investigation is to investigate the effect of tuning parameters of PLLs on their performance. For this reason, the tuning parameters of each PLL have been selected appropriately in order to have three different time responses (fast-medium-slow). A fast response is defined as the time response where the settling time is equal to 2T (T=20 ms), medium response is the time response where the settling time is 4T and slow response is where the settling time is equal to 6T. The regulation for the time response has been set based on a 50% symmetrical voltage sag, since the low voltage fault ride through operation will be examined in this Section. The design tuning parameters of the PLLs are selected based simulation results and on the theory of Appendix B. The tuning parameters for each PLL are presented in TABLE 2.1.

The investigation of the response of the three different PLLs has indicated three important conclusions as shown in Fig. 2.5 and Fig. 2.6 and as briefly mentioned below:

- the dq-PLL and the αβ-PLL present significant inaccuracies when an unbalanced low-voltage sag occurs. On the other hand, the ddsrf-PLL achieves an accurate response under unbalanced voltage conditions without affecting its time performance. These conclusions are demonstrated in Fig. 2.6.

- the fast tuning of a PLL can negatively affect the overshoot of the synchronization signals. When the PLL is set to achieve a fast time performance (the settling time regulates to 40 ms), then an undesired higher overshoot appears on the estimation of the synchronization signals. Fig. 2.5 depicts the overshoot on the estimation of the frequency for three different settling times (fast-medium-slow) for each PLL. This observation is an inspiration for the adaptive tuning mechanism that will be presented in Section 3.3.

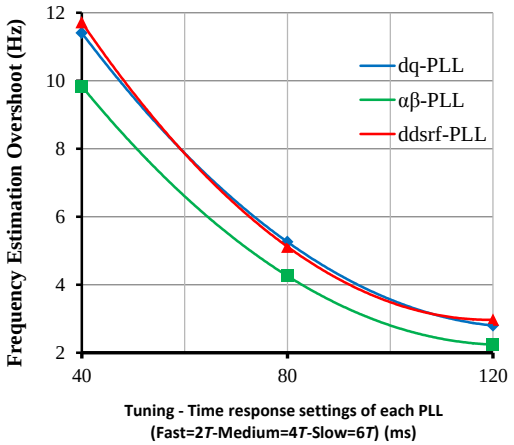

Fig. 2.5. Simulation results showing the effect of changing the settings/tuning of the time response of the three PLLs in terms of the overshoot of the frequency estimation under a symmetrical fault with 50% voltage sag.

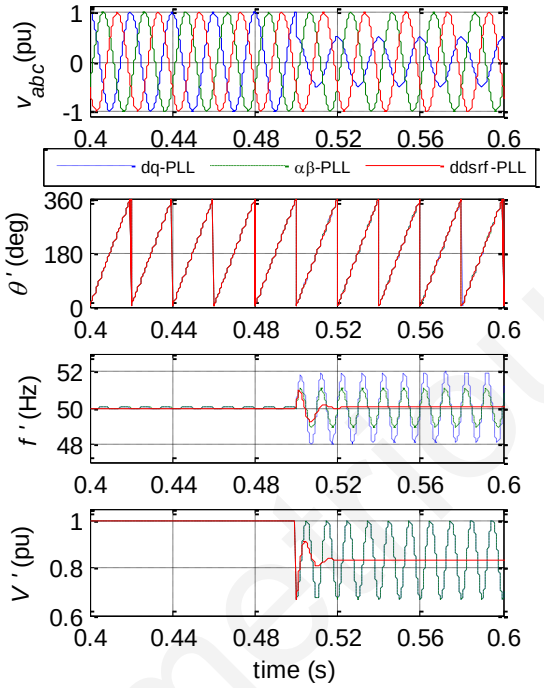

Fig. 2.6. Simulation results for the response of the three under investigation PLLs under a Type B [91] unbalanced fault with 50% voltage sag on phase A (when the PLLs are set to a medium time response according to TABLE 2.1).

- The dq-PLL and the ddsrf-PLL present identical overshoot on the estimation signals when a grid fault occurs as shown in Fig. 2.5. This fact is expected, since the two PLLs are using the same algorithm (dq-PLL) to track the grid phase angle. The additional decoupling network of ddsrf-PLL achieves an accurate decoupling of the positive sequence of the grid voltage without significantly affecting the time performance of the PLL and that is why the ddsrf-PLL can accurately operate under unbalanced conditions. On the other hand, the αβ-PLL presents a lower overshoot (under the same setting for the settling time) compared to the other PLLs due to the different algorithm that they use to track the phase angle as demonstrated in Fig. 2.5. This observation in combination with the abovementioned conclusion is the cornerstone of suggesting a new hybrid PLL, as it is proposed in Section 2.4.

Furthermore, the analytical benchmarking performed in this Section enables a full comparison between the three PLL algorithms in six important axes. These axes are:

- computational efficiency (1/complexity) of the synchronization algorithm
- dynamic performance of the synchronization

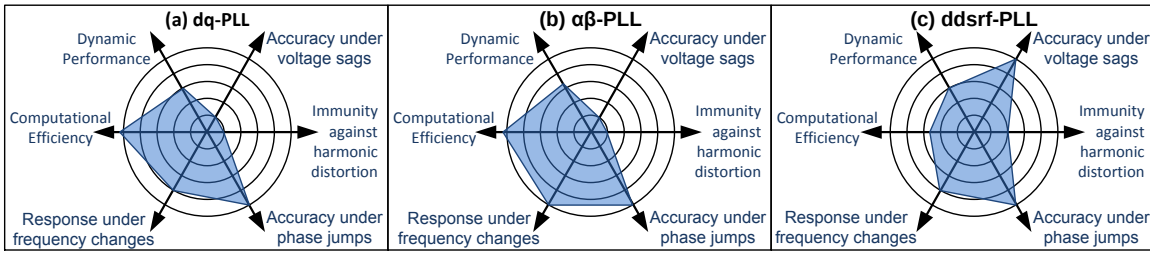

Fig. 2.7. Synopsis of the performance benchmarking between three synchronization methods: (a) the dq-PLL, (b) the αβ-PLL and (c) the ddsrf-PLL

- synchronization accuracy under balanced or unbalanced voltage sag
- immunity of the synchronization against harmonic distortion
- synchronization accuracy under phase jump events
- response of the synchronization under frequency change events

The synopsis of the performance comparison between the dq-PLL, the αβ-PLL and the ddsrf-PLL is presented in Fig. 2.7. Fig. 2.7 shows that only the ddsrf-PLL can achieve an accurate operation under unsymmetrical voltage conditions. Further, the αβ-PLL can achieve slightly faster dynamic performance in case where the three PLL are set in a way to present the same overshoot on the synchronization signals.

2.4 A new hybrid PLL (dαβ-PLL)

The investigation presented in Section 2.3 is the cornerstone for proposing a new hybrid PLL, named decoupled PLL designed in the αβ-frame (dαβ-PLL). According to this benchmarking, the decoupling network of the ddsrf-PLL enables an accurate synchronization response under unbalanced voltage conditions and the overshoot on the synchronization signals under grid fault is lower in case of αβ-PLL. These two observations can lead to the implementation of a new hybrid PLL, the dαβ-PLL, which inherits the advantages from both the ddsrf-PLL and the αβ-PLL.

2.4.1 The structure of the dαβ-PLL

The results of Fig. 2.6 prove that the decoupling network (two decoupling cells) of ddsrf-PLL enables an accurate performance under non-symmetrical conditions without affecting the dynamic performance of the synchronization. On the other hand dq-PLL and αβ-PLL fail to present an accurate response under asymmetrical conditions. Moreover, the simulation results in Fig. 2.5 show how the changing of the time response settings of the

under investigation PLLs affects the overshoot of the frequency estimation when a 50% balanced voltage sag occurs. Clearly, the desired faster operation of a PLL causes undesirably higher overshoots in the frequency. An important conclusion from Fig. 2.5 is that the overshoot of αβ-PLL is always lower (18% lower on average) in comparison to the other two PLLs. Further, the dq-PLL and ddsrf-PLL present very similar responses under balanced voltage sags, since the structure of the ddsrf-PLL is based on the dq-PLL and on two decoupling cells (for an accurate response under unbalanced conditions).

The new hybrid dαβ-PLL is developed by combining the structure of a corresponding PLL in order to inherit its specific advantage. Thus, the proposed hybrid dαβ-PLL is a combination of the decoupling cells of ddsrf-PLL (Fig. 2.4) in order to decouple the voltage sequences and the αβ-PLL algorithm (Fig. 2.3) in order to estimate the phase angle of the grid voltage, which offers lower estimation overshoot instead of the algorithm that is used in the dq-PLL (Fig. 2.2). The new hybrid dαβ-PLL aims at operating very accurately under balanced and unbalanced disturbances and also at having a lower phase angle and frequency overshoot than the ddsrf-PLL. It is worth to mention that a desired faster operation could be achieved by the suggested dαβ-PLL, if the PLLs are set in

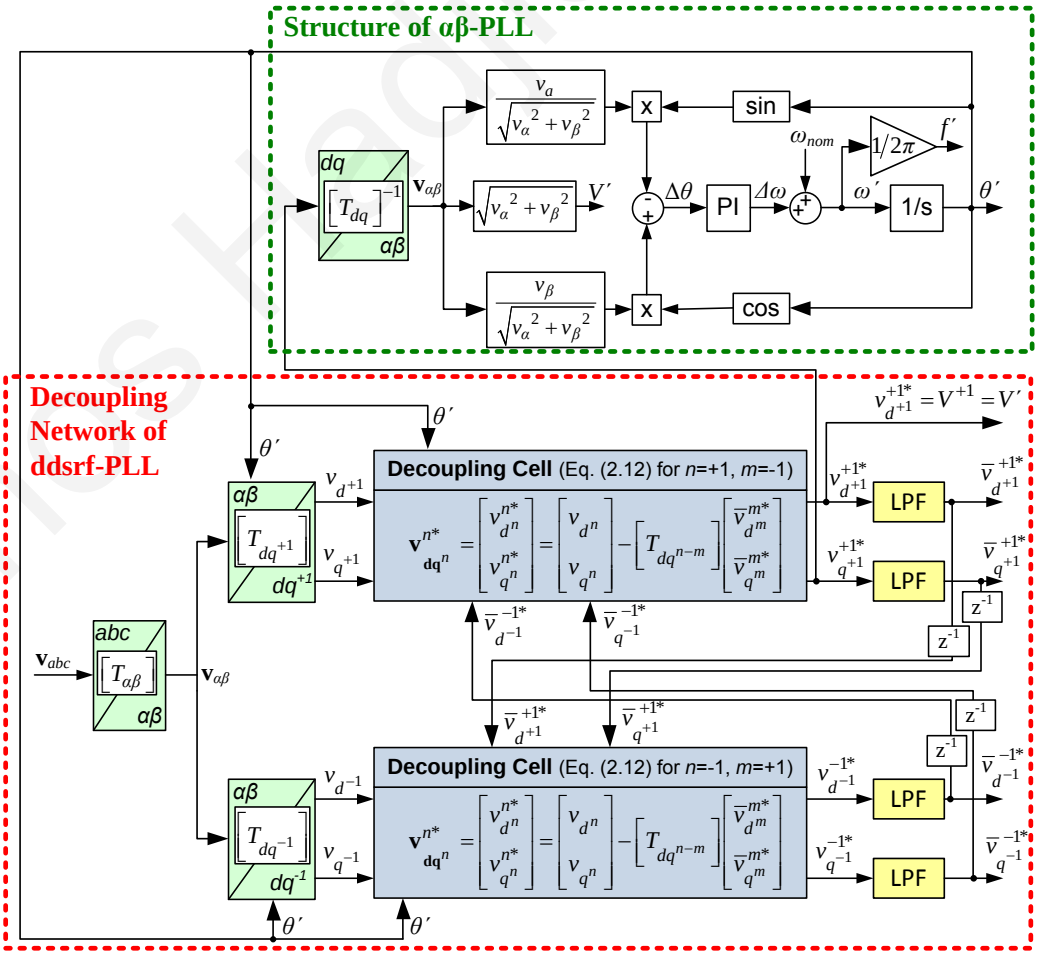

Fig. 2.8. The structure of the new hybrid dαβ-PLL.

a way to operate within the same frequency limits (frequency limits are defined according to the grid regulations [11]-[27]). The structure of the proposed dαβ-PLL is illustrated in Fig. 2.8. The new dαβ-PLL has been designed to also have three different time responses (fast-medium-slow) as shown in TABLE 2.1 in order to be reliable compared to the other PLLs. In the next sub-sections, a detailed simulation and experimental investigation of the dαβ-PLL are presented to prove its improved performance.

2.4.2 Simulation results

A comparison of the new proposed dαβ-PLL to the other PLLs is necessary in order to demonstrate its advantages. The comparison focuses especially on the dαβ-PLL and the ddsrf-PLL, which are the only ones that are able to operate accurately under unbalanced disturbances. In order to enable a fair investigation based on realistic conditions, a dynamic model of an interconnected GSC has been implemented among with its controller (GSC controller). Therefore, the operation of each synchronization unit is examined when the PLL operates within the controller loop of the GSC. This is essential since the synchronization method is the most critical part of the GSC controller and its response can affect the performance of the GSC and the operation of the whole RES.

Dynamic system model for the investigation

The dynamic ElectroMagnetic Transient (EMT) model for the GSC among with its controller has been developed in two simulation tools, PSCAD and MATLAB/Simulink, and the results are identical in both software. The dynamic model includes a DC source that emulates the produced power by a RES, a power electronic based GSC and its controller, a second-order LC filter and a three-phase voltage source (to emulate the power grid) as presented in Fig. 2.9. The GSC controller, which is presented in Fig. 2.9, has been developed for the dynamic model of this investigation. The GSC controller is designed on a Synchronous Reference Frame (SRF) using PI controllers [27], [29], [43] and consists of a synchronization method, a current controller, a PQ controller and a PWM unit.

The synchronization method estimates the phase angle of grid voltage, which is necessary for the transformation matrices. It is to be noted that the synchronization method may consist of the ddsrf-PLL or the new dαβ-PLL. Further, for improving the proper operation of the GSC under unbalanced voltage conditions, the vector $\mathbf{v}_{dq}$ that is used in the controller is considered equal to the vector $\mathbf{v}_{dq^{+1}}^{+1*}$ as estimated by the ddsrf-PLL or the dαβ-PLL.

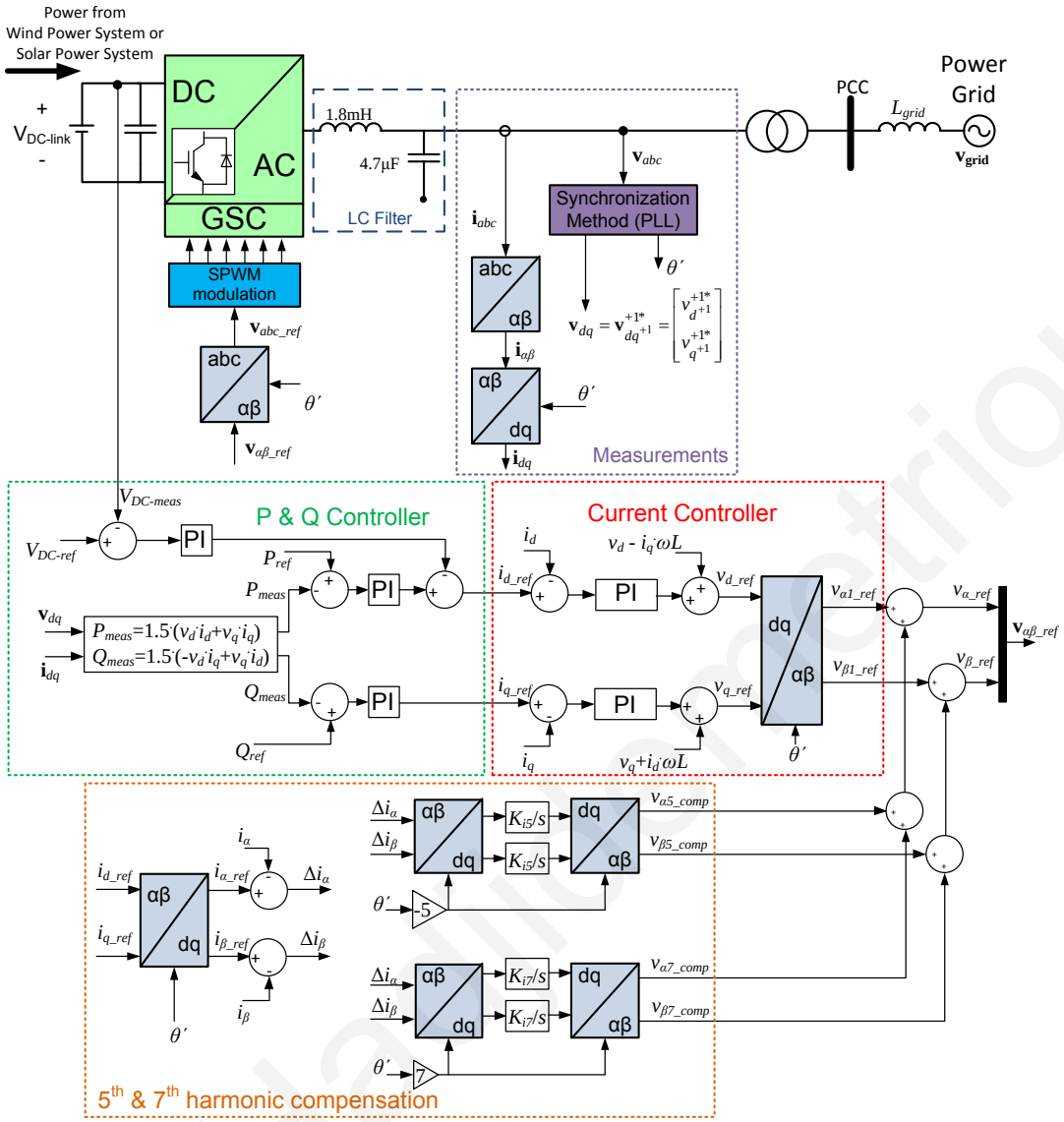

Fig. 2.9. An interconnected RES among with the associated controller of the GSC (including the PLL, the current controller and the PQ controller).

The PQ controller calculates the operating active (P_{meas}) and reactive (Q_{meas}) power conditions of the GSC based on the voltage ($\mathbf{v}_{dq}$) and current ($\mathbf{i}_{dq}$) measurement vectors and according to (A.10) of Appendix A . Then, the PQ controller generates the reference currents through PI controllers. It is noticeable that the PQ controller also controls the voltage of the DC-link ($V_{DC\text{-}meas}$) to be equal to the reference voltage ($V_{DC\text{-}ref}$) through a PI controller in order to ensure that all the produced energy by the RES will be properly injected into the grid.

The current controller [43] ensures that the GSC will track the reference currents by generating the corresponding reference voltage vector $\mathbf{v}_{ref}$ through PI controllers. The vector $\mathbf{v}_{ref}$ is initially generated in the dq^{+1}-frame ($\mathbf{v}_{dq\_ref}$) by the current controller and then expressed back to the stationary αβ-frame ($\mathbf{v}_{\alpha\beta\_ref}$) and to the natural abc-frame ($\mathbf{v}_{abc\_ref}$).

The vector $\mathbf{v}_{abc\_ref}$ is fed to the Sinusoidal Pulse Width Modulation (SPWM) unit to generate the pulses that drive the IGBTs of the GSC in order to control its operation. It should be mentioned that the current controller [43] of Fig. 2.9 cannot inject sinusoidal currents under unbalanced voltage sags. In case where such sinusoidal current injection is required under unbalanced faults, then more advanced current controllers need to be developed, such as the current controllers presented in Chapter 6 and in [40], [82]-[87]. Another important aspect for the GSC controller is that in case where there is background harmonic distortion coming from the grid, then the GSC controller should be enhanced with a Harmonic Compensation (HC) unit to improve the power quality of the GSC. The diagram of Fig. 2.9, shows that the controller developed for the investigation of this Section is enhanced with a HC algorithm [88]-[90] that eliminates the effect of the -5^{th} and $+7^{th}$ harmonics. This HC method transforms the corresponding harmonic currents into DC quantities by using -5ω and $+7\omega$ (frequency shifting). If other harmonics are contained in the currents, when currents are transformed into the dq^{-5}- and dq^{+7}-frames, these harmonics will be disturbed as a ripple, so a low pass filter or an integral controller is used before the signals are transformed back to the stationary frame and added to the reference signal in order to compensate the harmonics.

The dynamic simulation model implemented in both PSCAD and MATLAB/Simulink allows performing a detailed investigation for the performance of the dαβ-PLL as presented in the following Section.

Performance of the two PLLs under different time response settings

The operation of the dαβ-PLL and the ddsrf-PLL in an interconnected RES is simulated in PSCAD and the results are presented in Fig. 2.10 under an unbalanced voltage sag (Type E [91] - two-phase to ground fault), with a 50% voltage sag on phases B and C. The dαβ-PLL can detect accurately the positive and negative sequence voltages, as illustrated in Fig. 2.10. The operation of the dαβ-PLL and the ddsrf-PLL is demonstrated in Fig. 2.10(a)-(c) for the three different time response settings of each PLL, where it is noticed that the time response to detect the frequency and the phase angle is exactly the same for the two PLLs, but the overshoot of dαβ-PLL is lower by 29% on average, compared to the overshoot of the ddsrf-PLL.

The overshoot for the two PLLs is illustrated in Fig. 2.11 under an unbalanced fault (Type E [91] – two-phase to ground) with a 50% voltage sag into the two phases. Similarly, Fig. 2.12 summarizes the overshoot on the frequency estimation under unbalanced fault (Type B [91] - single-phase to ground) conditions with a 50% voltage sag in phase A. Fig. 2.11 and Fig. 2.12 actually summarize the estimation frequency overshoot when the two PLLs are regulated to fast (2*T*), medium (4*T*) and slow (6*T*) time response tuning settings. The simulation results show that the new dαβ-PLL has a better performance, since it operates accurately under unbalanced conditions and the overshoot of dαβPLL is on average 29% lower during two-phase to ground fault (see Fig. 2.11) and 45% lower under single-phase to ground fault (see Fig. 2.12) . The dαβ-PLL is also the preferable solution compared to the dq-PLL and αβ-PLL, since only the dαβ-PLL can accurately operate under unbalanced grid disturbances.

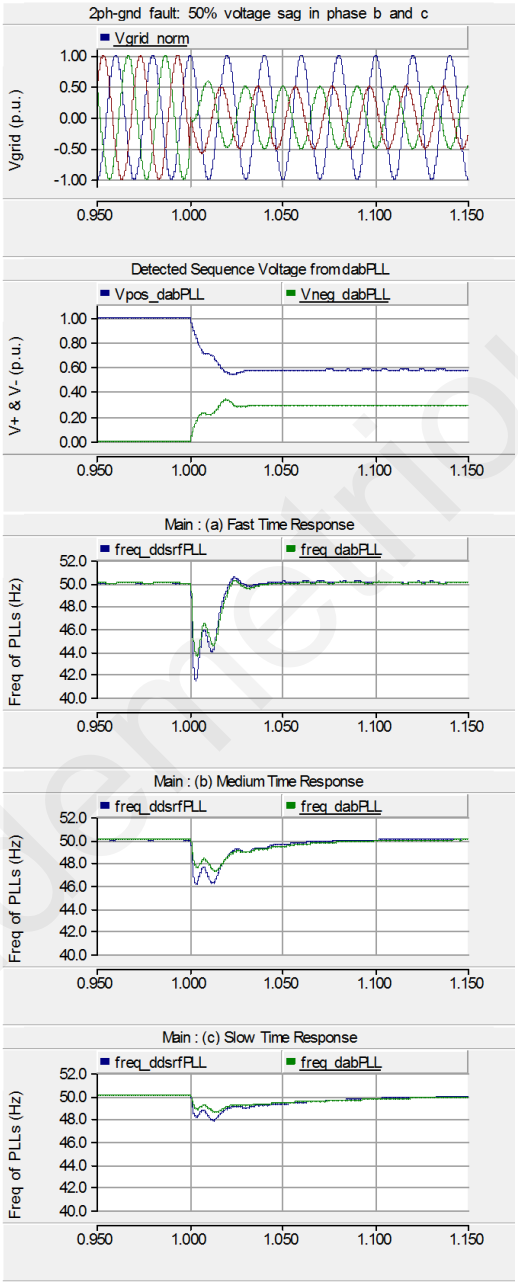

Fig. 2.10. Simulation results for 2-phase to ground fault with 50% voltage sag in phases b and c. Frequency overshoot of ddsrfPL and dαβPLL with respect to: (a) fast, (b) medium and (c) slow time response settings.

Performance of the two PLL under different grid faults

It is necessary to compare the performance of the two PLLs under different grid faults. A detailed performance comparison between the two PLLs requires an examination under all possible grid disturbances. For this investigation, the two PLLs are tuned in a way to fulfill the German Grid Codes (German GC) [11], [12], where the frequency operation window is from -2.5 Hz to +1.5 Hz around 50 Hz. Therefore, for any type of faults (A-G) [27], [91] and for any characteristic voltage (*D*) (10%-90%), where *D*=1-d

and *d* represents the voltage drop of the three-phase voltage vector [27], [91], each PLL should be tuned in a way to avoid any violation of the frequency constraints. The tuning settings of each PLL for this investigation are presented in TABLE 2.1. It is to be noticed that according to these tuning settings the overshoot of the frequency estimation of each PLL will never exceed the frequency limits of the German GC under any possible fault. A violation of the frequency limits can lead to an undesired disconnection of a RES from the grid. The investigation presented in this sub-section has been performed according to the MATLAB/Simulink model.

Both PLLs have been tested under all types of grid faults (A-G) [91] and for voltage characteristics from 10% to 90% of the nominal voltage. The comparison according to the frequency estimation overshoot is shown in Fig. 2.13, where the proposed dαβ-PLL presents on average a 19% lower overshoot. The settling performance of the estimated frequency of the two PLLs is presented in Fig. 2.14, where the new dαβPLL presents on average a 13.8% faster performance.

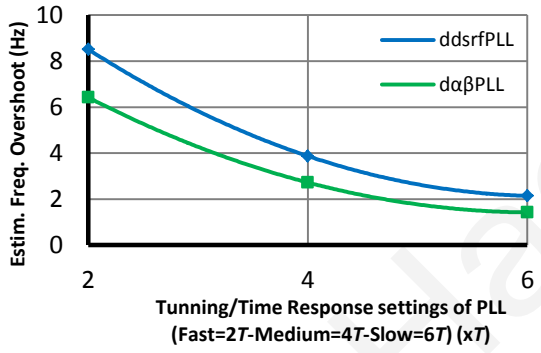

Fig. 2.11. Simulation results for 2-phase to ground fault with 50% voltage sag in phases b and c. Overshoot of ddsrf-PLL and dαβ-PLL on frequency estimation according to time response.

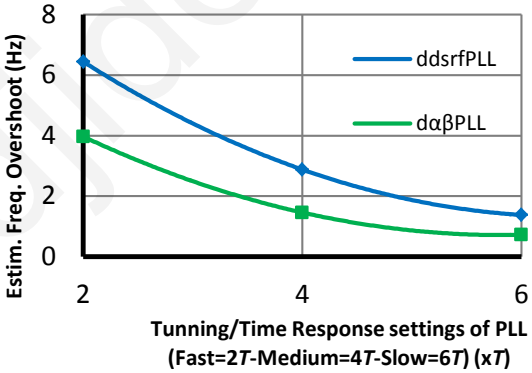

Fig. 2.12. Simulation results for 1-phase to ground fault with 50% voltage sag in phase a. Overshoot of ddsrf-PLL and dαβ-PLL on frequency estimation according to time response.

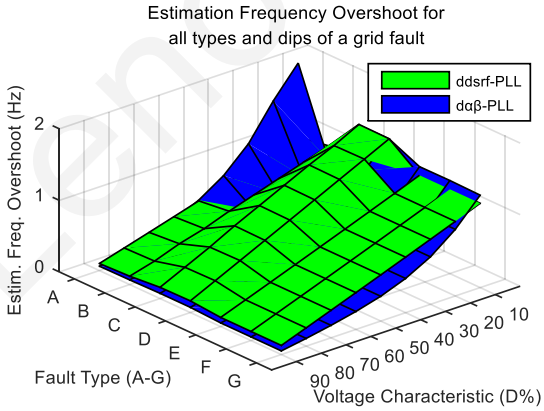

Fig. 2.13. Overshoot of the frequency estimation of dαβPLL and ddsrf-PLL for all types and all voltage characteristics of grid faults.

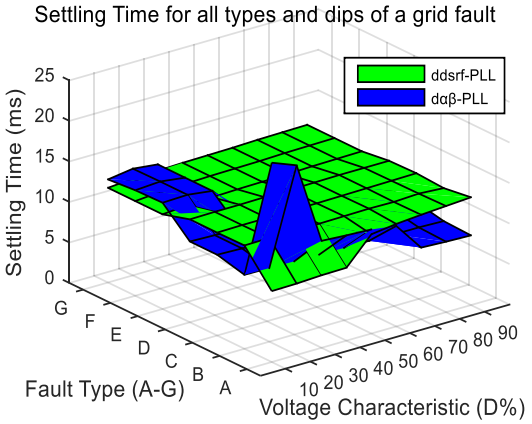

Fig. 2.14. Settling time of the frequency estimation of dαβ-PLL and ddsrf-PLL for all types and all voltage characteristics of grid faults.

The performance of both PLLs is also examined for the case of a phase change at the onset of the voltage fault. At time 1 s, a phase to phase fault with no ground (Type C) occurs with voltage characteristic of $\vec{D} = 0.5\angle 45^o$ pu, where $\vec{D}$ represents the relationship between the line impedance at the fault side and the source side according to [27]. The response of each PLL regarding the frequency estimation is presented under a 45° phase change voltage sag in Fig. 2.15.

The response of the proposed dαβ-PLL is also investigated under a number of high voltage faults. One example is shown in Fig. 2.16. In this case, a voltage rise in phase A to 130% of the nominal voltage is applied. The results of Fig. 2.16 demonstrate that the dαβ-PLL has an accurate performance. Overall, the dαβ-PLL presents similar performance under low and high voltage faults.

Frequency faults could also appear in the grid due to a loss of a large generator or a large load trip off. The accurate performance of the new PLL according to a 1 Hz step change is shown in Fig. 2.17.

All PLLs under investigation in this Section, including the dαβ-PLL, cannot perform accurately under harmonic distorted grid voltage. The response of the dαβ-PLL under low-order harmonic distorted voltage (with $|V_{-5}|$=0.1V_{nom} and $|V_{+7}|$=0.05$|V_{nom}|$) is presented in Fig. 2.18, where the frequency estimation of the PLL is disturbed due to the voltage harmonic pollution. Some novel methods for eliminating the effect of the harmonic voltage distortion without affecting the dynamic response of the synchronization are proposed in Chapter 4.

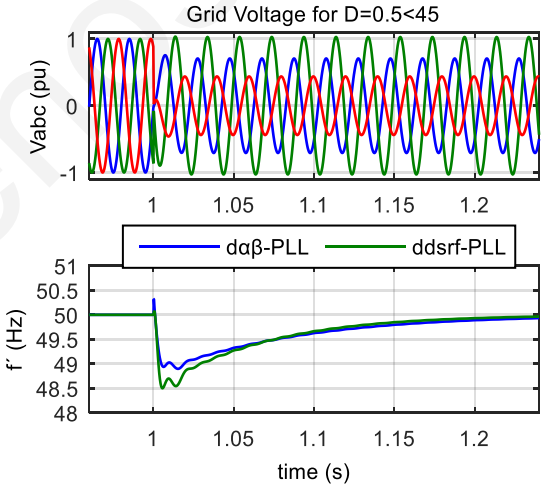

Fig. 2.15. Simulation results showing the response of the dαβ-PLL and ddsrf-PLL under a type C fault with phase change $\vec{D} = 0.5\angle 45^o$.

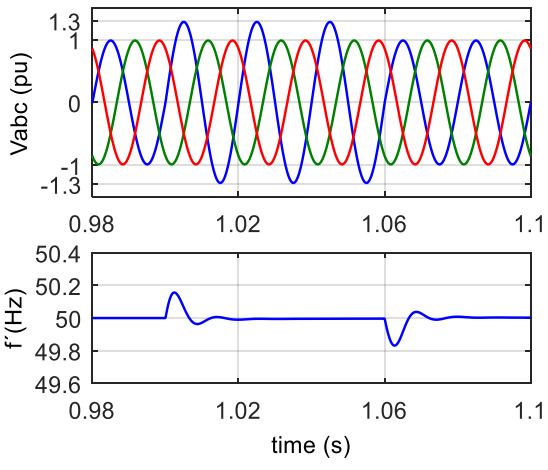

Fig. 2.16. Simulation results showing the response of the dαβ-PLL under an unbalanced voltage rise of phase A to 130% of the nominal voltage.

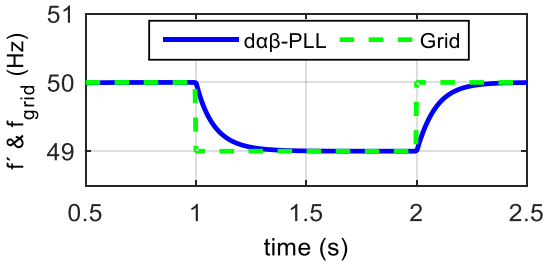

Fig. 2.17. Simulation results showing the response of the dαβ-PLL under a 1 Hz frequency step change.

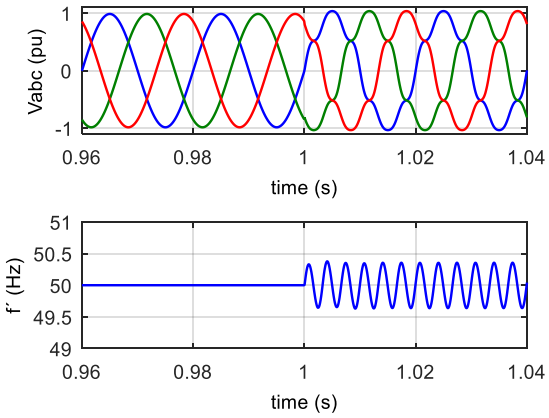

Fig. 2.18. Simulation results showing the response of the dαβ-PLL under a low-order harmonic distorted grid voltage.

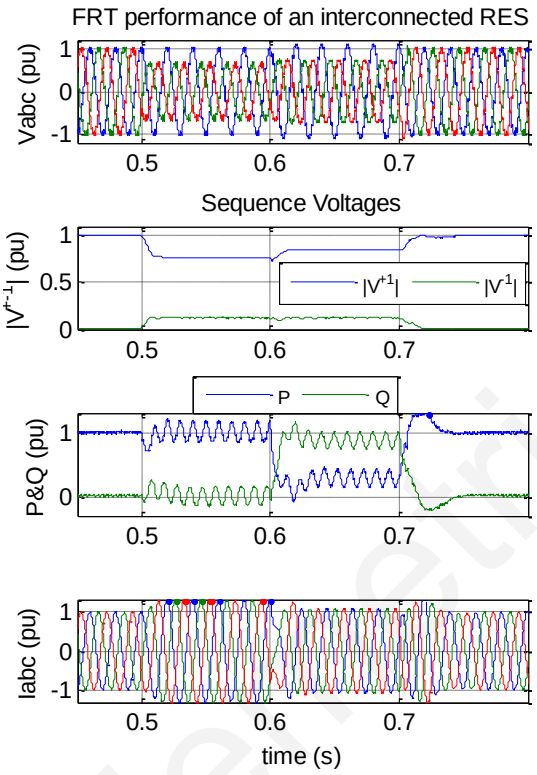

Fig. 2.19. Simulation results for the FRT performance of a RES that use the proposed PLL under Type E (d=40%) fault.

Response of the new PLL on the FRT control of RESs

The response of the PLL can affect the control of the GSC of the interconnected RES. The phase angle (θ) and the positive sequence grid voltage vector ($\mathbf{v}_{dq}$) are estimated from the PLL as θ' and $\mathbf{v}_{dq^{+1}}^{+1*}$ and are involved to the control of the GSC according to Fig. 2.9. The response of the PLL could affect the generation of the reference currents, the dynamics of the current controller and also the calculation of the *d*-*q* component of the grid voltage and of the injected currents. Clearly, a faster and accurate performance of the PLL is beneficial to the control of the GSC.

The use of a PLL on the control of the GSC of a RES is demonstrated for an FRT operation under an unbalanced fault in Fig. 2.19. The FRT control aims to provide voltage and frequency support to the grid during the fault. At time 0.5 s a type E fault occurs with a 40% voltage drop. After 10 ms (at 0.6 s) the FRT control is applied and the RES provides voltage and frequency support to the grid by injecting accurate (sinusoidal) positive sequence active and reactive currents with a ratio of *Q*:*P*=3:1 as shown in Fig. 2.19. The FRT control also limits the injected currents in a way to avoid any violation of the rated value of the GSC that could cause the trip of the converter or cause catastrophic results to

the inverter. Due to the fact that an unbalanced voltage sag occurs in this case study, the proper FRT operation of the RES requires an advanced PQ controller enhanced with FRT capabilities, such as those presented in [31], [33], [35], [92]-[96]. Furthermore, the proper current injection by the GSC under unbalanced voltage conditions requires the use of an advanced current controller, such as the one presented in Chapter 6. The voltage support is observed in Fig. 2.19 where the positive voltage at the PCC is increased from 0.76 pu to 0.85 pu when the FRT control is applied (at 0.6 s). The frequency support is observed by the injection of 0.316 pu of active power. The RES operates properly under the unbalanced voltage sag event due to the ability of the proposed PLL to estimate fast and accurately the phase angle and the voltage amplitude of the grid voltage under grid faults.

2.4.3 Experimental results

In order to verify the proper operation of the proposed dαβ-PLL, an experimental setup has been developed (Fig. 2.20 and Fig. 2.21) using a dSPACE DS1103 DSP board where the real-time controller of the GSC has been designed and a Danfoss FC302 2.2 kW inverter was used as the GSC. For consistency reasons, the controller of the experimental GSC implemented in the dSPACE board is identical to the controller that has been designed in the dynamic simulation models according to Fig. 2.9. Therefore, both the simulation models and the experimental setup can achieve an identical performance.

The first experiment aims to verify that the proposed dαβ-PLL outperforms the other PLLs under investigation. The new dαβ-PLL is used for synchronizing the GSC in an interconnected RES under normal operation conditions in the second experiment and under FRT operation conditions in the third experiment.

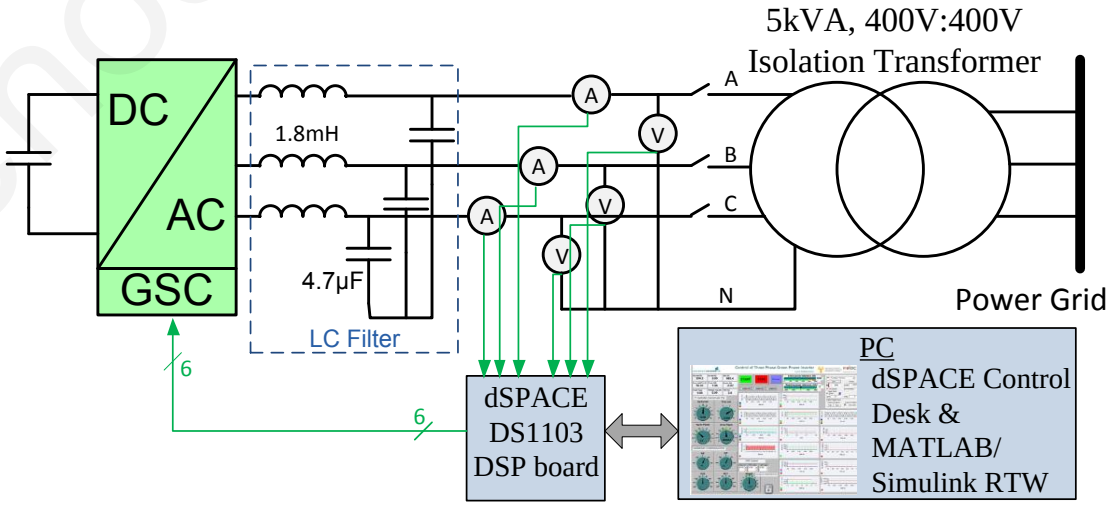

Fig. 2.20. Schematic of the experimental setup.

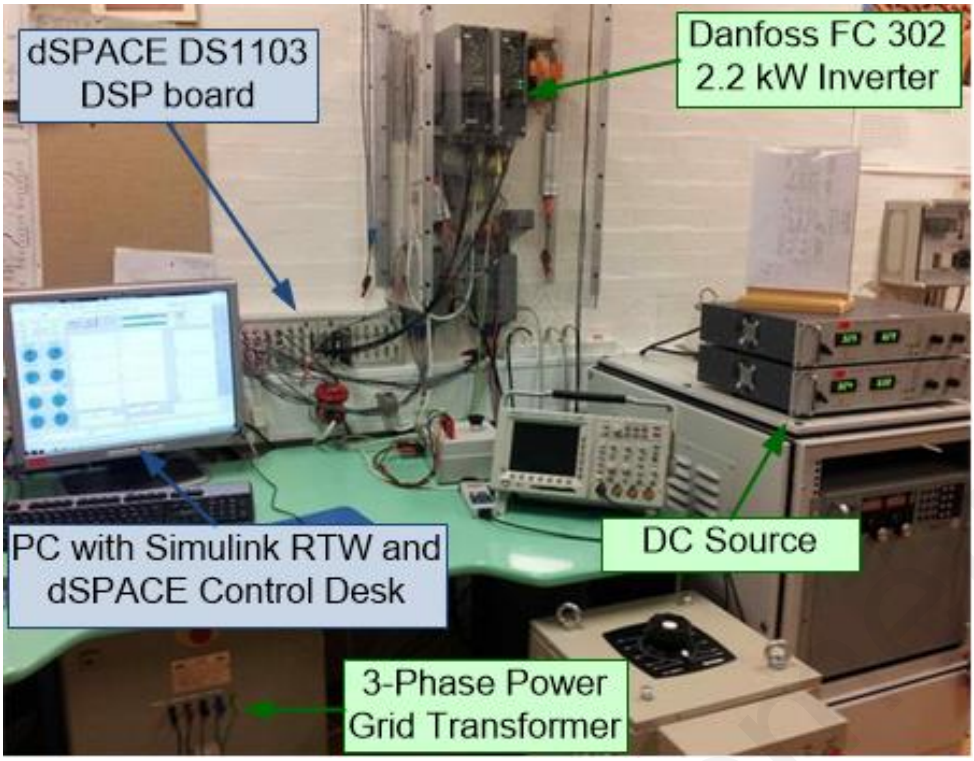

Fig. 2.21. Photo of the experimental setup.

Performance of the new dαβ-PLL

The performance of the suggested dαβ-PLL is verified by comparing the dαβ-PLL to the ddsrf-PLL, which is the only one of the three PLLs under consideration that operates accurately under unbalanced disturbances. The experimental performance of the two PLLs is presented in Fig. 2.22 under an unbalanced operating condition (1 phase to ground fault) with a 66% voltage sag in phase A. Both PLLs enable an accurate detection of the positive sequence voltage vector ($\mathbf{v}_{dq^{+1}}^{+1}$) through the estimation vector ($\mathbf{v}_{dq^{+1}}^{+1}$) of each PLL, which is a crucial aspect in the FRT operation of an interconnected RES. The tracking of the phase angle and frequency is shown in Fig. 2.22, where it can be observed that the overshoot on the estimated frequency of the dαβ-PLL is 46% lower than the overshoot of the ddsrf-PLL.

Use of the dαβ-PLL in an interconnected RES (normal operation)

Interconnected RES use power electronic converters in order to inject the produced energy to the power grid. The GSC is responsible for the grid synchronization and the applied control strategies on this converter are based on the fast and accurate detection of the phase angle of the grid voltage vector at the PCC from the PLL as shown in Fig. 2.9. Therefore, the response of the synchronization method directly affects the performance of

the whole RES. Therefore, it is necessary to test the RES performance when the proposed PLL is used in the synchronization unit of the GSC. The operation of the interconnected RES, where the control strategy uses the proposed dαβ-PLL, is presented in Fig. 2.23 under normal operation conditions. The interconnected RES is operating properly by injecting 2 kW and 0.5 kVAr to the power grid and the current total harmonic distortion (THD_i) is less than 3%.

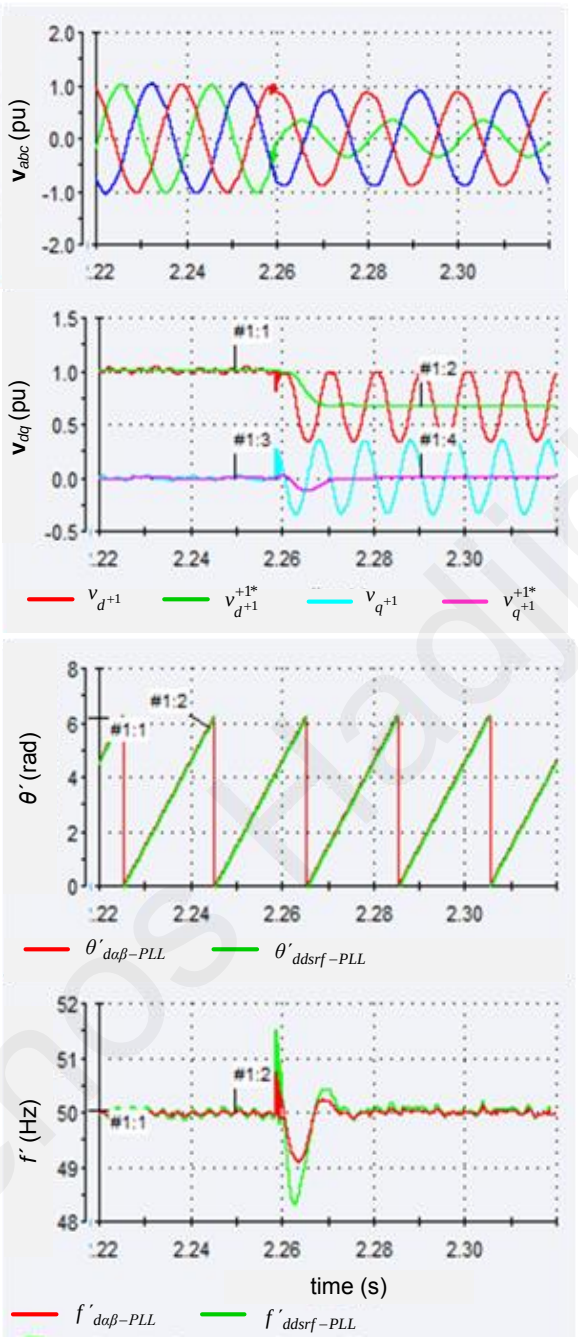

Fig. 2.22. Experimental operation of the dαβ-PLL and the ddsrf-PLL for 1-phase to ground fault, with a 64% voltage sag in phase a.

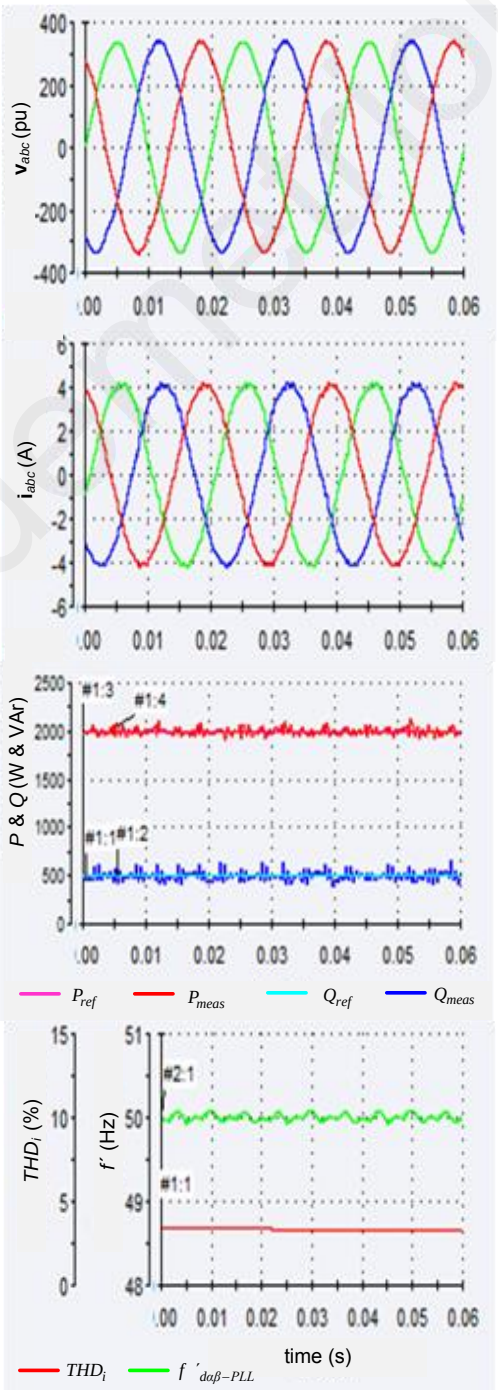

Fig. 2.23. Experimental operation of the interconnected RES under normal operation conditions, when the proposed dαβ-PLL is used as the synchronization method of the GSC.

The controllability of the interconnected RES and its transient response is tested by applying a step change to the active power reference (P_{ref}) from 1 kW to 2 kW. The results are presented in Fig. 2.24, where the reference currents in the *dq*-frame are controlled properly by the PQ controller while the current controller ensures that the phase currents are adjusted in order to track the new references within 3 ms.

Use of the dαβ-PLL in an interconnected RES (FRT operation)

When a low-voltage fault occurs in the power grid, the synchronization of the RES is not trivial, especially when the disturbances are unbalanced. Modern RES should be able to run FRT in order to support the power grid when a disturbance occurs, according to the modern grid regulations.

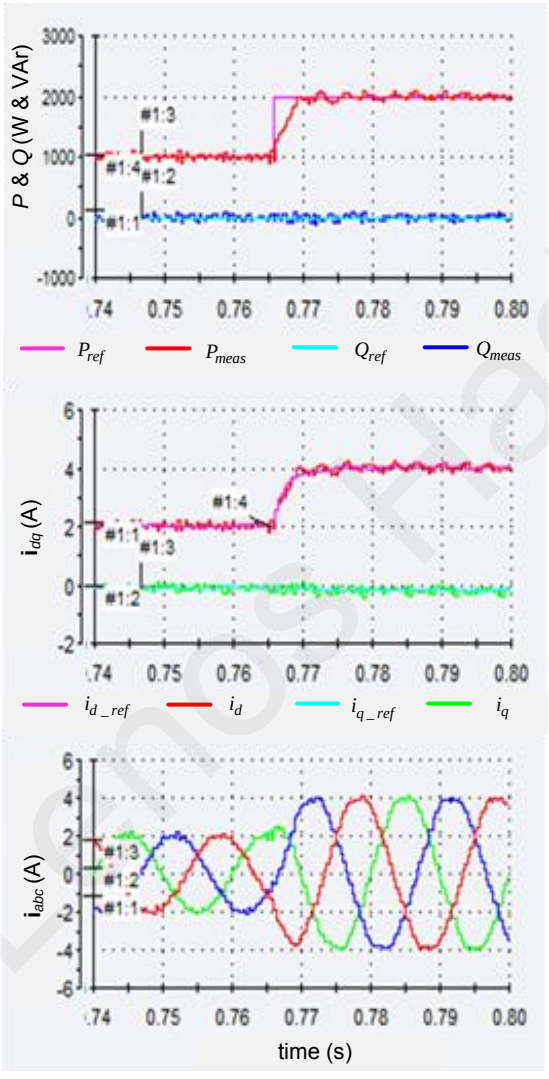

Fig. 2.24. Experimental transient operation of the interconnected RES under a step change of P_{ref} from 1 kW to 2 kW.

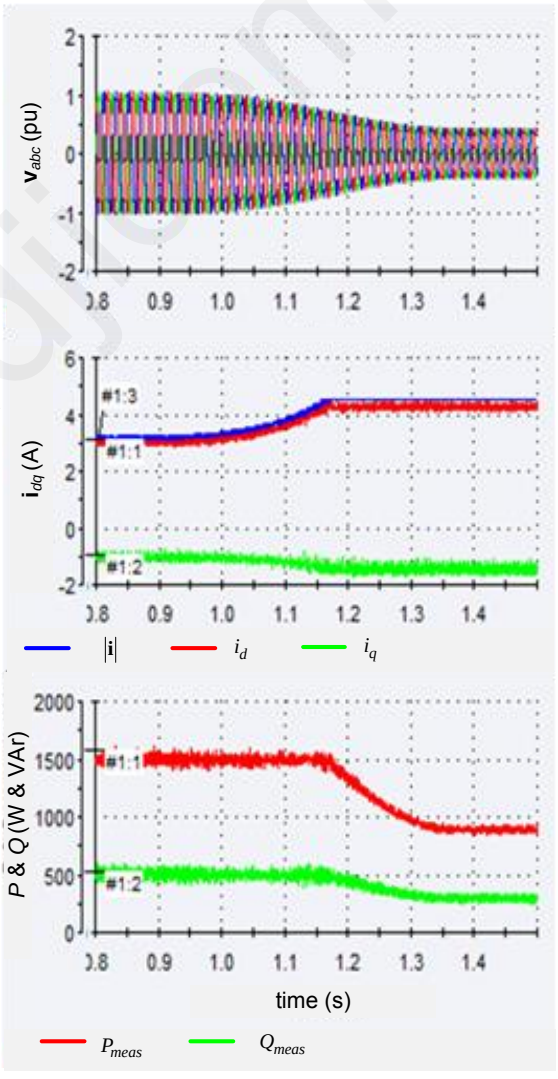

Fig. 2.25. FRT operation of the grid-connected RES during a symmetrical voltage sag.

The proper operation of the new dαβ-PLL has already been demonstrated in this Section under balanced and unbalanced grid conditions. The use of the proposed PLL in order to achieve an FRT operation is another important aspect, since the dαβ-PLL can detect fast (faster than the ddsrf-PLL for the same frequency deviation) and accurately the phase angle and the amplitude of the grid voltage.

The proposed PLL is employed in the GSC controller in order to achieve the FRT capability, demonstrated through the same experimental setup. The purpose of the FRT control strategy is to maintain the interconnection of the RES in order to operate in support to the power grid during voltage sag. The algorithm of the implemented FRT control [31], [33], [35], [92]-[96] is divided into two steps. In the first step, when the voltage sag occurs, the currents are increased ($\mathbf{i}_{dq}$ increases proportionally to the initial P and Q and proportionally to the voltage drop) in order to maintain the delivery of the initial active and reactive power until the currents of the RES reach the nominal value of the GSC. From this moment (step 2) the currents are kept constant to the nominal value and the active and reactive power are decreased in order to keep the GSC currents within the rating limits and to avoid the trip-disconnection of the RES.

The FRT operation of the RES is demonstrated in Fig. 2.25 for a 50% symmetrical voltage sag. As the voltage sags, the P and Q remain constant and the currents are increased until the limit of 4.5 A is reached (GSC rating). From this point, the currents remain constant and P and Q decrease in order to prevent violation of current limits. The FRT operation is achieved and the RES supports the grid during the voltage sag.

2.5 Conclusions

The main contribution of this Chapter is the proposition of the new hybrid synchronization method, named dαβ-PLL. The proposition of the dαβ-PLL was motivated by a benchmarking study for the effect of the time response settings on the overshoot of the estimated frequency and phase angle for three different PLLs. The investigation of dq-PLL, αβ-PLL and ddsrf-PLL motivates the proposal of a new PLL, which inherits the advantages of each PLL. Fig. 2.26 presents a synopsis of a benchmarking between the three PLLs that can be found in the literature and the proposed dαβ-PLL. The new hybrid dαβ-PLL is the most beneficial solution for grid synchronization compared to the other three PLLs under investigation, since it operates accurately under balanced and unbalanced conditions and also reduces the overshoot on the estimation of the phase angle and

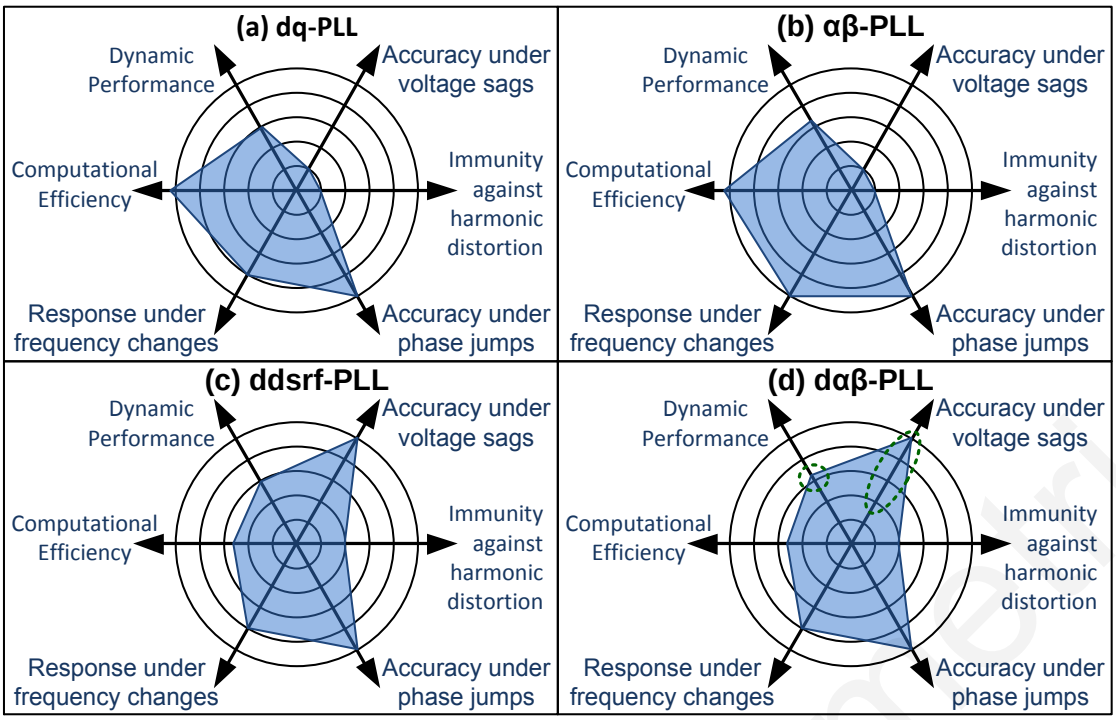

Fig. 2.26. Synopsis of the performance benchmarking between the three synchronization methods from the literature and the proposed method: (a) the dq-PLL, (b) the αβ-PLL, (c) the ddsrf-PLL, and (d) the dαβ-PLL.

frequency, which is the main drawback of the ddsrf-PLL. The lower frequency overshoot of dαβ-PLL leads to a faster time response without any violation of the frequency limits of the grid codes. Under specific circumstances, an even faster response may be needed from the synchronization to ensure an appropriate performance by the GSC under grid faults and thus, some adaptive tuning mechanisms are proposed in Chapter 3 to accelerate the response of the dαβ-PLL. It is worth to mention that the main disadvantage of the dαβ-PLL is the vulnerability against low order harmonics. The proposed dαβ-PLL could be very useful in the design of an FRT control for interconnected RES. The outstanding performance of the suggested dαβ-PLL is verified through experimental results, and the use of the new dαβPLL in an interconnected RES is illustrated through experiments for normal and FRT operation.

CHAPTER 3
ADAPTIVE TUNING MECHANISMS FOR FASTER SYNCHRONIZATION

3.1 Introduction

This Chapter proposes adaptive tuning mechanisms for three-phase synchronization methods in order to accelerate the dynamic response of a Phase-Locked Loop (PLL) and as a result to improve the performance of the GSC of a RES. The first adaptive mechanism (Section 3.3) modifies the tuning parameters of the PLL according to the type and voltage characteristics of the grid fault with the purpose of accelerating the performance of the synchronization. The proposed adaptive tuning mechanism adjusts the PLL parameters in real time according to the proposed fault classification unit (FCU) (Section 3.3.1) in order to accelerate the synchronization performance. The proposed adaptive tuning mechanism has been applied on the dαβ-PLL of Section 2.4 and therefore, the adaptive dαβ-PLL has been proposed [30], [31]. The beneficial effects of the adaptive tuning mechanism on the performance of the proposed adaptive dαβ-PLL are verified through simulation and experimental results. Furthermore, the benefits of using a faster synchronization method on the control of the GSC of RES [30]-[33] are also demonstrated in Sections 3.3.3-3.3.4.

Since the adaptive tuning mechanism can beneficially affect the performance of the GSC, some expansions on the tuning mechanism for the dαβ-PLL are proposed in Section 3.4 for further accelerating the synchronization performance. The adaptive tuning mechanism presented in Section 3.4.1, is inspired from the literature and is based on a Frequency-Phase Decoupling (FPD) technique. This mechanism is also applied on the structure of the dαβ-PLL and the FPD-dαβ-PLL is proposed [31]. This mechanism modifies the loop filter unit of a PLL in order to decouple the phase and the frequency estimation loops and additionally the integral coefficient of the loop filter is adaptively adjusted according to the disturbances presented at the input of the loop filter. The FPD tuning mechanism can also accelerate the dynamic performance of the FPD-dαβ-PLL as demonstrated through simulation results. It is obvious that the adaptive tuning mechanisms can enable a faster synchronization performance for the PLL, as shown by the two new

PLLs: the adaptive dαβ-PLL and the FPD-dαβ-PLL. It is worth mentioning that the reason of improvement (acceleration of the time performance) in the two new PLLs is different and thus, it is expected that by combining the two adaptive tuning mechanism in one new PLL, the performance of the new PLL will be further improved. Hence, the two tuning mechanisms have been combined in Section 3.4.2 and the adaptive FPD-dαβ-PLL has been developed [31], which inherits the advantages of each mechanism and therefore, the adaptive FPD-dαβ-PLL outperforms the other PLLs with regards to the dynamic performance under grid faults.

3.2 Literature review

3.2.1 Conventional and advanced three-phase synchronization methods

As already mentioned in Section 2.2, there are several PLL based synchronization methods for three-phase interconnected GSCs. The conventional methods, such the dq-PLL [59] and the αβ-PLL [60]-[62], fail to accurately track the grid phase angle under unbalanced grid faults. Therefore, there is a need to advance the synchronization methods in order to achieve an accurate performance under any grid disturbances and additionally to present fast dynamic response. As already mentioned in Section 2.2.2, the methods that advance the performance of the synchronization are mainly divided into two categories: the methods that apply a pre-filtering or pre-calculating stage within the phase detector unit in order to mitigate the effect of negative sequence (these methods were discussed in Section 2.2.2) and the methods that modified the loop filtering stage to achieve an improved response (see Section 3.2.2).

The methods based on a pre-filtering or pre-calculating stage [63], [64], [66]-[69], [73]-[78] were described in Section 2.2.2. In general, these methods enable an accurate operation of the synchronization method; however, the accuracy is usually compromised by a deceleration on the time response of the synchronization. A synchronization method, named ddsrf-PLL [79]-[81], was studied in Section 2.2.2 and Section 2.3 and can achieve a fast and accurate performance under unbalanced voltage conditions. The accuracy of ddsrf-PLL under non-symmetrical conditions is enabled by a novel decoupling network that achieves a very fast decomposition of the voltage sequence components. The dαβ-PLL [28], [29], [32], [33], proposed in Section 2.4, inherits the advantage of the decoupling network of [79]-[81] (ddsrf-PLL) and additionally enhances even more the time performance of the synchronization method by inheriting the algorithm of [60]-[62] for a

faster tracking of the grid phase angle. Therefore, the proposed dαβ-PLL (Section 2.4) can be considered as the most beneficial synchronization solution in terms of accuracy under unbalanced grid faults and in terms of fast dynamic response when an unbalanced fault occurs. For this reason, the dαβ-PLL is considered as the basis for applying the adaptive tuning mechanisms that are proposed in this Chapter, for advancing even more the dynamic response of the synchronization unit. The adaptive tuning mechanisms that are developed in this Chapter are actually based on real-time modifications on the loop filter stage of the PLL algorithm. Therefore, a literature review on methods based on loop filtering modifications is provided in the next sub-section.

3.2.2 Methods based on loop filtering stage modifications

This Chapter presents the novel adaptive tuning mechanisms for the PLL, which were developed during this dissertation, in order to enhance its performance in terms of dynamic response. The adaptive tuning mechanisms are based on an online modification of the tuning parameters and structure of the loop filter stage of the PLL in order to advance its performance. Hence, it is necessary to discuss the synchronization methods that can be found in the literature, which are based on loop filtering modification in order to improve the performance of a PLL. According to the literature, the modifications on the loop filtering stage may have several targets, such as: to cancel out the noise or oscillations of the synchronization signals; to improve the time performance of the synchronization; and to reduce the high overshoot on the synchronization signals.

As already mentioned in Section 2.2.2, one of the main drawbacks of the ddsrf-PLL is the high overshoot on the synchronization signals when a grid fault occurs. This high estimation overshoot can be minimized by using a Proportional-Integral-Derivative (PID) controller [97], instead of a PI controller, in the loop filter block of the PLL. According to [97], the derivative coefficient of the PID controller can reduce the estimation overshoot; however, the extra zero in the transfer function of the PID controller can affect the low pass filtering capability of the PLL. Thus, such a PLL that employs a PID controller in its loop filter will be vulnerable to high-order harmonic distortion. Hence, to attenuate inaccuracies due to the effect of high frequency harmonics of the grid voltage, the use of PID controllers is usually avoided in PLL algorithms.

Some other techniques have also been developed in [71], [98]-[100], where the PLL algorithms are still using PI controllers as loop filters, but in these cases the tuning parameters of the PI controller are adaptively changed in order to improve the

synchronization performance. An elegant solution has been proposed in [71] and applied to single-phase PLLs and to the conventional three-phase dq-PLL [59], where an intelligent adaptive mechanism has been introduced to adjust the integral coefficient of the PI controller in order to mitigate the frequency variation due to sudden large phase disturbances. Another important modification on the loop filter of a PLL is suggested in [71], which allows reducing the coupling between the frequency and phase estimation loops. This decoupling between the frequency and phase, in combination with the adaptation of the integral coefficient, achieves a significant improvement on the synchronization performance. Based on the response of the PLL transfer function in [71], the adaptation of integral coefficients does not contribute to the improvement of the time performance of the PLL. It can only affect the frequency overshoot due to the effect on the damping coefficient of the transfer function. Therefore, the improvements presented in [71] are caused mainly from the frequency-phase decoupling and secondly from the adaptive mechanism. Further, the adaptation technique of [71] does not consider how the type and voltage drop of a grid fault can affect the PLL response.

A simple frequency feedback term is used in [98] to adapt the tuning of the loop filter of a PLL. This can reduce the ripple noise and accelerate the PLL performance, but the undesired overshoot is also increased in this case. In [99] the PI parameters of the PLL can be changed between two different possible values in order to enable a slow and a fast response. The slow-tuned PLL can attenuate the harmonic oscillations under normal grid conditions and the fast-tuned PLL can achieve a dynamic transient response in case of grid faults. The PLL in [100] uses a non-linear PI controller as loop filter, where the tuning parameters are adjusted according to the phase estimation error to improve the transient PLL response. In general, the tuning parameters adaptation of the loop filter of a PLL can achieve significant performance improvement according to the adaptation purposes.

The adaptive tuning mechanism, proposed in Section 3.3, modifies the tuning parameters of the PLL according to the type and voltage characteristics of the grid fault with the purpose of accelerating the performance of the synchronization. This novel tuning mechanism (included in the adaptive dαβ-PLL) enables a faster performance under any voltage sag event without causing a higher overshoot on the frequency estimation. The adaptive mechanism in the proposed FPD-dαβ-PLL (Section 3.4.1) is actually applying the method described in [71] on the structure of the dαβ-PLL. Both tuning mechanisms enable a considerably faster time response for the synchronization of GSC under grid faults. The reasons of performance improvement in each mechanism are different and therefore, the

combination of the two adaptive mechanisms in the adaptive FPD-dαβ-PLL (Section 3.4.2) leads to an ever faster time response of the synchronization under grid faults. Such a fast synchronization method can beneficially affect the dynamic performance of a GSC of an interconnected RES. More particularly, in case of FRT operation of RES under grid faults, such a dynamic response by the GSC is critical in order to enable the proper voltage and frequency support of the grid by the RES and to avoid any catastrophic consequences for the GSC by a delayed response.

3.3 Adaptive dαβ-PLL

This Section proposes a novel adaptive tuning mechanism, which is applied on the structure of the dαβ-PLL to develop the adaptive dαβ-PLL. The novel adaptive tuning mechanism modifies the tuning parameters of the PLL according to the type and voltage characteristics of a low-voltage grid fault with the purpose of accelerating the performance of the synchronization. Therefore, to enable such an adaptive tuning mechanism, a Fault Classification Unit (FCU) (Section 3.3.1) is required to recognize in real-time the type and the level of a voltage dip. Then, the tuning adaptation methodology (Section 3.3.2) is developed, based on the FCU operation, in order to accelerate the time performance of the synchronization without causing a higher overshoot on the frequency estimation.

A higher frequency overshoot can violate the frequency operating limits of a grid connected RES according to the grid regulations and consequently, an undesired disconnection of RES may be caused. Such an undesired disconnection of RES during a grid fault event can potentially lead to cascading and catastrophic events for the whole power system. Furthermore, the faster time response of the synchronization by the proposed adaptive dαβ-PLL can beneficially affect the performance of the GSC, especially under FRT operation of RES as demonstrated in Sections 3.3.3 and 3.3.4.

3.3.1 Fault classification unit

The development of the adaptive tuning mechanism for adjusting the tuning parameters of a PLL based on the type of the grid fault requires the design of a Fault Classification Unit (FCU), which will enable the real-time recognition of the type and voltage characteristics of the fault. The proposed online FCU uses space vector analysis of the symmetrical sequence components of the grid voltage [101]-[103] in order to determine the type of fault and the characteristics of each low-voltage grid fault. The FCU should be able to classify the faults into seven different types (A-G) according to [91]. The fast

online performance of the FCU is enabled due to the novel use of the estimated phase angle and amplitude of the positive and the negative sequence of the grid voltage (θ^{+1}, θ^{-1}, V^{+1} and V^{-1}) from the PLL, instead of using the Fast Fourier Transformation (FFT). The fault characteristics estimated by the FCU will be used by the adaptive tuning mechanism to adapt the parameters of the PLL in order to accelerate its performance.

Fault characteristics on space vector analysis

According to the theory presented in Appendix A.5, any balanced or unbalanced grid voltage can be written as a summation of a positive and a negative sequence voltage vector ($\mathbf{v}^{+1}$ and $\mathbf{v}^{-1}$). The positive sequence of the voltage rotates with the positive fundamental rotational frequency ($+\omega$), while the negative sequence rotates in the opposite direction ($-\omega$). Therefore, a generic form of a grid voltage vector ($\mathbf{v}$) can be expressed by a summation of angular frequency phasors as,

$$\mathbf{v} = \mathbf{v}^{+1}e^{+j\omega t} + \mathbf{v}^{-1}e^{-j\omega t} \tag{3.1}$$

According to the phasors theory, the $\mathbf{v}^{+1}$ and $\mathbf{v}^{-1}$ can be represented by the corresponding amplitude V^{+1} and V^{-1} and the corresponding initial phase angle θ^{+1} and θ^{-1} of each sequence as,

$$\mathbf{v}^{+1} = V^{+1}e^{j\theta^{+1}} \text{ and } \quad \mathbf{v}^{-1} = V^{-1}e^{j\theta^{-1}} \tag{3.2}$$

The representation of the grid voltage in the complex plane based on space vector analysis [103] leads to an ellipse with major axis (r_{maj}), minor axis (r_{min}), inclination angle (φ_{incl}) and a Shape Index (SI) as defined by (3.3)-(3.6). Another useful term for the classification of the grid fault is the amplitude of the zero sequence voltage, as given by (3.7).

$$r_{maj} = V^{+1} + V^{-1} \tag{3.3}$$

$$r_{\min} = \left| V^{+1} - V^{-1} \right| \tag{3.4}$$

$$\varphi_{inc} = \frac{1}{2}\left(\theta^{+1} + \theta^{-1}\right) \tag{3.5}$$

$$SI = \frac{r_{\min}}{r_{maj}} \tag{3.6}$$

$$V^{0} = \frac{1}{3}\left(v_a + v_b + v_c\right) \tag{3.7}$$

The above-mentioned space vector analysis of the grid voltage is used to determine the characteristics of each fault according to [101]-[103], as also shown in TABLE 3.1.

TABLE 3.1: CHARACTERISTICS OF EACH TYPE OF FAULT

Fault Type	*Space Vector Analysis*				*Amplitude of Zero Sequence Voltage (V^0)*
	Shape Index (SI)	*Inclination Angle (φ_{incl})*	*Minor Axis (r_{min})*	*Major Axis (r_{maj})*	
A	1	-	$(1\text{-}d)V_n$	$(1\text{-}d)V_n$	0
B	$1\text{-}0.67d$	$\pm 30^o, 90^o$	$(1\text{-}0.67d)V_n$	V_n	$0.33d\,V_n$
C	$1\text{-}d$	$0^o, \pm 60^o$	$(1\text{-}d)V_n$	V_n	0
D	$1\text{-}d$	$\pm 30^o, 90^o$	$(1\text{-}d)V_n$	V_n	0
E	$\frac{3(1-d)}{3-d}$	$0^o, \pm 60^o$	$(1\text{-}d)V_n$	$(1\text{-}0.33d)V_n$	$0.33d\,V_n$
F	$\frac{3(1-d)}{3-d}$	$\pm 30^o, 90^o$	$(1\text{-}d)V_n$	$(1\text{-}0.33d)V_n$	0
G	$\frac{3(1-d)}{3-d}$	$0^o, \pm 60^o$	$(1\text{-}d)V_n$	$(1\text{-}0.33d)V_n$	0

These characteristics are required in order to classify the type of grid fault and the voltage characteristics, such as the voltage dip (d), by the FCU as shown in and in Fig. 3.1. The FCU needs to run in real-time, and therefore the quantities for the space vector analysis need to be estimated with very fast dynamics. Thus, the online space vector analysis is enabled by the use of the dαβ-PLL (see Section 2.4) in order to dynamically estimate the corresponding amplitude V^{+1} and V^{-1} and the corresponding initial phase angle θ^{+1} and θ^{-1} of each sequence, as shown in Fig. 3.2. Therefore, the amplitude and phase angle of each voltage sequence are estimated though the dαβ-PLL, by using (3.8) and (3.9).

$$V^{+1} = \sqrt{\left(\bar{v}_{d^{+1}}^{+1*}\right)^2 + \left(\bar{v}_{q^{+1}}^{+1*}\right)^2} \quad \text{and} \quad V^{-1} = \sqrt{\left(\bar{v}_{d^{-1}}^{-1*}\right)^2 + \left(\bar{v}_{q^{-1}}^{-1*}\right)^2} \tag{3.8}$$

$$\theta^{+1} = 0 \quad \text{and} \quad \theta^{-1} = \arctan\left(\frac{v_{q^{-1}}^{-1*}}{v_{d^{-1}}^{-1*}}\right) \tag{3.9}$$

It is to be noted that the $\bar{v}_{d^{+1}}^{+1*}$ and $\bar{v}_{q^{+1}}^{+1*}$ corresponds to the estimated components for the positive sequence voltage vector expressed in the dq^{+1}-frame and the $\bar{v}_{d^{-1}}^{-1*}$ and $\bar{v}_{q^{-1}}^{-1*}$ to the estimated components for the negative sequence in the dq^{-1}-frame respectively, as estimated by the dαβ-PLL (see Section 2.4). According to the transformation theory and the purposes of the PLL algorithm, the initial phase angle of the positive sequence of the voltage θ^{+1} can be considered equal to zero, since the PLL algorithm always tries to inline the grid voltage vector in the d^{+1}-axis of the dq^{+1}-frame.

Fault classification algorithm

The FCU algorithm takes as inputs the calculated quantities r_{maj}, r_{min}, φ_{incl}, *SI and* V^0 as defined by the space vector analysis (3.3)-(3.7) through the estimated values from the dαβ-PLL (3.8)-(3.9). The results from the space vector analysis in combination with the characteristics of each type of the fault (TABLE 3.1) are used from the FCU to determine the type and the voltage dip (*d*) of the fault as shown in Fig. 3.1. The FCU algorithm uses the r_{min} to determine if there is a fault. When a fault occurs, the *SI* is examined in order to clarify if the fault is balanced (Type A) or unbalanced (Type B-G). If the fault is unbalanced, then the φ_{incl} is used to separate the fault between a two-phase dip (C, E, or G) and a single-phase dip (B, D, or F). Then, the characteristics r_{maj} and the amplitude of the zero sequence voltage (V^0) of each fault are used in order to classify the fault to the right

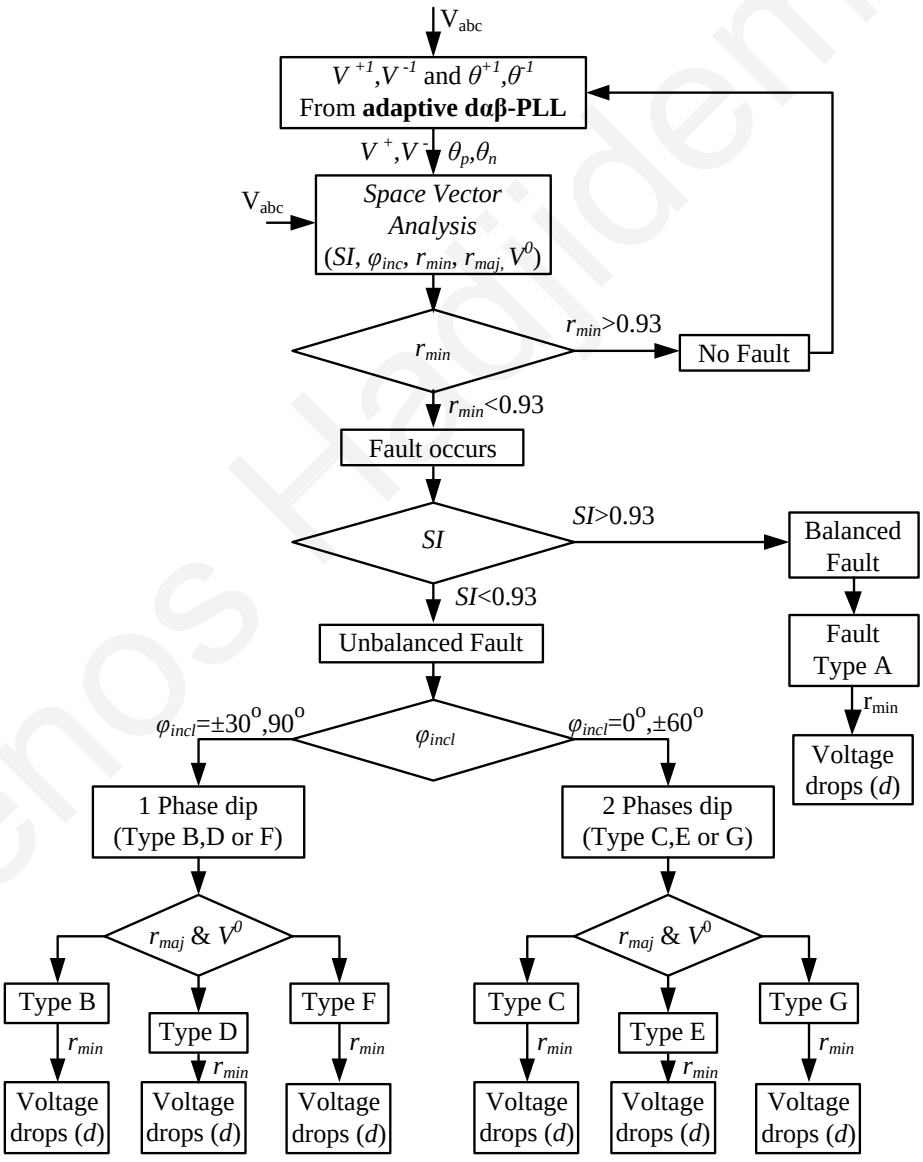

Fig. 3.1. The fault classification algorithm which detects the type and the characteristics of each low-voltage grid fault.

fault type according to TABLE 3.1. Finally, when the fault type has been detected, the information of r_{min} is used to specify the voltage drop characteristic (d) of the fault. The proposed fault classification algorithm, which enables the on-line classification of the grid fault, is analytically depicted in Fig. 3.1. It is worth to mention that the real-time FCU is developed to enable the adaptive tuning mechanism of the adaptive dαβ-PLL; however, such an on-line classification unit can be very useful in several power system applications (e.g., for online or post analysis of grid faults based on phasor measurements).

3.3.2 Development of the adaptive dαβ-PLL

The proposed adaptive dαβ-PLL is motivated through the fact that the overshoot on the estimated frequency is varied according to the tuning of the PLL and the characteristics of the grid faults, as already mentioned in Section 2.4 and in [28], [29]. Therefore, this Section proposes an adaptive tuning mechanism for adjusting the tuning parameter of a PLL in real-time (instead of uniformly constant tuning parameters) in order to achieve the faster desired time performance of the PLL for each fault, without causing any violation on the frequency window of the grid regulations. Violation on the frequency operation window of the RES can cause the disconnection of the RES according to the modern grid codes. The proposed tuning mechanism is applied on the structure of the dαβ-PLL and the adaptive dαβ-PLL is developed.

Structure of the adaptive dαβ-PLL

The adaptive dαβ-PLL inherits the structure of the dαβ-PLL [28], [29], but instead of constant parameters in the PI controller, the PI parameters are changed adaptively according to the fault characteristics as shown in Fig. 3.2. The structure of the adaptive dαβ-PLL is based on a cross feedback network with two decoupling cells to decompose the positive and negative voltage sequences. A delay of one sample (z^{-1}) is required on the cross feedback network to avoid any algebraic loop on the digital implementation of the PLL. The decomposition of the voltage sequences enable accurate estimation of each voltage sequence and a conventional PLL algorithm is then used to track the phase angle of the positive sequence of the grid voltage. The main idea of the adaptive dαβ-PLL is that the PI parameters of the phase angle tracking algorithm can be adaptively adjusted according to the fault characteristics, obtained by the FCU (Section 3.3.1), in order to achieve the fastest possible response of the PLL and consequently a faster performance of the RES when a fault occurs, without causing any violations on the frequency operation window of the GSC.

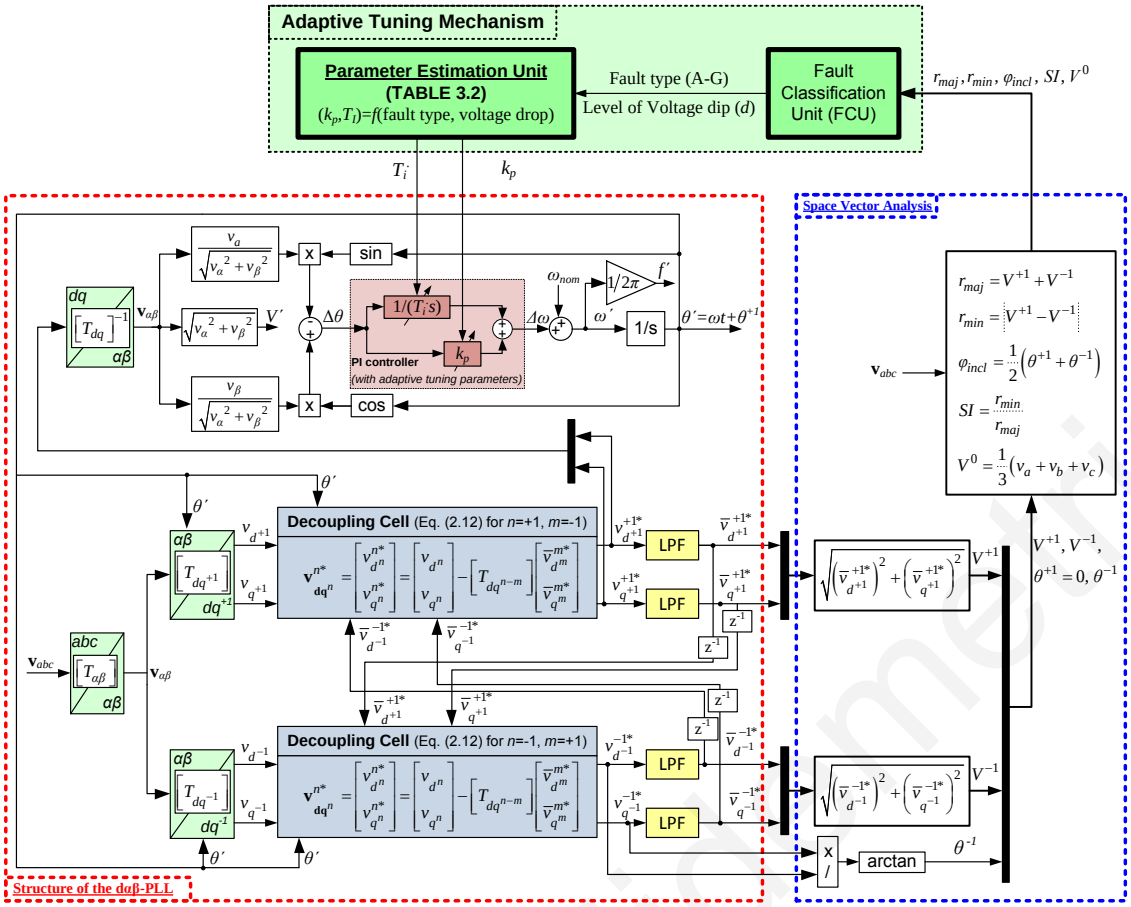

Fig. 3.2. The structure of the proposed adaptive dαβ-PLL.

The tuning of the low pass filters (LPF) and the details about the decoupling cells are described in detail in [28], [29]. The tuning of the adaptive PI controller is described in the following sub-section.

Methodology for the tuning adaptation

In the case of low-voltage grid faults, the modern grid codes require that the RES should remain interconnected with the grid and provide support to the power system during the fault. The appropriate frequency operation window of a RES according to the German grid codes [11], [12], [23] is from -2.5 Hz to +1.5 Hz around 50 Hz. The violation of these limits will cause the disconnection of the RES from the grid, which is undesired because it can lead to cascading failures of the grid. Therefore, the PLL algorithms that are used for the synchronization of the RES with the power grid should be tuned in a way to operate within the frequency limits under any permitted low-voltage grid faults.

On the other hand, in [29] and in Section 2.4, it has been proved that the time performance of the PLLs (adjusted by the PLL parameters) is inversely proportional to the

estimated frequency overshoot. Hence, for faster operation of a PLL there is a risk of violating the frequency window of the grid codes. The investigation of Section 2.4 also shows that the estimated frequency overshoot of the PLL depends on the type and voltage characteristics of the fault.

According to the above-mentioned conclusions, the knowledge of the type and voltage dip of the fault can be very useful for the faster possible tuning of the PLL without causing any violation on the frequency window. The adaptive dαβ-PLL proposes that the tuning of the PLL should be adaptively changed according to the fault characteristics in order to obtain the fastest possible synchronization performance under any low-voltage grid faults. Therefore the tuning (PI parameters) of the proposed PLL is adaptively changed based on a pre-calculated look-up table according to the real-time estimation of the type and voltage dip of the grid fault through the implemented FCU, as shown in TABLE 3.2.

The tuning of the PLL is based on the linearized small signal analysis of the PLL, as it is described in Appendix B. According to Appendix B, the transfer function of the dαβ-PLL can be estimated by,

$$H_\theta(s) = \frac{\theta'}{\theta_{grid}} = \frac{2\zeta\omega_n s + \omega_n^2}{s^2 + 2\zeta\omega_n s + \omega_n^2} = \frac{k_p s + \frac{1}{T_i}}{s^2 + k_p s + \frac{1}{T_i}} \tag{3.10}$$

where θ' is the estimated phase angle by the PLL, θ_{grid} is the grid phase angle, $\omega_n = 1/\sqrt{T_i}$ is the natural frequency and $\zeta = \left(k_p\sqrt{T_i}\right)/2$ is the damping coefficient. The transfer function of (3.10) shows that the PLL presents low-pass filtering capabilities, which is a very useful feature to attenuate inaccuracies under high frequency harmonics in the grid voltage. The desired response of the second-order system in (3.10) can be defined by the settling time (T_s), which is given by T_s=4.6/($\zeta\omega_n$) and ζ should be set to $1/\sqrt{2}$ for an optimally damped response [27]. Therefore, the tuning of the PLL can be achieved by adjusting the PI parameters given in (3.11) in order to define the time response of the PLL.

$$k_p = \frac{9.2}{T_s} \qquad \text{and} \qquad T_i = 0.047\zeta^2 T_s^2 \tag{3.11}$$

The PI parameters shown in TABLE 3.2 have been pre-calculated according to (3.11) and off-line tested through simulations for each fault in order to obtain the fastest possible performance of the PLL without violating the frequency limits for each specific

fault. The pre-calculation of the tuning parameters of TABLE 3.2 has been done according to the worst-case time of fault for each type of fault. Therefore, when the FCU detects no fault conditions (normal operation) the PLL parameters are set as k_p=12.35 and T_i=0.013 so that the German grid codes can be satisfied for the worst case grid faults (same tuning with the dαβ-PLL of Section 2.4 - initial parameters). In case that the FCU detects any low-voltage grid fault, which causes a lower voltage disturbance than the worst case fault, the PLL parameters are adapted from the initial parameters to the appropriate value according to TABLE 3.2 in order to accelerate the performance of the PLL and consequently to obtain a better response of the RES.

This could initially cost a higher frequency overshoot (but always without violating the frequency constraints). However, it can also lead to a faster and more accurate estimation of the phase angle and amplitude of the grid voltage. The accurate and faster estimation of the grid voltage characteristics (θ^+, θ^-, V^+ and V^-) will feed the FRT control algorithm of the RES to generate faster the reference currents and it will also assist the current control of the GSC to operate more accurately, when a fault occurs. The faster and more accurate synchronization of the RES under grid faults is beneficial for the power system since the RES will provide a more appropriate support to the power grid under faulty conditions, as it is demonstrated in Sections 3.3.3 and 3.3.4.

TABLE 3.2: LOOK-UP TABLE FOR THE K_p AND T_I TUNING PARAMETERS OF THE ADAPTIVE dαβ-PLL

(Initial tuning parameters K_p=12.35, T_i=0.013)								
Fault Type / **Voltage dip (d%)**		**A**	**B**	**C**	**D**	**E**	**F**	**G**
90	k_p	15.46	23.29	12.35	12.35	14.15	14.15	14.15
	T_i	0.00832	0.00367	0.01304	0.01304	0.00993	0.00993	0.00993
80	k_p	19.57	27.46	15.86	15.86	20.00	20.00	20.00
	T_i	0.00519	0.00264	0.00791	0.00791	0.00497	0.00497	0.00497
70	k_p	28.75	32.86	20.91	20.91	27.88	27.88	27.88
	T_i	0.00241	0.00184	0.00455	0.00455	0.00256	0.00256	0.00256
60	k_p	41.82	40.00	27.88	27.88	38.33	38.33	38.33
	T_i	0.00114	0.00124	0.00256	0.00256	0.00135	0.00135	0.00135
50	k_p	65.71	51.11	36.80	36.80	54.12	54.12	54.12
	T_i	0.00046	0.00076	0.00147	0.00147	0.00068	0.00068	0.00068
40	k_p	102.22	68.15	51.11	51.11	76.67	76.67	76.67
	T_i	0.00019	0.00043	0.00076	0.00076	0.00034	0.00034	0.00034
30	k_p	155.93	96.84	76.67	76.67	115.00	115.00	115.00
	T_i	0.00008	0.00021	0.00034	0.00034	0.00015	0.00015	0.00015
20	k_p	242.11	153.33	131.43	131.43	204.44	204.44	204.44
	T_i	0.00003	0.00008	0.00012	0.00012	0.00005	0.00005	0.00005

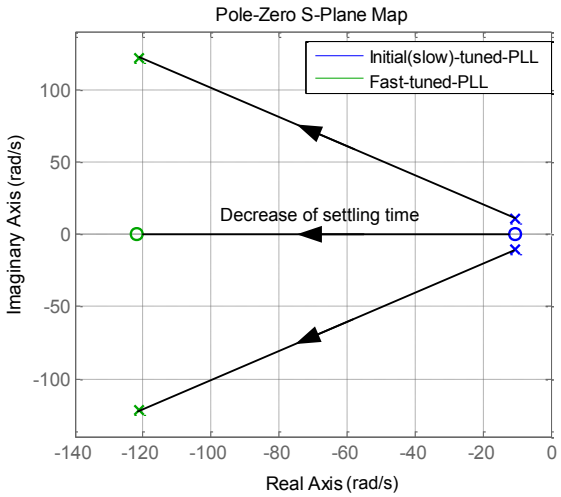

Fig. 3.3. Root locus of the proposed adaptive PLL transfer function showing the zero and poles placement in the whole range of possible tuning conditions.

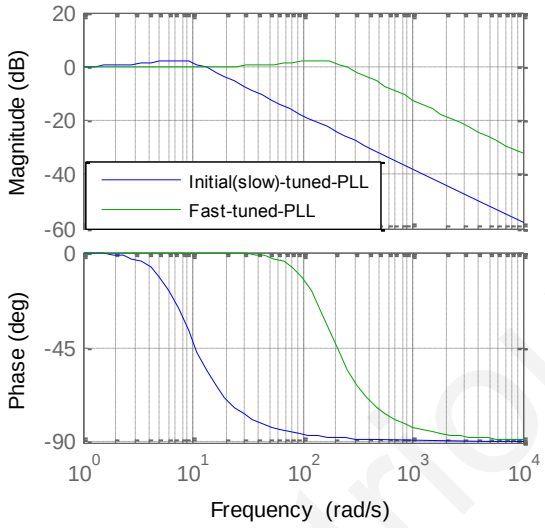

Fig. 3.4. Bode diagram of the proposed adaptive PLL for the two edge tuning conditions.

It is obvious that through the proposed adaptive PLL algorithm, the PI parameters can be varied within a wide range of values. Therefore, a further analysis is required to verify the stability of the proposed PLL in the whole range of possible tuning conditions. Since ζ is always set to $1/\sqrt{2}$ for an optimally damped response, the root locus is a function of the settling time T_s. The root locus of the proposed adaptive PLL transfer function is presented in Fig. 3.3 as a function of the settling time settings of the PLL, for all possible tuning conditions (from the initial-slow-tuned PLL to the fastest possible by the Table II fast-tuned PLL). The stability of the proposed PLL is proved in Fig. 3.3, since the two poles of the PLL are always placed on the left half S-plane for any selected tuning parameters of TABLE 3.2. The stability of the proposed PLL is also proved by the Bode-diagram of Fig. 3.4, where the slowest and the fastest possible tuning scenarios are depicted. Since ζ is always a constant, the adaptive tuning of the PLL is only affecting the natural frequency ω_n of the system and the stability of the proposed PLL is ensured within the range of the possible tuning conditions. The effect on the natural frequency of the PLL can cause different attenuation of high order harmonics, but the PLL still presents significant high-frequency filtering capabilities.

3.3.3 Simulation results

A simulation model has been implemented in MATLAB/Simulink to verify the accurate performance of the adaptive dαβ-PLL under several grid faults. The appropriate

operation of the proposed PLL needs to be ensured, and afterwards the use of the proposed adaptive dαβ-PLL in an interconnected RES should be investigated.

Performance of the adaptive dαβ-PLL

The operation of the adaptive dαβ-PLL under unbalanced grid faults requires to be demonstrated. Here, the response of the FCU and then the performance of the adaptive dαβ-PLL are presented. For example, at time 1 s a type B fault (single phase to ground) occurs with a voltage drop equal to 30%. Fig. 3.5 shows that the FCU detects the type of the fault (Fault Type=2=B) and the voltage drop (d=30%) within 4.8 ms (less than T/4, where T is the period of the grid voltage). Then, the parameters of the proposed dαβ-PLL are adaptively modified in order to accelerate the performance of the proposed PLL. The parameters k_p and T_i are changed from the initial parameters 12.35 and 0.013 to 92.44 and 0.00023 respectively, which are the desired parameters for the fastest possible response, without any violation on the frequency operation window, under the specific fault according to TABLE 3.2. Therefore, the estimation of the grid frequency is accelerated as shown in Fig. 3.5.

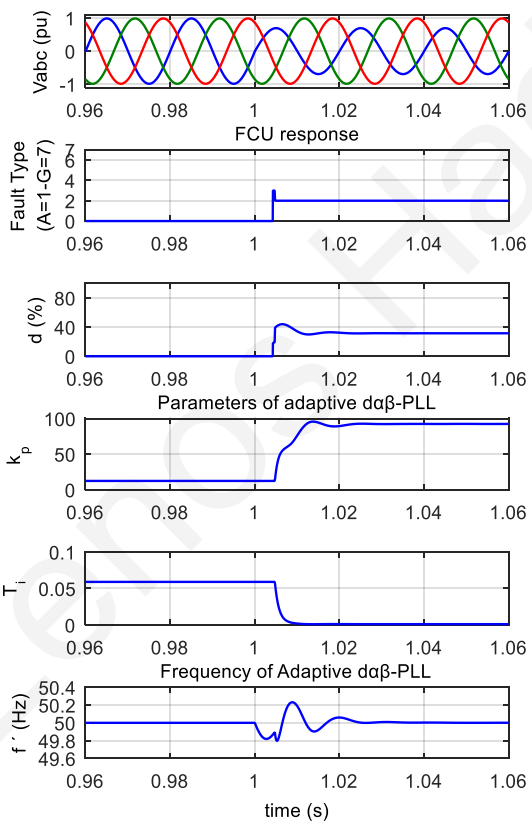

Fig. 3.5. Simulation results showing the operation of the proposed adaptive dαβPLL, including the response of the FCU, under fault type B with a voltage drop equal to 30%.

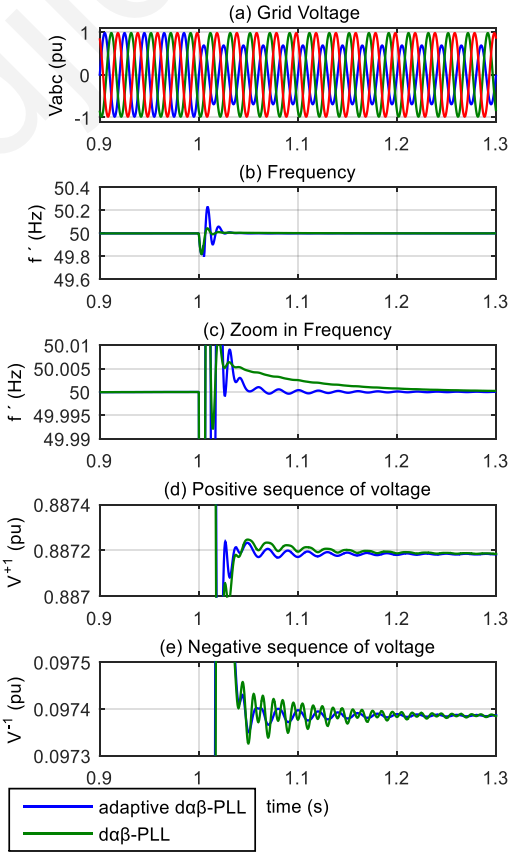

Fig. 3.6. Simulation results comparing the performance of the adaptive dαβ-PLL to the dαβ-PLL, under fault type B with voltage drop equal to 30%.

To prove the outstanding performance of the proposed adaptive dαβ-PLL, it is necessary to compare the response with the dαβ-PLL (with constant tuning parameters). The comparison is taking place for the same fault (Type B, d=30%). The simulation results of the comparison are illustrated in Fig. 3.6, where it is shown that the frequency estimation from the adaptive dαβ-PLL has a higher frequency overshoot but without violating the frequency limits. From Fig. 3.6(c) the settling time of the adaptive dαβ-PLL (for the required accuracy of 0.1% of the maximum allowed disturbances) is 44.3 ms instead of 117 ms of the dαβ-PLL. Therefore, the adaptive dαβ-PLL is 62% faster than the dαβ-PLL on the estimation of the grid frequency in this case. The adaptive dαβ-PLL can also estimate faster and more accurately the amplitude of the positive and negative sequence voltages as shown in Fig. 3.6(d)-(e). The accuracy of the estimated voltages and the time response of estimating the synchronization signals can directly affect the RES performance.

Using the new adaptive dαβ-PLL in an interconnected RES under FRT operation

It is interesting to observe the effect of the proposed adaptive dαβ-PLL on the control of the GSC of an interconnected RES (Fig. 3.7), especially under FRT operation. The appropriate operation of the RES under grid faults requires that the controller of the GSC is enhanced with an FRT control algorithm [31], [33], [92]-[96], such as the Flexible Positive and Negative Sequence Control (FPNSC) algorithm [31], [33], [92]-[94] and its modified version as presented in this Section, and an advanced current controller [40], [84]-[87] with the capability of accurate injection of positive and/or negative sequence currents under unbalanced voltage conditions, as the one proposed in Chapter 6.

The FPNSC algorithm is responsible to limit the current injection according to the converter ratings and to generate the positive and negative sequence reference currents that will feed the enhanced current controller during the fault so that the interconnected RES provides the appropriate support (injection of reactive Q and active P power) to the grid. The development of the FPNSC algorithm [92]-[94] is based on the instantaneous power theory presented in Appendix A.6. The FRT algorithm presented in this Section is actually a modification of the FPNSC algorithm in a way to enable the compatibility of this algorithm with the GSC of a RES. Therefore, the FPNSC algorithm is reformulated in this Section and the required voltage vector for generating the reference currents are taken directly from the advanced synchronization method. According to the FRT algorithm that has been applied in this Section, the reference current vector $\mathbf{i}^*$ can be defined separately

for the active $\mathbf{i}_p^*$ and reactive $\mathbf{i}_q^*$ components of the reference currents, as given by (3.12). $\mathbf{i}_p^*$ and $\mathbf{i}_q^*$ represent the component of currents that can cause a corresponding active and reactive power injection under the specific voltage conditions.

$$\mathbf{i}^* = \mathbf{i}_p^* + \mathbf{i}_q^* \tag{3.12}$$

Now each active and reactive reference current component can be defined as a summation of a corresponding positive ($\mathbf{i}_p^{*+1}$ and $\mathbf{i}_q^{*+1}$) and a negative ($\mathbf{i}_p^{*-1}$ and $\mathbf{i}_q^{*-1}$) sequence component as given by (3.13) and (3.14).

$$\mathbf{i}_p^* = \mathbf{i}_p^{*+1} + \mathbf{i}_p^{*-1} \quad \text{and} \quad \mathbf{i}_q^* = \mathbf{i}_q^{*+1} + \mathbf{i}_q^{*-1} \tag{3.13}$$

$$\begin{aligned} \mathbf{i}_p^{*+1} &= k_1 \frac{P^*}{\left|\mathbf{v}_{dq^{+1}}^{+}\right|^2} \mathbf{v}_{dq^{+1}}^{+}, \quad \mathbf{i}_p^{*-1} = (1-k_1) \frac{P^*}{\left|\mathbf{v}_{dq^{-1}}^{-}\right|^2} \mathbf{v}_{dq^{-1}}^{-} \quad \text{and} \\ \mathbf{i}_q^{*+1} &= k_2 \frac{Q^*}{\left|\mathbf{v}_{dq^{+1}}^{+}\right|^2} \mathbf{v}_{dq^{+1}\perp}^{+}, \; \mathbf{i}_q^{*-1} = (1-k_2) \frac{Q^*}{\left|\mathbf{v}_{dq^{-1}}^{-}\right|^2} \mathbf{v}_{dq^{-1}\perp}^{-} \end{aligned} \tag{3.14}$$

The positive sequence voltage vector $\mathbf{v}_{dq^{+1}}^{+}$ and its orthogonal version (90^o leading) $\mathbf{v}_{dq^{+1}\perp}^{+}$ expressed in the dq^{+1}-frame (rotating with $+\omega$) can be formulated through the estimated signals by the adaptive dαβ-PLL as given by (3.15), while the corresponding negative sequence vectors vector $\mathbf{v}_{dq^{-1}}^{-}$ and $\mathbf{v}_{dq^{-1}\perp}^{-}$ expressed in the dq^{-1}-frame (rotating with $-\omega$) can be calculated by (3.16).

$$\mathbf{v}_{dq^{+1}}^{+} = \begin{bmatrix} \bar{v}_{d^{+1}}^{+1*} \\ \bar{v}_{q^{+1}}^{+1*} \end{bmatrix} \quad \text{and} \quad \mathbf{v}_{dq^{+1}\perp}^{+} = \begin{bmatrix} \bar{v}_{q^{+1}}^{+1*} \\ -\bar{v}_{d^{+1}}^{+1*} \end{bmatrix} \tag{3.15}$$

$$\mathbf{v}_{dq^{-1}}^{-} = \begin{bmatrix} \bar{v}_{d^{-1}}^{-1*} \\ \bar{v}_{q^{-1}}^{-1*} \end{bmatrix} \quad \text{and} \quad \mathbf{v}_{dq^{-1}\perp}^{-} = \begin{bmatrix} \bar{v}_{q^{-1}}^{-1*} \\ -\bar{v}_{d^{-1}}^{-1*} \end{bmatrix} \tag{3.16}$$

Further, the P^* and Q^* are the active and reactive power set-points (according to the pre-fault produced power) and k_1 and k_2 are parameters that can be used easily to adjust between positive or negative current injection according to the FRT control plan and the grid codes. Therefore, the control could aim to raise the faulty positive sequence voltage (positive current injection) or to compensate the unbalanced voltage condition (negative current injection), or both. The advanced current controller [40], [84]-[87] (as the one proposed in Chapter 6) has to be able to provide accurate control under unbalanced faults

and to track the positive and/or negative sequence reference currents that are generated by the FRT algorithm of the PQ controller, as given by,

$$\mathbf{i}^{+1*} = \mathbf{i}_p^{*+1} + \mathbf{i}_q^{*+1} \quad \text{and} \quad \mathbf{i}^{-1*} = \mathbf{i}_p^{*-1} + \mathbf{i}_q^{*-1} \tag{3.17}$$

The control structure of the GSC of an interconnected RES with FRT capabilities is presented in Fig. 3.7. The GSC controller of Fig. 3.7 is enhanced with an advanced PQ controller which enables the FRT operation according to the FPNSC algorithm and includes an advanced current controller (see Chapter 6) which enables the accurate injection of positive and/or negative sequence of currents under balanced or unbalanced grid conditions. In the GSC controller of Fig. 3.7, the proposed adaptive dαβ-PLL is used for ensuring an accurate and fast synchronization under any grid fault.

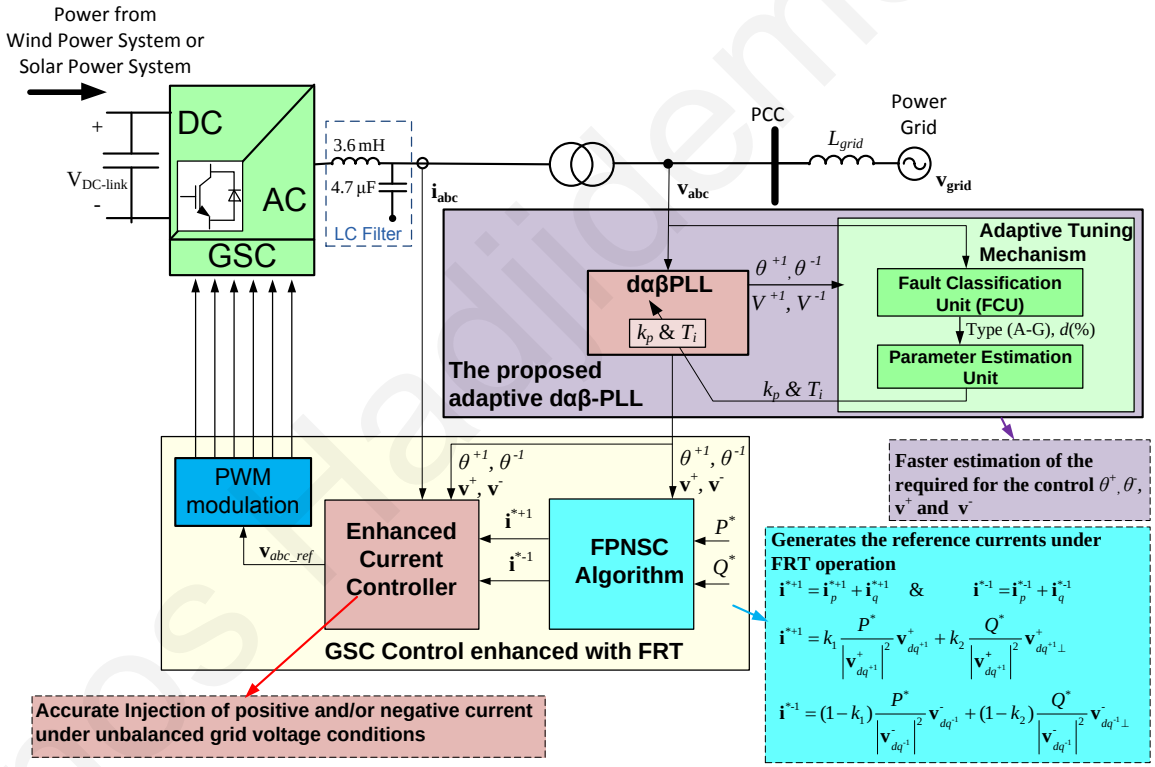

Fig. 3.7. Control structure of the GSC of a RES with FRT capability using the new adaptive dαβ-PLL for the optimal synchronization.

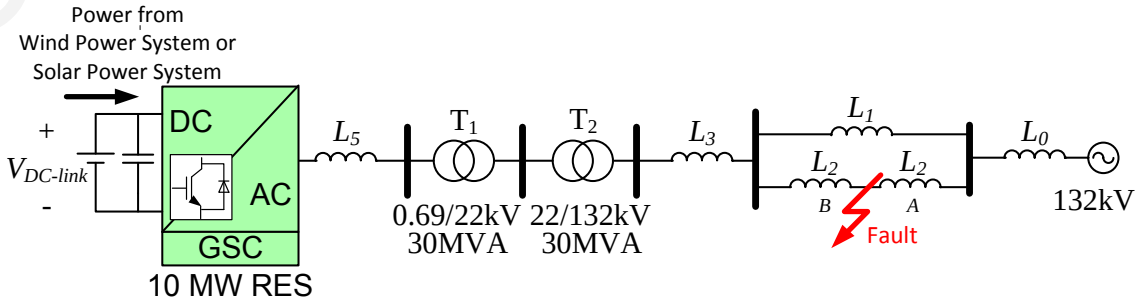

Fig. 3.8. A 10 MW RES interconnected to a small power system.

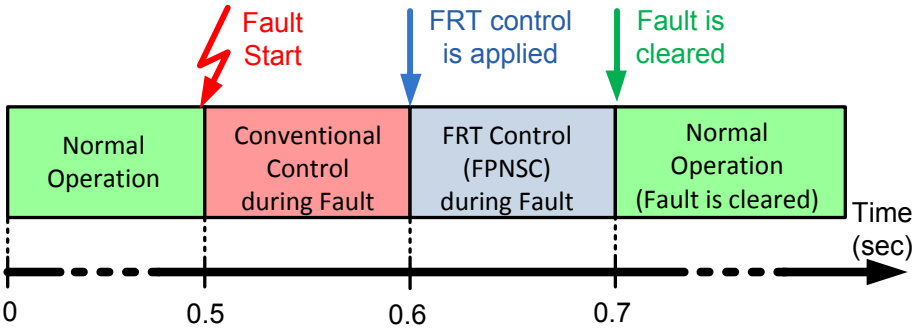

Fig. 3.9. Time schedule for the FRT control during the fault.

The simulation results are based on a realistic scenario, where a 10 MW GSC of a RES is interconnected to a small power system as shown in Fig. 3.8. The fault occurs in the middle of line 2 (Fig. 3.8) and the RES observes this fault as a voltage sag at the PCC. The time schedule of the operation of the test bed system is depicted in Fig. 3.9, where the fault occurs at 0.5 s and the GSC operates based on the conventional control until 0.6 s. Then, the FRT operation is applied until the fault is cleared at 0.7 s.

Simulation results are shown in Fig. 3.10 for the case that a Type B fault (single phase to ground) is observed at the PCC with a voltage dip (d=30%). The FRT control provides support to the grid by operating accurately and injecting full positive currents (k_1=k_2=1) with ratio Q^*/P^*=3/1 for enabling a proper voltage and frequency support. It is assumed that the produced energy by RES is constant during the fault. Fig. 3.10 demonstrates that the RES (with the new adaptive dαβ-PLL) could operate accurately under unbalanced fault conditions. The RES supports the grid by providing voltage support (the positive sequence of the grid voltage rises from 0.905 pu to

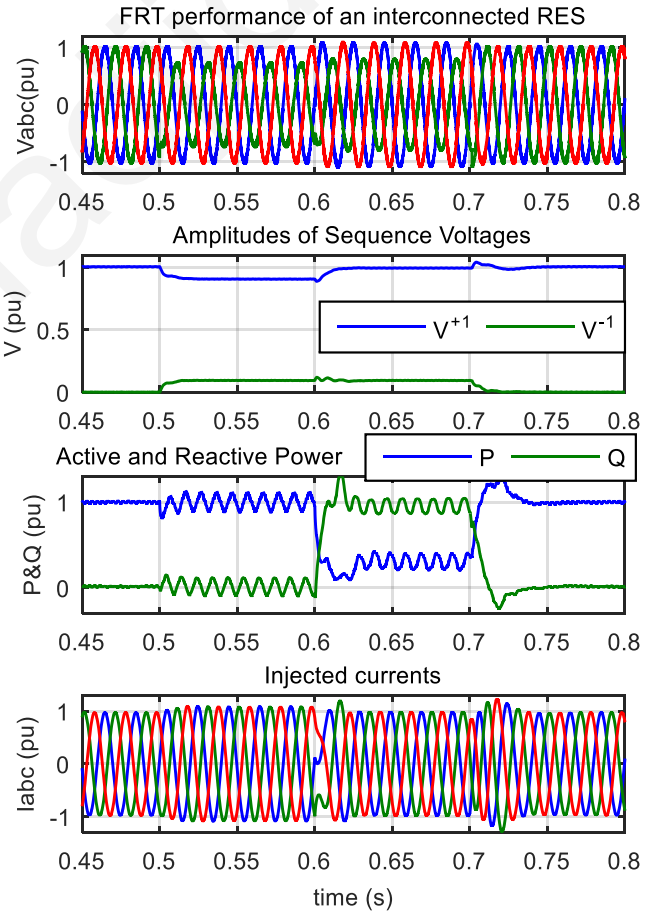

Fig. 3.10. Simulation results showing the operation of the proposed adaptive dαβ-PLL, including the response of the FCU, under fault type B with a voltage drop equal to 30%.

0.99 pu) and frequency support (by injecting 3.16 MW during the fault) (Fig. 3.10). Furthermore, the injected currents are properly limited within the converter ratings during the FRT operation and thus, violations of the rating limits (that can trip the GSC or can cause catastrophic failures for the GSC) are avoided.

Another interesting point that requires to be considered is the effect of the faster and more accurate performance of the adaptive dαβ-PLL in the control of the GSC of RES. In Fig. 3.5 and Fig. 3.6, it has been shown that the adaptive dαβ-PLL presents a faster and more accurate performance on the estimation of the phase angle and the amplitude of the grid voltage under grid faults compared to other PLLs. This fact could affect the accuracy of the reference currents that are generated from the FPNSC algorithm, which are a function of the positive and negative sequence of the voltage according to (3.13)-(3.17). Furthermore, the response of the current controller can be affected since the accuracy of calculating the sequences of the grid voltage and injecting currents is based on the accurate estimation of the phase angle from the adaptive dαβ-PLL. As shown in Fig. 3.11, the current controller of the RES that uses the proposed adaptive dαβ-PLL presents an outstanding performance compared to the RES that uses the dαβ-PLL since the injected currents are more accurate and a faster performance of the current control is achieved due to the better performance of the suggested PLL. When the fault occurs, a faster and more accurate performance of i_q is achieved by using the adaptive dαβPLL. Furthermore, a more precise and faster performance for i_d and i_q is achieved especially for FRT operation as illustrated in Fig. 3.11. This faster and more accurate performance is critical when the grid fault occurs, since the RES can operate in an appropriate way to provide support to the grid and avoid any cascading failures for both the power grid and the GSC.

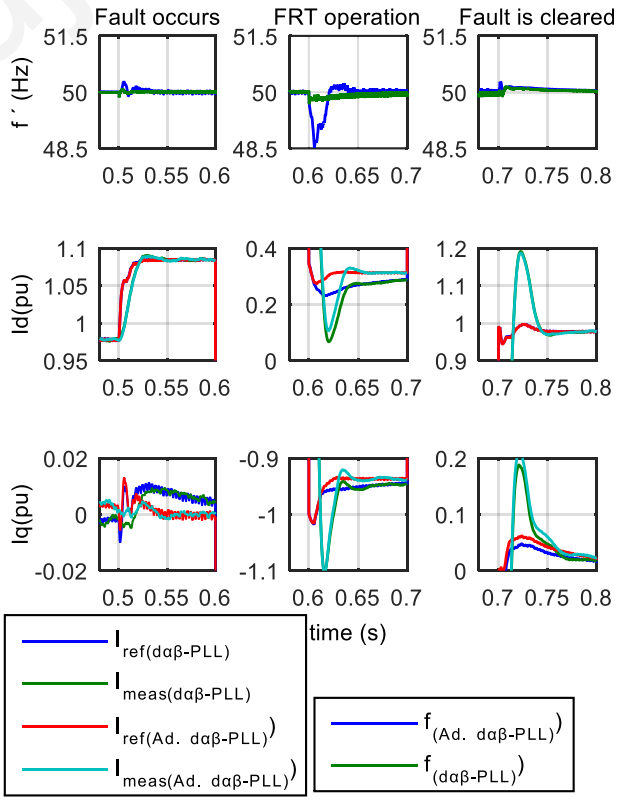

Fig. 3.11. Simulation results comparing the performance of the adaptive dαβ-PLL to the dαβ-PLL, under fault type B with voltage drop equal to 30%.

3.3.4 Experimental results

The performance of the adaptive dαβ-PLL requires an experimental validation as well. Therefore, an experimental setup is implemented using a Chroma 61704 programmable AC source to emulate the power grid, a Delta Elektronika SM600-10 DC source power supply to emulate the produced DC power by the RES and a Danfoss FC302 (2.2 kW) inverter as the GSC, as shown in Fig. 3.12 and Fig. 3.13. A three-phase load resistance has been connected in parallel to the AC source in order to prevent the absorption of active power from the AC source, since the AC source can only deliver active power. Therefore, the power generated by the GSC can be consumed from the parallel load and the proper operation of the AC source is ensured. The proposed PLL and the control of the GSC of an interconnected RES have been digitally developed using the MATLAB/Simulink Real Time Workshop and the dSPACE DS 1103 DSP board with a sampling frequency of 5 kHz.

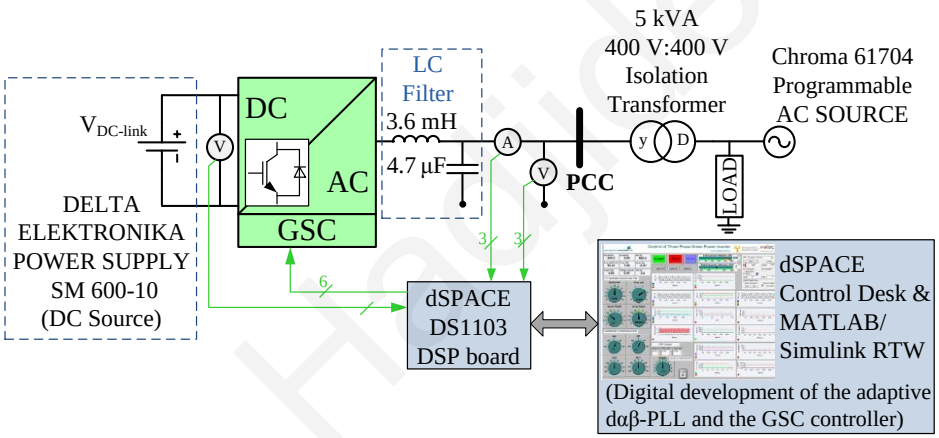

Fig. 3.12. Schematic of the experimental setup.

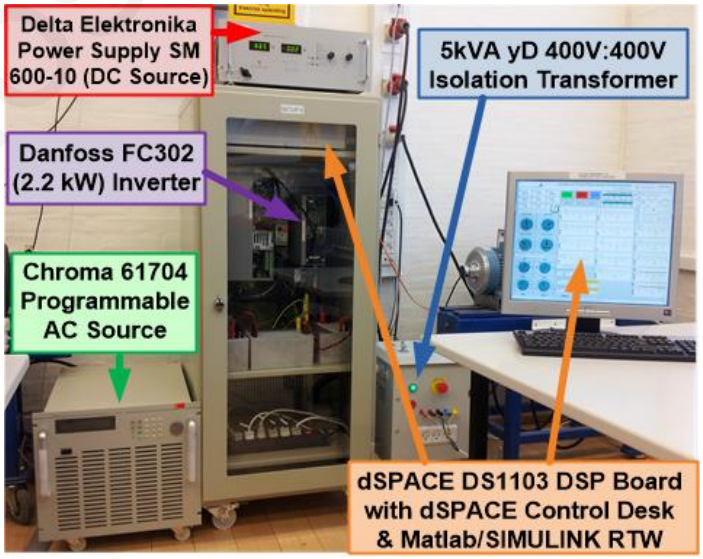

Fig. 3.13. Photo of the experimental setup.

Performance of the adaptive dαβ-PLL

The response of the proposed PLL is experimentally validated in this Section. The GSC is operating under normal operating conditions and at 0.788 s a Type D fault (propagation of a two phase fault with no ground through a yD transformer) occurs with a voltage drop at the PCC equal to 40.7%, as shown in Fig. 3.14. The FCU detects the grid and classifies the fault within 4.2 ms (less than $T/4$). Then the information about the type and the voltage dip (d) of the grid fault is used by the adaptive dαβ-PLL in order to adjust immediately the tuning of the PLL (the k_p and T_i are changed from their initial values to 51.46 and 0.00075 respectively). Therefore, the time performance of the proposed PLL is accelerated and consequently the accurate estimation of the phase angle, frequency and sequences of the grid voltage are achieved with a faster response. The performance acceleration of the adaptive dαβ-PLL causes a higher frequency estimation overshoot, but it is always within the limits of the German grid regulations.

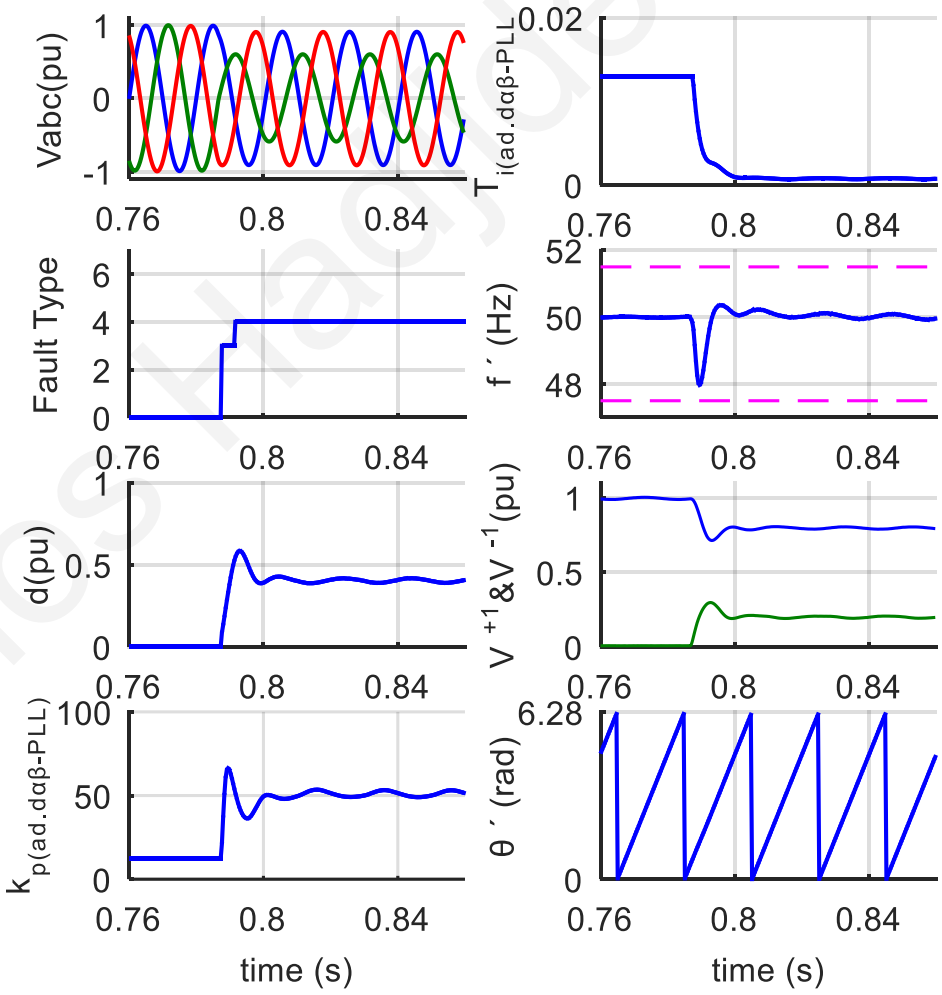

Fig. 3.14. Experimental results showing the operation of the proposed adaptive dαβ-PLL, including the response of the FCU, under fault type D with a voltage drop equal to 40.7%.

Using the new adaptive dαβ-PLL in an interconnected RES under FRT operation

The performance of the RES when using the proposed PLL and the effect of the outstanding performance of the PLL are experimentally demonstrated in this Section. The control structure of the GSC in the experimental setup is implemented as shown in Fig. 3.7, in the same way with the simulation model. The accurate and fast synchronization of the RES with the power grid is obtained through the adaptive dαβ-PLL. The FPNSC FRT control algorithm [31], [33], [92]-[94] is used for generating the reference currents according to (3.12)-(3.17) when a low-voltage fault occurs and an enhanced current controller that is presented in Chapter 6 is used for the accurate current injection during unbalanced faults.

The performance of the interconnected RES with the proposed PLL under FRT operation is demonstrated in Fig. 3.15. A rated 2.2 kW interconnected GSC is operating under normal operating conditions and it is injecting 2 kW (4.08 A peak) and 0 kVAr to the power grid. At 0.806 s a Type C (two phase with no ground) fault occurs with a 32% voltage dip at PCC. The FCU detects the fault type and voltage dip of the fault within 4.4 ms and the tuning parameters of the proposed PLL are immediately adapted to accelerate the accurate synchronization without violating the frequency limits of the grid code.

The controller of the RES detects the occurrence of the grid fault and therefore the FRT control is immediately applied to enable the accurate operation of the RES and the appropriate support of the faulty power system. The FRT control strategy (based on FPNSC algorithm) for low-voltage fault conditions is based on providing voltage and frequency support with a ratio Q^*:P^*=3 to the grid according to the modern grid codes. The FRT control in this case study uses the assumption that the produced apparent power from the RES is constant during the fault and equal to the pre-fault produced power (2 kW and 0 kVAr) as shown in Fig. 3.15. Consequently, when the fault occurs at 0.806 s the FRT control is activated and adjusts the injected positive sequence currents (k_1 and k_2 are set to one in the FPNSC algorithm) in order to inject 0.63 kW active and 1.89 kVAr reactive power into the power grid (Fig. 3.15). The injected active power (0.63 kW) is acting as frequency support to the grid (since the RES is injecting an amount of active power instead of disconnecting the RES from the grid) and the injected reactive power (1.89 kVAr) is acting as voltage support and it is trying to increase the positive sequence of the voltage of the grid. The injected current by the enhanced current controller is purely sinusoidal,

despite the unbalanced voltage conditions and the FRT control accomplishes to keep the injected current within the converter limits (4.5 A peak).

The outstanding performance of the adaptive dαβ-PLL is beneficially affecting the operation of the RES. The effect of using the proposed PLL can be observed on the accuracy of the current controller and on the accuracy of the generated reference currents from the FRT. The effect of the proposed PLL is demonstrated through the accuracy of the reference currents in Fig. 3.16. In case where the RES uses the adaptive dαβ-PLL for the synchronization, the reference currents are settling down 100 ms after a Type C (*d*=22%) fault occurs at 0.78 s. On the other hand, where the RES uses the initial structure of the dαβ-PLL for the synchronization, the reference currents require 500 ms to settle down. The faster and more accurate performance achieved by the RES, when the proposed PLL is used, is beneficial for the FRT operation of the RES and consequently for the power system since all the RES will support the grid in a more appropriate way. Further, the faster synchronization through the proposed PLL enables the fast and proper operation of the GSC and avoids any violation of the GSC rating limits that may cause failures on the GSC and on the power grid.

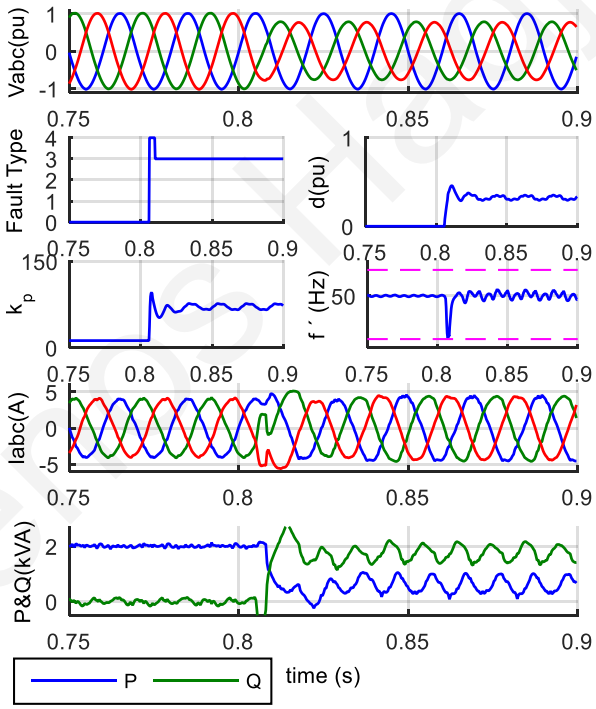

Fig. 3.15. Experimental results showing the FRT performance of the GSC of the RES when using the proposed PLL under a type C grid fault with a voltage drop equal to 32%.

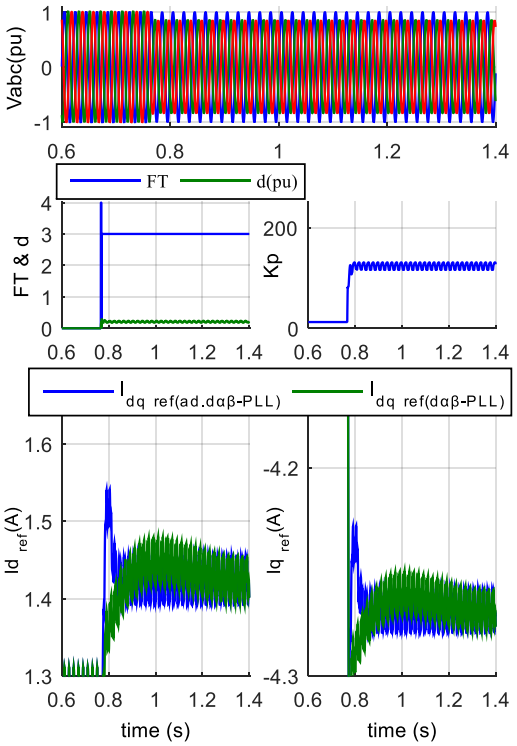

Fig. 3.16. Experimental results comparing the generated reference current from the FRT control when the synchronization is obtained from the adaptive dαβ-PLL and from the conventional dαβ-PLL, under fault type C with a voltage drop equal to 22%.

3.4 Expansions on the adaptive tuning mechanism for the dαβ-PLL

So far, the proposed adaptive mechanism for adjusting the tuning parameters of the dαβ-PLL, which has been presented in Section 3.3, has proved that it can enhance the time performance of synchronization according to the type and the voltage drop of the grid fault. Another very interesting modification of the PLL algorithm has been recently presented in [71], which can also lead to significant acceleration of the time performance of the PLL. The method in [71] suggests the decoupling between the frequency and the phase estimation loop in order to avoid undesired frequency swings due to phase or voltage variations. In [71], the Frequency-Phase Decoupling (FPD) technique is combined with an adaptation technique for adjusting the T_i parameter of the PI controller of the PLL in order to reduce the sudden frequency variations (overshoot). The results presented in [71] show a significant reduction of the frequency overshoot under phase faults, which can also be translated to acceleration of the time performance, since the tuning of the PLL can be set for faster operation without violating the frequency limits of the grid codes. The beneficial effect on the settling time and frequency overshoot of [71] is mostly caused by the FPD technique and less by the adaptive tuning of T_i. The adjustment of T_i can only lead to over-damped operation (small reduction of the frequency overshoot), but it cannot actually affect the settling time of the PLL according to the response of the second order transfer function, as explained in Section 3.3.2 and Appendix B. On the other hand, the adaptive tuning mechanism according to the type and voltage drop of the grid fault suggested in Section 3.3 can directly affect the settling time of the PLL and lead to a faster synchronization response without violating the frequency operation limits. Therefore, the improvements on the synchronization performance in the case of the adaptive dαβ-PLL presented in Section 3.3 and the adaptive PLL presented in [71] are caused by completely different reasons. Thus, the combination of the two techniques can lead to a new outstanding synchronization method that will present an even faster time performance.

3.4.1 FPD-dαβ-PLL

For this purpose, the decoupling between the phase and the frequency estimation loop has to be applied on the structure of the dαβ-PLL according to the theory of [71]. It is to be noted that in [71], the FPD method has only been applied on the structure of single-phase PLLs and on the structure of a conventional three-phase PLL (the dq-PLL as presented in Section 2.2.1).

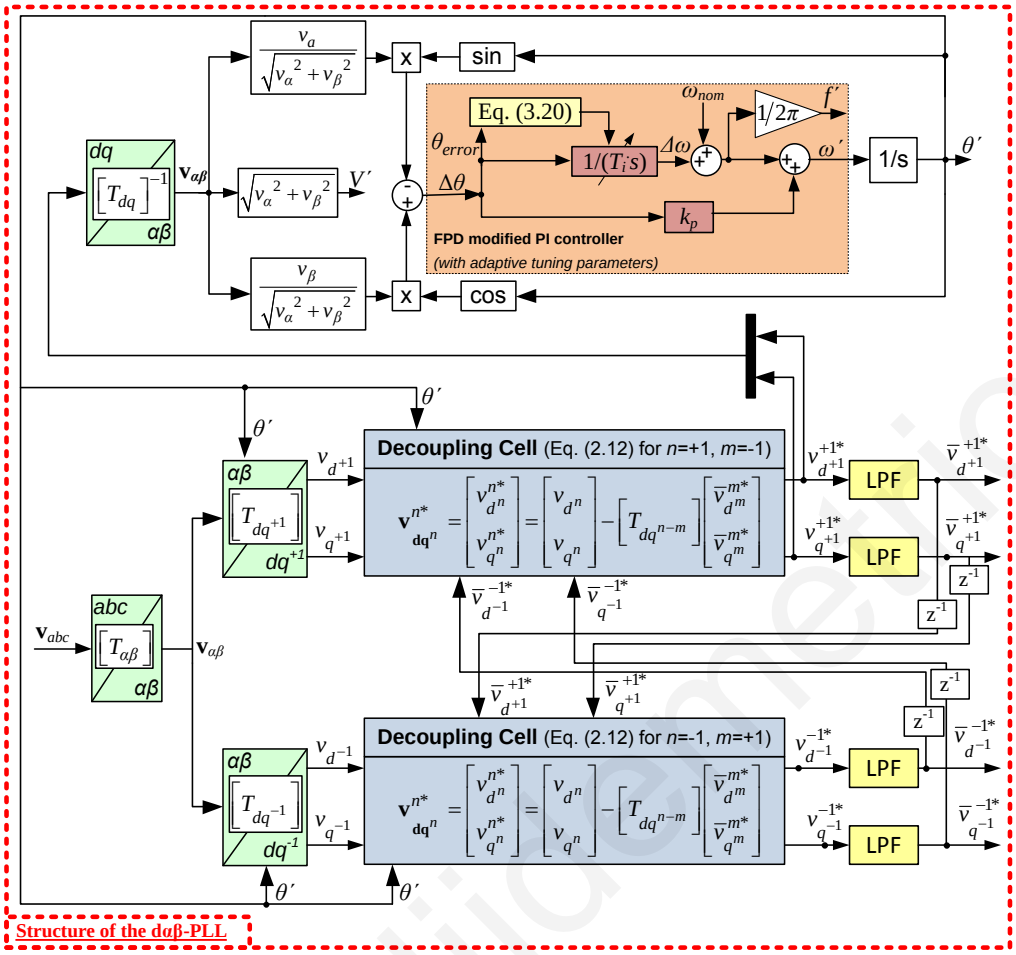

Fig. 3.17. The structure of the new FPD-dαβ-PLL.

According to the frequency estimation loop and to the structure of the dαβ-PLL, as shown in Fig. 2.8, the frequency estimation is given by,

$$f'_{(d\alpha\beta-PLL)} = \frac{1}{2\pi}\left[\theta_{error}\left(k_p + \frac{1}{T_i s}\right) + \omega_{nom}\right] \tag{3.18}$$

Now, in case where the FPD technique is applied on the structure of the dαβ-PLL in order to develop the new FPD-dαβ-PLL as presented in Fig. 3.17, the frequency estimation loop is modified and thus, the estimation of the grid frequency is given by (3.19) without considering the term $k_p \cdot \theta_{error}$, where the $\theta_{error}=\Delta\theta$ represents the difference between the grid frequency and the estimated one by the PLL.

$$f'_{(FPD-d\alpha\beta-PLL)} = \frac{1}{2\pi}\left(\theta_{error} \cdot \frac{1}{T_i s} + \omega_{nom}\right) \tag{3.19}$$

The decoupling between the frequency and the phase in the new FPD-dαβ-PLL is achieved by not considering the term $k_p \cdot \theta_{error}$ on the frequency estimation loop, and only considering it on the phase estimation loop as shown in Fig. 3.17. The implementation of the FPD-dαβ-PLL according to [71] also requires an adaptive mechanism for adjusting the

T_i parameter according to the phase error (θ_{error}) and the amplitude of the positive sequence of the voltage vector. The adaptive mechanism is achieved by multiplying the parameter T_i with the term described by,

$$\left(1+\lambda\cdot\frac{\theta_{error}}{\sqrt{\left(v_{d}^{+1*}\right)^{2}+\left(v_{q}^{+1*}\right)^{2}}}\right) \tag{3.20}$$

where the value of λ can be set in the range $50\leq\lambda\leq100$. The value of λ in this Chapter has been set to 100 according to [71]. The adaptive mechanism of (3.20) is actually adjusting the damping coefficient of the PLL algorithm (by adjusting the T_i parameter) in order to mitigate disturbances in the frequency due to the occurrence of a large phase error. The structure of the new FPD-dαβ-PLL, which is actually the modification proposed by [71] applied to the structure of dαβ-PLL, is presented in Fig. 3.17. The tuning parameter of FPD-dαβ-PLL are set to k_p=61.33 and T_i=0.00053, which are the parameters achieving the faster possible performance without violating the German grid code for the worst case low-voltage fault.

3.4.2 Adaptive FPD-dαβ-PLL

Now, to achieve an even faster synchronization time performance, it is necessary to combine the adaptive tuning mechanism of Section 3.3 with the new FPD-dαβ-PLL (presented in Section 3.4.1), which is based on the theory of [71]. The proposed outstanding synchronization method, named adaptive FPD-dαβ-PLL is presented in Fig. 3.18. The proposed adaptive FPD-dαβ-PLL inherits the structure of the new FPD-dαβ-PLL and combines it with the adaptive mechanism of Section 3.3 to adjust the tuning parameters of the PLL according to the type and the voltage drop of the grid fault.

Therefore, the adaptive tuning mechanism requires the FCU, as presented in Fig. 3.1 (Section 3.3.1), to determine the fault type and voltage dip and then the parameter estimation unit to adjust the tuning parameters. The parameter estimation unit is based on a pre-calculated look-up table (TABLE 3.3), which contains the faster possible tuning parameters (without violating the frequency operation window) of the FPD-dαβ-PLL for any possible type of low-voltage grid fault with a 20-100% voltage drop. The initial parameters of the adaptive FPD-dαβ-PLL are set to the slower tuning parameters of TABLE 3.3 (according to the worst case grid fault), which are the same with those of the FPD-dαβ-PLL, in order to avoid any violation on the frequency operation window of the

German grid codes. If any other grid fault occurs, the FCU will detect the characteristics of the fault and adjusts online the tuning parameters and thus, the performance of the adaptive FPD-dαβ-PLL will accelerate, but always without exceeding the grid code limits. In general, the adaptive tuning mechanism (including TABLE 3.3) has been designed according to the methodology described in Section 3.3.2.

The structure of the proposed adaptive FPD-dαβ-PLL is presented in Fig. 3.18 with all the required modules. The improvements caused from the FPD technique and the improvements caused from the adaptive tuning mechanism according to the grid fault are completely independent, and therefore, the response of the adaptive FPD-dαβ-PLL is expected to outperform the response of FPD-dαβ-PLL and the adaptive dαβ-PLL.

3.4.3 Performance comparison based on simulation results

A fair performance comparison of the four synchronization methods presented in this Section is required at this point. Therefore, in this sub-section the performance of the dαβ-PLL, the adaptive dαβ-PLL, the FPD-dαβ-PLL and the adaptive FPD-dαβ-PLL will be investigated.

TABLE 3.3 : LOOK-UP TABLE FOR THE K_P AND T_I TUNING PARAMETERS OF THE ADAPTIVE FPD-dαβ-PLL

(Initial Tuning Parameters K_p=61.33, T_i=0.00053)								
Fault Type / **Voltage dip (*d*%)**		**A**	**B**	**C**	**D**	**E**	**F**	**G**
90	k_p	61.3	161.4	110.8	110.8	96.8	96.8	96.8
	T_i (x10^{-6})	529	76.4	162	162	212	212	212
80	k_p	63.4	173.5	122.6	122.6	108.2	108.2	108.2
	T_i (x10^{-6})	494	66	132	132	170	170	170
70	k_p	76.6	200.0	139.4	139.4	127.8	12.8	12.8
	T_i (x10^{-6})	338	49.7	102	102	122	122	122
60	k_p	104.5	230.0	161.4	161.4	150.8	150.8	150.8
	T_i (x10^{-6})	182	37.6	76.4	76.4	87.4	87.4	87.4
50	k_p	139.4	255.6	191.7	191.7	176.9	176.9	176.9
	T_i (x10^{-6})	102	30.5	54.1	54.1	63.5	63.5	63.5
40	k_p	184.0	270.6	213.9	213.9	213.9	213.9	213.9
	T_i (x10^{-6})	58.8	27.2	43.5	43.5	43.5	43.5	43.5
30	k_p	242.1	296.8	245.3	245.3	248.6	248.6	248.6
	T_i (x10^{-6})	33.9	22.6	33.0	33.0	32.2	32.2	32.2
20	k_p	287.5	340.74	283.08	283.08	287.50	287.50	287.50
	T_i (x10^{-6})	24.1	17.1	24.8	24.8	24.1	24.1	24.1

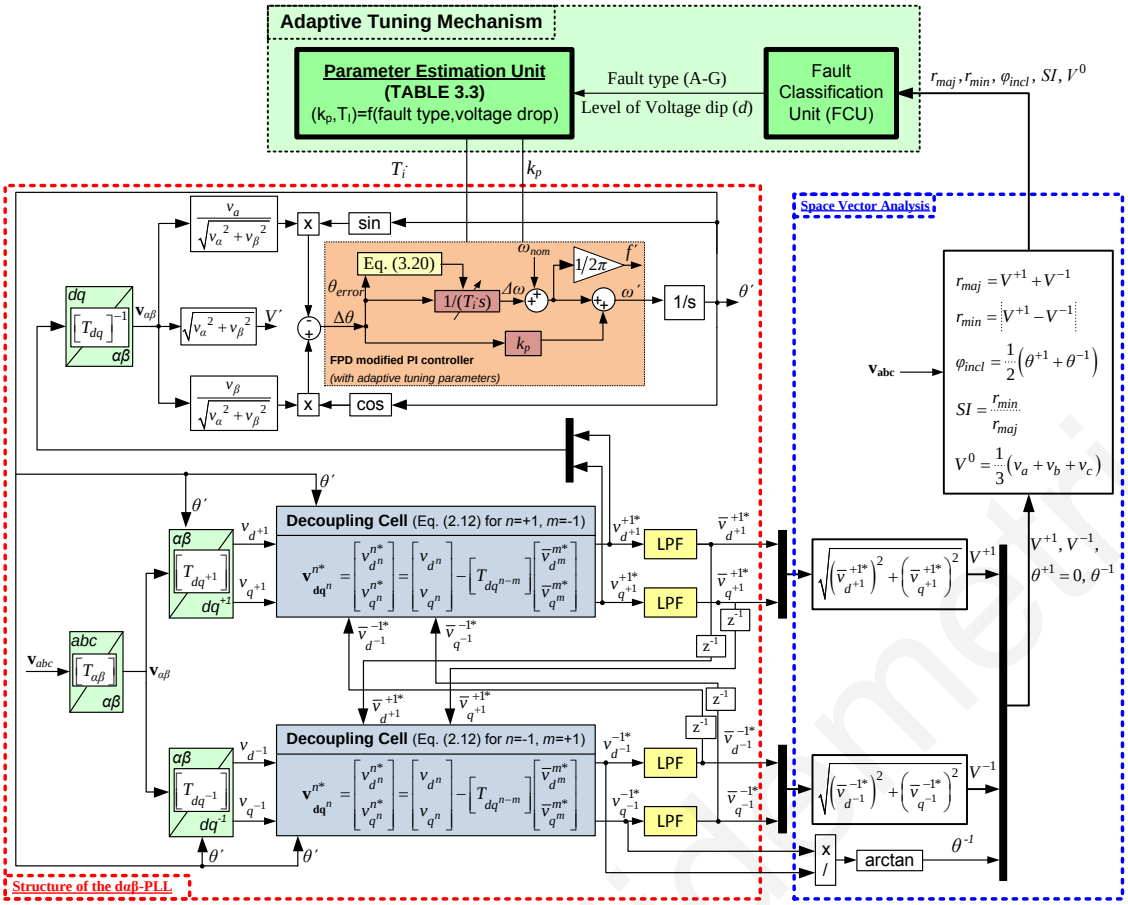

Fig. 3.18. The structure of the new adaptive FPD-dαβ-PLL.

The performance of the four PLL algorithms is presented in Fig. 3.19 when a Type E unbalanced grid fault occurs at 2 s with 33% of voltage drop. The comparison focuses on the phase error settling time (the required time for the phase error to remain within 1% of the maximum disturbance) and the frequency error settling time (the required time for the frequency error to remain within 1 mHz of the grid frequency), which are presented in TABLE 3.4.

The adaptive dαβ-PLL and the FPD-dαβ-PLL present similar time performance and are faster than the dαβ-PLL (as expected), as shown in TABLE 3.4. In the case of the adaptive dαβ-PLL, the improvements are caused by the exploitation of the different fault characteristics in the adaptation mechanism in order to accelerate the PLL response. In the case of the FPD-dαβ-PLL, the improvements are based on the decoupling between the frequency and the phase estimation loops and the adaptive mechanism of the integral coefficient under large phase variations.

The proposed adaptive FPD-dαβ-PLL presents an outstanding time performance, which is approximately three times faster than the adaptive dαβ-PLL and the FPD-dαβ-

PLL and approximately four times faster than the dαβ-PLL. The outstanding performance of the proposed adaptive FPD-dαβ-PLL was expected since the proposed PLL inherits the improvements of the adaptive dαβ-PLL and the improvements of the FPD-dαβ-PLL, which are completely independent. Eventually, the proposed adaptive FPD-dαβPLL presents the best time performance of the four PLLs under a low-voltage grid fault and therefore can affect beneficially the FRT performance of the GSC of an interconnected RES.

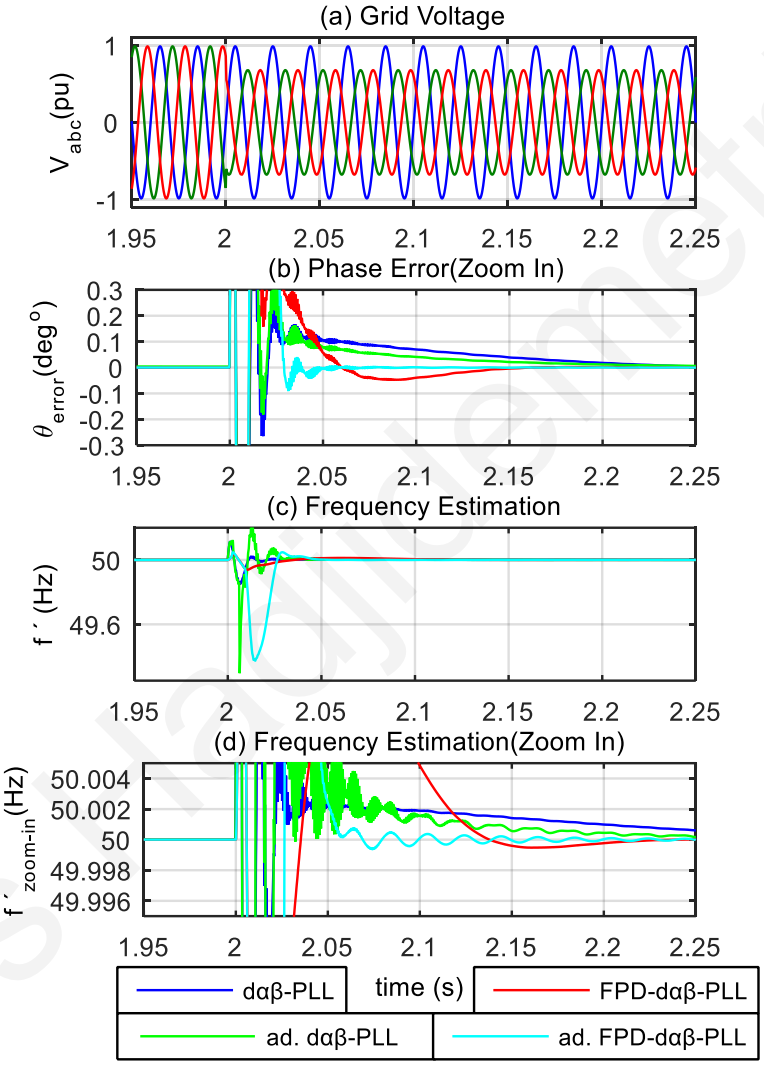

Fig. 3.19. Simulation results comparing the performance of all the implemented PLL algorithms for a Type E unbalanced fault with 33% of voltage drop.

TABLE 3.4: PARAMETERS OF PI CONTROLLER FOR PLLS

Synchronization Method	Phase Error Settling Time (ms)	Frequency Error Settling Time (ms)
dαβ-PLL	169	200
Adapt. dαβ-PLL	125	127
FPD-dαβ-PLL	116	124
Adapt. FPD-dαβ-PLL	46	53

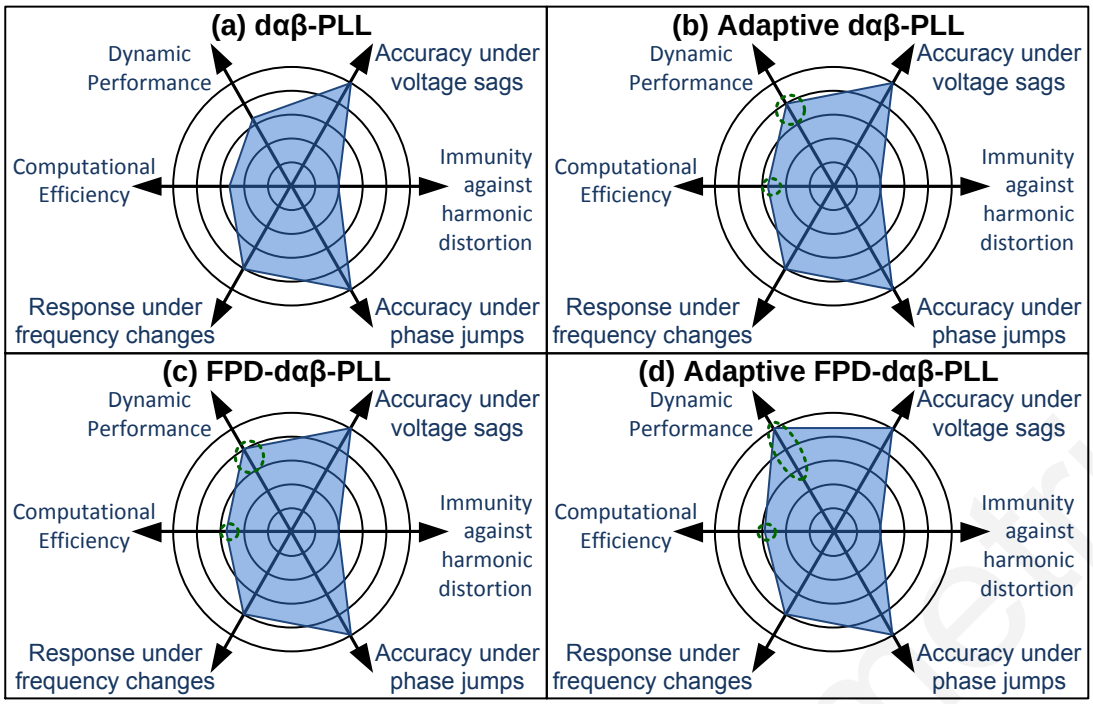

Fig. 3.20. Synopsis of the performance benchmarking between the four synchronization methods proposed in this Section: (a) the dαβ-PLL, (b) the adaptive dαβ-PLL and (c) the FPD-dαβ-PLL, and (d) the adaptive FPD-dαβ-PLL.

3.5 Conclusions

This Section proposes a new adaptive dαβ-PLL, which achieves a faster response and an accurate estimation of the phase angle and amplitude of the grid voltage under low-voltage grid faults. The proposed PLL improves the synchronization of the RES by using the proposed tuning adaptation mechanism according to the online estimation of the grid fault characteristics. The faster performance of the adaptive PLL beneficially affects the performance of the GSC of an interconnected RES, especially under FRT operation. Furthermore, a new synchronization method, named FPD-dαβPLL, is presented in this Chapter, where a method that decouples the frequency and phase estimation loop is applied to the structure of the dαβ-PLL in order to improve the performance of the PLL. Finally, the frequency-phase decoupling method is combined with the proposed tuning adaptation technique and therefore the adaptive FPD-dαβ-PLL is proposed. The new adaptive FPD-dαβ-PLL presents an outstanding performance, which overcomes the other under investigation synchronization methods in terms of time response. A synopsis of the performance evaluation of each PLL is presented in Fig. 3.20, where it is demonstrated that the proposed adaptive tuning mechanisms for the PLL (proposed within this Chapter) can significantly accelerate the time response of the synchronization with a minimum overhead regarding its complexity. The only disadvantage of the proposed synchronization method

of this chapter is the vulnerability against low order harmonic distortion. Therefore, it is higly recommended to use these synchronization methods in case where the RES is connected to a grid with negligible harmonic distortion (i.e., when the RES is connected to the medium or high voltage network where the effect of non-linear loads is insignificant). The acceleration of the synchronization by the proposed PLL can improve the FRT performance of the RES, which is critical in order to provide the appropriate support to the power grid when faults occur and to avoid failures on the GSC and on the power grid.

CHAPTER 4
THREE-PHASE FAST SYNCHRONIZATION WITH ROBUSTNESS AGAINST HARMONICS

4.1 Introduction

This chapter proposes two new Phase-Locked Loops (PLL) based synchronization methods that present fast dynamic response and great immunity against voltage harmonic distortion. The dynamic response of the synchronization enables the fast Fault Ride Through (FRT) operation of the RES and the accuracy under highly harmonic distorted grid conditions can significantly enhance the power quality of the grid-connected RES and of the entire power system.

The first synchronization method, named MSHDC-PLL, is presented in Section 4.3 and it is based on a novel Multi-Sequence/Harmonic Decoupling Cell (MSHDC) that enables the fast and accurate decomposition of the sequence and harmonic components of the grid voltage. The result is that the proposed MSHDC-PLL can achieve a fast and accurate response under unbalanced low-voltage sags and under highly harmonic distorted grid conditions. Such an outstanding synchronization response can beneficially affect the performance of the GSC of RES, especially in terms of power quality.

The only disadvantage of the MSHDC-PLL is the increased complexity of the algorithm that requires significant computational/processing power in order to be processed in real-time in the micro-controller which is embedded within the GSC. Therefore, another synchronization method is proposed, named DNαβ-PLL that achieves an exact equivalent performance to the MSHDC-PLL, but with significantly less complexity. The proposed DNαβ-PLL is presented in Section 4.4 and it is based on a decoupling network designed in the stationary αβ-frame. The complexity assessment of Section 4.4.4 shows a significant reduction in term of complexity, while the theoretical analysis (Section 4.4.3) and the simulation and experimental results (Section 4.4.6) prove an outstanding performance under any grid conditions. The outstanding synchronization performance by the proposed DNαβ-PLL enables the dynamic operation of the GSC and

more importantly enhances the power quality of the interconnected RES with great benefots on the power quality of the whole power system.

4.2 Literature review and state of the art

The controller of the GSC [27], [43]-[47] is based on the synchronization unit, the active and reactive power (PQ) controller and the current controller, as already shown in Fig. 1.5 of Chapter 1. The synchronization unit usually consists of a PLL algorithm to detect the phase and amplitude of the grid voltage at the point of common coupling (PCC). The PQ controller is responsible for generating the reference currents under normal and faulty grid conditions and the current controller ensures a proper current injection. The PQ and the current controllers are directly affected by the response of the synchronization method and therefore, the PLL performance is critical for an appropriate operation of grid-connected RES.

As already mentioned in Section 2.2, the synchronization method is usually based on a PLL algorithm when the controller of the GSC is designed on the synchronous rotating reference frame (*dq*-frame) with Proportional-Integral (PI) controllers [27], [43]-[47]. Conventional PLL algorithms, such as the dq-PLL [59] and the αβ-PLL [60]-[62], are simplified in structure and can provide proper operation only under normal operating voltage conditions. These PLLs are inaccurate under abnormal grid conditions, since they are sensitive to the oscillations of the synchronization signals caused by the existence of the negative sequence voltage (unbalanced conditions) and the low-order voltage harmonic distortion. These inaccuracies can affect the power quality of the RES.

One way to overcome these inaccuracies on the synchronization response is to adjust the tuning parameters of the PLL to reduce the bandwidth of the synchronization method as suggested by [99], [104]. Unfortunately, a significant deceleration of the time response of the synchronization is caused by reducing the PLL bandwidth.

A pre-calculating/pre-filtering stage is usually employed in the structure of the PLL in order to enhance its operation against asymmetric and distorted conditions. Some other PLLs [66]-[68] are enhanced with adaptive or notch filtering techniques to cancel out the oscillations caused by abnormal voltage conditions. These filters can unavoidably affect the dynamic response of the synchronization, and thus, the FRT operation of the RES will be negatively affected. The modified PLL in [78] is based on a non-linear adaptive approximation technique and presents higher degree of immunity to noise. However, the

very slow dynamics of this method do not allow it to be used in control loops. The three-phase enhanced PLL (3E-PLL) of [69] is accurate under unbalanced grid conditions, can relatively mitigate, but not eliminate, the effect of the harmonic distortion on the synchronization accuracy and presents slower dynamics compared to the ddsrf-PLL [79] (Section 2.2.2) and the dαβ-PLL [28], [29] (Section 2.4) as shown in [65].

The ddsrf-PLL [79] and the dαβ-PLL [28], [29] are designed in double reference frame and use a decoupling network to cancel out dynamically the double frequency oscillation of the positive sequence of the grid voltage due to the unbalanced voltage. These PLLs achieve a fast and accurate synchronization under balanced or unbalanced low-voltage grid faults and enable the FRT operation of RES. However, they are sensitive to voltage harmonic distortion. Similarly, the DSOGI-PLL [63], [64] is based on two second order generalized integrators in order to accurately calculate the positive sequence of voltage under unbalanced voltage. The DSOGI-PLL is accurate under asymmetric voltages but it is inaccurate under low-order harmonic distortion. Furthermore, the DSOGI-PLL presents a slower dynamic response compared to the ddsrf-PLL according to [65].

Some very interesting synchronization methods have been proposed in [73]-[76] based on Moving Average Filters (MAF). These MAF based PLLs are quite simplified in structure/complexity and are robust against unbalanced and harmonic distorted grid conditions. The MAF-PLL [73] is based on the structure of the dq-PLL and additionally it employs a MAF in its loop as shown in Fig. 4.1.

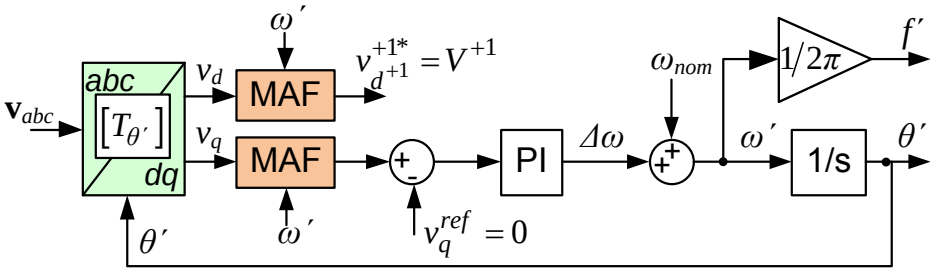

Fig. 4.1. The structure of the MAF-PLL.

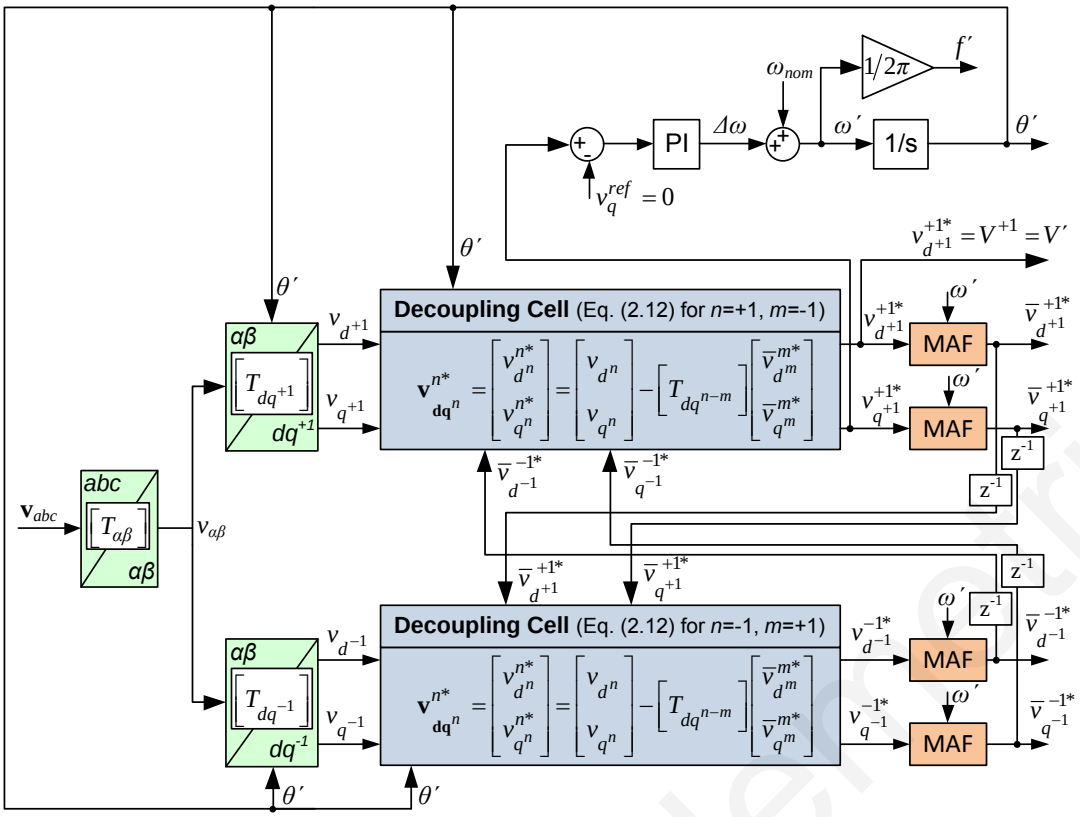

Fig. 4.2. The structure of the modified MRF-PLL.

Similarly the modified Multi Reference Frame (MRF) PLL [73] (modified MRF-PLL), inherits the structure of the ddsrf-PLL and replaces each Low-Pass Filter (LPF) of the decoupling network with a corresponding MAF as shown in Fig. 4.2. The MAF-PLL and the modified MRF-PLL present two main disadvantages. The first disadvantage is with regards to the discrete implementation of the MAF that causes some small inaccuracies when the grid frequency deviates from the nominal value. These inaccuracies can be minimized, but not eliminated, by adjusting the number of samples according to the operating frequency [73]. The only way to completely eliminate these inaccuracies is to use a variable sampling period for the PLL to adapt the window length of the MAF [77], but the variable sampling rate can cause restrictions on the GSC controller. Nevertheless, even if these inaccuracies are overcome, the second disadvantage of the MAF based PLLs is the slower dynamic performance compared to the ddsrf-PLL and dαβ-PLL.

As a conclusion, the ddsrf-PLL and the dαβ-PLL can be considered as the state-of-the-art synchronization solutions in terms of dynamic response and of accuracy under unbalanced voltage sags. However, they cannot operate accurately under a harmonic distorted environment. On the other hand, MAF based PLLs, such as the MAF-PLL and the modified MRF-PLL, can be considered as the state-of-the-art solution in terms of accuracy under unbalanced and harmonic distorted voltage conditions. Unfortunately, the

MAF based PLLs face some issues against non-nominal frequencies and more importantly present a slower dynamic response that may affect the dynamic operation of RES, which is especially critical under FRT operation. Thus, it is obvious that there is a need of three-phase synchronization methods that can achieve a very fast and very accurate response under any grid conditions (balanced or unbalanced low-voltage sags, frequency change, phase jump and harmonic distorted voltage). The very fast synchronization response is critical for the FRT operation of RES while the accuracy under any grid conditions is essential for the power quality of RES.

The two synchronization methods for three-phase GSCs, which are proposed within this Chapter, enable such an outstanding synchronization performance under any grid conditions. The first synchronization method proposed in Section 4.3, named MSHDC-PLL, can achieve a fast dynamic response and an accurate operation under unbalanced voltage sags and under highly harmonic distorted conditions. The only disadvantage of the MSHDC-PLL is the significantly increased complexity of the algorithm that requires a significant processing time for its real-time operation. Therefore, a second synchronization method, named DNαβ-PLL, is proposed in Section 4.4, which can also achieve a very fast and accurate performance under any grid conditions (equivalent performance with the MSHDC-PLL) and moreover, it requires significantly less processing time than the MSHDC-PLL. Hence, the proposed DNαβ-PLL can be considered as the state-of-the-art synchronization solution in terms of fast dynamic response under grid faults, of accuracy under any grid conditions and of computational efficiency of the algorithm. Therefore, the outstanding performance of the DNαβ-PLL can enable the proper FRT operation of RES under grid faults, can improve the power quality of RES under a highly harmonic distortion environment and can be easily applied in the embedded microcontroller of the GSC due to its decreased complexity.

4.3 MSHDC-PLL

According to the literature review of Section 4.2, it is obvious that there is a need to propose a new advanced synchronization method with fast dynamic response under grid faults and with accurate performance under any grid conditions (including voltage harmonic distortion). Such an advanced synchronization method can enable the proper FRT operation of RES according to the grid codes and moreover, can improve the power quality of grid-connected RES and as a consequence the power quality of the whole power system. Hence, this Section proposes a novel PLL based synchronization method that

presents such fast and accurate performance under any grid conditions. The design of the proposed synchronization method is based on a novel Multi-Sequence/Harmonic Decoupling Cell (MSHDC) (Section 4.3.1) as has been proposed by the author in [34], which enables the fast decomposition of the positive sequence of the voltage under unbalanced and harmonic distorted conditions. The proposed MSHDC-PLL (Section 4.3.2) is developed by combining the novel MSHDC for extracting the positive sequence of voltage with the algorithm of αβ-PLL [60]-[62] for a fast tracking of the phase angle of the positive sequence of the grid voltage. The outstanding performance of the proposed MSHDC-PLL is verified through simulation and experimental results in Section 4.3.3.

4.3.1 The novel Multi-Sequence/Harmonic Decoupling Cell (MSHDC)

The novel Multi-Sequence/Harmonic Decoupling Cell (MSHDC) enables the fast and accurate decomposition of the grid voltage components. Such a dynamic and accurate decoupling network is necessary to calculate the positive sequence of the grid voltage without any oscillations caused by harmonic distorted and unbalanced conditions in order to enable the proper grid synchronization of a RES. The proposed MSHDC is designed in multiple synchronous reference frames (rotating with angular velocity $+\omega$, $-\omega$, $\pm h\omega$ where ω is the fundamental grid frequency and h is the order of the most significant harmonic components of the grid voltage) according to the space vector transformation theory of Appendix A. Furthermore, the design of the MSHDC is enabled by an advanced voltage analysis of unbalanced and harmonic distorted voltage in several rotating frames, each frame rotated with the corresponding angular speed of the positive and the negative sequences and of each harmonic order as briefly explained in Appendix A.5.

Voltage analysis in multiple synchronous reference frames under abnormal conditions

According to the Clarke's transformation theory (Appendix A.3), the grid voltage $\mathbf{v}_{abc}$ can be expressed in the stationary reference frame ($\alpha\beta$-frame) as $\mathbf{v}_{\alpha\beta}$, as given by (4.1).

$$\mathbf{v}_{\alpha\beta} = \left[T_{\alpha\beta}\right]\mathbf{v}_{abc} \quad \text{and} \quad \mathbf{v}_{abc} = \left[T_{\alpha\beta}\right]^{-1}\mathbf{v}_{\alpha\beta} \tag{4.1}$$

where:

$$\mathbf{v}_{\alpha\beta} = \begin{bmatrix} v_\alpha \\ v_\beta \end{bmatrix}, \mathbf{v}_{abc} = \begin{bmatrix} v_a \\ v_b \\ v_c \end{bmatrix}, \left[T_{\alpha\beta}\right] = \frac{2}{3}\begin{bmatrix} 1 & -\frac{1}{2} & -\frac{1}{2} \\ 0 & \frac{\sqrt{3}}{2} & -\frac{\sqrt{3}}{2} \end{bmatrix}, \left[T_{\alpha\beta}\right]^{-1} = \begin{bmatrix} 1 & 0 \\ -\frac{1}{2} & \frac{\sqrt{3}}{2} \\ -\frac{1}{2} & -\frac{\sqrt{3}}{2} \end{bmatrix}$$

Similarly, by using the Park's transformation matrix $[T_{dq^{+1}}]$ (Appendix A.4) the grid voltage vector can also be expressed as $\mathbf{v}_{dq^{+1}}$ in the synchronous rotating reference frame (dq^{+1}-frame) rotating with the fundamental angular frequency ω, according to (4.2).

$$\mathbf{v}_{dq} = \left[T_{dq^n} \right]\Big|_{n=+1} \cdot \mathbf{v}_{\alpha\beta} \tag{4.2}$$

where:

$$\mathbf{v}_{dq} = \begin{bmatrix} v_d \\ v_q \end{bmatrix}, \quad \left[T_{dq^n} \right] = \begin{bmatrix} \cos(n\omega' t) & \sin(n\omega' t) \\ -\sin(n\omega' t) & \cos(n\omega' t) \end{bmatrix}$$

$\theta'=\omega' t$ represents the estimated phase angle of the positive sequence of the grid voltage and ω' the estimated fundamental angular frequency of the grid as given by the PLL algorithm.

Now, under normal operating conditions the grid voltage vector $\mathbf{v}_{abc}$ consists only of the positive sequence component $\mathbf{v}_{abc}^{+1}$. In this case, the transformation of the $\mathbf{v}_{abc} = \mathbf{v}_{abc}^{+1}$ into the corresponding dq^{+1}-frame leads to the vector $\mathbf{v}_{dq^{+1}}$, which consists only of the "oscillation-free/DC terms" $v_{d^{+1}}$, $v_{q^{+1}}$, as shown below,

$$\begin{aligned}
&\mathbf{v}_{dq^{+1}} = \left[T_{dq^{+1}} \right] \left(\left[T_{\alpha\beta} \right] \mathbf{v}_{abc}^{+1} \right) = \left[T_{dq^{+1}} \right] \mathbf{v}_{\alpha\beta}^{+1} \\
\Leftrightarrow\ &\mathbf{v}_{dq^{+1}} = \begin{bmatrix} \cos(\theta') & \sin(\theta') \\ -\sin(\theta') & \cos(\theta') \end{bmatrix} \cdot V^{+1} \begin{bmatrix} \cos(\omega t + \varphi^{+1}) \\ \sin(\omega t + \varphi^{+1}) \end{bmatrix} \\
\Leftrightarrow\ &\mathbf{v}_{dq^{+1}} = V^{+1} \begin{bmatrix} \cos(\theta')\cos(\omega t + \varphi^{+1}) + \sin(\theta')\sin(\omega t + \varphi^{+1}) \\ -\sin(\theta')\cos(\omega t + \varphi^{+1}) + \cos(\theta')\sin(\omega t + \varphi^{+1}) \end{bmatrix} \\
\Leftrightarrow\ &\mathbf{v}_{dq^{+1}} = \begin{bmatrix} v_{d^{+1}} \\ v_{q^{+1}} \end{bmatrix} = V^{+1} \begin{bmatrix} \cos(\theta' - \omega t - \varphi^{+1}) \\ \sin(\omega t + \varphi^{+1} - \theta') \end{bmatrix} = V^{+1} \begin{bmatrix} \cos(\varphi^{+1}) \\ \sin(\varphi^{+1}) \end{bmatrix}
\end{aligned} \tag{4.3}$$

φ^{+1} represents the initial phase angle of the positive sequence of the grid voltage. It is to be noted that (4.3) is valid only when the estimated by the PLL $\theta'=\omega' t$ can accurately estimate the grid phase angle.

In the case of abnormal voltage conditions (unbalanced and harmonic distorted) the grid voltage vector $\mathbf{v}_{abc}$ can be expressed as a summation of the positive $\mathbf{v}_{abc}^{+1}$ and the negative $\mathbf{v}_{abc}^{-1}$ sequences and all the harmonic components $\mathbf{v}_{abc}^{h}$ (h=±5, ±7, …) as shown in (4.4).

$$\mathbf{v}_{abc} = \mathbf{v}_{abc}^{+1} + \mathbf{v}_{abc}^{-1} + \mathbf{v}_{abc}^{+5} + \mathbf{v}_{abc}^{-5} + \mathbf{v}_{abc}^{+7} + \mathbf{v}_{abc}^{-7} + \ldots \tag{4.4}$$

It is to be noted that the voltage analysis does not consider only the -5th and +7th harmonic order (as it is expected in a three-phase system), since in case of unbalanced faults, both +5th, -5th and +7th, -7th harmonic orders are required to describe accurately the grid voltage vector. Now, If the generic voltage $\mathbf{v_{abc}}$ (with asymmetric conditions and harmonic distortion) is expressed in the corresponding dq^{+1}-frame, then the resulting vector $\mathbf{v}_{dq^{+1}}$ of (4.5) can be considered as a summation of the "oscillation-free/DC" vector $\mathbf{v}_{dq^{+1}}^{+1}$ and the oscillating vectors $\mathbf{v}_{dq^{+1}}^{m}$, where m=-1 for the negative sequence of voltage (unbalanced conditions) and m=±h for all the existing harmonic orders.

$$\mathbf{v}_{dq^{+1}} = \left[T_{\theta'}\right]\Big|_{\theta'=+\omega t} \cdot \left(\mathbf{v}_{abc}^{+1} + \sum_{h=-1,\pm5,\pm7,\ldots} \mathbf{v}_{abc}^{m} \right) = \left[T_{dq^{+1}} \right] \cdot \left(\mathbf{v}_{\alpha\beta}^{+1} + \sum_{m=-1,\pm5,\pm7,\ldots} \mathbf{v}_{\alpha\beta}^{m} \right)$$
$$\Leftrightarrow \mathbf{v}_{dq^{+1}} = \mathbf{v}_{dq^{+1}}^{+1} + \sum_{m=-1,\pm5,\pm7,\ldots} \mathbf{v}_{dq^{+1}}^{m} \qquad (4.5)$$

$$\text{where: } \mathbf{v}_{dq^{+1}}^{+1} = V^{+1} \begin{bmatrix} \cos(\varphi^{+1}) \\ \sin(\varphi^{+1}) \end{bmatrix},\ \mathbf{v}_{dq^{+1}}^{m} = V^{m} \begin{bmatrix} \cos\left((m-1)\omega t + \varphi^{m}\right) \\ \sin\left((m-1)\omega t + \varphi^{m}\right) \end{bmatrix}$$

It is worth mentioning that the vector $\mathbf{v}_{dq^{+1}}^{+1}$ represents the vector component $\mathbf{v}_{abc}^{+1}$ expressed in the corresponding dq^{+1}-frame, while the vector $\mathbf{v}_{dq^{+1}}^{m}$ represents the vector component $\mathbf{v}_{abc}^{m}$ also expressed in the corresponding dq^{+1}-frame. At this point, it is obvious that the existence of negative sequence (unbalanced conditions) and harmonic components (harmonic distortion) on the grid voltage causes oscillations on the voltage vector $\mathbf{v}_{dq^{+1}}$ when this is expressed in the dq^{+1}-frame. These oscillations can directly affect the synchronization method and the current and PQ controller of the GSC controller and as a consequence the performance of the whole RES is affected. Therefore, it is necessary to propose synchronization solutions that can estimate the oscillation-free voltage vector $\mathbf{v}_{dq^{+1}}^{+1}$.

Development of the MSHDC

In order to estimate the oscillation-free voltage vector $\mathbf{v}_{dq^{+1}}^{+1}$, which is particularly useful for the synchronization and the control of the GSC, a novel decoupling network is proposed based on the analysis of the voltage vector in multiple synchronous reference frames. According to (4.5), the voltage vector under abnormal grid conditions can be written as a summation of the positive sequence of the voltage $\mathbf{v}_{dq^{+1}}^{+1}$ and the negative sequence and all the harmonic components of the voltage $\mathbf{v}_{dq^{+1}}^{m}$, where m=-1,±5, ±7, … all

expressed in the dq^{+1}-frame. In general, abnormal grid voltage conditions are indicated by the presence of more than one rotating voltage vector (each one is rotating with a different speed) in the grid voltage as shown in (4.5).

According to the space vector transformation theory, any voltage vector $\mathbf{v}_{abc}$ can be expressed in any dq^n-frame, rotating with the corresponding $n\cdot\omega$ angular frequency, where n can be equal to any of the ±1, ±5, ±7 harmonic order depending on the existing components of the grid voltage, as given by (4.6).

$$\mathbf{v}_{dq^n} = \left[T_{dq^n}\right]\left(\left[T_{\alpha\beta}\right]\sum_{\substack{m=all\ existing\\ components}}\mathbf{v}^m_{abc}\right) = \left[T_{dq^n}\right]\left(\sum_{\substack{m=all\ existing\\ components}}\mathbf{v}^m_{\alpha\beta}\right) \tag{4.6}$$

$$\Leftrightarrow \mathbf{v}_{dq^n} = \sum_{\substack{m=all\ existent\\ components}}\mathbf{v}^m_{dq^n} = \mathbf{v}^n_{dq^n} + \sum_{m\neq n}\mathbf{v}^m_{dq^n}$$

where:

$$\mathbf{v}^n_{dq^n} = V^n\begin{bmatrix}\cos(\varphi^n)\\ \sin(\varphi^n)\end{bmatrix} \rightarrow \text{Oscillation-free},$$

$$\mathbf{v}^m_{dq^n} = V^m\begin{bmatrix}\cos\left((m-n)\omega t+\varphi^m\right)\\ \sin\left((m-n)\omega t+\varphi^m\right)\end{bmatrix} \rightarrow \text{Oscillating}$$

It should be noted that the vector $\mathbf{v}^n_{dq^n}$ represents the component of the voltage vector $\mathbf{v}^n_{abc}$ expressed in the corresponding dq^n-frame. Since, the vector $\mathbf{v}^n_{abc}$and the dq^n-frame rotate with the same angular speed $n\cdot\omega$, the $\mathbf{v}^n_{dq^n}$ is actually an oscillation-free/DC vector. On the other hand, the vector $\mathbf{v}^m_{dq^n}$ represents the component of the voltage vector $\mathbf{v}^m_{abc}$ also expressed in the corresponding dq^n-frame. Since the vector $\mathbf{v}^m_{abc}$ rotates with an angular speed of $m\cdot\omega$ and the dq^n-frame with an angular speed of $n\cdot\omega$, the resulting $\mathbf{v}^m_{dq^n}$ presents $(m\text{-}n)\cdot\omega$ oscillations as shown in (4.6). Therefore, an unbalanced and harmonic distorted voltage vector expressed in any dq^n-frame can be described as a superposition of one oscillation-free/DC vector and several oscillating vectors (due to the coupling effect between the rotating vectors). Now, according to Park's transformation theory in multiple reference frames, the oscillating vector $\mathbf{v}^m_{dq^n}$ can be expressed in terms of the oscillation-free vector $\mathbf{v}^m_{dq^m}$, which is expressed in the corresponding dq^m-frame, as given by,

$$\mathbf{v}_{dq^n}^{m} = \left[T_{dq^{(n-m)}} \right] \mathbf{v}_{dq^m}^{m} \tag{4.7}$$

where: $$\left[T_{dq^{(n-m)}} \right] = \begin{bmatrix} \cos\left((n-m)\omega' t\right) & \sin\left((n-m)\omega' t\right) \\ -\sin\left((n-m)\omega' t\right) & \cos\left((n-m)\omega' t\right) \end{bmatrix},$$

$$\mathbf{v}_{dq^m}^{m} = V^m \begin{bmatrix} \cos(\varphi^m) \\ \sin(\varphi^m) \end{bmatrix} \rightarrow \text{Oscillation-free vector}$$

It is to be noted that φ^m represents the initial phase angle of the voltage sequence/harmonic component $\mathbf{v}_{abc}^{m}$. Now, by substituting (4.7) in (4.6), the vector $\mathbf{v}_{dq^n}$ can be re-expressed in terms of oscillation-free vectors $\mathbf{v}_{dq^n}^{n}$ and $\mathbf{v}_{dq^m}^{m}$, as given by,

$$\mathbf{v}_{dq^n} = \mathbf{v}_{dq^n}^{n} + \sum_{m \neq n} \left[T_{dq^{(n-m)}} \right] \mathbf{v}_{dq^m}^{m} \tag{4.8}$$

The formulation of (4.8) is considered as the cornerstone for designing the proposed decoupling network. The representation of the grid voltage vector in all the rotating reference frames (dq^n-frame) of the contained vectors $\mathbf{v}_{abc}^{n}$ by using (4.8) is very useful in order to decouple and estimate accurately all the contained vectors. For example, if the grid voltage is unbalanced, containing a positive (+1) and a negative (-1) sequence component, and distorted with two main harmonics (with +5th and -5th order), then the voltage vector can be expressed as a superposition of the $\mathbf{v}_{abc}^{+1}$, $\mathbf{v}_{abc}^{-1}$, $\mathbf{v}_{abc}^{+5}$ and $\mathbf{v}_{abc}^{-5}$ rotating vectors, each one rotating with its own synchronous speed. Usually, the -5th is the main harmonic presented in the grid, but because this Chapter is examining a distorted voltage under unbalanced conditions, the +5th harmonic is not negligible since it will appear as a consequence of the existence of an unbalanced -5th harmonic (in the same way that the negative sequence appears under unbalanced conditions). Therefore, a representation of the voltage vector in each rotating reference frame (dq^n-frame) is given by the multiple use of (4.8) for n= +1, -1, +5 and -5, as given by (4.9), where Z is the two by two zero matrix.

$$\begin{bmatrix} \mathbf{v}_{dq^{+1}} \\ \mathbf{v}_{dq^{-1}} \\ \mathbf{v}_{dq^{+5}} \\ \mathbf{v}_{dq^{-5}} \end{bmatrix} = \underbrace{\begin{bmatrix} \mathbf{v}_{dq^{+1}}^{+1} \\ \mathbf{v}_{dq^{-1}}^{-1} \\ \mathbf{v}_{dq^{+5}}^{+5} \\ \mathbf{v}_{dq^{-5}}^{-5} \end{bmatrix}}_{\text{Oscillation-free vectors}} + \underbrace{\begin{bmatrix} Z & T_{dq^{+1-(-1)}} & T_{dq^{+1-(+5)}} & T_{dq^{+1-(-5)}} \\ T_{dq^{-1-(+1)}} & Z & T_{dq^{-1-(+5)}} & T_{dq^{-1-(-5)}} \\ T_{dq^{+5-(+1)}} & T_{dq^{+5-(-1)}} & Z & T_{dq^{+5-(-5)}} \\ T_{dq^{-5-(+1)}} & T_{dq^{-5-(-1)}} & T_{dq^{-5-(+5)}} & Z \end{bmatrix} \begin{bmatrix} \mathbf{v}_{dq^{+1}}^{+1} \\ \mathbf{v}_{dq^{-1}}^{-1} \\ \mathbf{v}_{dq^{+5}}^{+5} \\ \mathbf{v}_{dq^{-5}}^{-5} \end{bmatrix}}_{\text{Oscillating vectors}} \tag{4.9}$$

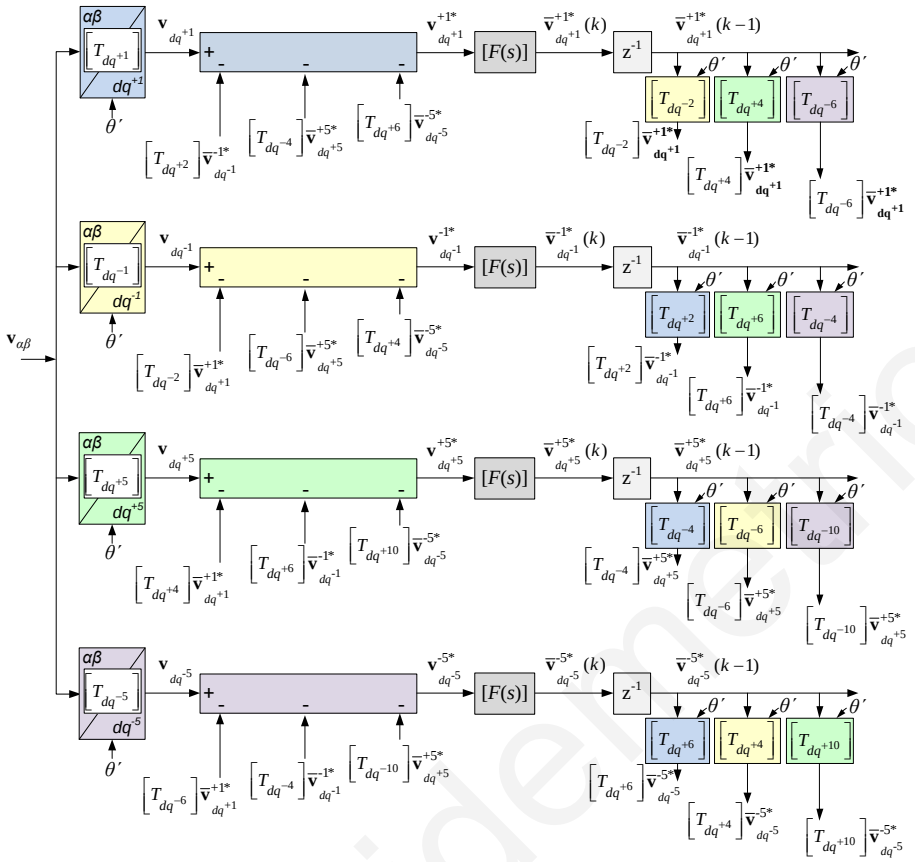

Fig. 4.3. The block diagram of the MSHDC.

Hence, in order to estimate the oscillation-free voltage vectors, (4.9) can be re-written as,

$$\begin{bmatrix} \mathbf{v}^{+1}_{dq^{+1}} \\ \mathbf{v}^{-1}_{dq^{-1}} \\ \mathbf{v}^{+5}_{dq^{+5}} \\ \mathbf{v}^{-5}_{dq^{-5}} \end{bmatrix} = \begin{bmatrix} \mathbf{v}_{dq^{+1}} \\ \mathbf{v}_{dq^{-1}} \\ \mathbf{v}_{dq^{+5}} \\ \mathbf{v}_{dq^{-5}} \end{bmatrix} - \begin{bmatrix} Z & T_{dq^{+1-(-1)}} & T_{dq^{+1-(+5)}} & T_{dq^{+1-(-5)}} \\ T_{dq^{-1-(+1)}} & Z & T_{dq^{-1-(+5)}} & T_{dq^{-1-(-5)}} \\ T_{dq^{+5-(+1)}} & T_{dq^{+5-(-1)}} & Z & T_{dq^{+5-(-5)}} \\ T_{dq^{-5-(+1)}} & T_{dq^{-5-(-1)}} & T_{dq^{-5-(+5)}} & Z \end{bmatrix} \begin{bmatrix} \mathbf{v}^{+1}_{dq^{+1}} \\ \mathbf{v}^{-1}_{dq^{-1}} \\ \mathbf{v}^{+5}_{dq^{+5}} \\ \mathbf{v}^{-5}_{dq^{-5}} \end{bmatrix} \tag{4.10}$$

Since, the vectors $\mathbf{v}_{dq^n}$ are known and the vectors $\mathbf{v}^n_{dq^n}$ are unknown, the estimation of the unknown vectors is enabled by replacing the unknown vector $\mathbf{v}^n_{dq^n}$ of the left side of (4.10) with the estimated vector $\mathbf{v}^{n*}_{dq^n}$, while the unknown vector of the right side of (4.10) is replaced by the filtered estimated vector $\bar{\mathbf{v}}^{n*}_{dq^n}$. The result is presented in (4.11), which can be used to developed the proposed Multi-Sequence/Harmonic Decoupling Cell (MSHDC) based on a cross-feedback network for the decoupling/decomposition of the voltage vector components as shown in Fig. 4.3.

$$\begin{bmatrix} \mathbf{v}_{dq^{+1}}^{+1*} \\ \mathbf{v}_{dq^{-1}}^{-1*} \\ \mathbf{v}_{dq^{+5}}^{+5*} \\ \mathbf{v}_{dq^{-5}}^{-5*} \end{bmatrix} = \begin{bmatrix} \mathbf{v}_{dq^{+1}} \\ \mathbf{v}_{dq^{-1}} \\ \mathbf{v}_{dq^{+5}} \\ \mathbf{v}_{dq^{-5}} \end{bmatrix} - \begin{bmatrix} Z & T_{dq^{+1-(-1)}} & T_{dq^{+1-(+5)}} & T_{dq^{+1-(-5)}} \\ T_{dq^{-1-(+1)}} & Z & T_{dq^{-1-(+5)}} & T_{dq^{-1-(-5)}} \\ T_{dq^{+5-(+1)}} & T_{dq^{+5-(-1)}} & Z & T_{dq^{+5-(-5)}} \\ T_{dq^{-5-(+1)}} & T_{dq^{-5-(-1)}} & T_{dq^{-5-(+5)}} & Z \end{bmatrix} \begin{bmatrix} \bar{\mathbf{v}}_{dq^{+1}}^{+1*} \\ \bar{\mathbf{v}}_{dq^{-1}}^{-1*} \\ \bar{\mathbf{v}}_{dq^{+5}}^{+5*} \\ \bar{\mathbf{v}}_{dq^{-5}}^{-5*} \end{bmatrix} \tag{4.11}$$

It should be mentioned that the filtered estimation vector $\bar{\mathbf{v}}_{dq^n}^{n*}$ is generated through a first-order low-pass filtering of the estimated vector $\mathbf{v}_{dq^n}^{n*}$, as given by,

$$\bar{\mathbf{v}}_{dq^n}^{n*} = [F(s)]\mathbf{v}_{dq^n}^{n*} \quad \Leftrightarrow \quad \begin{bmatrix} \bar{v}_{d^n}^{n*} \\ \bar{v}_{q^n}^{n*} \end{bmatrix} = [F(s)] \begin{bmatrix} v_{d^n}^{n*} \\ v_{q^n}^{n*} \end{bmatrix} \tag{4.12}$$

$$\text{where: } [F(s)] = \frac{\omega_f}{s+\omega_f} \begin{bmatrix} 1 & 0 \\ 0 & 1 \end{bmatrix}$$

The low-pass filter [$F(s)$] is required for eliminating any remaining oscillations and for enabling the proper operation of the proposed cross-feedback network. The design parameter ω_f of the proposed decoupling network should be set within the range $0.3\omega \leq \omega_f \leq 0.7\omega$ for enabling a reasonable trade-off between oscillation damping and time performance of the decoupling network, as will be demonstrated by the theoretical analysis of the decoupling network (see Section 4.4.3).

The block diagram of the proposed MSHDC is presented in Fig. 4.3, where it is shown that the design of the MSHDC is based on a cross-feedback decoupling network according to (4.11) and (4.12). The filtered estimation vectors $\bar{\mathbf{v}}_{dq^m}^{m*}$ are used as feedback vectors in order to cancel-out the oscillations presented in each dq^n-frame due to the coupling effect between the voltage vector components rotating with different speed. It should be noted that a sample delay is used for the feedback vectors $\bar{\mathbf{v}}_{dq^m}^{m*}$ in order to avoid any algebraic loops.

In a more generic way, (4.11) can be written as shown in (4.13), where all the non-negligible harmonics are included.

$$\mathbf{v}_{dq^n}^{n*} = \mathbf{v}_{dq^n} - \sum_{m \neq n} \left[T_{dq^{(n-m)}} \right] \bar{\mathbf{v}}_{dq^m}^{m*} \tag{4.13}$$

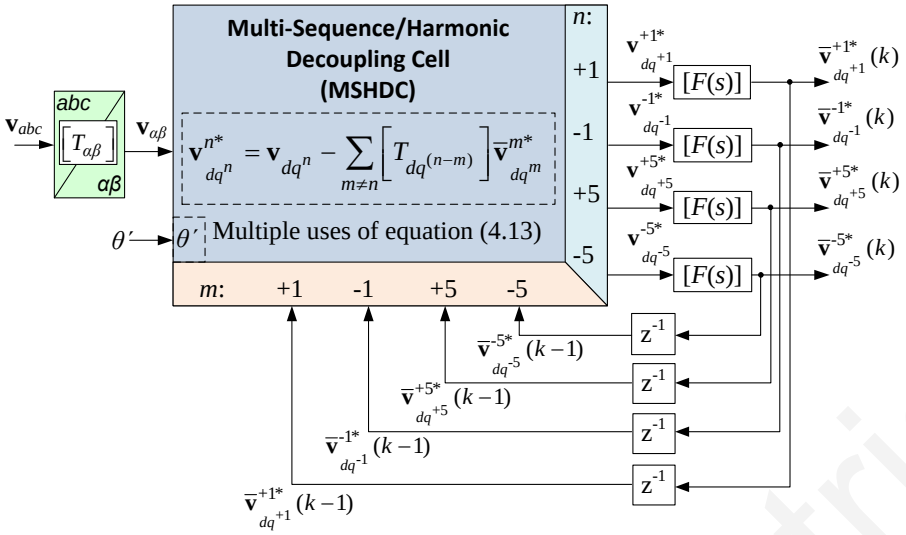

Fig. 4.4. The structure of the proposed MSHDC.

The proposed MSHDC can be developed by the multiple uses of (4.13), once for positive sequence (n=+1), once for negative sequence (n=-1) and twice for each non-negligible low-order harmonic (n=±h), as shown in Fig. 4.4. The MSHDC of Fig. 4.4 is considering only the positive and negative sequences and the +5th and -5th harmonics. It is noticeable, that the proposed MSHDC can be extended in order to consider all the non-negligible low-order harmonics.

The proposed MSHDC based on the multiple uses of (4.13) cancels out the oscillating vector in each rotating reference frame and enables the estimation of the desirable oscillation-free/DC vectors of the grid voltage. The MSHDC enables a fast and accurate decomposition of the positive and negative sequence components and of the non-negligible harmonic components. The vector $\mathbf{v}_{dq^{+1}}^{+1*}$, generated by the proposed MSHDC, accurately estimates the positive sequence component of the voltage vector $\mathbf{v}_{dq^{+1}}^{+1}$, which is a very important issue in the interconnected RES, since it can be used to achieve an accurate synchronization and appropriate control of the GSC. It is necessary to point out that the detection of the positive sequence voltage is given by the vector $\mathbf{v}_{dq^{+1}}^{+1*}$, which means that the time response of the estimation of the positive sequence voltage will not be affected directly from the low pass filter [F(s)]. Furthermore, the use of low-pass filters in a cross-feedback network results in a very fast dynamic response for the decomposition of the voltage vector, as will be proved in the theoretical analysis of the decoupling network in Section 4.4.3.

4.3.2 The structure of the proposed MSHDC-PLL

The proposed MSHDC-PLL can now be developed by combining the novel MSHDC for extracting the positive sequence of the voltage with the algorithm of the αβ-PLL [60]-[62] for a fast tracking of the phase angle of the positive sequence of the grid voltage. The MSHDC can detect fast and accurately the positive sequence of the grid voltage ($\mathbf{v}_{dq^{+1}}^{+1*}$), cleared for any oscillations from the existence of unbalanced and harmonic distorted voltage. Therefore, it is intuitive to use the MSHDC to provide an oscillation-free vector $\mathbf{v}_{dq^{+1}}^{+1*}$ for the positive sequence component and then the estimated vector $\mathbf{v}_{dq^{+1}}^{+1*}$ can be fed into any simple PLL algorithm in order to track the phase angle of the positive sequence component. For the simple PLL algorithms, the αβ-PLL algorithm [60]-[62] seems to be the preferable solution to be combined with the MSHDC since it presents a better dynamic response than the dq-PLL [59], as it has been proven in [28], [29] and in Section 2.3.

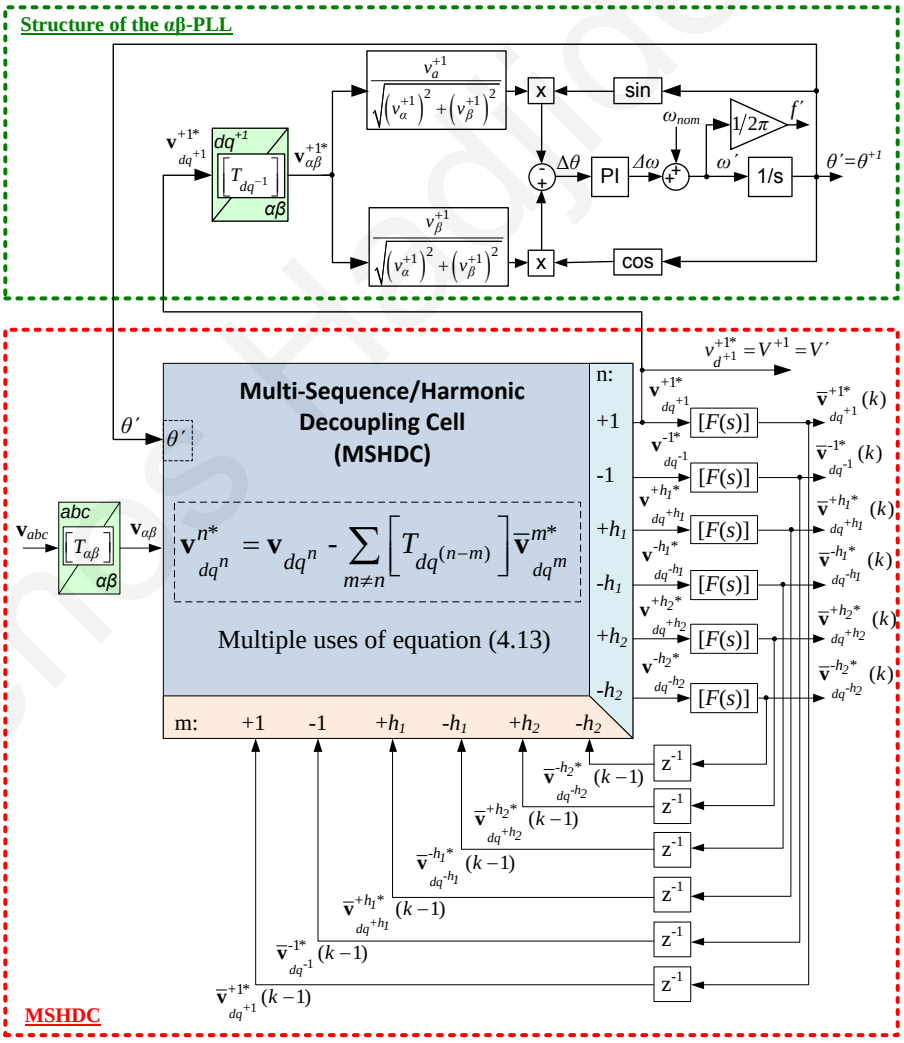

Fig. 4.5. The structure of the proposed MSHDC-PLL.

The structure of the proposed MSHDC-PLL is presented in Fig. 4.5, where it is shown that an MSHDC is used to dynamically estimate the oscillation-free vector $\mathbf{v}_{dq^{+1}}^{+1*}$ and then the αβ-PLL algorithm is used to estimate the phase angle ($\theta'=\theta^{+1}$) of the positive sequence of the grid voltage. The MSHDC has been used in the proposed PLL in its generic form in order to cancel out the oscillations from the unbalanced voltage (m=-1) and also the oscillations of the four most significant harmonics ($m=\pm h_1, \pm h_2$), as shown in Fig. 4.5.

Since the oscillation-free vector $\mathbf{v}_{dq^{+1}}^{+1*}$ has been estimated by the proposed decoupling network, the αβ-PLL algorithm (operating in the stationary reference frame) detects the phase angle of the positive sequence of the voltage. The phase detection is based on controlling the trigonometric equation (4.14) to track zero, so the detected angle (θ') tracks the phase angle of the positive sequence of the grid voltage (θ^{+1}).

$$\Delta\theta = \theta^{+1} - \theta' \approx \sin(\theta^{+1} - \theta') = \sin(\theta^{+1})\cos(\theta') - \sin(\theta')\cos(\theta^{+1}) \tag{4.14}$$

The tuning of the proposed MSHDC-PLL can be obtained according to the linearized small signal model analysis of a PLL, as presented in Appendix B. Therefore, the closed-loop transfer function of the MSHDC-PLL is given by,

$$H_\theta(s) = \frac{\theta'}{\theta^{+1}} = \frac{2\zeta\omega_n s + \omega_n^2}{s^2 + 2\zeta\omega_n s + \omega_n^2} = \frac{k_p s + \dfrac{1}{T_i}}{s^2 + k_p s + \dfrac{1}{T_i}} \tag{4.15}$$

The second order transfer function of (4.15) depicts that the PLLs present a low-pass filtering characteristic, therefore the stability of PLLs is ensured and also the attenuation of the detection error caused by possible noise and high order harmonics in the input signal is proved. Furthermore, the parameters of the PI controller of the PLLs may be chosen by,

$$k_p = \frac{9.2}{T_s} \qquad \text{and} \qquad T_i = 0.047\zeta^2 T_s^2 \tag{4.16}$$

where T_s is the settling time of the synchronization and the damping factor ζ is set to $1/\sqrt{2}$ in order to have an optimally damped system (with a 5% overshoot). For the purposes of this work the PI parameters have been set in a way to fulfill the German Grid Codes [11], [12], similar to the tuning procedure of the dαβ-PLL (Section 2.4). Thus, the proposed MSHDC-PLL can operate without violating the frequency operation window (from 47.5

Hz to 51.5 Hz) for any possible grid fault. Therefore, the settling time T_s is set to 0.745 s and as a consequence the tuning parameters of the MSHDC-PLL have been set to k_p=12.35 and T_i=0.013.

4.3.3 Simulation and experimental results

Since the basic idea, the principles, the formulation and the design guidelines for the proposed MSHDC-PLL have been defined in the previous sub-sections, simulation and experimental tests are required in order to prove that the proposed PLL meets the design expectations for a fast and accurate performance under any grid faults and under highly harmonic distortion.

Simulation results

A dynamic simulation model has been developed in MATLAB/Simulink in order to investigate the performance of the proposed MSHDC-PLL. It is reasonable that the proposed PLL should be compared to a conventional and a state-of-the-art PLL. The dαβ-PLL [28], [29] (Section 2.4) and the ddsrf-PLL [79] (Section 2.2.2) present the same accuracy under unbalanced voltages, but they are not robust against voltage harmonic distortion. Since the dαβ-PLL has a better dynamic response [28], [29] the proposed MSHDC-PLL is compared to the state-of-the-art dαβ-PLL and to the conventional dq-PLL [59].

The case study presented in Fig. 4.6, shows the response of the proposed MSHDC-PLL, the dαβ-PLL, and the conventional dq-PLL. At t=1 s the grid voltage at the PCC is distorted with -5th and +7th harmonics (V_{-5}=0.05|V_1|∠180^o and V_{+7}=0.03|V_1|∠160^o). Further, an unbalanced Type E fault (two phase to ground) with a 50% voltage sag

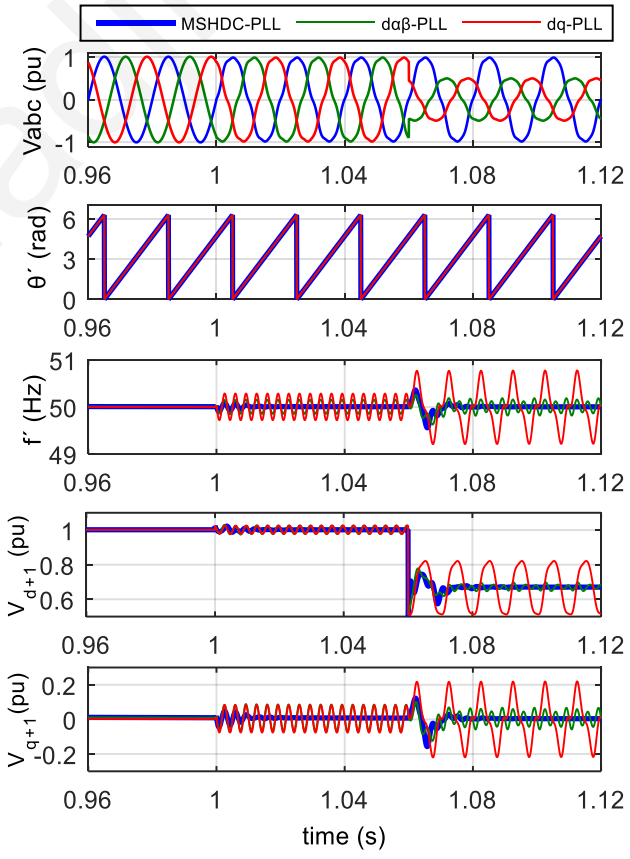

Fig. 4.6. Simulation results showing the performance of the proposed MSHDC-PLL, the dαβ-PLL and the dq-PLL under harmonic distorted voltage and unbalanced low-voltage grid fault.

occurs at 1.06 s. The estimation of the synchronization signals according to the conventional dq-PLL presents small oscillations due to the harmonic distortion and large oscillations due to the unbalanced voltage. The state-of-the-art dαβ-PLL presents small oscillations under harmonic distorted voltages regardless if the grid voltage is balanced or unbalanced. The proposed MSHDC-PLL presents an outstanding performance compared to the other two PLLs, since it can accurately estimate the phase angle, the amplitude and the frequency of the positive sequence of the grid voltage, free of any oscillations due to the harmonic distortion or the unbalanced grid conditions. Moreover, it is obvious from Fig. 4.6, that the accuracy of the proposed MSHDC-PLL does not affect its dynamic performance, since both the dαβ-PLL and the MSHDC-PLL present an equivalent dynamic response under any grid disturbances. Therefore, the proposed PLL prevails over the other PLLs due to the accurate and dynamic performance under harmonic distorted voltage and under unbalanced grid faults.

Experimental results

The proposed MSHDC-PLL is also experimentally validated using a dSPACE DS1103 DSP board to digitally implement the MSHDC-PLL algorithm and a California Instrument 4500LX AC source as the power grid.

The experimental results presented in Fig. 4.7 show the performance of the proposed MSHDC-PLL and the state-of-the-art dαβ-PLL under harmonic distorted grid voltage conditions (with $V_{-5}=0.05V_1\angle 180^o$) and under an unbalanced grid fault. Initially, the voltage is distorted with a -5th harmonic and then, at t=0.461s, a Type D (propagation through a Wye-Delta transformer of two phases with no ground fault) unbalanced fault occurs with a 37% voltage sag. Fig. 4.7 presents the performance of the two PLLs. The

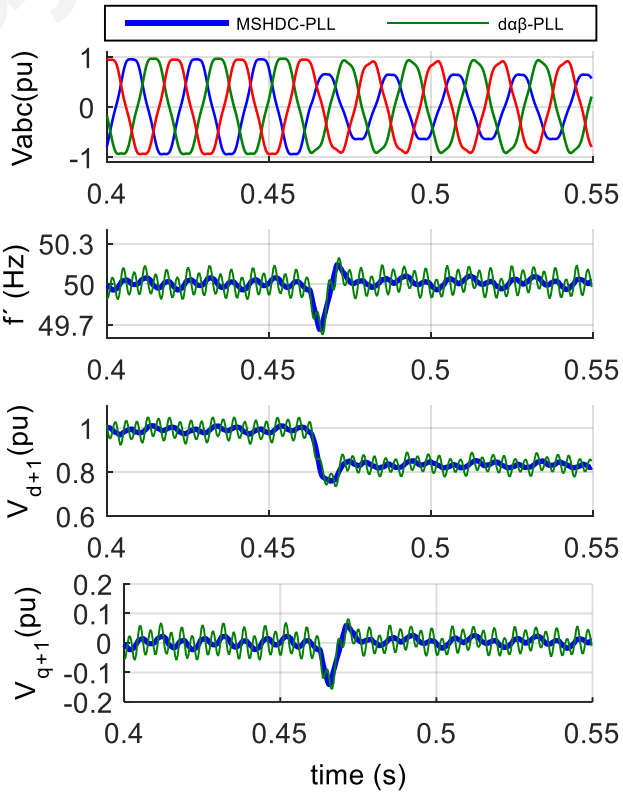

Fig. 4.7. Experimental results showing the performance of the proposed MSHDC-PLL and the dαβ-PLL under harmonic distorted voltage and unbalanced grid fault.

dαβ-PLL presents robustness against unbalanced faults, but the effect of the harmonic distortion is observable through the oscillations on the estimated synchronization signals. The proposed MSHDC-PLL presents an outstanding performance with robustness against unbalanced faults and against harmonic distortion (-5^{th} under balanced and -5^{th} and $+5^{th}$ under unbalanced fault). As shown in Fig. 4.7 , the estimated synchronization signals of the proposed PLL are free of oscillations since the MSHDC achieved to dynamically cancel out the oscillations caused by the voltage harmonics and the negative sequence of the voltage. The fast response obtained by the proposed PLL is essential in order to enable the dynamic FRT performance of RES when grid faults occur as specified by the modern grid codes. Furthermore, the accurate estimation of the positive sequence of the grid voltage by the MSHDC is essential for the accurate synchronization and is crucial for the GSC controller performance. The accurate detection of the positive sequence of the grid voltage can beneficially affect the GSC performance and especially the power quality of the GSC.

4.3.4 Conclusions

Section 4.3 proposes an advanced PLL algorithm enhanced with a novel multi-sequence/harmonic decoupling cell (MSHDC), called MSHDC-PLL, which can operate fast and accurately under unbalanced faults and under harmonic distorted voltage conditions. The use of the proposed PLL for the synchronization of the GSC on an interconnected RES can bring beneficial results. The accurate synchronization of the MSHDC-PLL can increase the quality of the injected power by RES and can enable the dynamic FRT operation of RES under grid faults.

Despite the outstanding performance of the proposed MSHDC-PLL, there are some disadvantages that should be pointed out. The first disadvantage is that the MSHDC-PLL can eliminate only the effect of the harmonic orders that are considered in the development of the MSHDC. Therefore, in the usual case where several harmonic orders exist in the grid voltage, the accurate operation of the MSHDC-PLL requires the development of a decoupling network that considers all the non-negligible harmonics. Further, each time that an additional harmonic order should be considered in the decoupling network, the computational efficiency of the MSHDC-PLL is significantly decreased. More specifically, if the decoupling network is designed to consider N voltage components (including the positive and negative sequence and a number of harmonic orders) then the required execution time of the synchronization is proportional to the square of N. Hence, in the next

Section (Section 4.4), a new synchronization method is proposed to overcome the two disadvantages of the MSHDC-PLL.

4.4 DNαβ-PLL

The synchronization unit in grid-connected RES is responsible to detect accurately and fast the voltage amplitude and phase angle of the positive sequence of the grid voltage at the PCC. Under normal grid operation conditions, conventional PLLs [59]-[62] can achieve accurate response by using Park's transformation to express the grid voltage to the synchronous rotating frame (dq^{+1}-frame), rotating with the synchronous speed of the positive sequence of the voltage, or to the stationary frame ($\alpha\beta$-frame). Unfortunately, the performance of the conventional synchronization methods is inaccurate under abnormal grid conditions due to the coupling effect between the existing voltage sequences and harmonics. Several methods proposed in the literature may present immunity against harmonics but this is usually compromised by a deceleration of the dynamic response of the synchronization.

In the previous Section (Section 4.3), a new synchronization method has been proposed, named MSHDC-PLL, which can achieve a fast and accurate response under unbalanced grid faults and harmonic distorted voltage conditions. Despite, the outstanding performance of the MSHDC-PLL, it has two disadvantage. First, the MSHDC-PLL can eliminate only the effect of the harmonic orders that are considered in the development of the MSHDC. Thus, to achieve an accurate response in the usual case where several harmonic orders exist in the grid voltage, the decoupling network should be designed considering all the non-negligible harmonics. Thus, if the MSHDC is designed to consider several harmonics, then the required execution time of the algorithm is significantly increased. It is worth to mention that the execution time is proportional to the number of voltage components that are considered in the design of the decoupling network. Hence, if the MSHDC-PLL is designed to consider several harmonics, then the processing of this PLL in the embedded microcontroller of the GSC can sometimes be impossible due to the increased required processing time.

Therefore, in this Section, a new synchronization method is proposed that overcomes the disadvantage of the MSHDC-PLL and can achieve the same accurate and dynamic response. The new DNαβ-PLL is developed based on an innovative decoupling network design in the $\alpha\beta$-frame (DNαβ), which enables an exact equivalent performance

with the MSHDC but requires a significantly less processing time. Hence, the new DNαβ-PLL can be designed to consider all the non-negligible harmonics and its execution time is remaining within reasonable limits for the real-time execution of the synchronization algorithm in conventional microcontrollers that are embedded within the GSC. Therefore, the proposed DNαβ-PLL is the most beneficial synchronization solution in terms of accuracy under unbalanced grid faults and harmonic distortion, in terms of dynamic response under any grid disturbances and in terms of computational efficiency. Further, the use of the DNαβ-PLL for the synchronization of the GSC can lead to significant performance improvement, especially in terms of the power quality of RES, as will be demonstrated within this Chapter.

4.4.1 - The novel Decoupling Network designed in αβ-frame (DNαβ)

The new DNαβ-PLL is based on a novel Decoupling Network designed in the αβ-frame (DNαβ), which can achieve a fast and accurate decomposition of the voltage vector components with less required processing time compared to the MSHDC (Section 4.3.1). The performance of the DNαβ (proposed in this Section) and the performance of the MSHDC (proposed in Section 4.3.1) are exactly equivalent and therefore can enable the same advanced synchronization performance. The difference between the two decoupling network is that the DNαβ is formulated and designed in the αβ-frame instead of in each synchronous reference frame, which requires significantly less Park's transformations for processing the algorithm in each control loop. Thus, the required processing time of the synchronization algorithm is minimized, which is a critical aspect on the real-time control of such power electronic applications.

Voltage analysis in stationary reference frame under abnormal grid conditions

The proposed decoupling network (DNαβ) is formulated and designed in the stationary *αβ*-frame. Therefore, it is necessary to begin with an in depth analysis in the *αβ*-frame of the grid voltage under abnormal grid conditions based on the space vector transformation theory that is briefly presented in Appendix A.

In case of harmonic distorted and unbalanced grids, the voltage can be analyzed as a sum of the existing rotating voltage vectors, each one rotating with a different speed. Thus, the grid voltage is a sum of positive (+1) and negative (-1) sequences and the

existing significant low-order harmonics (h_1,...,h_k) and can be expressed in the αβ-frame through the Clark's transformation matrix [$T_{\alpha\beta}$], as shown below.

$$\begin{aligned}
&\mathbf{v}_{\alpha\beta} = \left[T_{\alpha\beta}\right]\mathbf{v}_{abc} = \left[T_{\alpha\beta}\right]\left(\mathbf{v}_{abc}^{+1} + \mathbf{v}_{abc}^{-1} + \mathbf{v}_{abc}^{h1} + \cdots + \mathbf{v}_{abc}^{h_k}\right) \\
&\Leftrightarrow \mathbf{v}_{\alpha\beta} = \mathbf{v}_{\alpha\beta}^{+1} + \mathbf{v}_{\alpha\beta}^{-1} + \mathbf{v}_{\alpha\beta}^{h_1} + \cdots + \mathbf{v}_{\alpha\beta}^{h_k} \\
&\Leftrightarrow \mathbf{v}_{\alpha\beta} = \sum_{m=1,-1,h_1,..,h_k} V^m \begin{bmatrix} \cos(m\omega t + \theta^m) \\ \sin(m\omega t + \theta^m) \end{bmatrix}
\end{aligned} \tag{4.17}$$

where:
$$\left[T_{\alpha\beta}\right] = \frac{2}{3}\begin{bmatrix} 1 & -\frac{1}{2} & -\frac{1}{2} \\ 0 & \frac{\sqrt{3}}{2} & -\frac{\sqrt{3}}{2} \end{bmatrix} \tag{4.18}$$

Now, as already mentioned in Section 4.3.1, the voltage vector can equivalently be expressed in any dq^n-frame rotating with a corresponding $n\omega$ angular speed, as given by (4.19).

$$\begin{aligned}
&\mathbf{v}_{dq^n} = \left[T_{dq^n}\right]\left(\left[T_{\alpha\beta}\right]\sum_{m=1,-1,h_1,..,h_k}\mathbf{v}_{abc}^{m}\right) = \left[T_{dq^n}\right]\left(\sum_{m=1,-1,h_1,..,h_k}\mathbf{v}_{\alpha\beta}^{m}\right) \\
&\Leftrightarrow \mathbf{v}_{dq^n} = \sum_{m=1,-1,h_1,..,h_k}\mathbf{v}_{dq^n}^{m} = \mathbf{v}_{dq^n}^{n} + \sum_{m\neq n}\mathbf{v}_{dq^n}^{m}
\end{aligned} \tag{4.19}$$

where:

$$\mathbf{v}_{dq^n}^{n} = V^n\begin{bmatrix}\cos(\varphi^n)\\ \sin(\varphi^n)\end{bmatrix} \rightarrow \text{Oscillation-free vector},$$

$$\mathbf{v}_{dq^n}^{m} = V^m\left[T_{dq^{n-m}}\right]\begin{bmatrix}\cos(\varphi^m)\\ \sin(\varphi^m)\end{bmatrix} = V^m\begin{bmatrix}\cos\left((m-n)\omega t + \varphi^m\right)\\ \sin\left((m-n)\omega t + \varphi^m\right)\end{bmatrix} \rightarrow \text{Oscillating vector},$$

$$\left[T_{dq^{(n-m)}}\right] = \begin{bmatrix}\cos\left((n-m)\omega' t\right) & \sin\left((n-m)\omega' t\right)\\ -\sin\left((n-m)\omega' t\right) & \cos\left((n-m)\omega' t\right)\end{bmatrix}$$

The index n and m can be any of the existing sequences or harmonic components (+1, -1, h_1, …, h_k). It is to be noted that a harmonic order H_1 under unbalanced grid conditions, requires both $h_1 = +H_1$ and $h_2 = -H_1$ to be fully described (where H_1 can be equal to -5, +7, -11, +13), similarly to how an unbalanced fundamental component (1) requires both positive (+1) and negative (-1) sequence to be analyzed in detail under unbalanced faults. The transformation matrix $\left[T_{dq^{n-m}}\right]$ enables the transformation of a vector from the dq^m- to the dq^n-frame. It should be noted that the vector $\mathbf{v}_{dq^n}^{n}$ represents the component of

the voltage vector $\mathbf{v}_{abc}^{n}$ expressed in the corresponding dq^n-frame. Since, the angular speed of the vector $\mathbf{v}_{abc}^{n}$ and the dq^n-frame is the same, the $\mathbf{v}_{dq^n}^{n}$ is actually an oscillation-free/DC vector. On the other hand, the vector $\mathbf{v}_{dq^n}^{m}$ represents the component of the voltage vector $\mathbf{v}_{abc}^{m}$ also expressed in the corresponding dq^n-frame. Since the vector $\mathbf{v}_{abc}^{m}$ rotates with an angular speed of $m\cdot\omega$ and the dq^n-frame with an angular speed of $n\cdot\omega$, the resulting $\mathbf{v}_{dq^n}^{m}$ presents $(m\text{-}n)\cdot\omega$ oscillations as shown in (4.19).

As shown in (4.19), an abnormal grid voltage vector expressed in the dq^n-frame consists of an oscillation free vector $\mathbf{v}_{dq^n}^{n}$ and the sum of the oscillated vectors $\mathbf{v}_{dq^n}^{m}$. The oscillating vectors $\mathbf{v}_{dq^n}^{m}$ cause the inaccuracies on the conventional synchronization methods. Therefore, it is necessary to estimate each $\mathbf{v}_{dq^n}^{n}$ vector, cleared by the oscillations caused due to the coupling effect between the vectors rotating with different angular speeds. According to the transformation theory, (4.19) can be equivalently solved in terms of the oscillation-free/DC vector $\mathbf{v}_{dq^n}^{n}$ and then the right side of the equation can be expressed using the voltage vectors in $\alpha\beta$-frame, as given by,

$$\mathbf{v}_{dq^n}^{n} = \mathbf{v}_{dq^n} - \sum_{m\neq n}\mathbf{v}_{dq^n}^{m} = \left[T_{dq^n}\right]\mathbf{v}_{\alpha\beta} - \sum_{m\neq n}\left[T_{dq^n}\right]\mathbf{v}_{\alpha\beta}^{m} = \left[T_{dq^n}\right]\left(\mathbf{v}_{\alpha\beta} - \sum_{m\neq n}\mathbf{v}_{\alpha\beta}^{m}\right) \tag{4.20}$$

***Development of the DNαβ* decoupling network**

According to the above-mentioned voltage analysis and based on (4.20), the novel Decoupling Network designed in the $\alpha\beta$-frame (DNαβ) will be developed. The new decoupling network allows an accurate detection of each voltage vector component $\mathbf{v}^n$, by dynamically cancelling-out the oscillations that are created due to the coupling effect between the voltage components. The oscillations-free vector $\mathbf{v}_{dq^n}^{n}$ for each sequence or harmonic voltage can be calculated according to (4.20). However, since the vectors $\mathbf{v}_{\alpha\beta}^{m}$ cannot be accurately calculated due to the coupling effects, it is suggested to replace these vectors of (4.20) with the filtered estimated vectors $\bar{\mathbf{v}}_{\alpha\beta}^{*m}$ in order to determine the estimation vectors $\mathbf{v}_{\alpha\beta}^{n*}$ and $\mathbf{v}_{dq^n}^{n*}$, as given by,

$$\mathbf{v}_{dq^n}^{n*} = \left[T_{dq^n}\right]\mathbf{v}_{\alpha\beta}^{n*} = \left[T_{dq^n}\right]\left(\mathbf{v}_{\alpha\beta} - \sum_{m\neq n}\bar{\mathbf{v}}_{\alpha\beta}^{m*}\right) \tag{4.21}$$

It is worth mentioning that (4.21) consists the cornerstone of the proposed DNαβ. The estimation vectors require the low-pass filter [$F(s)$] (as shown in (4.24)) to eliminate

any remaining oscillations on the estimated voltage vector. The cut-off frequency (ω_f) should be set in the range of $0.3\omega \leq \omega_f \leq 0.7\omega$ for enabling a reasonable trade-off between oscillation damping and time performance of the decoupling network, where ω represents the nominal angular frequency of the grid. The proper range of ω_f is defined according to the theoretical analysis of the decoupling network, as will be demonstrated in Section 4.4.3. Since each vector is rotating with a different $n\cdot\omega$ speed, it is necessary that the filtering should be performed in the corresponding dq^n-frame for each vector (where the under consideration vector is described by an oscillation-free vector), in order to achieve an equivalent filtering on the voltage components. Thus, the estimated vectors $\mathbf{v}_{\alpha\beta}^{n*}$ must first be transformed to $\mathbf{v}_{dq^n}^{n*}$ using (4.22) and then to be filtered to $\bar{\mathbf{v}}_{dq^n}^{n*}$, as shown by (4.23).

$$\mathbf{v}_{dq^n}^{n*} = \left[T_{dq^n}\right]\mathbf{v}_{\alpha\beta}^{n*} \tag{4.22}$$

$$\bar{\mathbf{v}}_{dq^n}^{n*} = \left[F(s)\right]\mathbf{v}_{dq^n}^{n*} \tag{4.23}$$

where:
$$\left[F(s)\right] = \frac{\omega_f}{s+\omega_f}\begin{bmatrix}1 & 0\\ 0 & 1\end{bmatrix} \tag{4.24}$$

Then, the filtered estimation vector expressed in the dq^n-frame $\bar{\mathbf{v}}_{dq^n}^{n*}$ can be expressed back to the stationary $\alpha\beta$-frame by using,

$$\bar{\mathbf{v}}_{\alpha\beta}^{n*} = \left[T_{dq^{-n}}\right]\bar{\mathbf{v}}_{dq^n}^{n*} \tag{4.25}$$

Therefore, by combining (4.22)-(4.25), the filtered estimation vector expressed in the $\alpha\beta$-frame $\bar{\mathbf{v}}_{\alpha\beta}^{n*}$ can be defined as shown in (4.26) in terms of the estimation vector $\mathbf{v}_{\alpha\beta}^{n*}$. It is to be noted that the $\bar{\mathbf{v}}_{\alpha\beta}^{n*}$ of (4.26) is the vector that is used in the cross-feedback network of the proposed DNαβ.

$$\bar{\mathbf{v}}_{\alpha\beta}^{n*} = \left[T_{dq^{-n}}\right]\left[F(s)\right]\mathbf{v}_{dq^n}^{n*} = \left[T_{dq^{-n}}\right]\left[F(s)\right]\left[T_{dq^n}\right]\mathbf{v}_{\alpha\beta}^{n*} \tag{4.26}$$

The filtered estimation vector of (4.26) can be replaced in (4.21) to enable the estimation of each voltage vector and thus, the final equation of the DNαβ is obtained by,

$$\mathbf{v}_{dq^n}^{n*} = \left[T_{dq^n}\right]\mathbf{v}_{\alpha\beta}^{n*} = \left[T_{dq^n}\right]\left(\mathbf{v}_{\alpha\beta} - \sum_{m\neq n}\left[T_{dq^{-m}}\right]\left[F(s)\right]\left[T_{dq^m}\right]\mathbf{v}_{\alpha\beta}^{m*}\right) \tag{4.27}$$

Now, (4.27) can be re-written in terms of the voltage vector expressed only in the αβ-frame as shown in (4.28).

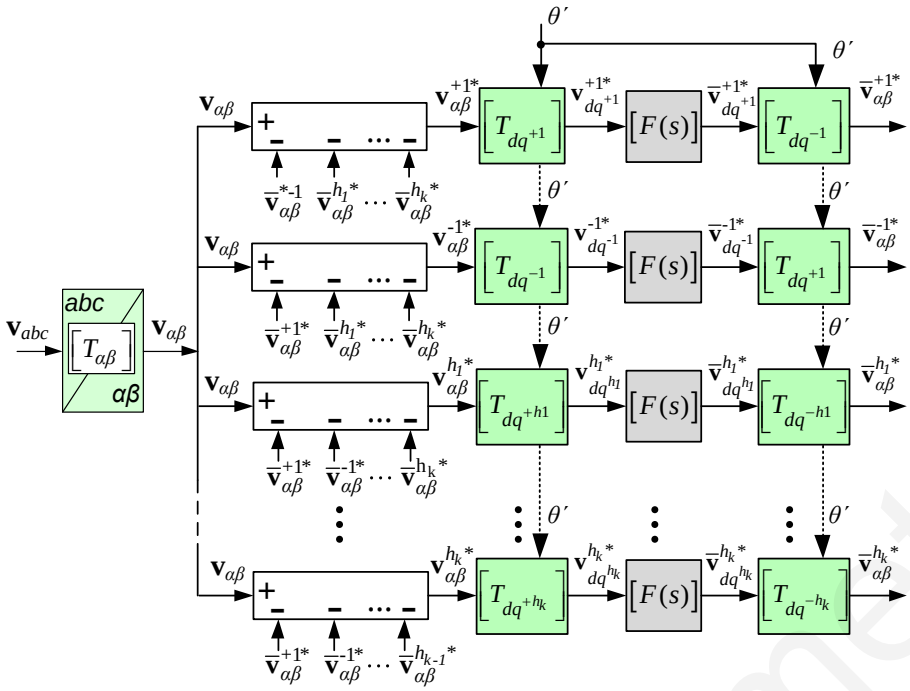

Fig. 4.8. The block diagram the DNαβ decoupling network.

$$\mathbf{v}_{\alpha\beta}^{n*} = \left(\mathbf{v}_{\alpha\beta} - \sum_{m \neq n} \left[T_{dq^{-m}} \right] \left[F(s) \right] \left[T_{dq^{m}} \right] \mathbf{v}_{\alpha\beta}^{m*} \right) \tag{4.28}$$

Hence, the proposed decoupling network (DNαβ) is based on the multiple use of (4.28) for n=+1, -1, h_1,..., h_k for estimating each oscillation-free voltage components $\bar{\mathbf{v}}_{dq^n}^{n*}$, as shown in the block diagram of the DNab in Fig. 4.8. The block diagram of Fig. 4.8 illustrates that the proposed DNαβ is a cross-feedback network with recursive filtering characteristics that allow fast, dynamic and accurate decoupling of the grid voltage components.

4.4.2 - The structure of the proposed DNαβ-PLL

The proposed DNαβ enables a proper decoupling between the existing voltage vector components and therefore can dynamically and accurately estimate the value of each voltage vector component ($\mathbf{v}_{\alpha\beta}^{n*}$ and $\mathbf{v}_{dq^n}^{n*}$). The proposed PLL can be implemented by using the estimation of the pure positive sequence voltage component ($\mathbf{v}_{\alpha\beta}^{+1*}$), estimated by the DNαβ, as an input to the conventional αβ-PLL algorithm [60]-[62]. The structure of the proposed DNαβ-PLL is presented in Fig. 4.9. The αβ-PLL algorithm [60]-[62] seems to be the preferable solution to be combined with the DNαβ since it presents a better dynamic response than the dq-PLL [59], as it has been proved in [28], [29] and in Section 2.3. Thus, the proposed DNαβ-PLL can achieve a fast and accurate detection of the phase angle of the

positive sequence of the voltage. The PLL algorithm is based on controlling the $\Delta\theta$ of (4.29) to track zero through a PI controller and so the detected angle (θ') tracks the phase angle of the positive sequence of the grid voltage (θ^{+1}).

$$\Delta\theta = \theta^{+1} - \theta' \approx \sin(\theta^{+1} - \theta') = \sin(\theta^{+1})\cos(\theta') - \sin(\theta')\cos(\theta^{+1}) \tag{4.29}$$

The tuning of the proposed DNαβ-PLL can be obtained according to the linearized small signal model analysis of a PLL, as presented in Appendix B. Further, the tuning procedure followed here is the same with the tuning procedure for MSHDC-PLL presented in Section 4.3.2. Therefore, the closed-loop transfer function of the DNαβ-PLL is given by (4.30), which is identical to the transfer function (4.15) of the MSHDC-PLL.

$$H_\theta(s) = \frac{\theta'}{\theta^{+1}} = \frac{2\zeta\omega_n s + \omega_n^2}{s^2 + 2\zeta\omega_n s + \omega_n^2} = \frac{k_p s + \frac{1}{T_i}}{s^2 + k_p s + \frac{1}{T_i}} \tag{4.30}$$

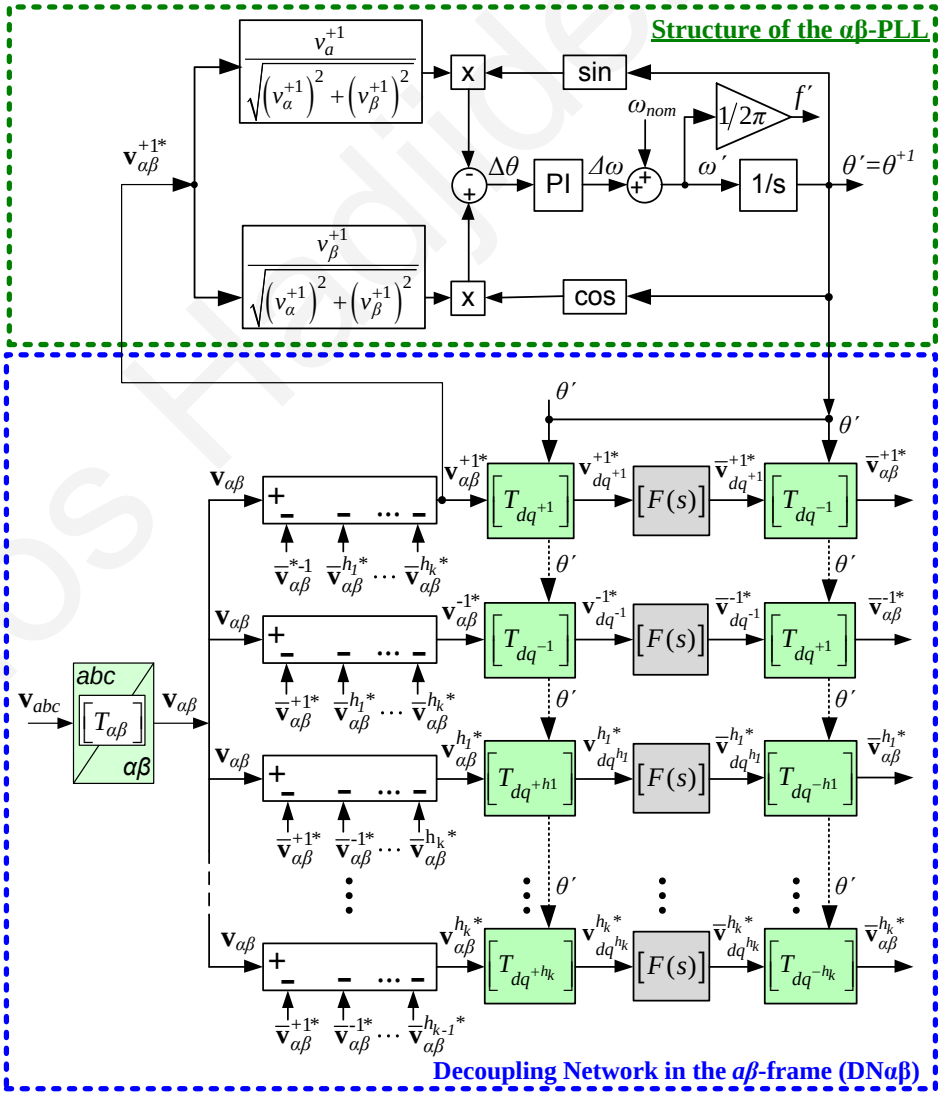

Fig. 4.9. The structure of the proposed DNαβ-PLL.

The second order transfer function of (4.15) depicts the low-pass filtering capabilities of the PLL and thus, the stability of PLLs is ensured and also the attenuation of the detection error caused by possible noise and high order harmonics in the input signal is proved. Furthermore, the parameters of the PI controller of PLLs may be chosen by,

$$k_p = \frac{9.2}{T_s} \qquad \text{and} \qquad T_i = 0.047\zeta^2 T_s^2 \tag{4.31}$$

where T_s is the settling time of the synchronization and the damping factor ζ is set to $1/\sqrt{2}$ in order to have an optimally damped system (with a 5% overshoot). For the purposes of this work, the DNαβ-PLL has been tuned in the same way with the MSHDC-PLL. Therefore, the PI parameters have been set in a way to fulfill the German Grid Codes [11], [12], similar to the tuning procedure of the dαβ-PLL (Section 2.4). Thus, the proposed DNαβ-PLL can operate without violating the frequency operation window (from 47.5 Hz to 51.5 Hz) for any possible grid fault. Therefore, the settling time T_s is set to 0.745 s and as a consequence the tuning parameters of the MSHDC-PLL have been set to k_p=12.35 and T_i=0.013. It is to be noted that the proposed DNαβ-PLL can also be tuned to a faster or slower response depending on the purpose of the application.

Another critical aspect for the design of the proposed DNαβ-PLL is to define which harmonics (n) are to be cancelled-out by the proposed decoupling network under general grid conditions. It is obvious that the accuracy of the PLL depends on the number of sequences and harmonics (N) eliminated by the decoupling network. Since an infinite number of harmonics is impossible to be considered due to complexity issues, the decoupling network should focus on eliminating the negative sequence and the most significant low-order pairs of harmonics. The rest of the harmonics can be ignored, since their effect is minimized due to the low-pass filtering characteristics of the DNαβ-PLL, as already mentioned. An investigation has been performed for the accuracy of the proposed PLL for different number of harmonics (N) considered by the DNαβ. The accuracy of the PLL has been studied according to the

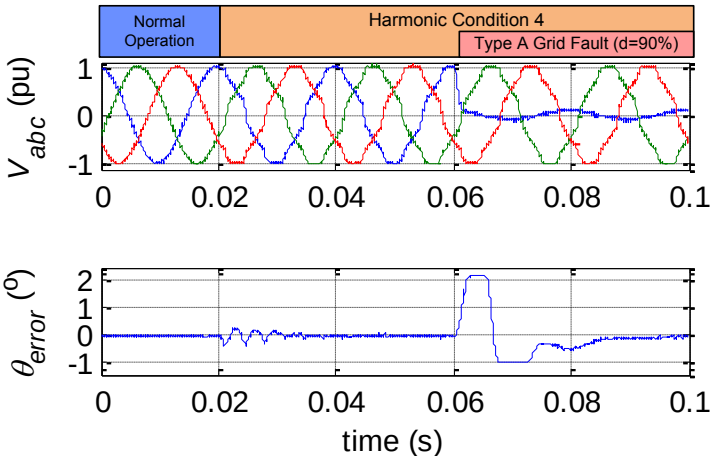

Fig. 4.10. Experimental results showing the estimated phase angle error of the DNαβ-PLL (implemented for N=10) under the worst case harmonic distortion (HC-4) and an unbalanced grid fault.

maximum harmonic distortion of the grid voltage as defined by the EN50160 standard [10]. This worst case set of harmonics is defined as harmonic conditions 4 (HC-4) and is analytically presented in TABLE 4.4. The investigation shows that when the DNαβ is designed with N=10 to eliminate the negative sequence and the pairs of harmonics up to order thirteen (n = ±1, ±5, ±7, ±11, ±13) the proposed PLL can achieve a very accurate response. The new DNαβ-PLL has been digitally developed in a TMS320F28335 digital signal processor (DSP). The experimental results of Fig. 4.10 present the response of the DNαβ-PLL (with N=10) under the worst-case harmonic distortion (HC-4) and under an unbalanced grid fault (Type B with 90% voltage sag (d)). The estimated phase angle error of the proposed PLL, presented in Fig. 4.10, is less than 0.05 degrees (θ_{error}<0.05^{o}) due to the effect of the harmonics that are not considered in the decoupling network and due to the discretization error imposed by the digital implementation of the PLL in the microcontroller. Thus, for an accurate PLL response and an adequate algorithm complexity, the DNαβ-PLL should be designed for N=10 to consider the harmonics up to order thirteen.

4.4.3 Theoretical analysis of the proposed DNαβ-PLL

An extensive theoretical analysis is required to define the transfer function, the expected response, and the optimal design parameters of the proposed DNαβ. The theoretical analysis shows that both MSHDC and DNαβ present an exact equivalent transfer function and therefore, the analysis presented here can directly be applied to both DNαβ and MSHDC. Furthermore, the analysis proves that the proposed decoupling network can achieve an outstanding response in terms of accuracy under harmonic distorted and unbalanced conditions and in terms of dynamic response. Further, the theoretical analysis of the decoupling network is useful for defining the design parameters of the proposed decoupling networks.

Equivalent performance of DNαβ-PLL and MSHDC

In this sub-section, the equivalent performance of the two decoupling network, the MSHDC and the DNαβ, will be proved. The estimated vector $\mathbf{v}_{dq^{+1}}^{+1*}$ is considered as the output of the MHDC and can be fed into any conventional PLL algorithm to accurately estimate the phase angle of the fundamental voltage as proposed by MSHDC-PLL in Section 4.3. The grid voltage vector expressed in the dq^{+1}-frame ($\mathbf{v}_{dq^{+1}}$) can be considered as the input voltage to the MSHDC. Similarly, the estimated vector $\mathbf{v}_{\alpha\beta}^{+1*}$ is considered as

the output of the DNαβ, which is similarly used to developed the corresponding DNαβ-PLL, while the input of the DNαβ is the grid voltage vector expressed in the *αβ*-frame ($\mathbf{v}_{\alpha\beta}$). The two estimated vectors are linked according to (4.22). Therefore, it is interesting to demonstrate the connection between the two decoupling networks.

The MSHDC is developed based on the multiple uses of (4.13). For completeness purposes (4.13) is re-produced below, in (4.32).

$$\mathbf{v}_{dq^n}^{n*} = \mathbf{v}_{dq^n} - \sum_{m\neq n}\left[T_{dq^{(n-m)}}\right]\bar{\mathbf{v}}_{dq^m}^{m*} \qquad \left|\cdot T_{dq^{-n}}\right. \tag{4.32}$$

Now, if both sides of (4.32) are multiplied by $\left[T_{dq^{-n}}\right]$, according to (4.22), (4.32) can be re-written as shown in (4.33).

$$\begin{aligned} & T_{dq^{-n}}\mathbf{v}_{dq^n}^{n*} = T_{dq^{-n}}\left(\mathbf{v}_{dq^n} - \sum_{m\neq n}\left[T_{dq^{(n-m)}}\right]\bar{\mathbf{v}}_{dq^m}^{m*}\right) \\ \Leftrightarrow \quad & \mathbf{v}_{\alpha\beta}^{n*} = T_{dq^{-n}}\mathbf{v}_{dq^n} - T_{dq^{-n}}\cdot\sum_{m\neq n}\left[T_{dq^{(n-m)}}\right]\bar{\mathbf{v}}_{dq^m}^{m*} \end{aligned} \tag{4.33}$$

Then, the filtered estimation vector $\bar{\mathbf{v}}_{dq^m}^{m*}$ of (4.33) can be replaced by the non-filtered estimation vector $\mathbf{v}_{dq^m}^{m*}$ according to (4.23), and thus (4.33) can be re-written as,

$$\mathbf{v}_{\alpha\beta}^{n*} = \mathbf{v}_{\alpha\beta} - T_{dq^{-n}}\cdot\sum_{m\neq n}\left[T_{dq^{(n-m)}}\right]\left[F(s)\right]\mathbf{v}_{dq^m}^{m*} \tag{4.34}$$

Similarly, the estimation vector expressed in the corresponding dq^m-frame can be expressed in the *αβ*-frame according to (4.22). Furthermore, the transformation matrix can be included within the summation of (4.34) and therefore, (4.34) is re-expressed as given by (4.35).

$$\mathbf{v}_{\alpha\beta}^{n*} = \mathbf{v}_{\alpha\beta} - \sum_{m\neq n}\left(T_{dq^{-n}}\left[T_{dq^{(n-m)}}\right]\right)\left[F(s)\right]\left[T_{dq^m}\right]\mathbf{v}_{\alpha\beta}^{m*} \tag{4.35}$$

Finally, by merging the two transformation matrices of (4.35), (4.35) can be written as,

$$\mathbf{v}_{\alpha\beta}^{n*} = \mathbf{v}_{\alpha\beta} - \sum_{m\neq n}\left[T_{dq^{-m}}\right]\left[F(s)\right]\left[T_{dq^m}\right]\mathbf{v}_{\alpha\beta}^{m*} \tag{4.36}$$

It is worth to mention that the analysis presented in (4.32)-(4.36) proves that the MSHDC and the DNαβ are exactly equivalent decoupling cells. The analysis begins with (4.32), which is the cornerstone equation of MSHDC, and by applying some space vector

transformations is equivalently re-expressed in the form of (4.36), which is the cornerstone equation of DNαβ. Hence, it is proven that both MSHDC and DNαβ can achieve an exact equivalent performance. The resulting synchronization method, the MSHDC-PLL and the DNαβ-PLL, can achieve an exact equivalent performance in terms of dynamic response and accuracy under harmonic distorted and unbalanced conditions. The only difference between the two PLLs is the complexity/required processing time of each algorithm, as will be discussed in detail in Section 4.4.4. Since, the two decoupling networks are exact equivalents; the theoretical analysis of the next sub-section is considering only the DNαβ, although the results of this theoretical analysis are valid for both decoupling networks.

Theoretical response of the DNαβ

An accurate operation of the DNαβ-PLL under the worst case harmonic distortion requires that the DNαβ has to be developed for N=10 to eliminate the negative sequence and the pairs of harmonics up to order thirteen (n = ±1, ±5, ±7, ±11, ±13), according to Section 4.4.2. Therefore, the theoretical analysis of the proposed decoupling network (DNαβ), developed for N=10, is demonstrated in this Section, where the transfer function of the DNαβ $\left(\mathbf{v}_{\alpha\beta}^{+1*}/\mathbf{v}_{\alpha\beta}\right)$ is extracted. The DNαβ is developed by the multiple use of (4.28) for n = ±1, ±5, ±7, ±11, ±13. Thus, (4.28) for n=+1 can be written as shown in (4.37).

$$\mathbf{v}_{\alpha\beta}^{+1*} = \mathbf{v}_{\alpha\beta} - \sum_{m\neq 1}\left[T_{dq^{-m}}\right]\left[F(s)\right]\left[T_{dq^{m}}\right]\mathbf{v}_{\alpha\beta}^{m*}$$

$$\Leftrightarrow \mathbf{v}_{\alpha\beta}^{+1*} = \mathbf{v}_{\alpha\beta} - \left(\begin{array}{l} \left[T_{dq^{+1}}\right]\left[F(s)\right]\left[T_{dq^{-1}}\right]\mathbf{v}_{\alpha\beta}^{-1*} + \\ \left[T_{dq^{-5}}\right]\left[F(s)\right]\left[T_{dq^{+5}}\right]\mathbf{v}_{\alpha\beta}^{+5*} + \left[T_{dq^{+5}}\right]\left[F(s)\right]\left[T_{dq^{-5}}\right]\mathbf{v}_{\alpha\beta}^{-5*} + \\ \left[T_{dq^{-7}}\right]\left[F(s)\right]\left[T_{dq^{+7}}\right]\mathbf{v}_{\alpha\beta}^{+7*} + \left[T_{dq^{+7}}\right]\left[F(s)\right]\left[T_{dq^{-7}}\right]\mathbf{v}_{\alpha\beta}^{-7} + \\ \left[T_{dq^{-11}}\right]\left[F(s)\right]\left[T_{dq^{+11}}\right]\mathbf{v}_{\alpha\beta}^{+11*} + \left[T_{dq^{+11}}\right]\left[F(s)\right]\left[T_{dq^{-11}}\right]\mathbf{v}_{\alpha\beta}^{-11*} + \\ \left[T_{dq^{-13}}\right]\left[F(s)\right]\left[T_{dq^{+13}}\right]\mathbf{v}_{\alpha\beta}^{+13*} + \left[T_{dq^{+13}}\right]\left[F(s)\right]\left[T_{dq^{-13}}\right]\mathbf{v}_{\alpha\beta}^{-13*} + \end{array}\right) \quad (4.37)$$

In order to extract the transfer function of the DNαβ $\left(\mathbf{v}_{\alpha\beta}^{+1*}/\mathbf{v}_{\alpha\beta}\right)$, (4.37) should be expressed only in terms of the vectors $\mathbf{v}_{\alpha\beta}^{+1*}$ and $\mathbf{v}_{\alpha\beta}$. Therefore, each vector $\mathbf{v}_{\alpha\beta}^{m*}$ of (4.37), where $m\neq$+1, should be replaced by the recursive use of (4.28). The recursive character of the DNαβ can also be observed through the block diagram of Fig. 4.8. Thus, (4.37) can be re-written as,

$$\mathbf{v}_{\alpha\beta}^{+1*} = \mathbf{v}_{\alpha\beta} -$$

$$\begin{pmatrix}
\left[T_{dq^{+1}}\right]\left[F(s)\right]\left[T_{dq^{-1}}\right]\left(\mathbf{v}_{\alpha\beta} - \left[T_{dq^{-1}}\right]\left[F(s)\right]\left[T_{dq^{+1}}\right]\mathbf{v}_{\alpha\beta}^{+1*} - \sum_{m\neq+1,-1}\bar{\mathbf{v}}_{\alpha\beta}^{m*}\right) + \\
\left[T_{dq^{-5}}\right]\left[F(s)\right]\left[T_{dq^{+5}}\right]\left(\mathbf{v}_{\alpha\beta} - \left[T_{dq^{-1}}\right]\left[F(s)\right]\left[T_{dq^{+1}}\right]\mathbf{v}_{\alpha\beta}^{+1*} - \sum_{m\neq+1,+5}\bar{\mathbf{v}}_{\alpha\beta}^{m*}\right) + \\
\left[T_{dq^{+5}}\right]\left[F(s)\right]\left[T_{dq^{-5}}\right]\left(\mathbf{v}_{\alpha\beta} - \left[T_{dq^{-1}}\right]\left[F(s)\right]\left[T_{dq^{+1}}\right]\mathbf{v}_{\alpha\beta}^{+1*} - \sum_{m\neq+1,-5}\bar{\mathbf{v}}_{\alpha\beta}^{m*}\right) + \\
\vdots \qquad\qquad \vdots \qquad\qquad \vdots \qquad\qquad \vdots \\
\left[T_{dq^{-13}}\right]\left[F(s)\right]\left[T_{dq^{+13}}\right]\left(\mathbf{v}_{\alpha\beta} - \left[T_{dq^{-1}}\right]\left[F(s)\right]\left[T_{dq^{+1}}\right]\mathbf{v}_{\alpha\beta}^{+1*} - \sum_{m\neq+1,+13}\bar{\mathbf{v}}_{\alpha\beta}^{m*}\right) + \\
\left[T_{dq^{+13}}\right]\left[F(s)\right]\left[T_{dq^{-13}}\right]\left(\mathbf{v}_{\alpha\beta} - \left[T_{dq^{-1}}\right]\left[F(s)\right]\left[T_{dq^{+1}}\right]\mathbf{v}_{\alpha\beta}^{+1*} - \sum_{m\neq+1,-13}\bar{\mathbf{v}}_{\alpha\beta}^{m*}\right)
\end{pmatrix} \tag{4.38}$$

According to the analysis above, the remaining vectors $\mathbf{v}_{\alpha\beta}^{m*}$ of (4.38) should also be expressed only in terms of the vectors $\mathbf{v}_{\alpha\beta}^{+1*}$ and $\mathbf{v}_{\alpha\beta}$ in order to extract the transfer function of the DNαβ. Such an analysis should continue recursively. However, due to the recursive character of the decoupling network, it is impossible to express (4.38) in terms only of vectors $\mathbf{v}_{\alpha\beta}^{+1*}$ and $\mathbf{v}_{\alpha\beta}$. Hence, in order to enable the extraction of the transfer function of the DNαβ, all the vectors that are filtered by [F(s)] for three or more times can be ignored in the further analysis, due to their slower dynamics. By observing (4.38), all the vectors that are filtered for three or more times are within the summation series. Thus, by ignoring these multiple filtered vectors, (4.38) can be simplified as,

$$\mathbf{v}_{\alpha\beta}^{+1*} = \mathbf{v}_{\alpha\beta} - \begin{pmatrix}
\left[T_{dq^{+1}}\right]\left[F(s)\right]\left[T_{dq^{-1}}\right]\left(\mathbf{v}_{\alpha\beta} - \left[T_{dq^{-1}}\right]\left[F(s)\right]\left[T_{dq^{+1}}\right]\mathbf{v}_{\alpha\beta}^{+1*}\right) + \\
\left[T_{dq^{-5}}\right]\left[F(s)\right]\left[T_{dq^{+5}}\right]\left(\mathbf{v}_{\alpha\beta} - \left[T_{dq^{-1}}\right]\left[F(s)\right]\left[T_{dq^{+1}}\right]\mathbf{v}_{\alpha\beta}^{+1*}\right) + \\
\left[T_{dq^{+5}}\right]\left[F(s)\right]\left[T_{dq^{-5}}\right]\left(\mathbf{v}_{\alpha\beta} - \left[T_{dq^{-1}}\right]\left[F(s)\right]\left[T_{dq^{+1}}\right]\mathbf{v}_{\alpha\beta}^{+1*}\right) + \\
\vdots \qquad\qquad \vdots \qquad\qquad \vdots \\
\left[T_{dq^{-13}}\right]\left[F(s)\right]\left[T_{dq^{+13}}\right]\left(\mathbf{v}_{\alpha\beta} - \left[T_{dq^{-1}}\right]\left[F(s)\right]\left[T_{dq^{+1}}\right]\mathbf{v}_{\alpha\beta}^{+1*}\right) + \\
\left[T_{dq^{+13}}\right]\left[F(s)\right]\left[T_{dq^{-13}}\right]\left(\mathbf{v}_{\alpha\beta} - \left[T_{dq^{-1}}\right]\left[F(s)\right]\left[T_{dq^{+1}}\right]\mathbf{v}_{\alpha\beta}^{+1*}\right) +
\end{pmatrix} \tag{4.39}$$

Now, (4.39) can easily be re-arrange in the following form.

$$\mathbf{v}_{\alpha\beta}^{+1*} = \mathbf{v}_{\alpha\beta} - \begin{pmatrix} \left[T_{dq^{+1}}\right]\left[F(s)\right]\left[T_{dq^{-1}}\right] + \\ \left[T_{dq^{-5}}\right]\left[F(s)\right]\left[T_{dq^{+5}}\right] + \dots \\ \dots + \left[T_{dq^{+13}}\right]\left[F(s)\right]\left[T_{dq^{-13}}\right] \end{pmatrix} \left(\mathbf{v}_{\alpha\beta} - \left[T_{dq^{-1}}\right]\left[F(s)\right]\left[T_{dq^{+1}}\right]\mathbf{v}_{\alpha\beta}^{+1*}\right) \tag{4.40}$$

The transfer function of $\left[T_{dq^{-h}}\right] \cdot [F(s)] \cdot \left[T_{dq^{+h}}\right]$, where h is the corresponding sequence (+1 or -1) or the corresponding harmonic order thirteen (±5, ±7, ±11, ±13), can be defined in the complex-frequency domain by using a lengthy mathematical analysis. This analysis is based on expressing the Park's Transformations in terms of the Euler formula [27], [37] as defined in (4.41).

$$\begin{aligned} &\left[T_{dq^{n-m}}\right] = \begin{bmatrix} \cos\left((n-m)\omega' t\right) & \sin\left((n-m)\omega' t\right) \\ -\sin\left((n-m)\omega' t\right) & \cos\left((n-m)\omega' t\right) \end{bmatrix} \\ \Leftrightarrow \quad &\left[T_{dq^{n-m}}\right] = \frac{1}{2}\begin{bmatrix} \left(e^{j(n-m)\omega' t} + e^{-j(n-m)\omega' t}\right) & -j\left(e^{j(n-m)\omega' t} - e^{-j(n-m)\omega' t}\right) \\ j\left(e^{j(n-m)\omega' t} - e^{-j(n-m)\omega' t}\right) & \left(e^{j(n-m)\omega' t} + e^{-j(n-m)\omega' t}\right) \end{bmatrix} \end{aligned} \tag{4.41}$$

Then, by utilizing (4.41) in combination with the Laplace property for frequency shifting ($e^{at} = F(s-a)$) and on the fact that v_b=-j·v_a (according to the geometry of the $\alpha\beta$-frame), the complex first-order transfer function of $TFT_h = \left[T_{dq^{-h}}\right] \cdot [F(s)] \cdot \left[T_{dq^{+h}}\right]$ can be extracted as,

$$TFT_h = \left[T_{dq^{-h}}\right]\left[F(s)\right]\left[T_{dq^{+h}}\right] = \frac{\omega_f}{s + (\omega_f - j \cdot h \cdot \omega')} \tag{4.42}$$

Substituting $TFT_h = \left[T_{dq^{-h}}\right] \cdot [F(s)] \cdot \left[T_{dq^{+h}}\right]$ of (4.42) into (4.40) yields,

$$\mathbf{v}_{\alpha\beta}^{+1*} = \mathbf{v}_{\alpha\beta} - \begin{pmatrix} TFT_{-1} + TFT_{+5} + TFT_{-5} + TFT_{+7} + TFT_{-7} + \\ TFT_{+11} + TFT_{-11} + TFT_{+13} + TFT_{-13} \end{pmatrix} \left(\mathbf{v}_{\alpha\beta} - TFT_{+1}\mathbf{v}_{\alpha\beta}^{+1*}\right) \tag{4.43}$$

Finally, by re-solving (4.43), the transfer function of the proposed DNαβ is derived as,

$$\frac{\mathbf{v}_{\alpha\beta}^{+1*}}{\mathbf{v}_{\alpha\beta}} = \frac{1 - \left(TFT_{-1} + TFT_{+5} + TFT_{-5} + TFT_{+7} + TFT_{-7} + \dots + TFT_{+13} + TFT_{-13}\right)}{1 + TFT_{+1}\left(TFT_{-1} + TFT_{+5} + TFT_{-5} + TFT_{+7} + TFT_{-7} + \dots + TFT_{+13} + TFT_{-13}\right)} \tag{4.44}$$

If the corresponding TFT_h terms of (4.42) are substituted into (4.44), then the nineteenth-order complex transfer function of the proposed DNαβ can be extracted.

According to (4.44), the grid voltage vector $\mathbf{v}_{\alpha\beta}$ (which includes the positive and negative sequence and several harmonics) consists of the input voltage vector of the DNαβ and the $\mathbf{v}_{\alpha\beta}^{+1*}$ is the output estimation vector of the positive sequence component of the DNαβ expressed in the stationary reference frame.

Therefore, in order to investigate the response of the proposed DNαβ-PLL and to determine the proper value of the design parameter ω_f, the Bode diagram of the proposed DNαβ is presented in Fig. 4.11. The results of Fig. 4.11 verify that the proposed DNαβ according to (4.44) does not affect the dynamic estimation of the desired fundamental positive sequence voltage component, since at 50 Hz the decoupling network presents unity amplitude gain and zero phase shifting. Furthermore, the DNαβ can effectively eliminate the negative sequence and the low-order harmonic components considered in the development of the decoupling network. According to Fig. 4.11 , the DNαβ can eliminate the voltage vector components rotating with -50, ±250, ±350, ±550 and ±650 Hz, which are the frequency of the negative sequence and the most significant low-order harmonics. It is to be mentioned that the high-order harmonics are not affected by the decoupling network. This is not a problem for the synchronization, since the high-order harmonics are eliminated due to the second-order transfer function (4.30) of the PLL algorithm. As a conclusion, the accurate and dynamic response of the synchronization can be guaranteed since the DNαβ decouples the effect of the negative sequence and low-order harmonics without affecting the dynamics of the estimation.

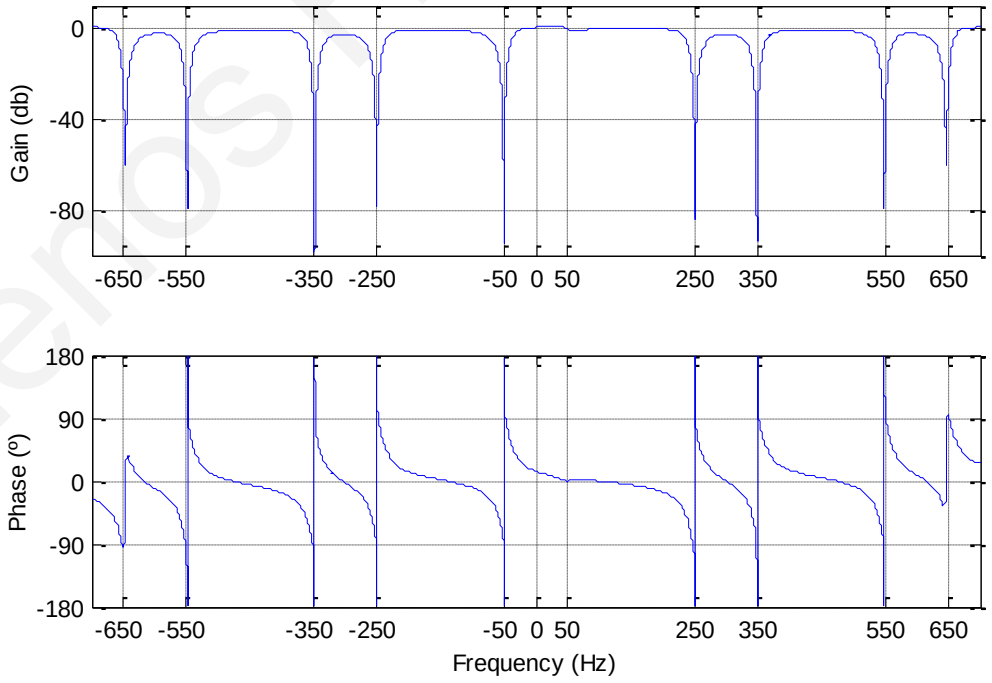

Fig. 4.11. Bode diagram of the proposed decoupling network (DNαβ).

The design parameter ω_f can affect the quality factor of the filter, the oscillation damping, and the time performance of the proposed DNαβ. Therefore, an investigation according to the transfer function (4.44) of the decoupling network shows that a reasonable trade-off can be achieved by setting the parameter ω_f within the range $0.3 \cdot \omega_n \leq \omega_f \leq 0.7 \cdot \omega_n$, where ω_n is the nominal angular frequency of the grid at $2\pi \cdot 50$ rad/s. For $\omega_f \leq 0.3 \cdot \omega_n$ the response of the DNαβ is over-damped but the dynamic response of the estimation is negatively affected. On the other hand, for $\omega_f \geq 0.7 \cdot \omega_n$ the response of the DNαβ is very fast but undesired oscillations are presented on the estimation vectors.

The step response regarding the estimation of the input voltage according to DNαβ of the proposed PLL is presented in Fig. 4.12. In Fig. 4.12(a) the estimation of the positive sequence of the voltage when a unity positive sequence step input is applied in the decoupling network. It is obvious that the proposed DNαβ enable a very fast decomposition of the grid voltage components and thus, it enables a very accurate estimation within 10 ms. Another important aspect, is the ability of the DNαβ to eliminate the coupling effect of negative sequence and the harmonic components of the voltage. Fig. 4.12(b) presents the effect of a negative sequence step input with an amplitude of 0.5 pu on the estimation of the positive sequence of the voltage. It is proven, that the proposed DNαβ can immediately decouple the effect of the negative sequence occurrence on the estimation of the positive sequence component. Similarly, Fig. 4.12(c) presents the effect of a fifth-order harmonic step input with an amplitude of 0.3 pu on the estimation of the positive sequence of the voltage. Again, it is proven that the decoupling network can immediately decouple the effect of the harmonic distortion on the estimation of the positive sequence component.

An in depth theoretical analysis of the proposed decoupling networks is presented within this Section. The analysis shows that both the MSHDC-PLL and the DNαβ-PLL can achieve an exact equivalent performance. The only difference between the two synchronization methods is the required processing time as will be demonstrated in Section 4.4.4. Further, the theoretical analysis of the proposed PLL proves that the proposed synchronization can achieve a very accurate response under unbalanced and harmonic distorted conditions without affecting the dynamic response of the synchronization. This outstanding synchronization performance will also be verified through simulation and experimental results in Section 4.4.6.

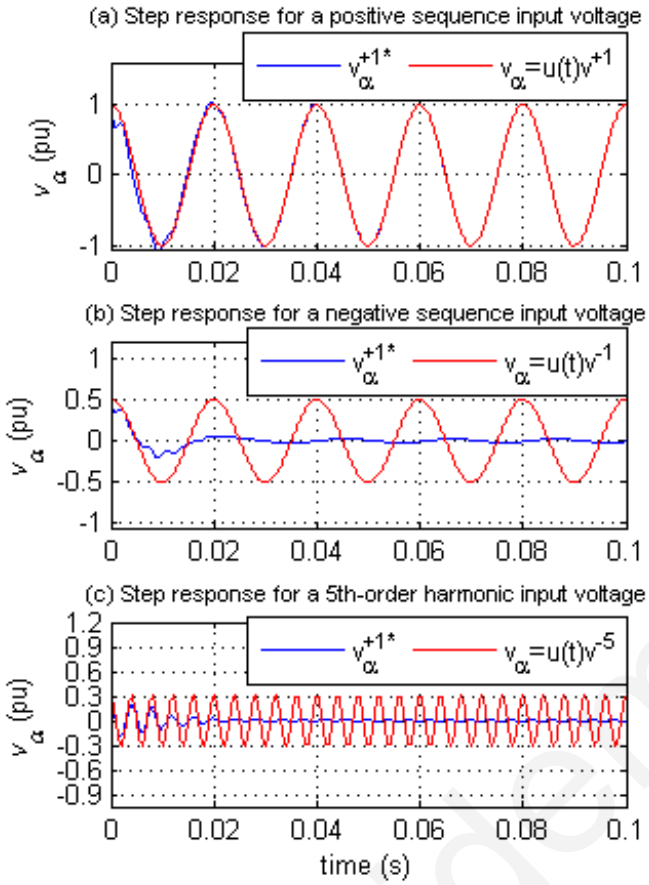

Fig. 4.12. The time response of the proposed decoupling network (DNαβ) for (a) a step response for a positive sequence step input voltage, (b) a step response for a negative sequence step input voltage, and (c) a step response for a 5th-order harmonic step input voltage.

4.4.4 Complexity assessment

An assessment of the complexity of the PLL algorithm is essential for real-time practical applications. For the purpose of this experimental benchmarking investigation, a 32-bit TMS320F28335 DSP of Texas Instruments has been used, since it is a conventional and widely used microcontroller for controlling such power electronics applications. The complexity of several PLL algorithms, including the proposed in this Section DNαβ-PLL and the proposed in Section 4.3 MSHDC-PLL has been assessed based on the required processing time of each algorithm to be executed in the TMS320F28335 DSP.

The recursive filter of the proposed DNαβ enables a dynamic decoupling of the voltage without affecting the time response of the DNαβ-PLL. The detailed analysis of the recursive filtering character of the proposed decoupling network is already performed in Section 4.4.3. The DNαβ and MSHDC [28] present the same transfer function and therefore an equivalent response as proven in Section 4.4.3. However, the decoupling in DNαβ is always performed in the *αβ*-frame in contrast to the MSHDC, where the decoupling is developed in each dq_n-frame. The complete decoupling of a voltage vector

with N components (positive, negative sequence and N-2 harmonics) using the proposed DNαβ requires the process of N $\left(\mathbf{v}_{\alpha\beta} - \sum_{m\neq n} \bar{\mathbf{v}}_{\alpha\beta}^{m*}\right)$ multi-subtractions, $2N$ $[T_{dq^n}]$ transformation matrices, and N $[F(s)]$ low pass filters in each control loop. In comparison, in case of the MSHDC, the algorithm requires the execution of N $\left(\mathbf{v}_{dq^n} - \sum_{m\neq n} \bar{\mathbf{v}}_{dq^n}^{m*}\right)$ multi-subtractions, N^2 $[T_{dq^n}]$ matrix transformations, and N $[F(s)]$ matrix low-pass filters in each control loop.

The complexity comparison between the two decoupling networks is analytically presented in TABLE 4.1. For the proper accuracy of both PLLs, harmonics up to order thirteen (N=10) should be eliminated by the decoupling network as already explained in Section 4.4.2, since the effect of higher order harmonics is minimized by the low pass filtering characteristic of the decoupling network. Therefore, the proposed DNαβ requires only twenty transformation matrices ($2N$) in comparison with one hundred transformations (N^2) required by the MSHDC. Since, the process of each transformation matrix requires 2.4 μs in the TMS320F28335 DSP, the proposed PLL requires considerable less execution time than the MSHDC-PLL. More details about the complexity analysis of the two synchronization methods are presented in TABLE 4.1, where the complexity of the two decoupling networks (for N=10) is analyzed in terms of the required operations (32-bit multiplications, 32-bit additions and 32-bit subtractions) in each control step. It is to be noted that the analysis in terms of the required operations has been verified according to the assembly code of the DSP. Hence, the proposed DNαβ achieves an equivalent with the MSHDC fast and accurate decoupling of the voltage as proven in Section 4.4.3 and additionally, requires significantly less processing time, which is important in such real-time applications.

TABLE 4.1: COMPLEXITY COMPARISON BETWEEN THE DNAB AND THE MSHDC

Decoupling Network	**Complexity analysis in each control loop**			
	$\left(\mathbf{v}_{dq^n} - \sum_{m\neq n} \bar{\mathbf{v}}_{dq_n}^{*m}\right)$ *or* $\left(\mathbf{v}_{\alpha\beta} - \sum_{m\neq n} \bar{\mathbf{v}}_{\alpha\beta}^{*m}\right)$	$[T_{dq}{}^n]$	$[F(s)]$	Total
MSHDC (N=10)	N	N^2	N	640 Multiplications 120 Additions 280 Subtractions
DNαβ (N=10)	N	$2N$	N	160 Multiplications 40 Additions 200 Subtractions

Notes: - **Each** $\left(\mathbf{v}_{\alpha\beta} - \sum_{m\neq n} \bar{\mathbf{v}}_{\alpha\beta}^{m*}\right)$ **or** $\left(\mathbf{v}_{dq^n} - \sum_{m\neq n} \bar{\mathbf{v}}_{dq^n}^{m*}\right)$ → requires $2\cdot(N\text{-}1)$ Subtractions
- **Each** $[T_{dq}]$ → requires 6 Multiplications + 1 Addition + 1 Subtractions
- **Each** $[F(s)]$ → requires 4 Multiplications + 2 Additions

TABLE 4.2: RESPONSE AND PROCESSING TIME OF SEVEN DIFFERENT PLLS

PLL algorithm	Required Processing Time (μs)	Dynamic Response under grid faults	Accurate Response under			
			Balanced voltage	Unbalanced voltage	Harmonic distortion	$f \neq$ nominal
dq-PLL	7.9	Fast	+	-	-	+
ddsrf-PLL	15.2	Fast	+	+	-	+
dαβ-PLL	17.3	Fast	+	+	-	+
MAF-PLL	8.5	Slow	+	+	+	-
mod. MRF-PLL	16.0	Slow	+	+	+	-
MSHDC-PLL	258.2	Fast	+	+	+	+
DNαβ-PLL	**63.7**	**Fast**	**+**	**+**	**+**	**+**

TABLE 4.2 presents the required processing time in μs, the accuracy and the dynamic response of seven different PLL algorithms, the dq-PLL [59] (Section 2.2.1), the ddsrf-PLL [79] (Section 2.2.2), the proposed dαβ-PLL [28], [29] (Section 2.4), the MAF-PLL [73], [75] (Section 4.2), the modified MRF-PLL [73], [74] (Section 4.2), the proposed MSHDC-PLL (for N=10) [34] (Section 4.3), and the proposed DNαβ-PLL (for N=10) [35] (Section 4.4). It has to be noted that the dq-PLL is inaccurate for unbalanced or harmonic distorted voltages and that the ddsrf-PLL and the proposed dαβ-PLL are fast but inaccurate under harmonic distorted voltages. The MAF-PLL and the modified MRF-PLL are accurate under unbalanced and harmonic distorted voltages, but they present slow dynamics and possible inaccuracies under non-nominal frequencies. The MSHDC-PLL and the new DNαβ-PLL present fast and accurate response under unbalanced, harmonic distorted voltages and under any grid frequency. Both PLLs have been designed for N=10, to consider the ±1, ±5, ±7, ±11, ±13 orders of sequences/harmonics. It is obvious that the proposed DNαβ-PLL presents the most outstanding performance, since it presents a fast and accurate response under any abnormal grid conditions and furthermore, requires 63.7 μs instead of 258.2 μs required by the corresponding MSHDC-PLL due to the significantly less required transformations.

Fig. 4.13 presents the required processing time of the main units of the GSC controller, sensor sampling, the synchronization method, the PQ controller and the current controller, when they are executed in a conventional microcontroller, such as the TMS320F28335 DSP of Texas Instruments. The results in Fig. 4.13(a) show that the new DNαβ-PLL requires a processing time of 63.7 μs (as already mentioned in TABLE 4.2). The required processing time for the sensor sampling (3.5 μs), current controller (43.3 μs) and PQ controller (10.3 μs) are also presented in Fig. 4.13(a), where the GSC controller operates in real-time with a sampling rate of 7.5 kHz. The adequate complexity of the DNαβ-PLL (implemented with N=10) in comparison to the MSHDC-PLL, which presents

the same dynamic and accurate performance, is very important since it enables the real-time execution of the algorithm using proper sampling rates. Experimental results of Fig. 4.13(b) show that the MSHDC-PLL requires an execution time of 258.2 μs in each control loop in the TMS320F28335 DSP. Thus, for a real-time execution of the GSC control method, the sampling rate has to be decreased from 7.5 kHz to 3 kHz as shown in Fig. 4.13, when the MSHDC-PLL is used. Such a reduction on the sampling rate of the GSC controller is undesired since low sampling rates can affect the accuracy and the performance of the GSC. Therefore, the proposed DNαβ-PLL can be straightforwardly applied to a real-time controller of RES and can enable a fast and accurate synchronization under abnormal grid conditions in order to enhance the power quality of the RES.

(a)

(b)

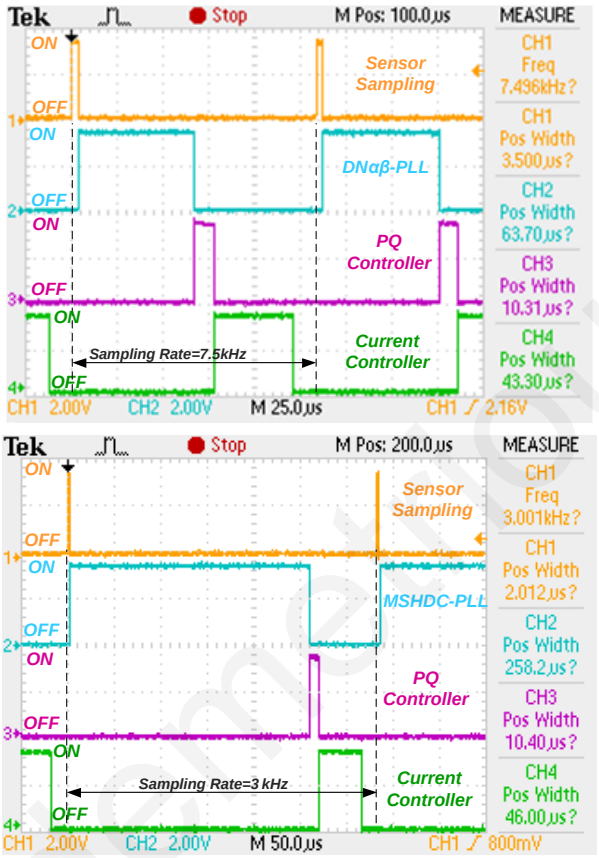

Fig. 4.13. Required processing time for each unit of the GSC controller in TMS320F28335 DSP: (a) when the proposed DNαβ-PLL is used (t_{div}=25μs/div), and (b) when the MSHDC-PLL is used (t_{div}=50μs/div). To be noted that when the signal is ON the corresponding algorithm is executed.

4.4.5 An enhanced GSC control for an interconnected RES

Advanced GSC control strategies have to be designed to meet the modern grid requirements for interconnecting RES. According to Fig. 4.14, the GSC control is based on the PLL algorithm to ensure the grid synchronization, the PQ controller to generate the reference currents under normal and FRT operation and the current controller to enable a proper and high quality current injection. It is seen from Fig. 4.14, that the response of the synchronization is directly affecting the performance of the PQ and current controller and consequently the operation of the entire RES. Therefore, the design of an enhanced GSC is essential to investigate how the accurate operation of the new DNαβ-PLL under harmonic distorted voltage and grid disturbances can beneficially affect the response of the GSC of a RES in terms of power quality.

The PQ controller is responsible for generating the reference currents under normal and faulty grid conditions. Under normal grid conditions, the generation of the reference currents is a conventional procedure [27] and should be able to control the voltage of the DC-link ($V_{DC\text{-}link}$) and the active (P) and reactive (Q) power exchange. In case of balanced or unbalanced low voltage grid faults, the PQ controller is also responsible for the FRT operation of the RES [31], [33], [92]-[96]. This means that the generation of the reference currents should ensure a proper voltage and frequency support without any violation on the GSC converter ratings. The generation of the reference currents from the FRT method requires the definition of two important ratios. The first ratio k_{VF} is defined by (4.45) and determines the ratio between the voltage and the frequency support.

$$k_{VF} = \frac{Q^*}{P^*} \tag{4.45}$$

During the fault, the generated active power is considered as constant from the RES and therefore, through the ratio k_{VF} the reference active (P^*) and reactive (Q^*) power for the GSC control can be calculated. The ratio k_{VF} is usually defined within the grid codes for interconnecting RES and is dependent on the voltage sag of the faulty grid at the PCC as shown in Fig. 1.3 of Chapter 1. The second ratio k_{PN}, which is defined in (4.46) regulates the current injection between the full positive (k_{PN}=1) and the full negative sequence (k_{PN}=0) and is dependent on the target of the FRT strategy.

$$k_{PN} = \frac{\left|\mathbf{i}^*\right| - \left|\mathbf{i}^{-1*}\right|}{\left|\mathbf{i}^{+1*}\right| - \left|\mathbf{i}^{-1*}\right|} \tag{4.46}$$

Usually a full positive sequence current injection is chosen to support the faulty grid, but in some cases, the injection of negative sequence currents can be useful in the FRT strategy in terms of compensating the unbalanced grid conditions.

The PQ controller presented in this Section is enhanced with FRT operation in order to enable the proper support of the grid by the RES under grid faults. The FRT control algorithm presented in this Section is based on the instantaneous power theory presented in Appendix A.6 and on FPNSC algorithm of [92]-[94]. The presented FRT controller is a modification of the FPNSC algorithm in a way to enable the compatibility of this algorithm with the synchronization and controller of the GSC of a RES. Therefore, the FPNSC algorithm is reformulated in this Section and the required voltage vector for generating the reference currents are taken directly from the advanced synchronization method. According to the FRT algorithm that has been applied in this Section, the

reference current vector $\mathbf{i}^*$ can be defined separately for the active $\mathbf{i}_p^*$ and reactive $\mathbf{i}_q^*$ components of the reference currents, as given by (4.47). $\mathbf{i}_p^*$ and $\mathbf{i}_q^*$ represent the component of currents that can cause a corresponding active and reactive power injection under the specific voltage conditions. The reference currents ($\mathbf{i}^*$) are calculated based on the active and reactive power references and on the positive and negative voltage vector as defined in (4.47)-(4.48).

$$\mathbf{i}_p^* = \mathbf{i}_p^{*+1} + \mathbf{i}_\mathbf{p}^{*-1} \text{ and } \quad \mathbf{i}_q^* = \mathbf{i}_q^{*+1} + \mathbf{i}_q^{*-1} \tag{4.47}$$

where:

$$\begin{aligned} \mathbf{i}_\mathbf{p}^{+1*} &= k_{PN} \frac{P^*}{\left|\mathbf{v}_{dq^{+1}}^{+1}\right|^2} \mathbf{v}_{dq^{+1}}^{+1}, \qquad \mathbf{i}_p^{-1*} = (1-k_{PN}) \frac{P^*}{\left|\mathbf{v}_{dq^{-1}}^{-1}\right|^2} \mathbf{v}_{dq^{-1}}^{-1} \\ \mathbf{i}_q^{+1*} &= k_{PN} \frac{Q^*}{\left|\mathbf{v}_{dq^{+1}}^{+1}\right|^2} \mathbf{v}_{dq^{+1}\perp}^{+1}, \qquad \mathbf{i}_q^{-1*} = (1-k_{PN}) \frac{Q^*}{\left|\mathbf{v}_{dq^{-1}}^{-1}\right|^2} \mathbf{v}_{dq^{-1}\perp}^{-1} \end{aligned} \tag{4.48}$$

where $\mathbf{i}_p{}^{+1*}$ and $\mathbf{i}_q{}^{+1*}$ define the positive sequence active and reactive power components of the reference current vector respectively and the $\mathbf{i}_p{}^{-1*}$ and $\mathbf{i}_q{}^{-1*}$ the corresponding negative sequence components. The positive sequence voltage vector $\mathbf{v}_{dq^{+1}}^{*+1}$ and its orthogonal version (90^o leading) $\mathbf{v}_{dq^{+1}\perp}^{*+1}$ expressed in the dq^{+1}-frame (rotating with $+\omega$) can be formulated through estimated signals by the proposed DNαβ-PLL as given by (4.49), while the corresponding negative sequence vectors $\mathbf{v}_{dq^{-1}}^{-1*}$ and $\mathbf{v}_{dq^{-1}\perp}^{-1*}$ expressed in the dq^{-1}-frame (rotating with $-\omega$) can be calculated by (4.50).

$$\mathbf{v}_{dq^{+1}}^{+1*} = \begin{bmatrix} \bar{v}_{d^{+1}}^{+1*} \\ \bar{v}_{q^{+1}}^{+1*} \end{bmatrix} \text{ and } \mathbf{v}_{dq^{+1}\perp}^{+1*} = \begin{bmatrix} \bar{v}_{q^{+1}}^{+1*} \\ -\bar{v}_{d^{+1}}^{+1*} \end{bmatrix} \tag{4.49}$$

$$\mathbf{v}_{dq^{-1}}^{-1*} = \begin{bmatrix} \bar{v}_{d^{-1}}^{-1*} \\ \bar{v}_{q^{-1}}^{-1*} \end{bmatrix} \text{ and } \mathbf{v}_{dq^{-1}\perp}^{-1*} = \begin{bmatrix} \bar{v}_{q^{-1}}^{-1*} \\ -\bar{v}_{d^{-1}}^{-1*} \end{bmatrix} \tag{4.50}$$

The FRT algorithm is also in charge of maintaining the injected currents within the converter ratings, especially under low-voltage grid faults. In case of violation on the GSC ratings, the reference currents should be modified in a way to maintain the k_{VF} and k_{PN} ratios and to ensure a proper limitation of the injected currents.

Since the reference currents have been calculated, the current controller has to ensure the proper injection of high quality currents in the power grid. This is not a trivial

aspect when positive and/or negative sequence currents should be injected under unbalanced and harmonic distorted voltage. Advanced current control techniques are required to enable the high quality current control under abnormal grid conditions, as suggested in [40], [84]-[87]. For the purposes of this Section, the current controller presented in Chapter 6 and in [40] has been implemented, which requires a simplified structure and can achieve a high quality positive or negative current injection under faulty and distorted grid voltage. The selected current controller is a simplified solution with low control efforts. It consists of a conventional current controller enhanced with harmonic and unbalanced compensation modules and can achieve a high quality positive or negative sequence current injection under normal conditions and under unbalanced grid faults.

The structure of the enhanced GSC controller that has been developed is presented in Fig. 4.14. The implemented GSC controller achieves proper and high quality operation even under grid faults and harmonic distorted voltage. This GSC will be used in the investigation of the effect of the accurate synchronization on the RES performance in the next Section.

4.4.6 Simulation and experimental results

The new synchronization method (DNαβ-PLL) has been proposed and analyzed in Section 4.4 and an advanced GSC controller has been implemented in Section 4.4.5. Simulation and experimental results will be presented in this Section regarding the response of the new DNαβ-PLL under a harmonic distorted voltage and under several grid disturbances. Furthermore, the beneficial effect of accurate synchronization, through the new DNαβ-PLL, on the performance of the grid-connected RES is also investigated. This innovative investigation proves the significant impact of the accurate synchronization on the response of the RES and demonstrates the considerable enhancement of the power quality of the RES due to the proposed DNαβ-PLL.

Experimental setup

An experimental setup has been implemented to verify the work presented in this Section. The experimental setup is considering the response of the new synchronization method and the effect on the performance of GSC control of a RES. A Delta Elektronika Power Supply (SM 600-10) operates as a DC source to emulate the energy produced from the RES and a Danfoss FC302 2.2 kW inverter acts as the GSC. A California Instruments 4500LX programmable AC source in combination with a parallel connected 3 kW load is

used to emulate the power grid. For the experimental investigation presented in this Section, the PLL algorithm and the enhanced control of the GSC have been designed using a dSPACE DS1103 DSP board in combination with the dSPACE Control Desk and MATLAB/Simulink Real Time Workshop. The sampling rate and the switching frequency of the designed GSC controller have been set to 7.5 kHz. The schematic of the experimental setup is presented in Fig. 4.14 and the corresponding photo in Fig. 4.15. The exact same setup has been implemented as a simulation model in MATLAB/Simulink to ensure the proper operation of synchronization and GSC control before applying them on the real system.

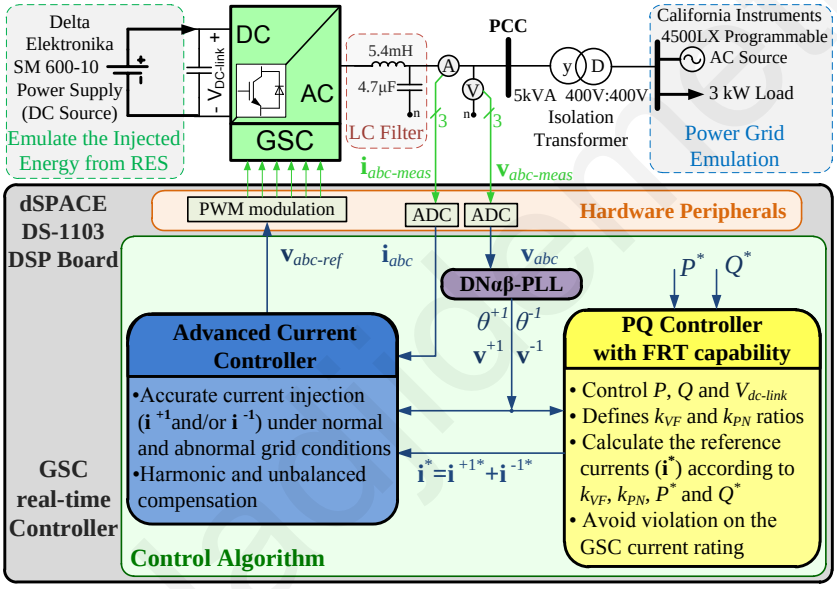

Fig. 4.14. Schematic of the experimental setup and the diagram of the advanced controller for the grid-connected RES.

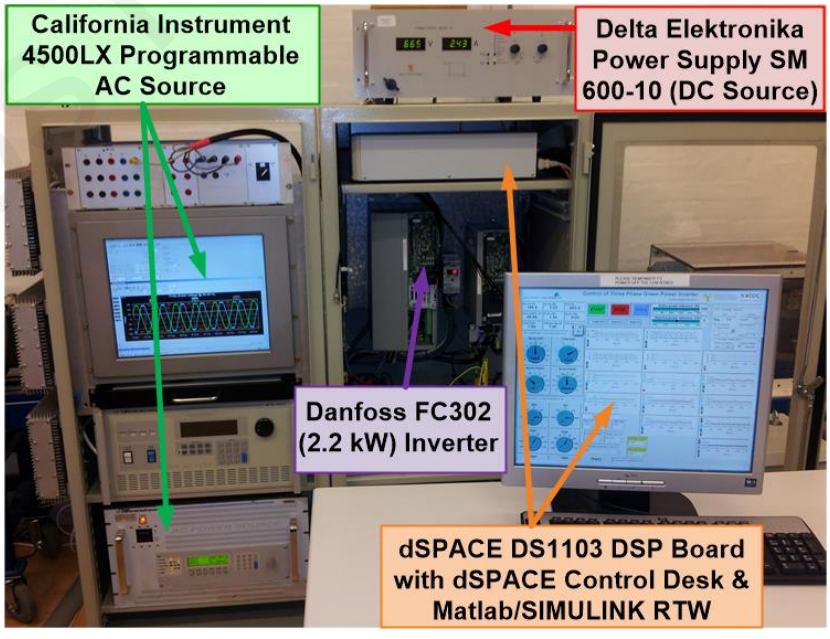

Fig. 4.15. Photo of the experimental setup.

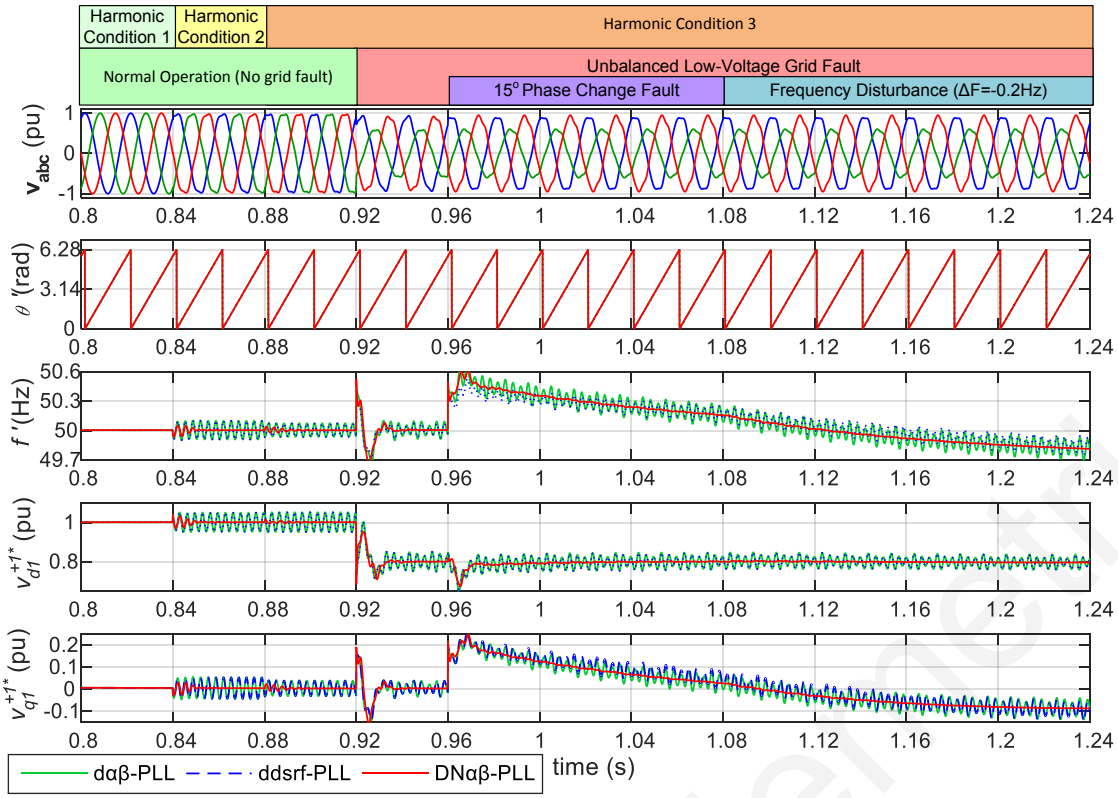

Fig. 4.16. Simulation results comparing the PLL response of the new DNαβ-PLL, the ddsrf-PLL, and the dαβ-PLL under several abnormal grid conditions.

Response of the new synchronization method

The DNαβ-PLL aims to achieve a robust and accurate operation under a harmonic distorted grid without affecting the dynamic synchronization response in case of grid faults. Such an accurate and dynamic response by the proposed PLL has been theoretically proven in Section 4.4.3. This outstanding performance needs to also be verified through simulation and experimental results.

A simulation case study presented in Fig. 4.16 provides a comparison between the response of the proposed DNαβ-PLL, the dαβ-PLL [28], [29] (Section 2.4), and the ddsrf-PLL [79] (Section 2.2.2) (all PLLs are set according to the same tuning conditions as explained in Section 2.4). It is obvious that the proposed PLL achieves an accurate response under highly distorted grid voltage, where the Harmonic Conditions (HC) 1-3 are explained in TABLE 4.4. The ddsrf-PLL and dαβ-PLL present similar dynamic performance, but their accuracy is affected by the harmonic distortion. Moreover, Fig. 4.16 demonstrates that the accurate response of the new PLL is achieved without affecting the dynamic performance of the synchronization since the DNαβ-PLL presents a similar dynamic response with the dαβ-PLL and ddsrf-PLL under several faults. The proper and robust performance of the new PLL is verified under an unbalanced low-voltage grid fault

(Type D with a voltage sag (*d*) of 37% [91]), a 15^{o} phase shifting fault and a frequency step of -0.2 Hz. The appropriate performance of the proposed PLL is also experimentally validated under harmonic distorted voltage and unbalanced grid fault as shown in Fig. 4.17. The experimental results prove the accurate and dynamic response of the new PLL under harmonic distorted voltage and grid disturbances.

Synchronization methods based on MAF are simplified regarding the complexity (TABLE 4.2) and can achieve accurate performance under unbalanced and harmonic distorted voltages. A MAF-PLL [73], [75] (Section 4.2) inherits the structure of the conventional dq-PLL [59] and uses a MAF to clear out the oscillations caused by harmonics and unbalance conditions. A modified MRF-PLL [[73], [74] (Section 4.2) inherits the structure of the multi reference frame ddsrf-PLL [79] and replaces each low pass filter with a corresponding MAF to improve its filtering capabilities against harmonics and unbalanced conditions. The accuracy of these PLLs can be slightly affected when the operating frequency deviates from the nominal value due to the discrete implementation of the MAF. Even if these inaccuracies are overcome by using a variable sampling rate [77] (which is not an indicative solution in many control applications) the main disadvantage of these PLLs is the slow dynamic performance.

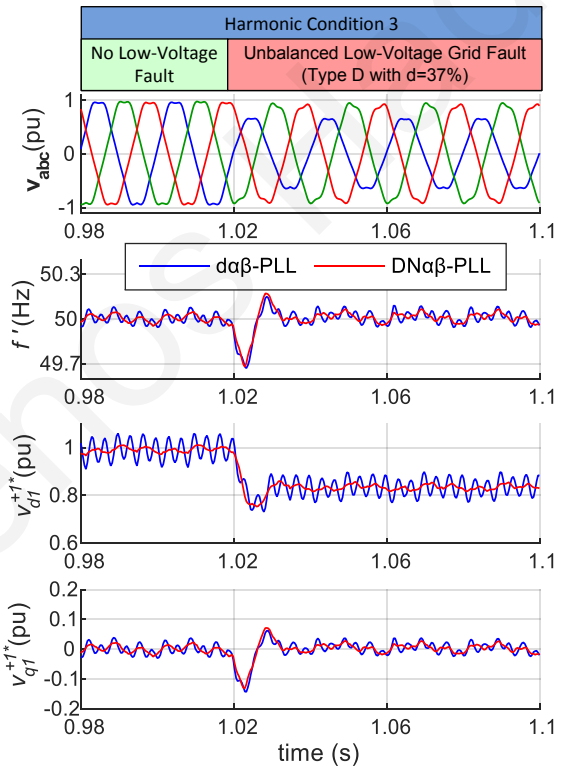

Fig. 4.17. Experimental results presenting the accurate response of the new DNαβ-PLL under harmonic distorted and unbalanced grid voltage.

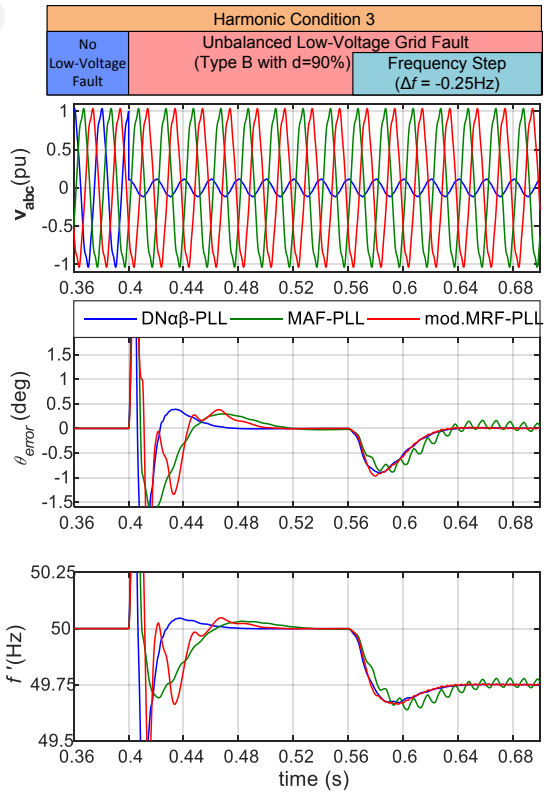

Fig. 4.18. The FRT performance of a grid-connected RES, when the new DNαβ-PLL is used for the synchronization, under unbalanced grid fault and

TABLE 4.3: SUMMARY OF THE RESULTS OF FIG. 4.18

Grid Conditions	MAF-PLL	mod. MRF-PLL	DNαβ-PLL
Harm. Distort. & f=50 Hz	√	√	√
Harm. Distort. & **a Voltage Sag occurs**	**slow**	**slow**	**fast**
• Settling Time (θ_{error}<0.1°)	99.7 ms	89 ms	57 ms
• Peak-Peak Phase error at 50 Hz	0 °	0 °	0 °
• Peak-Peak Freq. error at 50 Hz	0 Hz	0Hz	0Hz
Harm. Dist./Unbalanced & **Freq. Step**			Fast & accurate
• Settling Time (f_{error}<0.01 Hz)	130 ms	74 ms	70 ms
• Peak-Peak Phase error at 49.75 Hz	0.19 °	0.05 °	0 °
• Peak-Peak Freq. error at 49.75 Hz	0.041 Hz	0.012 Hz	0 Hz

Therefore, a performance comparison between the proposed PLL, the MAF-PLL and the modified MRF-PLL is presented in Fig. 4.18 and TABLE 4.3 . For the purpose of this comparative analysis the three PLLs are tuned according to [73]. The simulation results show that these PLLs are accurate under nominal operating frequency, harmonic distorted and unbalanced voltage. The frequency deviation from the nominal value in combination with the harmonic and unbalanced grid conditions can cause inaccuracies on the estimated signals of MAF-PLL as shown in Fig. 4.18 and TABLE 4.3. The enhanced filtering capability of the modified MRF-PLL, especially for the oscillations caused by the negative sequence, significantly minimizes the inaccuracies under a non-nominal frequency operation. On the other hand, the accuracy of the proposed DNαβ-PLL is not affected by the harmonic distortion, the unbalanced conditions, and the frequency deviation. In addition, the new PLL presents a significantly faster dynamic performance compared to the PLLs based on MAF as demonstrated in Fig. 4.18 and TABLE 4.3, especially under low-voltage grid faults. The fast dynamic operation of the new PLL is particularly important for the proper FRT operation of RES under grid faults. Therefore, the increased complexity of the proposed PLL (TABLE 4.2) is paid back by a very accurate and fast synchronization performance.

RES performance when using the proposed PLL

The results, presented in Fig. 4.16 and Fig. 4.17, show that the proposed PLL achieves an accurate synchronization and the oscillation-free estimation of the synchronization signals (θ' *and* $\mathbf{v}_{dq^{+1}}^{+1*}$). As shown in (4.47)-(4.48), the synchronization signals are used from the PQ controller to generate the reference currents. Additionally, the operation of the current controller [40] (Chapter 6) is based on an accurate estimation of the synchronization signals so it is expected that the accurate synchronization is directly affecting the GSC control and as a consequence the performance of the RES. An experimental investigation is presented here to prove how the accurate synchronization through the proposed PLL can enhance the power quality of the RES.

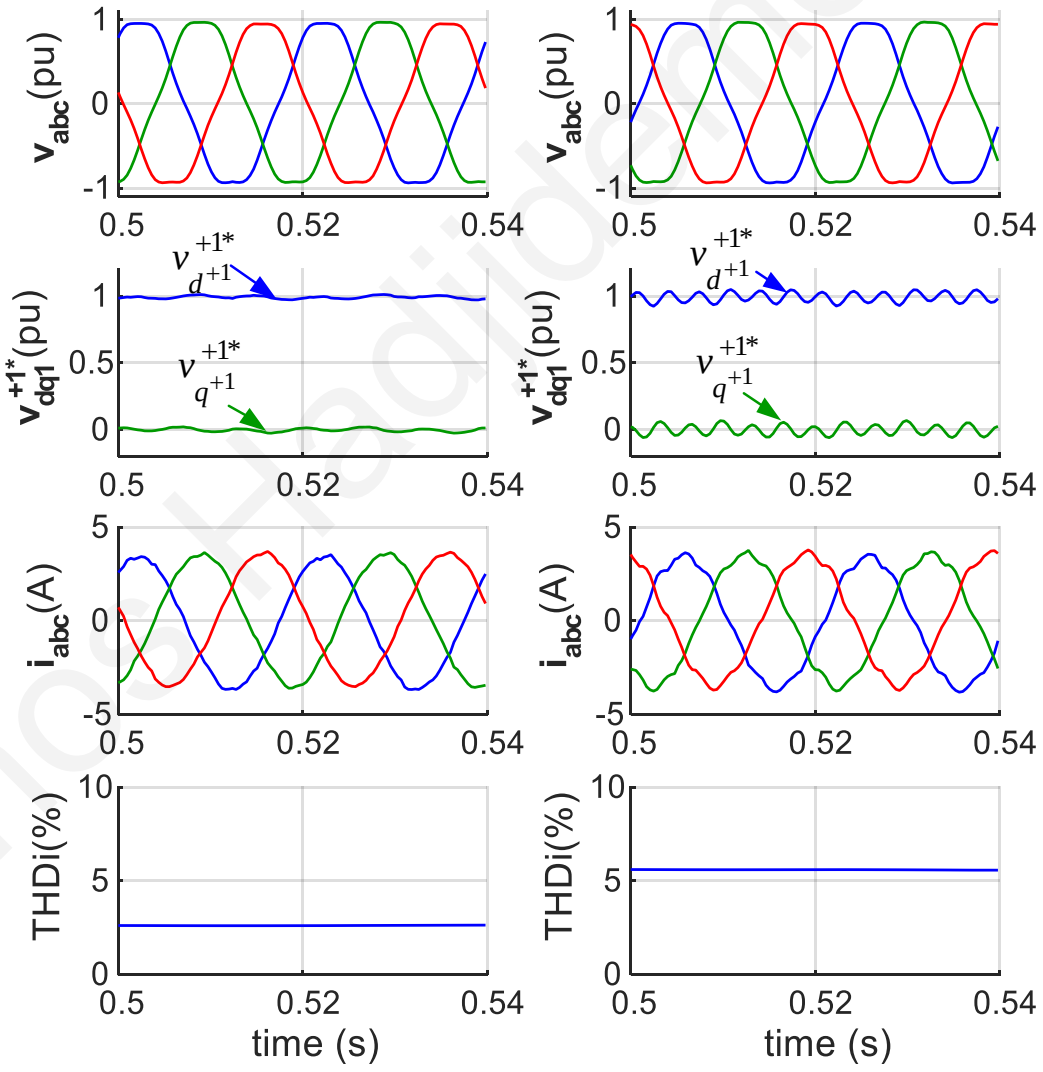

(α) RES response (with DNαβ-PLL) (b) RES response (with dαβ-PLL)

Fig. 4.19. Experimental results for the performance of the RES under harmonic distorted voltage, when using (a) the proposed DNαβ-PLL and (b) the dαβ-PLL for the synchronization of the GSC.

TABLE 4.4: THE IMPACT OF THE ACCURATE SYNCHRONIZATION THROUGH THE PROPOSED SYNCHRONIZATION ON THE POWER QUALITY OF RES

Grid Operating Conditions			Synchronization Method	
			dαβ-PLL	DNαβ-PLL
Low Voltage Fault	Voltage Harmonic Distortion	Freq (Hz)	THD(%) of the injected currents	
No Fault	HC-1	50	2.45	2.45
No Fault	HC-2	50	5.60	2.60
ULVF-1	HC-2	50	6.50	4.00
ULVF-1	HC-2	49.5	6.65	4.20
No Fault	HC-3	50	5.10	2.90
ULVF-1	HC-3	50	6.05	4.40
ULVF-1	HC-3	49.5	6.30	4.55

Index:

- ULVF-1: Type D Unbalanced Low Voltage Fault with d=37%
- HC-1: Harmonic Cond. 1 (High-frequency harmonics (HFH)=0.1%)
- HC-2: Harmonic Cond. 2 (THD_V=5% with $|V_5|$=4.9%, HFH=0.1%)
- HC-3: Harmonic Cond. 3 (THD_V=4.57% with $|V_5|$=4%,$|V_7|$=2%, HFH=0.1%)
- HC-4: Harmonic Cond. 4 ($|V_5|$=6%, $|V_7|$=5%, $|V_{11}|$=3.5%, $|V_{13}|$=3%, $|V_{17}|$=2%, $|V_{19}|$=1.5%, $|V_{23}|$=1.5%, $|V_{25}|$=1.5%, $|V_{19}|$=1.5%, HFH=0.1%)

The steady state performance of the grid-connected RES based on experimental results is presented in Fig. 4.19 under a highly harmonic distorted grid voltage (with harmonic condition 2 (HC-2) as explained in TABLE 4.4). Fig. 4.19(a) demonstrates the RES performance when the proposed DNαβ-PLL is used for the synchronization. It is shown that the new PLL estimates accurately the synchronization signals and therefore the reference currents are generated without any oscillations due to the harmonic distortion. Therefore, the RES achieves to inject high quality currents with a total harmonic distortion (THD_i) of 2.6%. On the other hand, Fig. 4.19 (b) presents the RES operation when the RES uses the dαβ-PLL for the synchronization. The inaccuracies of the dαβ-PLL, caused by the harmonic distortion, raise oscillations on the synchronization signals and therefore, the generated reference currents and the operation of the current controller are affected. Consequently, the RES with a non-robust synchronization against harmonics presents a low quality current injection with a THD_i of 5.6% (outside of the grid code limits) under harmonic distorted grid voltage. This experimental case study proves that the accurate synchronization is a key aspect for the power quality of the RES.

A further experimental investigation to prove the beneficial effect of the accurate synchronization on the power quality of the RES is summarized in TABLE 4.4. TABLE 4.4 compares the power quality of the RES when using a robust and a non-robust synchronization method under several harmonic conditions and several grid faults. It can be seen that the accurate operation of the proposed PLL enhances the RES performance

and enables a high quality current injection under any grid conditions. The experimental results of TABLE 4.4 prove the significant contribution of the proposed DNαβ-PLL in the power quality of grid-connected RES.

The dynamic response of the GSC is a critical aspect, especially under low-voltage grid faults, where the RES should immediately support the faulty grid. The fast response of the RES, when a fault occurs, is directly affected from the dynamic performance of the synchronization. The proposed PLL achieves an accurate response under harmonic distorted voltage without compensating its dynamic response, as proven in Fig. 4.16-Fig. 4.18. Thus, it is important to prove that the proposed DNαβ-PLL can enable the proper dynamic FRT performance of the RES when a fault occurs in order to meet the grid regulations. The experimental case study presented in Fig. 4.20 shows the RES performance when operating under harmonic distorted voltage (harmonic condition 2 as shown in Table IV) and an unbalanced low-voltage grid fault occurs. The RES is operating in the 80% of the GSC ratings before the occurrence of the low-voltage fault. When the fault occurs, the proposed DNαβ-PLL ensures the accurate and fast estimation of the synchronization signals as shown in Fig. 4.20. The proper synchronization enables the fast and adequate FRT operation of the PQ control algorithm to ensure the full positive current injection (k_{PN}=1), the support of the grid with k_{VF}=0, and the limitation of the current injection within the converter limits.

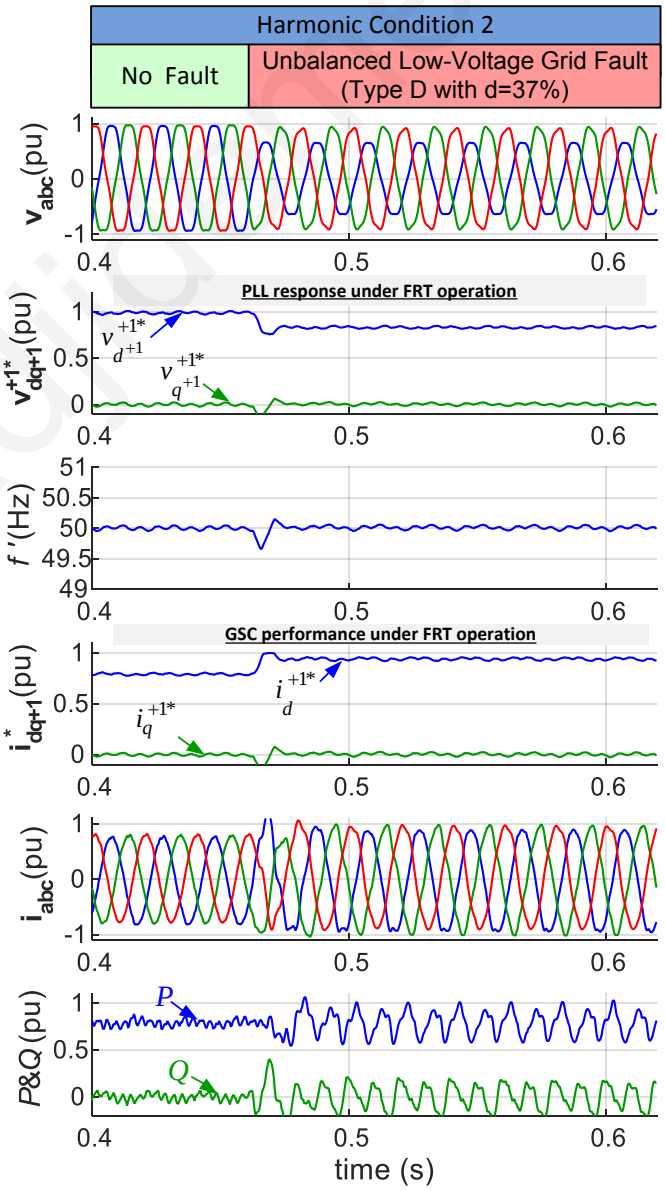

Fig. 4.20. The FRT performance of a grid-connected RES, when the new DNαβ-PLL is used for the synchronization, under unbalanced grid fault and harmonic distorted voltages.

4.5 Conclusions

This Section proposed two novel synchronization methods, the MSHDC-PLL and the DNαβ-PLL. Both synchronization methods achieve an accurate, dynamic and robust performance under harmonic distorted voltage and under several grid disturbances. Although the two new synchronization methods present an exact equivalent response as proven by the theoretical analysis, the proposed DNαβ-PLL is a preferable solution, since the real time execution of the algorithm requires significantly less processing time compared to the MSHDC-PLL. In general, the proposed DNαβ-PLL is an ideal solution for the synchronization of the GSC of RES due to its accuracy against harmonic distortion, the dynamic response under grid faults and the computational efficiency of the algorithm that allows the real-time execution of synchronization in conventional microcontrollers. The only limitation of the DNαβ-PLL is the fact that is vulnerable against inter-harmonics. The inter-harmonics are generated as a result of adding more and more power electronic converters to the power system. The interaction between these converters may result to harmonics that are non-integer multiples of the grid frequency. These inter-harmonics can be minimized by the low-pass filtering characteristics of the PI controller, but cannot be completely eliminated by the proposed synchronization. A synopsis of the comparison between the proposed synchronization methods, within this Chapter, and some advanced techniques from the literature is presented in Fig. 4.21, where it is obvious that the proposed DNαβ-PLL is a state-of-the-art synchronization method. Further, the robust and accurate response of the new PLL enhances the RES performance by improving the power quality of the injected currents and by enabling the proper FRT operation under grid disturbances.

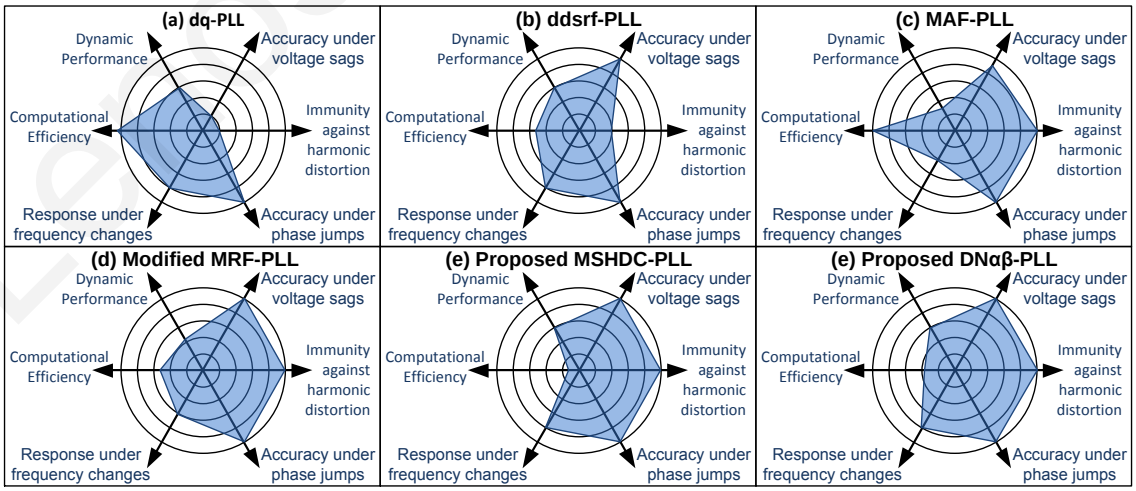

Fig. 4.21. Synopsis of the performance benchmarking between the six synchronization methods examined in this Section: (a) the conventional dq-PLL, (b) the ddsrf-PLL and (c) the MAF-PLL, (d) the modified MRF-PLL, (e) the proposed MSHDC-PLL and (f) the proposed DNαβ-PLL.

CHAPTER 5
A SYNCHRONIZATION SCHEME FOR SINGLE-PHASE INVERTERS UNDER HARMONIC DISTORTION AND GRID DISTURBANCES

5.1 Introduction

Single-phase inverters are used for converting direct current (DC) into alternating current (AC). Single-phase inverters are widely used as the Grid Side Converter (GSC) of rooftop PV systems that convert the produced power by PV from the DC-bus and properly inject this power into the grid, with which the injected current has to be synchronized as shown in Fig. 5.1. In addition, the integration of PV energy into the power grid has to follow the international standards [5]-[10] and the modern grid codes [11]-[27], which require an injection of high quality power in the normal operation mode. Furthermore, as the capacity of rooftop PV is significantly increased, the Fault Ride Through (FRT) capability by the single-phase GSC is becoming necessary, even for PVs connected to the low-voltage distribution network, as it is observed in recent studies in Japan [22] and the Italian technical rules issued in 2012 [20]. In light of the the above issues, this chapter proposes two new Phase Locked Loop (PLL) based synchronization methods for single-phase GSCs that can enhance the grid interconnection of rooftop PV systems. The first method presented in Section 5.3, named MHDC-PLL, is based on a novel Multi-Harmonic Decoupling Cell for dynamically eliminating the effect of the harmonic distortion. Thus, a fast and accurate synchronization method can be achieved with beneficial impact on the operation of the single-phase PV system. The only disadvantages of the MHDC-PLL are the increased complexity and the inaccurate response under non-nominal frequency conditions. Therefore, the frequency adaptive MHDC-PLL is proposed in Section 5.4, which overcomes these two issues. The frequency adaptive MHDC-PLL is based on a frequency adaptive Quadrature Signal Generator (QSG) for an accurate response under any frequency and on a novel decoupling network with decreased complexity which can dynamically eliminate the harmonic inaccuracies. The new frequency adaptive MHDC-PLL can achieve a fast and accurate synchronization under any grid conditions and

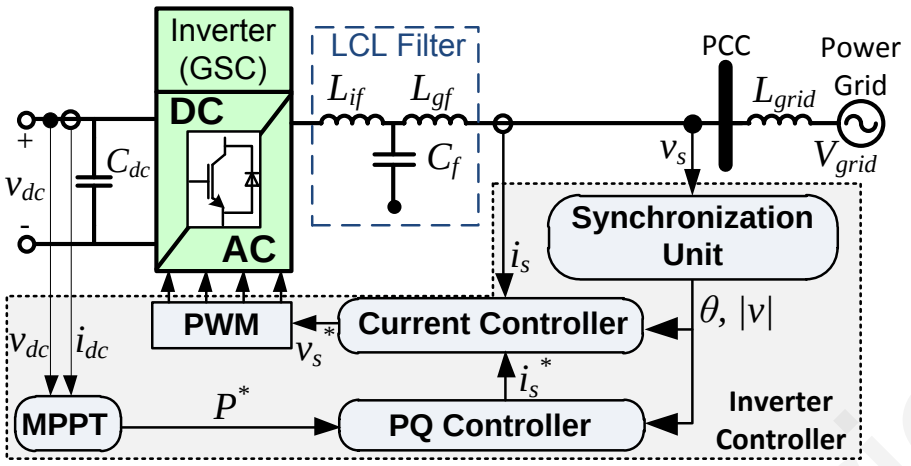

Fig. 5.1. The structure of a single-phase inverter among with its controller when operating as the GSC for the interconnection of a PV system.

therefore is an ideal synchronization solution for single-phase PV systems. The use of the proposed frequency adaptive MHDC-PLL can enable the dynamic performance of the GSC which is required for an appropriate FRT response, while the robustness of the synchronization against harmonics can beneficially affect the power quality of the PV systems.

5.2 Literature review

A typical single-stage single-phase inverter that is used as a GSC for the interconnection of rooftop PVs (with rated power below 5 kW) is shown in Fig. 5.1. For this system, the control of the GSC is based on the PQ controller which generates the reference currents, and the current controller which holds the responsibility for an appropriate current injection as described in [27], [48]-[53]. The PQ controller can be implemented in the stationary or synchronous reference frames as a closed-loop or an open-loop controller. Thus, a Proportional-Resonant (PR) controller in the stationary reference frame or a Proportional-Integral (PI) controller in the synchronous reference frame can be adopted in the design of the current controller. Since the injected current has to be synchronized with the grid voltage, the response of both controllers will be affected by the performance of the synchronization method. Among a large number of reported synchronization techniques, Phase-Locked Loop (PLL) algorithms have become the most widely used solutions for such power electronic applications. Hence, PLL based synchronization methods in single-phase PV systems require further improvement as depicted in [105]-[107] to ensure a proper operation of the PV systems.

With respect to the PLL synchronization, a common PLL based technique [107], [108] to estimate the phase angle (θ) of the grid voltage (v_s) in single-phase systems is enabled by generating a quadrature voltage vector in the stationary reference frame ($\mathbf{v}_{\alpha\beta}$). Then, this vector is transformed into the Synchronous Reference Frame (SRF) ($\mathbf{v}_{dq}$) (see Appendix A.4), where a simple PI controller regulates the voltage v_q to zero and therefore the phase angle is extracted as shown in dq-PLL [59] (see Section 2.2.1). In each PLL technique, a different Quadrature Signal Generator (QSG) is used to generate the vector $\mathbf{v}_{\alpha\beta}$. A straightforward $T/4$ delay transport technique is used in [27], [107], [108] as a QSG, where T is the fundamental period of the grid voltage. Inaccuracy in the case of low or high order harmonics is the main drawback of this PLL system due to the lack of filtering. The enhanced PLL (e-PLL) presented in [50], [70]-[72], [107], [108] is based on an adaptive filtering technique to generate the in quadrature voltage vector. The e-PLL presents slow dynamic response and its robustness against low- and high-order harmonics is limited. An interesting PLL based in Inverse Park Transform (IPT-PLL) is presented in [71], [107]-[110]. The IPT-PLL is based on a forward and a backwards Parks' transformation and two low pass filters, presents a fast response under disturbances and can filter out the high frequency harmonics. Another widely used synchronization method, named SOGI-PLL, is presented in [71], [107]-[110] and uses a Second Order Generalized Integrator (SOGI) as the QSG. The SOGI-PLL and the IPT-PLL present an equivalent response with regards to their dynamic response and their accuracy against high-order harmonics. However, these PLLs cannot accurately operate under low-order harmonic distortion. Finally, [111] presents a Hilbert based PLL technique. The harmonics effect is eliminated by this method, but unfortunately, it has practical implementation problems in the case of a real-time application with time-dependent signals.

More advanced PLL techniques have been presented in the recent literature, which enable the robustness of the synchronization against low-order harmonics. Techniques proposed in [112], [113] are based on adaptive or notch filters to minimize the effect of harmonics. Some other methods presented in [114], [115] apply repetitive and multi resonant controllers on the PLL and/or the current controller of the PV system in order to enable an accurate operation under harmonic distortion. Furthermore, an interesting technique is proposed in [116] and is based on Moving Average Filters (MAFs). Although, all the prior-mentioned methods within this paragraph can achieve an accurate response under harmonics, the dynamic response of the synchronization is undesirably affected. Therefore, the harmonic robustness comes at the expense of performance deceleration of

the PV system, which adversely affects the performance of the grid tied PV systems, especially in the case of grid faults.

In light of the above issues, this chapter proposes two novel PLL-based synchronization methods, which can achieve an accurate and fast synchronization performance under several grid voltage disturbances and also when the distribution grid contains both low- and high-order harmonics. The first method named MHDC-PLL is presented in Section 5.3 and uses a combination of $T/4$ delay transportation [27], [107], [108] and an IPT method [71], [107]-[110] in order to generate the in-quadrature voltage vector free of any high-order harmonics. Then, a novel Multi-Harmonic Decoupling Cell (MHDC) is developed in multiple SRFs to dynamically cancel out the oscillations due to low-order voltage harmonics. It is worth mentioning that the MHDC is based on a novel analysis of a single-phase voltage in multiple synchronous reference frames that has not previously mentioned in the literature. The proposed MHDC-PLL can achieve a fast synchronization under voltage sag events and a very accurate response under harmonic distorted grid conditions. The main drawbacks of the MHDC-PLL are the increased complexity and the inaccurate response under non-nominal frequencies. Hence, a second synchronization method (frequency adaptive MHDC-PLL) is proposed in Section 5.4 in order to overcome these problems. The frequency adaptive MHDC-PLL is based on a frequency adaptive QSG which is accurate under any frequency conditions and can eliminate the effect of high order harmonics. Further, the decoupling network of the frequency adaptive MHDC-PLL is enhanced in terms of complexity and thus, a robust synchronization can be achieved with significantly less required processing time. The fast and accurate synchronization by the proposed frequency adaptive MHDC-PLL is theoretically proved and is validated based on simulation and experimental results. Furthermore, an investigation has been performed in order to demonstrate the beneficial effect of the new advanced synchronization scheme on the operation of a PV system. The investigation shows that the proposed synchronization can enable an appropriate FRT response of PV systems under grid disturbances and can enhance the power quality of the injected currents.

5.3 MHDC-PLL

A new synchronization method, named MHDC-PLL, is proposed in this Section which presents a dynamic response under disturbances and a great immunity against harmonic distortion. The proposed synchronization is based on three modules: the QSG,

the MHDC and the *dq*-PLL algorithm. The QSG generates the in-quadrature voltage vector ($\mathbf{v}_{\alpha\beta}$) and filters the high-order harmonics of the grid voltage (v_s). The MHDC module achieves the fast and accurate decoupling of the fundamental voltage vector from the oscillations caused by the low-order harmonics. Finally, the harmonic-free voltage signal is used by the *dq*-PLL technique to extract the phase angle of the fundamental grid voltage.

5.3.1 Quadrature Signal Generator (QSG)

The QSG developed for the proposed synchronization is a combination of an IPT [71], [107]-[110], which can be considered as a band pass filter, and a *T*/4 delay transportation [27], [107], [108] as it is shown in Fig. 5.2. The voltage (v_α') is produced by using one forward and one inverse Park transformation and two first-order Low Pass Filters (LPFs), as shown in Fig. 5.2. The forward and inverse Park transformation can be achieved by setting the (*n*-*m*) equal to +1 and -1 respectively in (5.1) according to the theory explained in Appendix A.4; ω' is the estimated frequency by the PLL.

$$\left[T_{dq^{n-m}}\right]=\begin{bmatrix}\cos(n-m)\omega' t & \sin(n-m)\omega' t\\ -\sin(n-m)\omega' t & \cos(n-m)\omega' t\end{bmatrix} \tag{5.1}$$

Thus, the voltage vector $\mathbf{v}_{\alpha\beta}'$ is generated according to the forward transformation of (5.2), the first-order LPF of (5.3) and the backward transformation of (5.4).

$$\mathbf{v}_{dq}' = \begin{bmatrix} v_d' \\ v_q' \end{bmatrix} = \left[T_{dq^{+1}}\right]\begin{bmatrix} v_s \\ v_\beta' \end{bmatrix} \tag{5.2}$$

$$\bar{\mathbf{v}}_{dq}' = \frac{\omega_{f1}}{s+\omega_{f1}}\mathbf{v}_{dq}' \quad \Leftrightarrow \quad \begin{bmatrix} \bar{v}_d' \\ \bar{v}_q' \end{bmatrix} = \frac{\omega_{f1}}{s+\omega_{f1}}\begin{bmatrix} v_d' \\ v_q' \end{bmatrix} \tag{5.3}$$

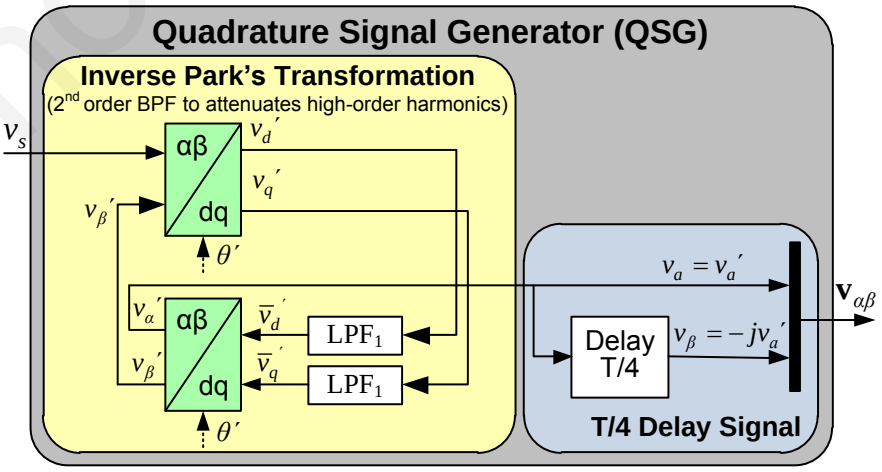

Fig. 5.2. The structure of the quadrature signal generator (QSG) that is used in the proposed MHDC-PLL.

$$\mathbf{v}_{\alpha\beta}{}' = \begin{bmatrix} v_\alpha{}' \\ v_\beta{}' \end{bmatrix} = \begin{bmatrix} T_{dq^{-1}} \end{bmatrix} \begin{bmatrix} \bar{v}_d{}' \\ \bar{v}_q{}' \end{bmatrix} \tag{5.4}$$

Where ω_{f1} is the cut-off frequency of the LPF_1 (the appropriate value of the design parameter ω_{f1} is defined in the following analysis).

In order to derive the transfer function of the IPT, it is necessary to express (5.1) in terms of the Euler formula as shown below.

$$\begin{bmatrix} T_{dq^{n-m}} \end{bmatrix} = \frac{1}{2} \begin{bmatrix} \left(e^{j(n-m)\omega' t} + e^{-j(n-m)\omega' t}\right) & -j\left(e^{j(n-m)\omega' t} - e^{-j(n-m)\omega' t}\right) \\ j\left(e^{j(n-m)\omega' t} - e^{-j(n-m)\omega' t}\right) & \left(e^{j(n-m)\omega' t} + e^{-j(n-m)\omega' t}\right) \end{bmatrix} \tag{5.5}$$

By using the Laplace property for frequency shifting ($e^{at} = F(s-a)$), the voltage vectors $\mathbf{v}_{dq}{}'$ and $\mathbf{v}_{\alpha\beta}{}'$ of (5.2) and (5.4) can be expressed in the complex-frequency domain as shown in (5.6) and (5.7), respectively.

$$\mathbf{v}_{dq}{}' = \begin{bmatrix} v_d{}' \\ v_q{}' \end{bmatrix} = \frac{1}{2} \begin{bmatrix} \left(v_s(s-j\omega') + v_s(s+j\omega')\right) & -j\left(v_\beta{}'(s-j\omega') - v_\beta{}'(s+j\omega')\right) \\ j\left(v_s(s-j\omega') - v_s(s+j\omega')\right) & \left(v_\beta{}'(s-j\omega') + v_\beta{}'(s+j\omega')\right) \end{bmatrix} \tag{5.6}$$

$$\mathbf{v}_{\alpha\beta}{}' = \begin{bmatrix} v_\alpha{}' \\ v_\beta{}' \end{bmatrix} = \frac{1}{2} \begin{bmatrix} \left(\bar{v}_d{}'(s-j\omega') + \bar{v}_d{}'(s+j\omega')\right) & j\left(\bar{v}_q{}'(s-j\omega') - \bar{v}_q{}'(s+j\omega')\right) \\ -j\left(\bar{v}_d{}'(s-j\omega') - \bar{v}_d{}'(s+j\omega')\right) & \left(\bar{v}_q{}'(s-j\omega') + \bar{v}_q{}'(s+j\omega')\right) \end{bmatrix} \tag{5.7}$$

The transfer functions $v_a{}'/v_s$ and $v_\beta{}'/v_s$ can be derived as shown in (5.8) and (5.9) respectively, by substituting (5.6) into (5.3) and then (5.3) into (5.7).

$$\frac{v_a{}'}{v_s} = \frac{k\omega' s}{s^2 + k\omega' s + \omega'^2}; \quad k = \frac{\omega_{f1}}{\omega'} \tag{5.8}$$

$$\frac{v'_\beta}{v_s} = \frac{k\omega'^2}{s^2 + k\omega' s + \omega'^2}; \quad k = \frac{\omega_{f1}}{\omega'} \tag{5.9}$$

The second-order transfer functions of (5.8) and (5.9) represent a band-pass and a low-pass filter respectively. Therefore, for optimally damped second-order filters, the factor k is set to $\sqrt{2}$ and therefore, ω_{f1} is set to $2\pi \cdot f_N \cdot \sqrt{2}$ rad/s since ω' represents the estimation of the operating angular frequency of the grid (normally at $2\pi \cdot f_N$ rad/s), where f_N is the nominal system frequency (50 or 60 Hz). The transfer function in (5.8) is actually a second-order band pass filter, which attenuates the zero-frequency (DC offset) and the high-order frequency harmonics without affecting the amplitude and phase angle of the

fundamental voltage at the nominal frequency, as it can be observed by the Bode diagram shown in Fig. 5.9 of Section 5.4.4. The generated voltage v_{β}' is a 90°-shifted voltage with respect to the measured voltage v_s according to (5.9), but v_{α}' and v_{β}' present different harmonic attenuation to the grid voltage due to the different filtering capability of (5.8) and (5.9).

Distinguished from the IPT-PLL, the use of v_{β}' is avoided in the proposed PLL, since the different harmonic filtering effects of v_{α}' and v_{β}' require a more complicated design for the MHDC. Instead, in the proposed QSG, the generation of the quadrature vector $\mathbf{v}_{\alpha\beta}$ is obtained by the $T/4$ delay transportation of the filtered v_{α}' as shown in Fig. 5.2, which makes the voltages v_{α} and v_{β} to present identical low order harmonic distortions. Therefore, the transfer function of the proposed QSG is given by considering that $v_{\alpha}=v_{\alpha}'$ and $v_{\beta}=-jv_{\alpha}'$ in (5.8).

5.3.2 Multi Harmonic Decoupling Cell (MHDC) module

The voltage vector $\mathbf{v}_{\alpha\beta}=[v_{\alpha}\ v_{\beta}]^{\mathrm{T}}$ is free of any zero or high frequency oscillations due to the QSG. The QSG acts as a second-order band-pass filter, but the low-order harmonics remain in the in-quadrature voltages. In order to cancel out the oscillations caused by the low-order harmonics through the proposed MHDC, a comprehensive analysis of the in-quadrature voltages is conducted as follows. *It is to be noted that the following analysis of a single-phase in-quadrature voltage vector in multiple synchronous reference frames constitutes one of the main novel parts of this dissertation*. Since the v_{β} is $T/4$ delayed from v_{α}, the $\mathbf{v}_{\alpha\beta}$ can be expressed as a summation of the fundamental component (n=1) and the low-order odd harmonics (n=3, 5, 7, 9, ...), as shown in (5.10),

$$\begin{aligned}\mathbf{v}_{\alpha\beta}&=\begin{bmatrix}v_{\alpha}\\ v_{\beta}\end{bmatrix}=V^{1}\begin{bmatrix}\cos(\omega t+\theta_1)\\ \cos(\omega(t-\frac{\mathrm{T}}{4})+\theta_1)\end{bmatrix}+\sum_{n=3,5,7,9,\ldots}V^{n}\begin{bmatrix}\cos(n\omega t+\theta_n)\\ \cos\left(n\omega(t-\frac{\mathrm{T}}{4})+\theta_n\right)\end{bmatrix}\\ \Leftrightarrow\ \mathbf{v}_{\alpha\beta}&=V^{1}\begin{bmatrix}\cos(\omega t+\theta_1)\\ \cos(\omega t-\frac{\pi}{2}+\theta_1)\end{bmatrix}+\sum_{n=3,5,7,9,\ldots}V^{n}\begin{bmatrix}\cos(n\omega t+\theta_n)\\ \cos(n\omega t-\frac{n\pi}{2}+\theta_n)\end{bmatrix}\end{aligned}\qquad(5.10)$$

where V^n and θ_n represent the amplitude and the initial phase angle respectively of the corresponding voltage component.

The voltage vector of (5.10) can be rewritten as shown in (5.11), where the summation of the harmonics can be divided into two groups according to the harmonic-order (i.e., 4*l*-1 and 4*l*+1 with *l* being 1, 2, 3, …).

$$\mathbf{v}_{\alpha\beta} = V^1\begin{bmatrix}\cos(\omega t+\theta_1)\\ \sin\left(\omega t+\theta_1\right)\end{bmatrix} + \sum_{n=3,7,11\ldots} V^n\begin{bmatrix}\cos(n\omega t+\theta_n)\\ \cos\left(n\omega t-\frac{3\pi}{2}+\theta_n\right)\end{bmatrix} + \sum_{n=5,9,13\ldots} V^n\begin{bmatrix}\cos(n\omega t+\theta_n)\\ \cos\left(n\omega t-\frac{\pi}{2}+\theta_n\right)\end{bmatrix} \tag{5.11}$$

Using basic trigonometric identities, (5.11) can be expressed as (5.12), where it is clear that the sign of the angular speed of each component depends on the harmonic order (i.e., 4*l* ± 1).

$$\mathbf{v}_{\alpha\beta} = V^1\begin{bmatrix}\cos(\omega t+\theta_1)\\ \sin\left(\omega t+\theta_1\right)\end{bmatrix} + \sum_{n=3,7,11\ldots} V^n\begin{bmatrix}\cos(-n\omega t-\theta_n)\\ \sin\left(-n\omega t-\theta_n\right)\end{bmatrix} + \sum_{n=5,9,13\ldots} V^n\begin{bmatrix}\cos(n\omega t+\theta_n)\\ \sin\left(n\omega t+\theta_n\right)\end{bmatrix} \tag{5.12}$$

Therefore, the voltage vector $\mathbf{v}_{\alpha\beta}$ can be expressed by (5.13), in which sgn(*n*) defines the speed direction of each harmonic component vector.

$$\mathbf{v}_{\alpha\beta} = V^n\begin{bmatrix}\cos(\omega t+\theta_1)\\ \sin\left(\omega t+\theta_1\right)\end{bmatrix} + \sum_{\substack{n=3,5,\\ 7,9,\ldots}} V^n\begin{bmatrix}\cos\left((\mathrm{sgn}(n)\cdot\left(n\omega t+\theta_n\right)\right)\\ \sin\left((\mathrm{sgn}(n)\cdot\left(n\omega t+\theta_n\right)\right)\end{bmatrix} \tag{5.13}$$

$$\text{where}\quad \mathrm{sgn}(n) = \sin n\frac{\pi}{2} = \begin{cases}+1 & \textit{for } n = 1,5,9,\ldots\\ -1 & \textit{for } n = 3,7,11,\ldots\end{cases}$$

The voltage vector $\mathbf{v}_{\alpha\beta}$ can then be translated into any n^{th} synchronous reference frame ($dq^{n\mathrm{sgn}(n)}$-frame) with a rotating speed equal to $n\cdot\mathrm{sgn}(n)\cdot\omega$, where ω is the fundamental angular frequency. The voltage vector expressed to the $dq^{n\mathrm{sgn}(n)}$-frame ($\mathbf{v}_{dq^{n\cdot\mathrm{sgn}(n)}}$) can be calculated by multiplying the $\mathbf{v}_{\alpha\beta}$ with the transformation matrix [$T_{dq^{n\cdot\mathrm{sgn}(n)}}$] of (5.1) as shown in (5.14). The voltage vector $\mathbf{v}_{dq^{n\cdot\mathrm{sgn}(n)}}$ in (5.14) contains an oscillation-free vector $\mathbf{v}^{\,n}_{dq^{\mathrm{n\cdot sgn(n)}}}$, which is actually the voltage component V^n rotating at the corresponding synchronous $\mathrm{sgn}(n)\cdot n\cdot\omega$ angular speed. Furthermore, it contains some oscillation vectors ($\mathbf{v}^{\,m}_{dq^{n\cdot\mathrm{sgn}(n)}} = [T_{dq^{n\cdot sgn(n)-m\cdot sgn(m)}}]\,\mathbf{v}^{\,m}_{dq^{m\cdot\mathrm{sgn}(m)}}$) based on the effect of the rest of the voltage components.

$$\mathbf{v}_{dq^{n\cdot\mathrm{sgn}(n)}} = \begin{bmatrix} v_{d^{\,n\cdot\mathrm{sgn}(n)}} \\ v_{q^{\,n\cdot\mathrm{sgn}(n)}} \end{bmatrix} = \left[T_{dq^{\,n\cdot\mathrm{sgn}(n)}} \right] \cdot \mathbf{v}_{\alpha\beta}$$

$$\Leftrightarrow \mathbf{v}_{dq^{n\cdot\mathrm{sgn}(n)}} = V^n \begin{bmatrix} \cos\left(\mathrm{sgn}(n)\cdot\theta_n\right) \\ \sin\left(\mathrm{sgn}(n)\cdot\theta_n\right) \end{bmatrix} + \sum_{m\neq n} \left\{ V^m \left[T_{dq^{n\cdot\mathrm{sgn}(n)-m\cdot\mathrm{sgn}(m)}} \right] \begin{bmatrix} \cos(\theta_m) \\ \sin(\theta_m) \end{bmatrix} \right\} \qquad (5.14)$$

$$\Leftrightarrow \mathbf{v}_{dq^{n\cdot\mathrm{sgn}(n)}} = \mathbf{v}^{n}_{dq^{n\cdot\mathrm{sgn}(n)}} + \sum_{m\neq n} \left\{ \left[T_{dq^{n\cdot\mathrm{sgn}(n)-m\cdot\mathrm{sgn}(m)}} \right] \mathbf{v}^{m}_{dq^{m\cdot\mathrm{sgn}(m)}} \right\}$$

Oscilations free term — Oscilation terms

To enable the design of the proposed MHDC, the voltage vector should be expressed in all reference frames of the existing frequency components. Since the QSG has eliminated the effect of high frequency harmonics (as it behaves like a second-order band-pass filter), the proposed method presented here deals only with the effect of the four most significant low-order harmonics. Therefore, the voltage vector should be expressed in the fundamental (+1) and the most significant harmonics (+3, +5, +7, +9) reference frames as shown in (5.15), where *Z* represents a 2x2 zero matrix.

$$\begin{bmatrix} \mathbf{v}_{dq^{+1}} \\ \mathbf{v}_{dq^{-3}} \\ \vdots \\ \mathbf{v}_{dq^{+9}} \end{bmatrix} = \begin{bmatrix} T_{dq^{+1}} \\ T_{dq^{-3}} \\ \vdots \\ T_{dq^{+9}} \end{bmatrix} \mathbf{v}_{\alpha\beta} = \begin{bmatrix} \mathbf{v}^{+1}_{dq^{+1}} \\ \mathbf{v}^{+3}_{dq^{-3}} \\ \vdots \\ \mathbf{v}^{+9}_{dq^{+9}} \end{bmatrix} + \begin{bmatrix} Z & T_{dq^{+1-(-3)}} & \cdots & T_{dq^{+1-(+9)}} \\ T_{dq^{-3-(+1)}} & Z & \cdots & T_{dq^{-3-(+9)}} \\ \vdots & \vdots & \ddots & \vdots \\ T_{dq^{+9-(+1)}} & T_{dq^{+9-(-3)}} & \cdots & Z \end{bmatrix} \begin{bmatrix} \mathbf{v}^{+1}_{dq^{+1}} \\ \mathbf{v}^{+3}_{dq^{-3}} \\ \vdots \\ \mathbf{v}^{+9}_{dq^{+9}} \end{bmatrix} \qquad (5.15)$$

Now, (5.15) can be easily re-written in the form of (5.16) by solving the equation in terms of the oscillation-free vectors $\mathbf{v}^{n}_{dq^{n\cdot\mathrm{sgn}(n)}}$.

$$\begin{bmatrix} \mathbf{v}^{+1}_{dq^{+1}} \\ \mathbf{v}^{+3}_{dq^{-3}} \\ \vdots \\ \mathbf{v}^{+9}_{dq^{+9}} \end{bmatrix} = \begin{bmatrix} T_{dq^{+1}} \\ T_{dq^{-3}} \\ \vdots \\ T_{dq^{+9}} \end{bmatrix} \mathbf{v}_{\alpha\beta} - \begin{bmatrix} Z & T_{dq^{+1-(-3)}} & \cdots & T_{dq^{+1-(+9)}} \\ T_{dq^{-3-(+1)}} & Z & \cdots & T_{dq^{-3-(+9)}} \\ \vdots & \vdots & \ddots & \vdots \\ T_{dq^{+9-(+1)}} & T_{dq^{+9-(-3)}} & \cdots & Z \end{bmatrix} \begin{bmatrix} \mathbf{v}^{+1}_{dq^{+1}} \\ \mathbf{v}^{+3}_{dq^{-3}} \\ \vdots \\ \mathbf{v}^{+9}_{dq^{+9}} \end{bmatrix} \qquad (5.16)$$

Since, the vectors $\mathbf{v}_{dq^{n\cdot\mathrm{sgn}(n)}}$ and $\mathbf{v}_{\alpha\beta}$ are known and the vectors $\mathbf{v}^{n}_{dq^{n\cdot\mathrm{sgn}(n)}}$ are unknown, the estimation of the unknown vectors is enabled by replacing the unknown vectors $\mathbf{v}^{n}_{dq^{n\cdot\mathrm{sgn}(n)}}$ of the left side of (5.16) with the estimated vectors $\mathbf{v}^{n*}_{dq^{n\cdot\mathrm{sgn}(n)}}$, while the unknown vector of the right side of (5.16) is replaced by the filtered estimated vector

$\bar{\mathbf{v}}_{dq^{n\cdot\mathrm{sgn}(n)}}^{n*}$. The resulting equation presented in (5.17) can be used to develop the proposed Multi-Harmonic Decoupling Cell (MHDC) based on a cross-feedback network for decoupling of the voltage vector components as shown in Fig. 5.3.

$$\begin{bmatrix} \mathbf{v}_{dq^{+1}}^{+1*} \\ \mathbf{v}_{dq^{-3}}^{+3*} \\ \vdots \\ \mathbf{v}_{dq^{+9}}^{+9*} \end{bmatrix} = \begin{bmatrix} T_{dq^{+1}} \\ T_{dq^{-3}} \\ \vdots \\ T_{dq^{+9}} \end{bmatrix} \mathbf{v}_{\alpha\beta} - \begin{bmatrix} Z & T_{dq^{+1-(-3)}} & \cdots & T_{dq^{+1-(+9)}} \\ T_{dq^{-3-(+1)}} & Z & \cdots & T_{dq^{-3-(+9)}} \\ \vdots & \vdots & \ddots & \vdots \\ T_{dq^{+9-(+1)}} & T_{dq^{+9-(-3)}} & \cdots & Z \end{bmatrix} \begin{bmatrix} \bar{\mathbf{v}}_{dq^{+1}}^{+1*} \\ \bar{\mathbf{v}}_{dq^{-3}}^{+3*} \\ \vdots \\ \bar{\mathbf{v}}_{dq^{+9}}^{+9*} \end{bmatrix} \tag{5.17}$$

It is to be mentioned that the filtered estimated vectors $\bar{\mathbf{v}}_{dq^{n\cdot\mathrm{sgn}(n)}}^{n*}$ are derived by filtering the estimated vectors $\mathbf{v}_{dq^{n\cdot\mathrm{sgn}(n)}}^{n*}$ according to (5.18).

$$\bar{\mathbf{v}}_{dq^{n\cdot\mathrm{sgn}(n)}}^{n*} = [F(s)]\left\{\mathbf{v}_{dq^{n\cdot\mathrm{sgn}(n)}}^{n*}\right\} \tag{5.18}$$

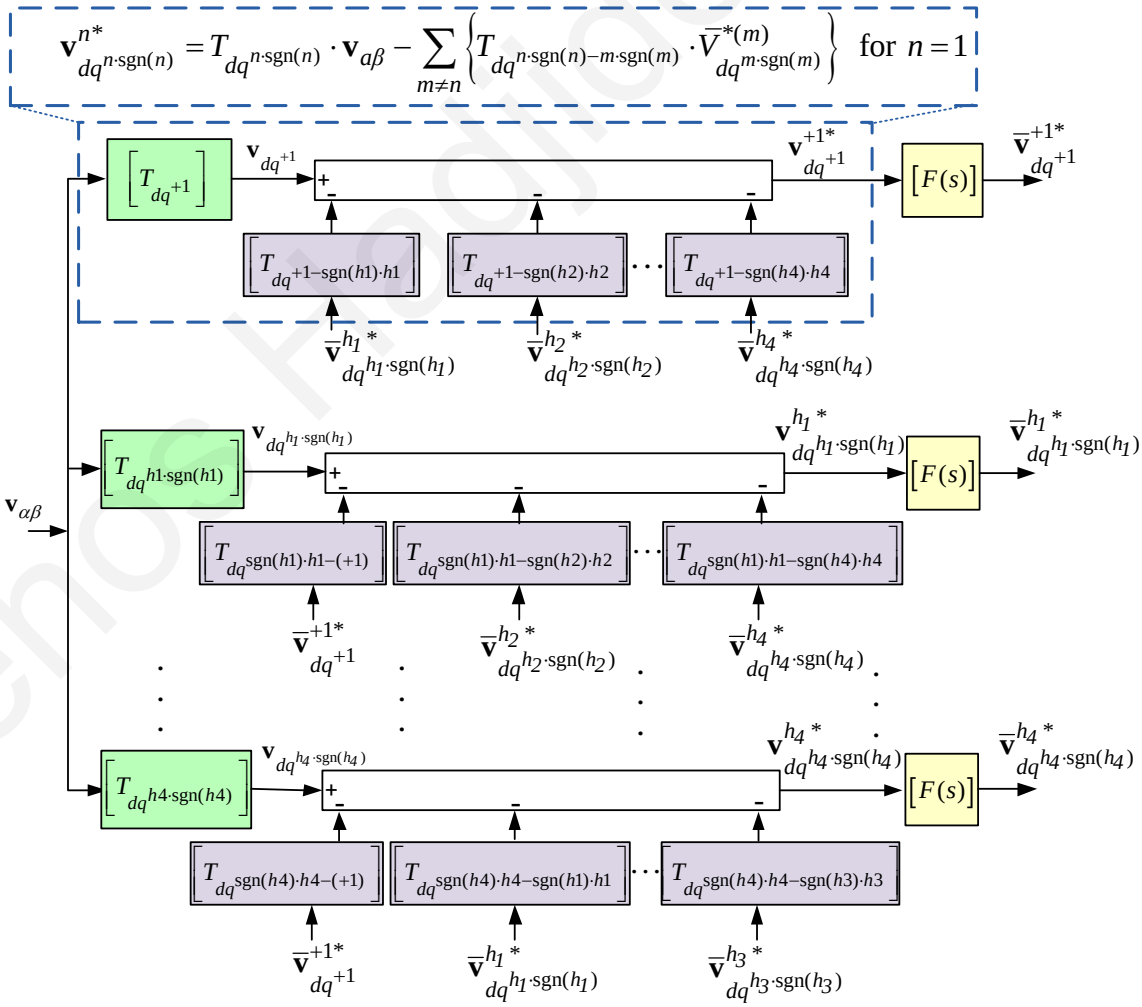

Fig. 5.3. The block diagram of the proposed Multi-Harmonic Decoupling Cell (MHDC).

where

$$[F(s)] = \begin{bmatrix} \dfrac{\omega_{f2}}{s+\omega_{f2}} & 0 \\ 0 & \dfrac{\omega_{f2}}{s+\omega_{f2}} \end{bmatrix} \tag{5.19}$$

Finally, (5.17) can be rewritten as (5.20), which is the main equation of the proposed MHDC.

$$\mathbf{v}_{dq^{n\cdot\mathrm{sgn}(n)}}^{n*} = T_{dq^{n\cdot\mathrm{sgn}(n)}} \cdot \mathbf{v}_{a\beta} - \sum_{m\neq n} \left\{ T_{dq^{n\cdot\mathrm{sgn}(n)-m\cdot\mathrm{sgn}(m)}} \cdot \bar{\mathbf{v}}_{dq^{m\cdot\mathrm{sgn}(m)}}^{*(m)} \right\} \tag{5.20}$$

The design parameter ω_{f2} should be set equal to $\omega_n/3$, where ω_n is the nominal angular frequency of the grid at $2\pi 50$ rad/s. The proper selection of the design parameter ω_{f2} is defined in Section 5.4.4 as a result of the theoretical analysis of the MHDC. The block diagram of the proposed MHDC is represented in Fig. 5.3. The multiple uses of (5.20) as a cross-feedback network in the MHDC (once for the fundamental and for each harmonic component) can dynamically eliminate the cross-coupling effects and can achieve an accurate generation of the oscillation-free signal $\mathbf{v}_{dq^{+1}}^{+1*}$, which then can be used for an accurate synchronization.

5.3.3 The structure of the MHDC-PLL

The produced voltage vector $\mathbf{v}_{dq^{+1}}^{+1*}$ by the MHDC is free of any high- and low-order harmonic oscillations as discussed in Section 5.3.1 and 5.3.2 respectively. Thus, the produced vector $\mathbf{v}_{dq^{+1}}^{+1*}$ can be considered as a good approximation of the fundamental component of the grid voltage expressed in the dq^{+1}-frame as shown below,

$$\begin{aligned} \mathbf{v}_{dq^{+1}}^{+1*} \approx \mathbf{v}_{dq^{+1}}^{+1} = \left[T_{dq^{+1}}\right] \cdot \mathbf{v}_{\alpha\beta}^{+1} = \begin{bmatrix} \cos\theta' & \sin\theta' \\ -\sin\theta' & \cos\theta' \end{bmatrix} \begin{bmatrix} V^1 \cdot \cos\theta \\ V^1 \cdot \cos(\theta - \mathrm{T}/4) \end{bmatrix} \\ \Leftrightarrow \quad \mathbf{v}_{dq^{+1}}^{+1*} \approx \begin{bmatrix} V^1 \cdot \cos(\theta-\theta') \\ V^1 \cdot \sin(\theta-\theta') \end{bmatrix} \approx \begin{bmatrix} V^1 \\ V^1 \Delta\theta \end{bmatrix} \end{aligned} \tag{5.21}$$

where θ' is the estimated phase angle by the proposed PLL and θ is the real phase angle of the fundamental component of the grid voltage. Since the error $\Delta\theta=\theta-\theta'$ is very small in steady state, then $v_{q^{+1}}^{+1*}$ can be assumed as a linearized approximation of $\Delta\theta$ as shown in (5.21).

Therefore, the estimated $v_{d^{+1}}^{+1*}$ represents the amplitude of the fundamental component of the grid voltage (V^1) and the $v_{q^{+1}}^{+1*}$ can be considered by a simple PLL algorithm, such as the *dq*-PLL [59], in order to lock the phase angle of the grid voltage as shown in Fig. 5.4. The structure of the *dq*-PLL is presented in Fig. 5.4, where a Proportional-Integral (PI) controller is used in the dq^{+1}-frame to extract the phase angle of the fundamental voltage. The tuning process of such a PLL is based on the linearized small signal analysis of the PLL as presented in Appendix B. In the case that the transfer function of the PI controller is given by $k_p+1/(T_i s)$, the closed-loop transfer function of the PLL can be simplified to the second order transfer function of (5.22) when the PLL is designed for a per unit voltage. The tuning parameters k_p and T_i can be calculated according to (5.23), where ζ should be set to $1/\sqrt{2}$ for an optimally damped PLL response and the Settling Time (ST) for the MHDC-PLL has been set to 100 ms.

$$\frac{\theta'}{\theta} = \frac{k_p s + 1/T_i}{s^2 + k_p s + 1/T_i} \tag{5.22}$$

$$k_p = \frac{9.2}{T_s} \qquad \text{and} \qquad T_i = 0.047\zeta^2 T_s^2 \tag{5.23}$$

To sum up, the proposed MHDC-PLL consists of three main modules: the proposed QSG in Section 5.3.1, the MHDC as proposed in Section 5.3.2, and the PLL algorithm of Section 5.3.3. The structure of the new MHDC-PLL with all the modules is presented in

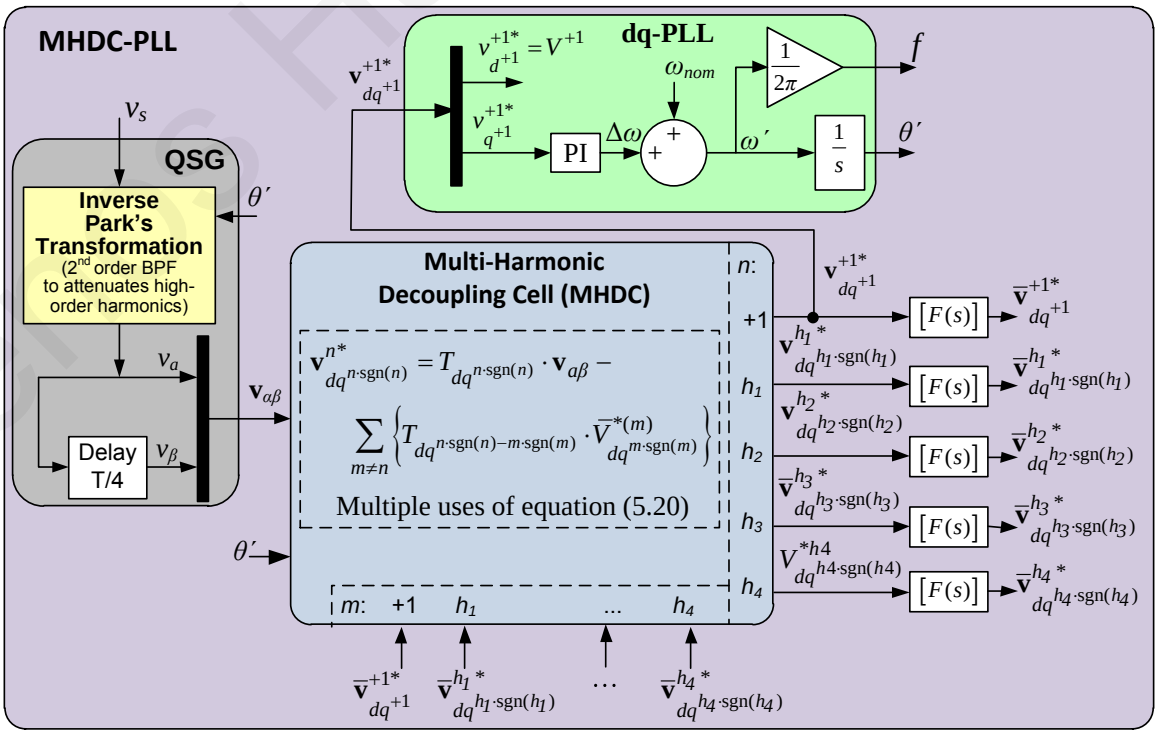

Fig. 5.4. The structure of the proposed MHDC-PLL.

Fig. 5.4 and the designed parameters for the MHDC-PLL are presented in TABLE 5.1. The proposed synchronization technique can achieve an accurate and dynamic response under distorted voltage and under grid disturbances (e.g., voltage sag, phase change) as demonstrated in Section 5.3.4. The accuracy and the fast performance of the proposed PLL can potentially affect the response of the GSC controller and as a result, the performance of the whole grid-tied inverter in terms of power quality and in terms of fast FRT operations.

5.3.4 Simulation and experimental results

The performance of the proposed PLL requires verification through simulation and experimental results. Therefore, an experimental setup and an identical simulation model (in MATLAB/Simulink) have been implemented according to the structure of the single-phase grid-tied inverter as presented in Fig. 5.1. All the parameters of the implemented experimental setup are listed in TABLE 5.1. The proposed synchronization method claims an outstanding performance in terms of accuracy under harmonic distorted grid voltage. Therefore, the proper response of the MHDC-PLL should be tested under harmonic distorted voltage and under other several grid voltage disturbances, such as phase jump, voltage sag, and frequency variation.

The response of the proposed MHDC-PLL is compared with the response of a widely use synchronization method, such as the SOGI-PLL [71], [107]-[110]. The same tuning parameters have been used in both PLLs according to TABLE 5.1. The simulation results for the response of the two PLLs are presented in Fig. 5.5 under several voltage conditions. The voltage at the beginning of the simulation is purely sinusoidal. A significant low-order voltage harmonic distortion (THD_V=2.93%) is injected by the grid at $t = 0.3$ s with $|V_5|$=2% and $|V_7|$=2% relative to the fundamental and 0.75% of high-order harmonics. It is clearly observed in Fig. 5.5 that, for low-order harmonic distorted voltage ($t > 0.3$ s) the SOGI-PLL presents significant oscillations due to the harmonics effect, while the proposed MHDC-PLL achieves a very accurate response and is robust against harmonics due to the multi-frequency notch filtering character of the MHDC on the selected

TABLE 5.1: PARAMETERS FOR THE EXPERIMENTAL SETUP

Nominal conditions	V_N=230 Vrms, f_N=50 Hz, S_N=1 kVA, V_{PV}=400 V
Sampling and PWM	$f_{SAMPLING} = f_{PWM}$ =10 kHz
Design guidelines for the MHDC-PLL	Tuning Parameters → (k_P=92, T_I=0.000235) $\omega_{f1}=2\pi 50\sqrt{2}$ rad/s, $\omega_{f2}=2\pi 50/3$ rad/s
LCL filter	L_{if}=3.6 mH, C_f = 2.35 μF, L_{gf} = 4 mH
Hardware in the loop	DS1103 dSPACE
DC Source	Delta Elektronika SM 600-10
AC Source	California Instrument MX-30
Inverter	Semikron SEMITeach (B6CI)

harmonics. The PLLs are also tested under several voltage disturbances. For example, the MHDC-PLL presents a very accurate and dynamic response when subjected under the following sequence of events: a -30° phase change at 0.4 s, a 25% voltage sag at 0.6 s, and a 0.8 Hz frequency step at 0.8 s, despite the voltage harmonic distortion. A higher overshoot on the synchronization signals is presented by the proposed PLL due to the fast dynamic response of the MHDC regarding the fundamental frequency voltage component. The only disadvantage of the proposed MHDC-PLL is indicated under non-nominal grid frequencies as shown in Fig. 5.5 for $t > 0.8$ s due to the imperfect response of the T/4 delay component used in QSG under frequencies which are different from the nominal one.

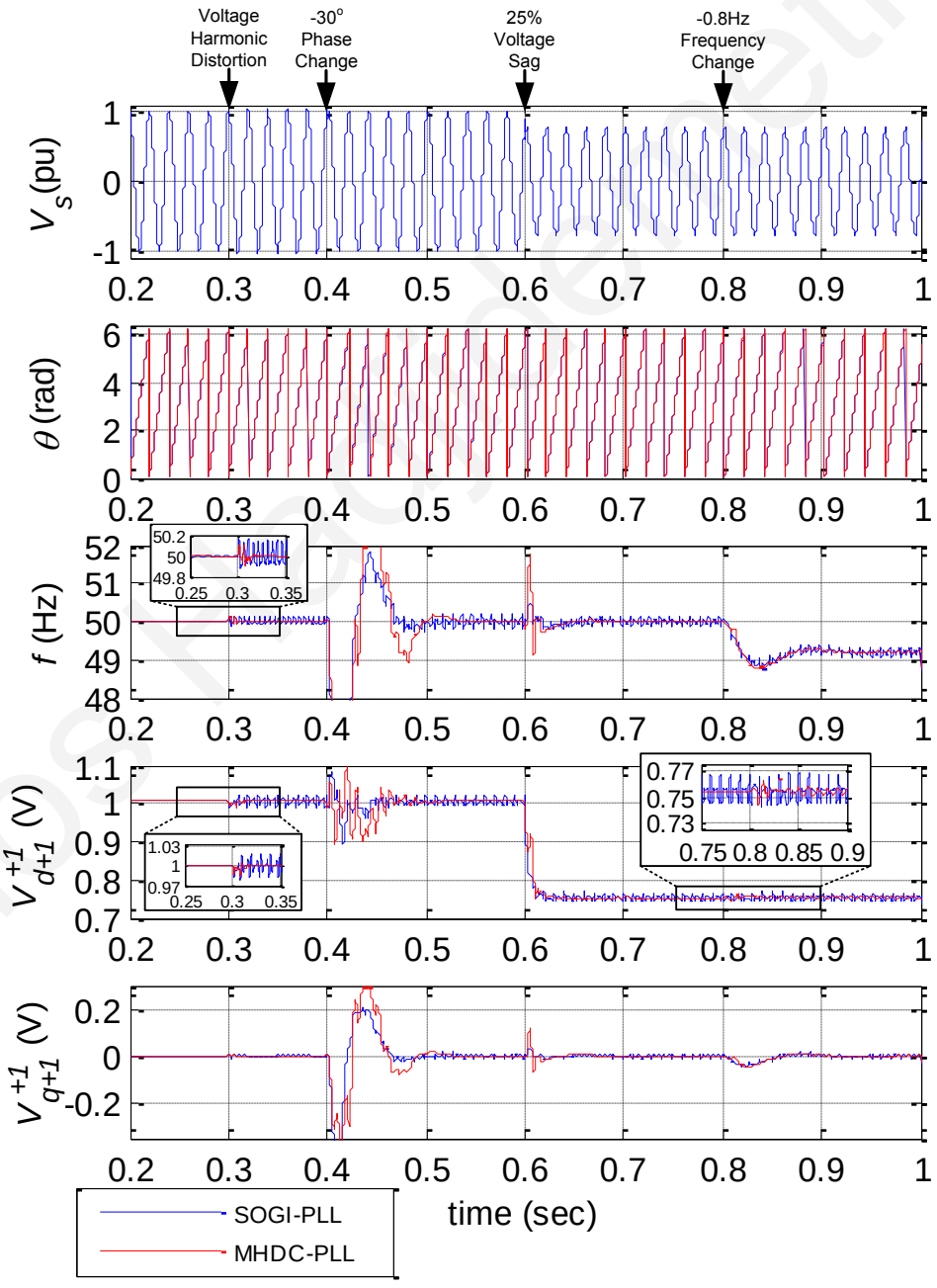

Fig. 5.5. Simulation results for the response of SOGI-PLL and the proposed MHDC-PLL under harmonic distorted voltage and phase step change, voltage sag, and frequency step change.

The robust performance of the proposed PLL is also validated according to the experimental results of Fig. 5.6. The experimental synchronization signals are depicted in the channels 1-4 of the oscilloscope by using the Digital to Analogue Converter (DAC) of the dSPACE board. The monitoring signals θ', f', v_q' and v_d' of Fig. 5.6 represent the synchronization signals that are estimated by the two PLLs. The responses of the SOGI-PLL (left side) and the proposed MHDC-PLL (right side) are presented in Fig. 5.6 under several grid conditions: (a) under normal operating conditions, (b) when a harmonic distortion ($|V_5|$=2% and $|V_7|$=2% relative to the fundamental and 0.12% of high-order harmonics) is applied on the grid voltage, (c) under a 25% voltage sag, (d) under a -30^o phase jump, and (e) under a -0.8Hz frequency step change. The proposed MHDC-PLL presents immunity against harmonic distortion according to Fig. 5.6(b). Moreover, the MHDC-PLL presents equivalent dynamic response compared to the SOGI-PLL under several grid disturbances (without any harmonic distortion) as shown in Fig. 5.6(c)-(e). Therefore, the harmonic robustness and a fast dynamic response are achieved by the proposed synchronization method. The only

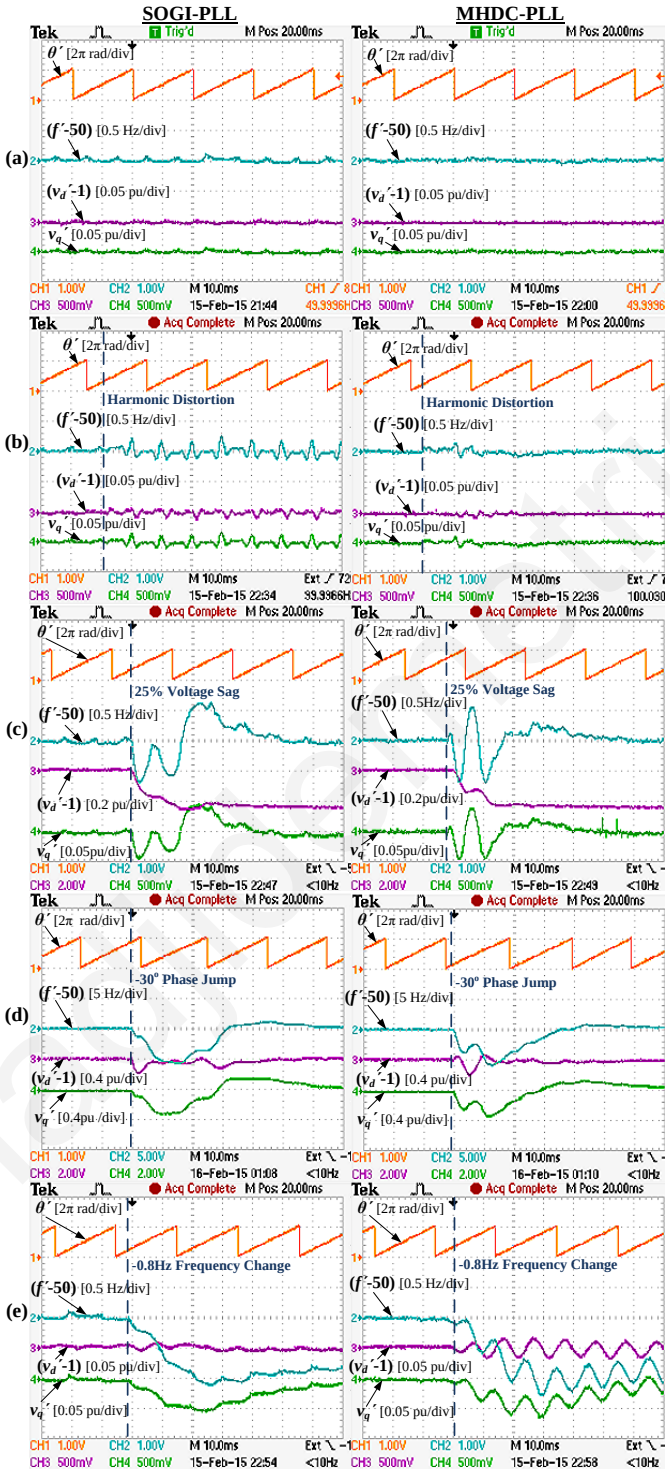

Fig. 5.6. Experimental results for the synchronization response of the SOGI-PLL (left hand side) and of the MHDC-PLL (right hand side). The performance of PLLs are presented (a) under normal grid conditions, (b) when harmonic distortion is applied on the grid voltage, (c) under a voltage sag, (d) under a phase jump and (e) under a frequency step change.

disadvantage of the proposed PLL is demonstrated in Fig. 5.6 (e), where the MHDC-PLL presents some small oscillation on the synchronization signals under a non-nominal frequency due to the imperfect response of the discrete implemented T/4 delay component under variable frequency environment. It should be noted that these oscillations can be minimized but not eliminated by rounding the number of samples considered in the T/4 delay component to the nearest integer. It is to be noted that the disturbances during the experimental tests were manually recreated by a programmable AC source. Therefore, the same disturbance was recreated for each PLL as shown in Fig. 5.6, but the moment of fault was not a controllable variable and thus, the voltage phase at the instant of fault (and the initial disturbance) is different for each PLL.

The proposed MHDC-PLL presents an accurate and fast response under grid disturbances with great immunity against harmonic distortion as it has been validated though simulation and experimental results. The only disadvantage of the MHDC-PLL is the inaccurate response under non-nominal frequencies and the relatively increased complexity of the algorithm. This outstanding response of the synchronization method can be beneficial for single-phase grid-tied inverter systems since an accurate synchronization can enhance its dynamic response under normal and FRT operation, and can improve the power quality of the injected current to the grid as has been shown in [36] .

5.3.5 Conclusions

This Section has proposed a novel single-phase MHDC-PLL, which can achieve a fast and accurate synchronization under a distorted grid voltage. The estimation accuracy of the synchronization signals is enabled by the proposed MHDC, which can cancel out the oscillations induced by low-order harmonics, but without affecting the transient response of the PLL. Simulation and experimental results have verified the accurate and dynamic response of the proposed PLL under highly distorted grid voltages and under several grid disturbances (e.g., voltage sag, phase jump). The only disadvantages of the proposed PLL are the small oscillation on the synchronization signals under non-nominal frequency and the relatively increased complexity of the synchronization method. The dynamic response and the immunity against voltage harmonic distortion of the proposed synchronization method can beneficially affect the performance of grid-tied inverters, especially in terms of power quality improvement.

5.4 Frequency adaptive MHDC-PLL

In the prior-art work, several advanced PLL-based synchronization methods can be found as already mentioned in Section 5.2. These methods may achieve a fast dynamic response under grid disturbances; however, they are inaccurate under harmonic distortion or may present robustness against harmonics but their dynamic response is undesirably affected. In Section 5.3, a novel synchronization method is proposed, named MHDC-PLL, which is based on a novel Multi Harmonic Decoupling Cell (MHDC) and can achieve an accurate performance under harmonic distortions without affecting its dynamic responses. Some minor disadvantages of the MHDC-PLL are, however, the increased complexity in terms of heavy computation burden and the inaccurate response under non-nominal frequencies (e.g., a frequency jump).

This Section aims to address these major issues and thus to improve the performance of the MHDC-PLL by proposing a frequency adaptive MHDC-PLL. In Section 5.4.1, a frequency adaptive Quadrature Signal Generator (QSG) is developed to enable an accurate response under non-nominal frequencies. In Section 5.4.2, the MHDC is reformulated in such a way to achieve an equivalent fast and accurate performance under harmonic distortion and grid disturbances, but with a decrease in complexity and required processing time. Finally, in Section 5.4.3, the development of the frequency adaptive MHDC-PLL is proposed. A performance theoretical analysis and a complexity assessment of the proposed synchronization scheme is performed in Section 5.4.4, while Section 5.4.5 demonstrates simulation and experimental results of the frequency adaptive MHDC-PLL.

5.4.1 Frequency adaptive Quadrature Signal Generator (QSG)

The MHDC-PLL proposed in Section 5.3 and in [36]-[38] employs: a Quadrature Signal Generator (QSG) unit to generate the in-quadrature voltage vector ($\mathbf{v}_{\alpha\beta}$) that is free of high-order harmonics, the MHDC to dynamically decouple the effect of low-order harmonics, and the *dq*-PLL algorithm to estimate the phase angle of the fundamental voltage component ($\mathbf{v}^{+1}$). The QSG of the initial MHDC-PLL (Section 5.3.1) suffers from the non-ideal and unsatisfactory responses of the QSG under frequency changes as already highlighted in 5.3.4. Hence, this section proposes a frequency adaptive scheme to address this issue.

The QSG of the MHDC-PLL (Section 5.3.1) is based on a combination of an Inverse Park's Transformation (IPT) method for cancelling the high-order harmonics and

on a $T/4$ delay unit, where T is the period of the grid voltage, to generate the in-quadrature voltage vector. The IPT method is based on a forward Park's transformation, on a low-pass filter $\omega_{f1}/(s+\omega_{f1})$, and on a backward Park's transformation as described in Section 5.3.1. It should be noted that the IPT method is not used for the in-quadrature vector $\mathbf{v}_{\alpha\beta}$ generation, since the filtering effect of IPT on v_α and v_β is different. Thus, a more complicated design of the MHDC is required for cancelling out the low-order harmonics. Similarly here, the IPT is only used for filtering the high-order harmonics of the grid voltage v_s. Therefore, the v_α is free of high-order harmonics and then a T/4 delay unit is used for generating the in-quadrature voltage vector $\mathbf{v}_{\alpha\beta}$.

The $T/4$ delay unit of Section 5.3.1 can accurately perform in a digital controller, only when the ratio between the sampling rate (f_s) and the grid frequency (f_{grid}) is an integer and multiple of four. Thus, in the case where the ratio ($f_s/4 \cdot f_{grid}$) is an integer, the in-quadrature voltage vector $\mathbf{v}_{\alpha\beta}$ can equivalently be expressed in the continuous and in the discrete-time domains as,

$$\begin{aligned} \text{Continuous-time} \rightarrow \mathbf{v}_{\alpha\beta}(t) &= \begin{bmatrix} v_a(t) \\ v_\beta(t) \end{bmatrix} = \begin{bmatrix} v_a(t) \\ v_\alpha(t - T/4) \end{bmatrix} \\ \text{Discrete-time} \rightarrow \mathbf{v}_{\alpha\beta}(k) &= \begin{bmatrix} v_a(k) \\ v_\beta(k) \end{bmatrix} = \begin{bmatrix} v_a(k) \\ v_\alpha(k - f_s/4\ f_{grid}) \end{bmatrix} \end{aligned} \tag{5.24}$$

Unfortunately, in the case where the ratio ($f_s/4 \cdot f_{grid}$) is not an integer, the $T/4$ delay unit of Section 5.3.1 can only approach the closest sample ($k_{T/4}$) to the $T/4$ delayed signal, where $k_{T/4}$ is the rounded $f_s/(4 \cdot f_{grid})$. Hence, when the grid frequency varies, the generated discrete-time $v_\beta(k)$ can present a phase shift error $\Delta\varphi$ from its desired continuous-time signal $v_\beta(t)$ as explained by,

$$v_\beta(k) = v_\alpha(k - k_{T/4}) \qquad \Leftrightarrow \qquad v_\beta(t) = v_\alpha(t - T/4 \pm \Delta\varphi) \tag{5.25}$$

In the worst case scenario, the phase error $\Delta\varphi$ is equal to $180 \cdot f_s/f_{grid}$. For instance, when f_s=10 kHz, the phase error can reach 0.89 degrees, when f_{grid}=49.505 Hz. Such a phase shift error on the in-quadrature voltage vector $\mathbf{v}_{\alpha\beta}$ causes significant oscillations on the voltage signals expressed in the synchronous reference frame. As a result, undesired inaccuracies on the synchronization signals are raised. A straight forward way to overcome this issue is to use a variable sampling rate as discussed in [65] to ensure that the $f_s/(4 \cdot f_{grid})$ is always an integer under any grid frequency. However, in such grid-tied inverter

applications, the variable sampling rate is usually not an option, due to several restrictions on the controller design.

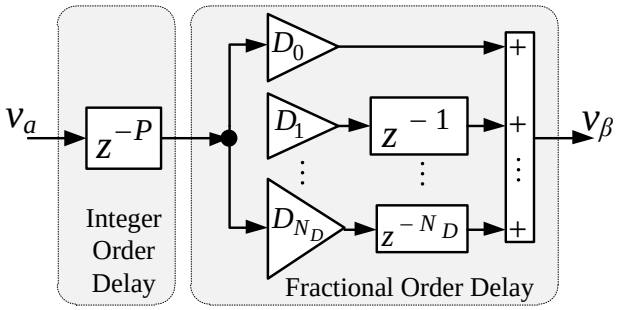

Fig. 5.7. Structure of the proposed frequency adaptive QSG.

Hence, a novel frequency adaptive implementation of the $T/4$ delay unit is introduced in the following to enable an accurate operation of the MHDC-PLL under any grid frequency. The proposed frequency adaptive $T/4$ delay unit is developed in a digital controller by splitting the $T/4$ delay unit (i.e., $z^{-(fs/fgrid)/4}$) into an integer order delay (z^{-P}) and a fractional order delay (z^{-F}) as shown in Fig. 5.7. Then, the fractional order delay (z^{-F}) is approximated using the *Langrange* interpolation polynomial finite-impulse-response filter [117] as,

$$z^{-(f_s/f_{grid})/4} = z^{-(P+F)} \tag{5.26}$$

$$\text{where: } z^{-P} = \overset{\text{Integer Order Delay}}{}, \; z^{-F} = \overset{\text{Fractional Order Delay}}{} \approx \sum_{l=0}^{N_D} D_l \cdot z^{-l} \; ; \; D_l = \prod_{\substack{i=0 \\ i \neq l}}^{N_D} \frac{F-i}{l-i} \quad \text{and } l = 0,1,2...,N_D$$

with N_D being the *Langrange* interpolation polynomial order, and N_D=3 being selected in this work.

Such an adaptive $T/4$ delay unit according to (5.26) and Fig. 5.7 is then employed in the digital controller in order to generate the in-quadrature voltage vector $\mathbf{v}_{\alpha\beta}$. The discrete-time $v_\beta(k)$ can accurately estimate the continuous-time $v_\beta(t)=v_\alpha(t-T/4)$ due to the *Langrange* interpolation and thus, the use of the adaptive $T/4$ delay on the structure of the proposed frequency adaptive MHDC-PLL (as shown in Fig. 5.8) can enable an accurate synchronization at any grid frequency.

5.4.2 Reformulation of the MHDC for complexity reduction

The decoupling network (MHDC) of Section 5.3.2 can achieve a dynamic cancellation of the low-order voltage harmonics and hence a fast and accurate synchronization can be ensured under any grid conditions (i.e., grid faults, high harmonic distortion). The major disadvantage of the MHDC of Section 5.3.2 is the increased complexity (processing burden) of the decoupling network, which may be sufficiently high in such real-time applications. Hence, a re-formulation of the decoupling network is

proposed in the following in order to minimize the required processing time of the algorithm and to still achieve an exact equivalent response with the conventional MHDC of Section 5.3.2. The complexity minimization is achieved by re-designing the decoupling network in the stationary reference frame ($\alpha\beta$-frame) instead of performing this in each $dq^{n\mathrm{sgn}(n)}$-frame as it has initially been proposed in Section 5.3.2.

The re-design of the decoupling network for dynamically cancelling out the low-order harmonics requires the analysis of the grid voltage under high harmonic distortion. As it is proved in Section 5.4.4, the QSG is filtering out only the high-order harmonics (due to the IPT) and then it generates the v_β component by delaying the v_α for a period of $T/4$. Thus, under harmonic distorted conditions, the vector $\mathbf{v}_{\alpha\beta}$ can be expressed as a summation of the fundamental component (n=1) and of the low-order harmonics (n=3, 5, 7, 9, 11, 13, …), as given by,

$$\mathbf{v}_{\alpha\beta} = \mathbf{v}_{\alpha\beta}^{1} + \mathbf{v}_{\alpha\beta}^{3} + \mathbf{v}_{\alpha\beta}^{5} + \ldots \quad \Leftrightarrow$$
$$\mathbf{v}_{\alpha\beta} = V^{1}\begin{bmatrix} \cos(\omega t + \theta_1) \\ \cos(\omega(t - \frac{\mathrm{T}}{4}) + \theta_1) \end{bmatrix} + \sum_{n=3,5,7,\ldots} V^{n}\begin{bmatrix} \cos(n\omega t + \theta_n) \\ \cos(n\omega(t - \frac{\mathrm{T}}{4}) + \theta_n) \end{bmatrix} \tag{5.27}$$

where V^n and θ_n represent the amplitude and the initial phase angle of each voltage component respectively and ω is the angular grid frequency. Based on the structure of the QSG and by using basic trigonometric identities, (5.27) can be analyzed into,

$$\mathbf{v}_{\alpha\beta} = \sum_{n=1,3,5,7,\ldots} \mathbf{v}_{\alpha\beta}^{n} = \sum_{n=1,3,5,7,\ldots} V^{n}\begin{bmatrix} \cos(\mathrm{sgn}(n)\cdot n\omega t + \theta_n) \\ \sin\left(\mathrm{sgn}(n)\cdot n\omega t + \theta_n\right) \end{bmatrix} \tag{5.28}$$

where sgn(n) defines the speed direction of each component and is given by,

$$\mathrm{sgn}(n) = \sin\left(\frac{n\pi}{2}\right) = \begin{cases} +1 & \text{for } n = 1,5,9,13,\ldots \\ -1 & \text{for } n = 3,7,11,\ldots \end{cases} \tag{5.29}$$

It is worth noticing that the sgn(n) is inserted in this analysis due to the QSG-based $\mathbf{v}_{\alpha\beta}$, as explained in Section 5.3.2.

According to (5.28) the direct calculation of each voltage component $\mathbf{v}_{\alpha\beta}^{n}$ is not possible due to the coupling effect among the existing components. However, an accurate estimation especially of the fundamental voltage component $\mathbf{v}_{\alpha\beta}^{1}$ is necessary for the grid synchronization of a grid-tied inverter and thus, a novel decoupling network is proposed

hereafter. The development of the decoupling network requires to express (5.28) in terms of any voltage component $\mathbf{v}_{\alpha\beta}^{n}$ as,

$$\mathbf{v}_{\alpha\beta}^{n} = \mathbf{v}_{\alpha\beta} - \sum_{m\neq n} \mathbf{v}_{\alpha\beta}^{m} \Leftrightarrow \begin{bmatrix} v_{\alpha}^{n} \\ v_{\beta}^{n} \end{bmatrix} = \begin{bmatrix} v_{\alpha} \\ v_{\beta} \end{bmatrix} - \sum_{m\neq n} \begin{bmatrix} v_{\alpha}^{m} \\ v_{\beta}^{m} \end{bmatrix} \tag{5.30}$$

Since the vectors $\mathbf{v}_{\alpha\beta}^{m}$ are unknown, the estimation of the voltage component $\mathbf{v}_{\alpha\beta}^{n}$ by the estimation vector $\mathbf{v}_{\alpha\beta}^{n*}$ is enabled in (5.31) by replacing the unknown vectors $\mathbf{v}_{\alpha\beta}^{m}$ of (5.30) with the corresponding filtered estimation vectors $\bar{\mathbf{v}}_{\alpha\beta}^{m*}$.

$$\mathbf{v}_{\alpha\beta}^{n*} = \mathbf{v}_{\alpha\beta} - \sum_{m\neq n} \bar{\mathbf{v}}_{\alpha\beta}^{m*} \tag{5.31}$$

The filtered estimation vectors $\bar{\mathbf{v}}_{\alpha\beta}^{m*}$ are produced by filtering out the corresponding estimation vector $\mathbf{v}_{\alpha\beta}^{m*}$ in order to eliminate any remaining oscillations after subtracting the coupling effect caused by the existence of other harmonic components. Since each estimation vector $\mathbf{v}_{\alpha\beta}^{m*}$ rotates with a different sgn(m)·m·ω, an equivalent filtering cannot be directly achieved for each component. Therefore, for an equivalent filtering of all the voltage components, it is first necessary to express each estimated vector $\mathbf{v}_{\alpha\beta}^{m*}$ into a corresponding synchronous reference frame rotating with a sgn(m)·m·ω speed ($dq^{\text{sgn}(m)m}$-frame) by using Park's transformation theory of Appendix A.4. Thus, the m component of the estimation voltage vector expressed in the corresponding $dq^{\text{sgn}(m)m}$-frame ($\mathbf{v}_{dq^{\text{sgn}(m)m}}^{m*}$) is given by,

$$\mathbf{v}_{dq^{\text{sgn}(m)m}}^{m*} = \begin{bmatrix} v_{d\,\text{sgn}(m)\cdot m} \\ v_{q\,\text{sgn}(m)\cdot m} \end{bmatrix} = \left[T_{dq^{\text{sgn}(m)\cdot m}} \right] \mathbf{v}_{\alpha\beta}^{m*} \tag{5.32}$$

$$\text{where } \left[T_{dq^{\text{sgn}(m)\cdot m}} \right] = \begin{bmatrix} \cos(\text{sgn}(m)m\omega t) & \sin(\text{sgn}(m)m\omega t) \\ -\sin(\text{sgn}(m)m\omega t) & \cos(\text{sgn}(m)m\omega t) \end{bmatrix}$$

It should be noted that each vector $\mathbf{v}_{dq^{\text{sgn}(m)m}}^{m*}$ is actually described as a non-rotating vector, since both the $dq^{\text{sgn}(m)m}$-frame and the m voltage component rotate with the same sgn(m)·m·ω angular speed. Therefore, an equivalent filtering can now be achieved since all the voltage components can be expressed as non-rotating vectors according to (5.32). Therefore, the filtered estimation vector $\bar{\mathbf{v}}_{dq^{\text{sgn}(m)m}}^{m*}$ expressed in a corresponding $dq^{\text{sgn}(m)m}$-frame is generated by filtering the corresponding estimation vector component $\mathbf{v}_{dq^{\text{sgn}(m)m}}^{m*}$ according to,

$$\bar{\mathbf{v}}_{dq^{\mathrm{sgn}(m)m}}^{m*} = \begin{bmatrix} \bar{v}_{d\ sgn(m)m}^{m*} \\ \bar{v}_{q\ sgn(m)m}^{m*} \end{bmatrix} = \left[F(s)\right]\mathbf{v}_{dq^{\mathrm{sgn}(m)m}}^{m*} \tag{5.33}$$

$$\text{where} \quad \left[F(s)\right] = \frac{\omega_{f2}}{s+\omega_{f2}}\begin{bmatrix} 1 & 0 \\ 0 & 1 \end{bmatrix}$$

and ω_{f2} is the cut-off frequency of the low-pass filter [$F(s)$] and should be set to $2\pi 50/3$ rad/s according to the theoretical analysis that is presented in Section 5.4.4. Finally, the filtered estimation vector $\bar{\mathbf{v}}_{\alpha\beta}^{m*}$, required by (5.31) to develop the decoupling network, can be calculated based on Park's transformations and is given by,

$$\bar{\mathbf{v}}_{\alpha\beta}^{m*} = \begin{bmatrix} \bar{v}_{\alpha}^{m*} \\ \bar{v}_{\beta}^{m*} \end{bmatrix} = \left[T_{dq^{-\mathrm{sgn}(m)\cdot m}}\right]\bar{\mathbf{v}}_{dq^{\mathrm{sgn}(m)m}}^{m*} \tag{5.34}$$

Submitting (5.32) to (5.33) and then (5.33) to (5.34), (5.31) can be re-written as,

$$\mathbf{v}_{\alpha\beta}^{n*} = \mathbf{v}_{\alpha\beta} - \sum_{m\neq n}\left[T_{dq^{-\mathrm{sgn}(m)m}}\right]\left[F(s)\right]\left[T_{dq^{\mathrm{sgn}(m)m}}\right]\mathbf{v}_{\alpha\beta}^{m*} \tag{5.35}$$

Finally, (5.35) is the cornerstone of the proposed decoupling network (improved MHDC) as shown in Fig. 5.8. Hence, the multiple use of (11) for n=1, 3, 5, 7, … in a cross feed-back decoupling network enables a dynamic estimation of each voltage component $\mathbf{v}_{\alpha\beta}^{n*}$. It should be pointed out that the cross feed-back network is required to dynamically eliminate the coupling effect between the fundamental component and all the significant low-order harmonic components. It is important to mention that the improved MHDC can achieve an exact equivalent performance with the initial MHDC of Section 5.3.2, but the complexity of the improved MHDC is decreased, as it is proved in Section 5.4.4.

5.4.3 Development of the frequency adaptive MHDC-PLL

The proposed frequency adaptive MHDC-PLL can now be developed based on the adaptive QSG (as described in Section 5.4.1), the improved MHDC (as described in Section 5.4.2) and the *dq*-PLL algorithm of [59] for estimating the phase angle of the fundamental component of the grid voltage as shown in Fig. 5.8. The new frequency adaptive MHDC-PLL can achieve a fast and accurate synchronization under any grid disturbance and under highly harmonic distortion. The complexity of the synchronization has been significantly decreased compared to the MHDC-PLL of Section 5.3, as it will be proved in Section 5.4.4.

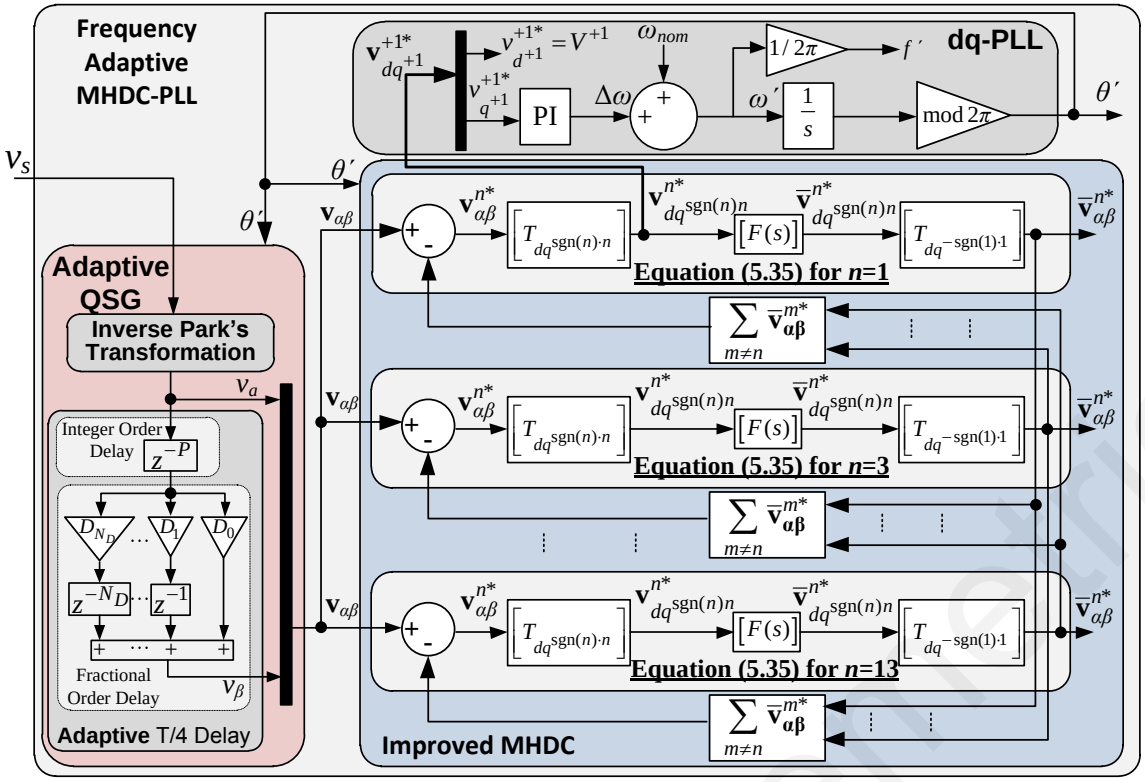

Fig. 5.8. The structure of the proposed frequency adaptive MHDC-PLL.

The adaptive QSG is based on the IPT method in order to filter out the high-order harmonics and then the proposed frequency adaptive T/4 delay unit is used to generate the voltage vector $\mathbf{v}_{\alpha\beta}$. The proposed frequency adaptive method overcomes the inaccuracies under non-nominal frequencies caused by the initial QSG of Section 5.3.1 and thus, an accurate operation can be achieved under any grid frequency.

Then, the $\mathbf{v}_{\alpha\beta}$ is fed to the proposed improved MHDC as shown in Fig. 5.8, in order to dynamically cancel out the effect of the low-order harmonics with minimum computational burden. For a proper design of the improved MHDC, it is first necessary to define the number of harmonic-orders that are considered and eliminated by the decoupling network. An investigation is performed on the accuracy of the frequency adaptive MHDC-PLL under the worst-case voltage harmonic distortion according to EN50160 standards (see HC3 on TABLE 5.3). The investigation shows that a very accurate synchronization (error in phase angle estimation $\theta_{error}=\theta_{grid}-\theta'$ less than 0.00035 rad) can be achieved, when the improved MHDC is designed for N=7, considering the fundamental (n=1) and the effect of the six most significant harmonic components (n=3, 5, 7, 9, 11, 13) in single-phase systems. The effect of the higher order harmonics is minimized due to the second-order band-pass filtering characteristics of IPT as mentioned in Section 5.3.1. Therefore, the decoupling network of the frequency adaptive MHDC-PLL is designed for N=7 as

TABLE 5.2: DESIGN PARAMETERS OF FREQUENCY ADAPTIVE MHDC-PLL

IPT unit	Filtering parameter → $\omega_{f1}=2\pi 50\sqrt{2}$ rad/s
Adaptive T/4 delay unit	*Langrange* interpolation order → $N_D=3$
Improved MHDC	Multiple use of (11) for n=1, 3, 5, 7 , 9, 11, 13 Filtering parameter → $\omega_{f2}=2\pi 50/3$ rad/s
dq-PLL	Tuning parameters → $k_P=92$, $T_I=0.000235$

shown in Fig. 5.8 in order to achieve an accurate synchronization under any harmonic distorted grid conditions. Thus, the fast and accurate estimation of the fundamental voltage component $\mathbf{v}_{dq^{+1}}^{1*}$ expressed in the dq^{+1}-frame is enabled by the improved MHDC. This estimation voltage vector is free of any low- and high-order harmonics and therefore, the conventional dq-PLL algorithm of [59] can be used to accurately estimate the phase angle and the amplitude of the grid voltage, as demonstrated in Fig. 5.8.

The conventional dq-PLL system [59] is a closed-loop synchronization system, which aims to force the per unit $v_{q^{+1}}^{1*}$ to track zero. The synchronization algorithm is based on a Proportional-Integral (PI) controller, whose transfer function is given by $k_p+1/(T_i \cdot s)$, with k_p and T_i being the controller parameters. Therefore, based on a linearized small signal analysis, the transfer function of the PLL is given by the second order transfer function of (5.36), where it is obvious that the tuning parameters (k_p and T_i) can affect the response of the synchronization unit.

$$\frac{\theta'}{\theta}=\frac{k_p s+1/T_i}{s^2+k_p s+1/T_i} \tag{5.36}$$

$$\text{where: } k_p=\frac{9.2}{ST} \text{ and } T_i=0.047\zeta^2 ST^2$$

According to the theory of Appendix B, for an optimally damped response of the PLL, the damping coefficient ζ should be set to $1/\sqrt{2}$; the Settling Time (ST) has been set to 100 ms for the purposes of this work. Hence, the tuning parameters k_p and T_i of the frequency adaptive MHDC-PLL have been set to 92 and $2.35 \cdot 10^{-4}$, respectively.

The proposed frequency adaptive MHDC-PLL can achieve a fast and accurate response under any harmonic distortion and under any grid faults and the required processing time of the proposed synchronization algorithm is significantly less compared to the original MHDC of Section 5.3.2, as it will be demonstrated in Section 5.4.4 and Section 5.4.5. All the design parameters for developing the proposed frequency adaptive MHDC-PLL are summarized in TABLE 5.2.

5.4.4 Performance theoretical analysis and complexity evaluation

This Section aims to prove that the proposed frequency adaptive MHDC-PLL (based on the improved MHDC) and the MHDC-PLL (based on MHDC of Section 5.3.2) can achieve an equivalent advanced performance under any harmonic distorted grid voltage and that the proposed improved MHDC (Section 5.4.2) requires significantly less processing time in each control loop compared to the MHDC of Section 5.3.2.

Performance Theoretical Analysis

The proposed improved MHDC, as shown in Fig. 5.8, is based on the multiple use of (5.35) for accurately estimating each voltage component. By analyzing (5.35), it can be proved that the improved MHDC can achieve an exact equivalent response with the original MHDC proposed in Section 5.3.2. Thus, by multiplying both sides of (5.35) with the transformation matrix $\left[T_{dq^{\mathrm{sgn}(n)n}}\right]$ and applying Park's transformation theory, (5.35) can be equivalently re-written as,

$$\mathbf{v}_{dq^{\mathrm{sgn}(n)n}}^{n*} = \left[T_{dq^{\mathrm{sgn}(n)n}}\right]\mathbf{v}_{\alpha\beta} - \sum_{m\neq n}\left[T_{dq^{\mathrm{sgn}(n)n}}\right]\left[T_{dq^{-\mathrm{sgn}(m)m}}\right]\left[F(s)\right]\mathbf{v}_{dq^{\mathrm{sgn}(m)m}}^{m*} \tag{5.37}$$

Then, by using (5.33), and by merging the transformation matrices, (5.37) can be re-written as (5.38), which is the cornerstone equation of MHDC as given by (5.20) as well as in Section 5.3.2.

$$\mathbf{v}_{dq^{n\cdot\mathrm{sgn}(n)}}^{n*} = T_{dq^{n\cdot\mathrm{sgn}(n)}}\cdot\mathbf{v}_{\alpha\beta} - \sum_{m\neq n}\left\{T_{dq^{n\cdot\mathrm{sgn}(n)-m\cdot\mathrm{sgn}(m)}}\cdot\bar{\mathbf{v}}_{dq^{m\cdot\mathrm{sgn}(m)}}^{*(m)}\right\} \tag{5.38}$$

Since (5.35) can be re-written in the form of (5.38) and (5.20) as well, it is proven that the MHDC of Section 5.3.2 and the improved MHDC of the frequency adaptive MHDC-PLL can achieve an exact equivalent response in terms of estimating the voltage vector of the fundamental voltage component. Hence, the following theoretical analysis for the performance of the proposed decoupling cell presented in this Chapter is valid for both the MHDC and the improved MHDC of Section 5.3.2 and 5.4.2 respectively.

An extensive theoretical analysis is required to define the transfer function, the expected response, and the optimal design parameters of the MHDC and the improved MHDC proposed in this Chapter. The ratio $\left(\mathbf{v}_{\alpha\beta}^{+1*}/\mathbf{v}_{\alpha\beta}\right)$ is considered as the transfer function of both decoupling cells and the output vector $\mathbf{v}_{\alpha\beta}^{+1*}$ or its equivalent vector

expressed in dq^{+1}-frame ($\mathbf{v}_{dq^{+1}}^{+1*}$) can be fed into any conventional PLL to accurately estimate the phase angle of the fundamental voltage. Since the two decoupling cells are exact equivalents, the theoretical analysis will be presented only for the case of the improved MHDC. Therefore, by replacing n=+1 into (5.35) and according to the block diagram of the improved MHDC as presented in Fig. 5.8, the required estimated vector $\mathbf{v}_{\alpha\beta}^{+1*}$ for enabling the grid synchronization can be expressed as,

$$\mathbf{v}_{\alpha\beta}^{+1*} = \mathbf{v}_{\alpha\beta} - \sum_{m\neq+1}\left[T_{dq^{-\mathrm{sgn}(m)m}}\right]\left[F(s)\right]\left[T_{dq^{\mathrm{sgn}(m)m}}\right]\mathbf{v}_{\alpha\beta}^{m*} \tag{5.39}$$

An expansion of (5.39) for the odd harmonics up to order thirteen is given by,

$$\mathbf{v}_{\alpha\beta}^{+1*} = \mathbf{v}_{\alpha\beta} - \begin{pmatrix} \left[T_{dq^{+3}}\right]\left[F(s)\right]\left[T_{dq^{-3}}\right]\mathbf{v}_{\alpha\beta}^{+3*} + \left[T_{dq^{-5}}\right]\left[F(s)\right]\left[T_{dq^{+5}}\right]\mathbf{v}_{\alpha\beta}^{+5*} + \\ \left[T_{dq^{+7}}\right]\left[F(s)\right]\left[T_{dq^{-7}}\right]\mathbf{v}_{\alpha\beta}^{+7*} + \left[T_{dq^{-9}}\right]\left[F(s)\right]\left[T_{dq^{+9}}\right]\mathbf{v}_{\alpha\beta}^{+9*} + \\ \left[T_{dq^{+11}}\right]\left[F(s)\right]\left[T_{dq^{-11}}\right]\mathbf{v}_{\alpha\beta}^{+11} + \left[T_{dq^{-13}}\right]\left[F(s)\right]\left[T_{dq^{+13}}\right]\mathbf{v}_{\alpha\beta}^{+13*} \end{pmatrix} \tag{5.40}$$

Now, for extracting the transfer function of the improved MHDC $\left(\mathbf{v}_{\alpha\beta}^{+1*}/\mathbf{v}_{\alpha\beta}\right)$, it is necessary to express (5.40) only in terms of $\mathbf{v}_{\alpha\beta}^{+1*}$ and $\mathbf{v}_{\alpha\beta}$. Thus, each vector $\mathbf{v}_{\alpha\beta}^{m*}$ of (5.40), where $m \neq +1$, should be replaced by using (5.35). Therefore, according to the recursive character of the improved MHDC, (5.40) can be re-written as,

$$\mathbf{v}_{\alpha\beta}^{+1*} = \mathbf{v}_{\alpha\beta} - \begin{pmatrix} \left[T_{dq^{+3}}\right]\left[F(s)\right]\left[T_{dq^{-3}}\right]\left(\mathbf{v}_{\alpha\beta} - \left[T_{dq^{-1}}\right]\left[F(s)\right]\left[T_{dq^{+1}}\right]\mathbf{v}_{\alpha\beta}^{+1*} - \sum_{m\neq+1,+3}\bar{\mathbf{v}}_{\alpha\beta}^{m*}\right) + \\ \left[T_{dq^{-5}}\right]\left[F(s)\right]\left[T_{dq^{+5}}\right]\left(\mathbf{v}_{\alpha\beta} - \left[T_{dq^{-1}}\right]\left[F(s)\right]\left[T_{dq^{+1}}\right]\mathbf{v}_{\alpha\beta}^{+1*} - \sum_{m\neq+1,+5}\bar{\mathbf{v}}_{\alpha\beta}^{m*}\right) + \\ \left[T_{dq^{+7}}\right]\left[F(s)\right]\left[T_{dq^{-7}}\right]\left(\mathbf{v}_{\alpha\beta} - \left[T_{dq^{-1}}\right]\left[F(s)\right]\left[T_{dq^{+1}}\right]\mathbf{v}_{\alpha\beta}^{+1*} - \sum_{m\neq+1,+7}\bar{\mathbf{v}}_{\alpha\beta}^{m*}\right) + \\ + \quad \cdots \quad + \quad \ldots \quad + \\ \left[T_{dq^{-13}}\right]\left[F(s)\right]\left[T_{dq^{+13}}\right]\left(\mathbf{v}_{\alpha\beta} - \left[T_{dq^{-1}}\right]\left[F(s)\right]\left[T_{dq^{+1}}\right]\mathbf{v}_{\alpha\beta}^{+1*} - \sum_{m\neq+1,+13}\bar{\mathbf{v}}_{\alpha\beta}^{m*}\right) \\ \end{pmatrix} \tag{5.41}$$

Such an analysis should be recursively continued; however, due to the cross-coupling effect between the voltage component is impossible to express (5.41) in terms only of vectors $\mathbf{v}_{\alpha\beta}^{+1*}$ and $\mathbf{v}_{\alpha\beta}$. Thus, to enable the extraction of the transfer function of the improved MHDC and without affecting the overall theoretical analysis, all the vectors which are filtered by $[F(s)]$ for three or more times can be ignored in the further analysis due to their slower dynamics. The vectors that are filtered for three or more times are actually the vectors within the summation series of (5.41). Hence, by ignoring this summation series, (5.41) can be simplified into (5.42)

$$\mathbf{v}_{\alpha\beta}^{+1*} = \mathbf{v}_{\alpha\beta} - \left(\begin{array}{l} \left[T_{dq^{+3}}\right]\left[F(s)\right]\left[T_{dq^{-3}}\right]\left(\mathbf{v}_{\alpha\beta} - \left[T_{dq^{-1}}\right]\left[F(s)\right]\left[T_{dq^{+1}}\right]\mathbf{v}_{\alpha\beta}^{+1*}\right) + \\ \left[T_{dq^{-5}}\right]\left[F(s)\right]\left[T_{dq^{+5}}\right]\left(\mathbf{v}_{\alpha\beta} - \left[T_{dq^{-1}}\right]\left[F(s)\right]\left[T_{dq^{+1}}\right]\mathbf{v}_{\alpha\beta}^{+1*}\right) + \\ \left[T_{dq^{+7}}\right]\left[F(s)\right]\left[T_{dq^{-7}}\right]\left(\mathbf{v}_{\alpha\beta} - \left[T_{dq^{-1}}\right]\left[F(s)\right]\left[T_{dq^{+1}}\right]\mathbf{v}_{\alpha\beta}^{+1*}\right) + \\ \left[T_{dq^{-9}}\right]\left[F(s)\right]\left[T_{dq^{+9}}\right]\left(\mathbf{v}_{\alpha\beta} - \left[T_{dq^{-1}}\right]\left[F(s)\right]\left[T_{dq^{+1}}\right]\mathbf{v}_{\alpha\beta}^{+1*}\right) + \\ \left[T_{dq^{+11}}\right]\left[F(s)\right]\left[T_{dq^{-11}}\right]\left(\mathbf{v}_{\alpha\beta} - \left[T_{dq^{-1}}\right]\left[F(s)\right]\left[T_{dq^{+1}}\right]\mathbf{v}_{\alpha\beta}^{+1*}\right) + \\ \left[T_{dq^{-13}}\right]\left[F(s)\right]\left[T_{dq^{+13}}\right]\left(\mathbf{v}_{\alpha\beta} - \left[T_{dq^{-1}}\right]\left[F(s)\right]\left[T_{dq^{+1}}\right]\mathbf{v}_{\alpha\beta}^{+1*}\right) \end{array} \right) \tag{5.42}$$

Now, the transfer function of $T_{dq^{-h}} \cdot [F(s)] \cdot T_{dq^{+h}}$, where h is the corresponding harmonic order, can be defined in the complex-frequency domain as shown in (5.43), by using a lengthy mathematical analysis (similar to the one presented in Section 5.3.1). This analysis is based on the Park's Transformations in terms of the Euler formula as defined in (5.5), on the Laplace property for frequency shifting ($e^{at} = F(s-a)$), and on the fact that v_b=-j·v_a as shown in Section 5.3.1 and 5.4.1. Therefore, the analysis concludes into the complex first-order transfer function as given by,

$$TFT_h = T_{dq^{-h}} \cdot [F(s)] \cdot T_{dq^{+h}} = \begin{cases} \dfrac{\omega_{f2}}{s + (\omega_{f2} + jh\omega')} & for\ h = -3, -7 \\ \dfrac{\omega_{f2}}{s + (\omega_{f2} - jh\omega')} & for\ h = 1, 5, 9 \end{cases} \tag{5.43}$$

Thus, substituting $TFT_h = T_{dq^{-h}} \cdot [F(s)] \cdot T_{dq^{+h}}$ of (5.43) into (5.42) yields,

$$\mathbf{v}_{\alpha\beta}^{+1*} = \mathbf{v}_{\alpha\beta} - \left(TFT_{-3} + TFT_{+5} + TFT_{-7} + TFT_{+9}\right)\left(\mathbf{v}_{\alpha\beta} - TFT_{+1} \cdot \mathbf{v}_{\alpha\beta}^{+1*}\right) \tag{5.44}$$

Finally, the transfer function of the improved MHDC of Section 5.4.2 and the initial MHDC of Section 5.3.2 can be derived as,

$$\frac{\mathbf{v}_{\alpha\beta}^{+1*}}{\mathbf{v}_{\alpha\beta}} = \frac{1-\left(TFT_{-3}+TFT_{+5}+TFT_{-7}+TFT_{+9}+TFT_{-11}+TFT_{+13}\right)}{1+TFT_{+1}\cdot\left(TFT_{-3}+TFT_{+5}+TFT_{-7}+TFT_{+9}+TFT_{-11}+TFT_{+13}\right)} \tag{5.45}$$

If the corresponding TFT_h terms of (5.43) are substituted according to (5.45), then the fifteenth-order complex transfer function of the proposed improved MHDC can be extracted. The $v_{\alpha\beta}$ is the input voltage vector of the MHDC (as it is calculated from the QSG) and $\mathbf{v}_{\alpha\beta}^{+1*} = T_{dq^{-1}} \cdot \mathbf{v}_{dq^{+1}}^{+1*}$ is the equivalent output of the MHDC expressed in the stationary reference frame.

For developing the proposed MHDC-PLL of Section 5.3, the QSG proposed in Section 5.3.1 is connected in series with the proposed MHDC of 5.3.2 in order to dynamically extract the fundamental component of the grid voltage as shown in Fig. 5.4 and then a simple PLL algorithm will be used in order to extract the phase angle. Similarly, for developing the proposed frequency adaptive MHDC-PLL of Section 5.4, the frequency adaptive QSG of 5.4.1 is connected in series with the improved MHDC of 5.4.2. It is to be noted that both QSG and frequency adaptive QSG present the same transfer function as given in (5.8), when the grid frequency is equal to its nominal value. Thus, the transfer functions of MHDC-PLL and of the frequency adaptive MHDC-PLL QSG are given by (5.46), by multiplying the transfer function of (5.8) and (5.45).

$$\left(\frac{v_\alpha^{+1*}}{v_s}\right) = \left(\frac{v_a}{v_s}\right)\left(\frac{\mathbf{v}_{\alpha\beta}^{+1*}}{\mathbf{v}_{\alpha\beta}}\right) \quad \text{and} \quad \left(\frac{v_\beta^{+1*}}{v_s}\right) = -j\cdot v_\alpha^{+1*} = -j\cdot v_a\left(\frac{\mathbf{v}_{\alpha\beta}^{+1*}}{\mathbf{v}_{\alpha\beta}}\right) \tag{5.46}$$

Therefore, in order to investigate the response of the proposed PLL and also to design the parameter ω_{f2} of the proposed MHDC and the improved MHDC, the Bode diagrams of the QSG (v_a/v_s) of (5.8), the proposed improved MHDC $\left(\mathbf{v}_{\alpha\beta}^{+1*}/\mathbf{v}_{\alpha\beta}\right)$ of (5.45), and the series combination of the two (v_α^{+1*}/v_s) of (5.46) are presented in Fig. 5.9. The corresponding results for $\left(v_\beta^{+1*}/v_s\right)$ are similar with a 90^o-delay on the output signal as shown in (5.46). The results of Fig. 5.9 verify that the proposed MHDC and the improved MHDC according to (5.45) does not affect the dynamic estimation of the amplitude and the phase angle of the fundamental voltage component at 50 Hz. Furthermore, the MHDC and the improved MHDC can effectively eliminate the low-order harmonic components considered in the decoupling network, but it cannot affect the high order harmonics. The third, seventh and eleventh harmonics are presented as negative frequency harmonics in

the Bode diagram according to the sgn(n) induced construction of the voltage vector $\mathbf{v}_{\alpha\beta}$ as explained in Section 5.4.2. The Bode diagram regarding the QSG is actually a band-pass second-order filter according to (5.8) as mentioned in Section 5.3.1, which can eliminate the effect of the zero- and high-order harmonics. The series combination of the proposed QSG and MHDC (QSG+MHDC) represent the response of the proposed PLL according to (5.46). As it can be observed in the Bode diagram, the QSG+MHDC inherits the benefits of both units and thus, the desired accurate response can be achieved since the low-order harmonics are completely eliminated by the MHDC and the zero- and high-order harmonics are minimized by the QSG. Furthermore, a dynamic response can be guaranteed since the MHDC decouples the effect of the low-order harmonics without affecting the dynamics of the estimation. Hence, the two PLLs that have been proposed within this chapter (MHDC-PLL and frequency adaptive MHDC-PLL) can achieve a fast dynamic response under grid disturbances and present a great robustness against harmonic distortion.

The design parameter ω_{f2} can affect the quality factor of the filter, the oscillation damping, and the time performance of the proposed MHDC and the improved MHDC. Therefore, an investigation through simulation results shows that a reasonable trade-off can be achieved by setting $\omega_{f2} = \omega_n/3$.where ω_n is the nominal angular frequency of the grid at $2\pi\cdot50$ rad/s. For $\omega_{f\,2} < \omega'/3$ the response of the decoupling networks can present some unwanted oscillations and for $\omega_{f\,2} > \omega'/3$ the response of the decoupling networks is overdamped.

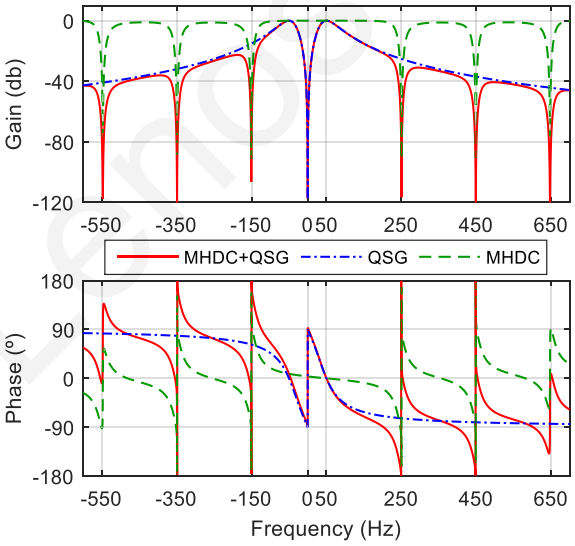

Fig. 5.9. Bode diagram of the proposed QSG, MHDC or improved MHDC, and the series combination of the two.

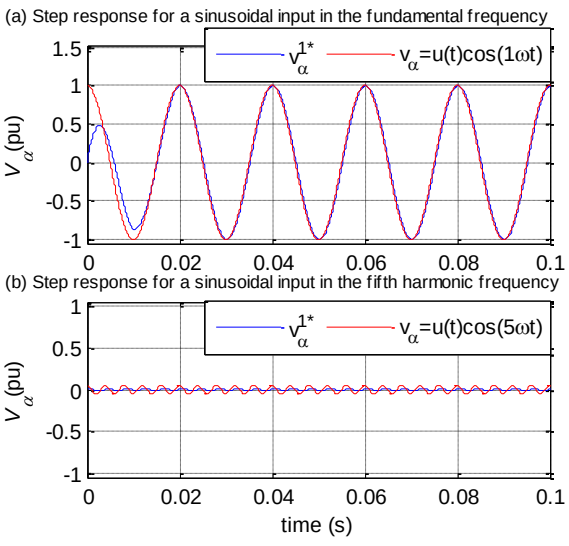

Fig. 5.10. The step response of the series combination of the QSG and the MHDC.

The step response regarding the estimation of the input voltage according to the proposed MHDC-PLL and the frequency adaptive MHDC-PLL (QSG + MHDC) is presented in Fig. 5.10. The response of the series combination of the QSG and the MHDC is presented in Fig. 5.10(a) for a step sinusoidal input in the fundamental frequency. The results verify the fast dynamic response of the proposed PLL since the input voltage is estimated with a settling time less than 0.014 s. Fig. 5.10(b) presents the step response for a sinusoidal step input with a 5% amplitude in the frequency of the fifth harmonic. The results show an immediate and complete elimination of the harmonic.

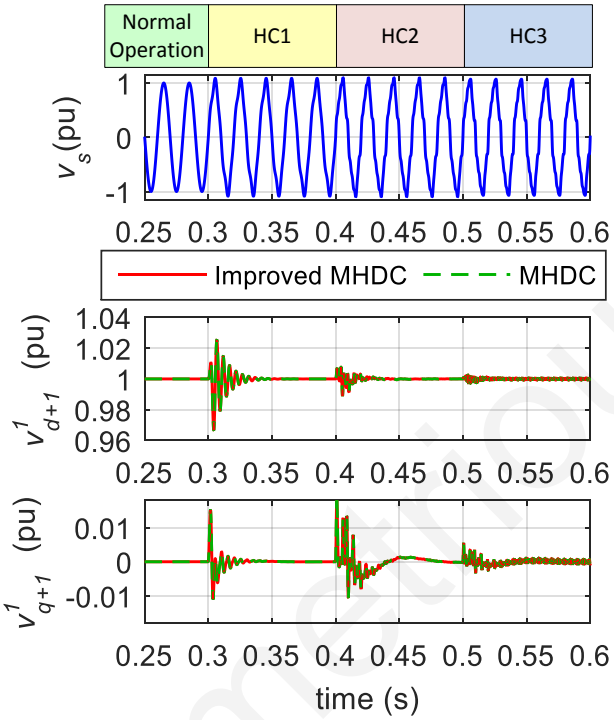

Fig. 5.11. Comparison of the performance of the proposed improved MHDC of Section 5.4.2 and of the proposed MHDC of Section 5.3.2.

TABLE 5.3: DEFINITION OF SEVERAL HARMONIC CONDITIONS (HC)

Normal Operation	Pure sinusoidal grid voltage
HC1	$\|V_3\|$=5% and $\|V_5\|$=6%
HC2	$\|V_3\|$=5%, $\|V_5\|$=6%, $\|V_7\|$=5%, $\|V_9\|$=1.5%, $\|V_{11}\|$=3.5%
HC3	Worst case harmonic distortion according to EN50160: $\|V_3\|$=5%, $\|V_5\|$=6%, $\|V_7\|$=5%, $\|V_9\|$=1.5%, $\|V_{11}\|$=3.5%, $\|V_{13}\|$=3%, $\|V_{15}\|$=0.5%, $\|V_{17}\|$=2%, $\|V_{19}\|$=1.5%, $\|V_{h>20}\|$=0.3%

Further, simulation based investigation has been performed in MATLAB/Simulink (as presented in Fig. 5.11) about the performance of the two decoupling networks under several Harmonic Conditions (HC), where HC1, HC2 and HC3 are defined in TABLE 5.3. It is to be noted that both decoupling networks have been designed to consider the odd harmonics up to order thirteen. Both the MHDC of Section 5.3.2 and the improved MHDC Section 5.4.2 present an exact equivalent response as theoretically proved in this Section and moreover, both decoupling networks present a fast dynamic response under grid disturbances and a great immunity against harmonics as has been already proved according to the theoretical analysis of the MHDC and improved MHDC. An investigation, presented in Fig. 5.11, shows that both the MHDC-PLL and the frequency improved MHDC-PLL can achieve a very accurate response under the worst-case harmonic distortion (HC3). Therefore, both decoupling networks enable the fast and accurate estimation of the vector $\mathbf{v}^{*1}_{dq+1}$ under any grid conditions, which is used for the grid synchronization of a single-phase inverter.

Complexity assessment

Although the two decoupling networks present an equivalent response, the improved MHDC proposed in Section 5.4.2 requires a significantly less processing time compared to the MHDC of Section 5.3.2, as it is analyzed below. For a fair complexity analysis, both decoupling networks need to be designed for N=7, to consider the fundamental component (n=1) and the effect of the six most significant harmonic components (n=3, 5, 7, 9, 11, 13). It is to be noted that the design of decoupling networks for N=7 is necessary to enable the synchronization methods to achieve a very accurate response under the worst-case harmonic distortion as mentioned in Section 5.4.3. Therefore, the process of the MHDC of Section 5.3.2 for N=7 requires the repeated processing of (5.20) for seven times. As a consequence, in each control step the decoupling network should process N multi-subtractions $\left(\mathbf{v}_{dq^{\mathrm{sgn}(n)n}} - \sum_{m\neq n} \bar{\mathbf{v}}^{*m}_{dq^{\mathrm{sgn}(m)m}}\right)$, N^2 transformation matrices $\left[T_{dq^{\mathrm{sgn}(n)n}}\right]$, and N low-pass filtering matrices [$F(s)$]. In the case of the improved MHDC of Section 5.4.2, for N=7, (5.35) must be repeated for seven times as well. At each control step the improved MHDC should process N multi-subtractions $\left(\mathbf{v}_{\alpha\beta} - \sum_{m\neq n} \bar{\mathbf{v}}^{*m}_{\alpha\beta}\right)$, 2$N$ transformation matrices, and N low-pass filtering matrices [$F(s)$]. It is obvious that the proposed improved MHDC of Section 5.4.2 requires the processing of 2N=14 transformation matrices instead of N^2=49 matrices of the initial MHDC of Section 5.3.2. The complexity comparison is summarized in TABLE 5.4. A further complexity analysis is also presented in TABLE 5.4, where the two decoupling networks have been analyzed in terms of the required additions, subtractions and multiplications at each control step. It is obvious that the re-formulation of the decoupling cell according to the proposed improved MHDC (Section 5.4.2) can significantly decrease the required processing time of the synchronization algorithm. The decreased complexity of the new improved MHDC is particularly useful, since the real-time operation of the inverter is enabled and a higher sampling rate can be adapted by the inverter controller for an improved performance.

TABLE 5.4: COMPLEXITY COMPARISON OF THE TWO DECOUPLING NETWORKS

Decoupling Network	**Complexity analysis in each control loop**			
	Multi-subtractions	$\left[T_{dq^{\mathrm{sgn}(n)n}}\right]$	**[$F(s)$]**	**Total mathematical operations**
MHDC of Section 5.3.2 (N=7)	N	N^2	N	322 Multiplications 63 Additions 133 Subtractions
Improved MHDC of Section 5.4.2 (N=7)	N	$2N$	N	112 Multiplications 28 Additions 98 Subtractions

TABLE 5.5: PERFORMANCE COMPARISON OF THE TWO PLLS

PLL algorithm	Required Processing Time (%)	Dynamic response under grid faults	Accurate Response under		
			Voltage sag, phase shift	Frequency jump ($f \neq 50$ Hz)	Harmonic distortion
MHDC-PLL	100%	Fast	+	-	+
Freq. Adapt. MHDC-PLL	39%	Fast	+	+	+

Further, an in-depth experimental complexity analysis has been performed, based on a widely used microcontroller, such as the Texas Instrument TMS320F28335 digital signal processor. The investigation demonstrates a significant improvement with regards to the algorithm complexity, since the process of the frequency adaptive MHDC-PLL at each control loop requires 54.6 μs instead of 140 μs in the case of the initial MHDC-PLL of Section 5.3.2. Therefore, the new frequency improved MHDC-PLL requires 61% less processing time compared to the initial MHDC-PLL (proposed in Section 5.3.2), as summarized in TABLE 5.5. It is important to mention that an inverter controller based on the frequency adaptive MHDC-PLL can achieve a sampling rate of 8 kHz on TMS320F28335 (54.6 μs for the synchronization and 63 μs for the rest units of the inverter controller). On the other hand, if the inverter controller is based on the initial MHDC-PLL the sampling rate should be decreased to 4 kHz on TMS320F28335 (140 μs for the synchronization and 63 μs for the rest of the units of the inverter controller). It is to be noted that the reduction of the sampling rate of the controller can negatively affect the accuracy and the performance of the inverter.

5.4.5 Simulation and experimental results

The performance of the proposed frequency adaptive MHDC-PLL has been tested through simulation and experimental results in order to demonstrate the outstanding response of the new synchronization method. Both the simulation and the experimental setup are designed according to the grid interconnected inverter of Fig. 5.1. The simulation based investigation has been performed in MATLAB/Simulink. The experimental setup is based on a TMS320F28335 microcontroller (where the inverter controller has been applied), a Semikron SEMITeach (B6CI) inverter, a California Instrument 2253IX AC power source for emulating the grid, and an Elektro-Automatik EA-PSI 9750-20 DC power supply for emulating the DC bus of a PV system. It is worth mentioning that in both simulation and experimental studies, an 8 kHz sampling rate has been used for the inverter controller.

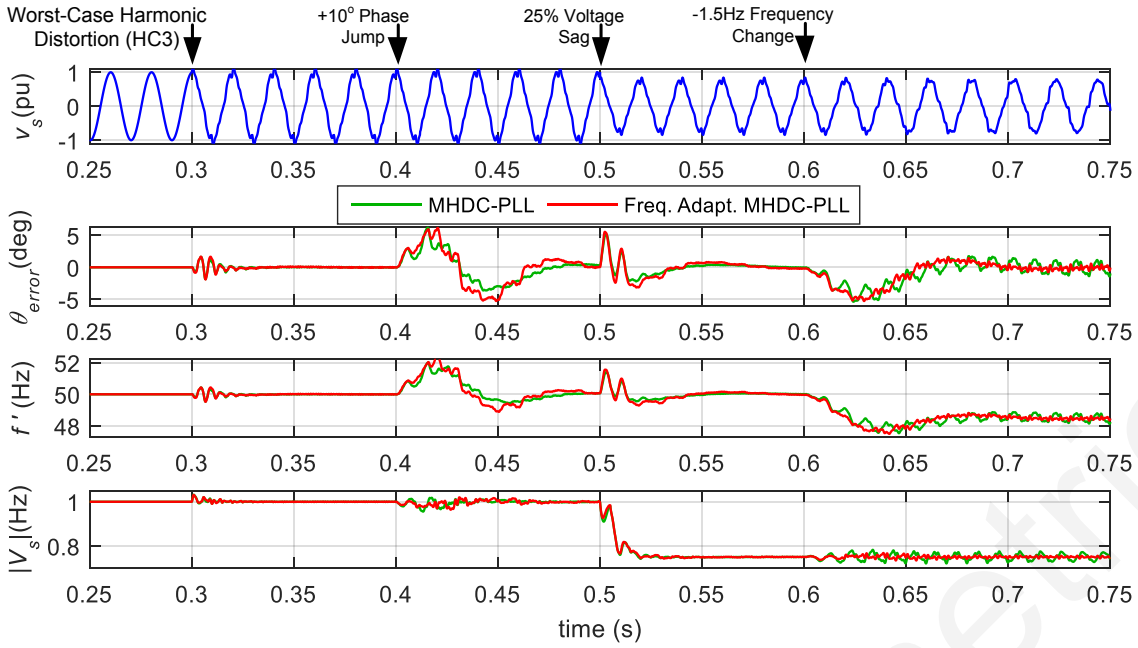

Fig. 5.12. Simulation results for the response of the frequency adaptive MHDC-PLL (Section 5.4) and the MHDC-PLL (Section 5.3) under harmonic distortion, phase jump, voltage sag and frequency change events.

Simulations performed in MATLAB/Simulink show the synchronization response of the proposed frequency adaptive MHDC-PLL, as demonstrated in Fig. 5.12. The results of Fig. 5.12 show the synchronization response of the frequency adaptive MHDC-PLL and the MHDC-PLL of Section 5.3.2 under the worst-case harmonic distortion (HC3 of TABLE 5.3) at 0.3 s, a 10^o phase jump at 0.4 s, a 25% voltage sag at 0.5 s and -1.5 Hz frequency change at 0.6 s. The performance comparison of Fig. 5.12 between the two PLLs, proves that the frequency adaptive implementation of the QSG (Section 5.4.1) enables the accurate synchronization under non-nominal frequencies ($0.6<t<0.75$ s). Therefore, the frequency adaptive MHDC-PLL not only requires a significantly less processing time compared to the initial MHDC-PLL as shown in Section 5.4.4, but additionally, it can also achieve a superior performance under any grid conditions, as summarized in TABLE 5.5. From Fig. 5.12, it is obvious that the new frequency adaptive MHDC-PLL presents a very accurate response (even under the worst-case harmonic distortion for t>0.3 s) and a very fast synchronization under any grid disturbance (e.g., phase jump, voltage sag, frequency change).

The superior synchronization performance of the proposed frequency adaptive MHDC-PLL has also been experimentally verified as shown in Fig. 5.13. The experimental results of Fig. 5.13(a) demonstrate the response of the new synchronization method when the worst-case harmonic distortion (HC3 of TABLE 5.3) occurs at the grid voltage. The experiments show that the proposed PLL can decouple the effect of

harmonics within 10 ms. The initial voltage in Fig. 5.13(b)-(d) has harmonic distortion with the worst-case harmonics (HC3) and then a grid disturbance is applied. According to Fig. 5.13(b), a fast and accurate synchronization is achieved under a 25% voltage sag, which can enable a proper FRT operation of the grid tied inverter. Fig. 5.13(c) demonstrates the operation of the new PLL under a 1 Hz frequency change. It is worth mentioning that the frequency adaptive MHDC-PLL presents a very accurate response under non-nominal frequencies due to the adaptive QSG. Finally, the fast and accurate synchronization response under a 10^{o} phase jump is demonstrated in Fig. 5.13(d). According to the experiments of Fig. 5.13, the proposed frequency adaptive MHDC-PLL can achieve a fast and accurate synchronization under any grid conditions. Such an advanced PLL based synchronization method can be an ideal solution for the synchronization of grid tied inverters.

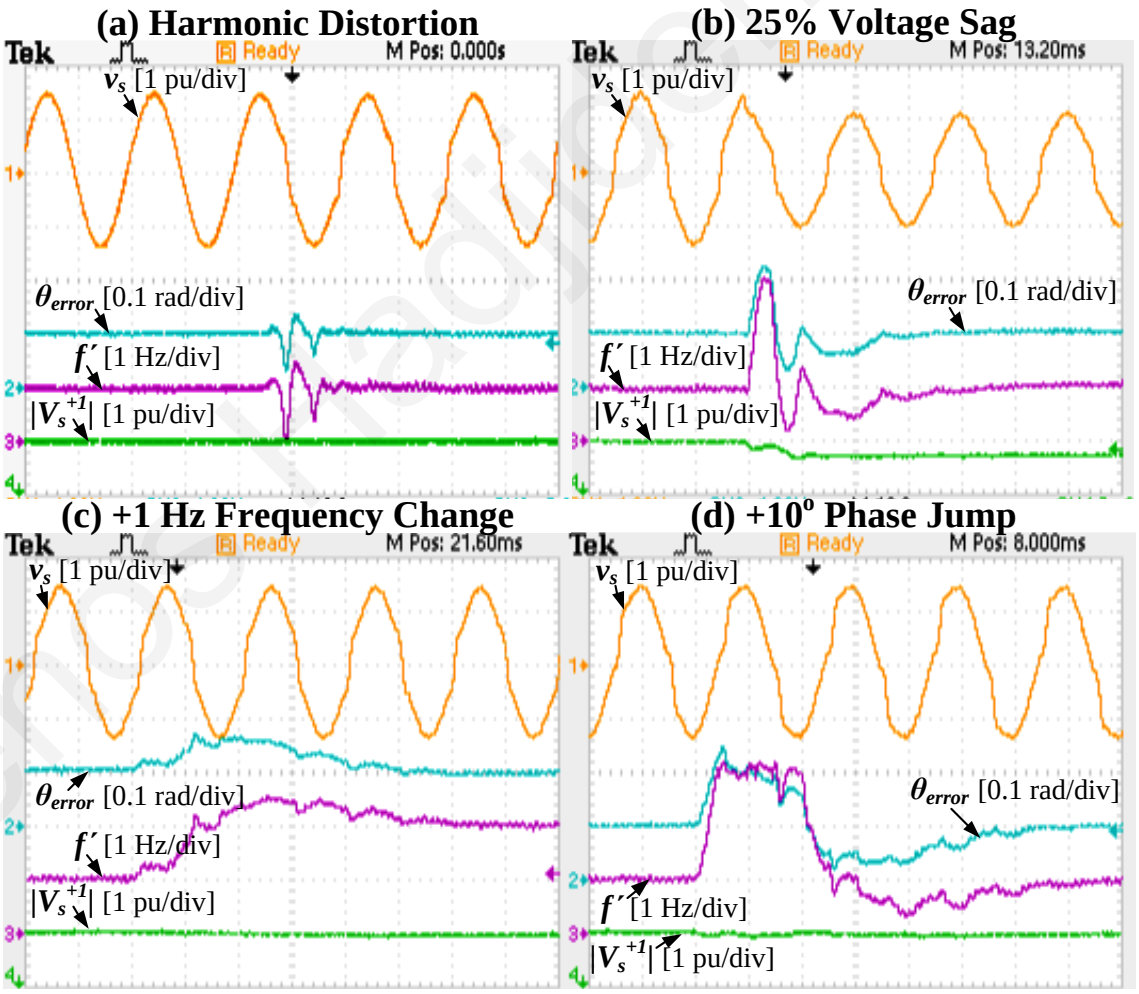

Fig. 5.13. Experimental results for the synchronization response of the frequency adaptive MHDC-PLL under: (a) a harmonic distorted voltage, (b) a 25% voltage sag, (c) a 1 Hz frequency change, and (d) a 10^{o} phase jump. The time division of the results is 10 ms/div.

The synchronization accuracy under harmonic distortion can be very beneficial for the power quality of the grid-tied inverter as discussed in [35] and [36], while the dynamic response of the synchronization, especially under voltage sags, can enable a proper FRT operation of the inverter in order to enhance the stability of the power system under grid faults. A simulation based investigation has been performed here to demonstrate the beneficial effect of a fast and accurate synchronization on the operation of the grid-tied inverter as shown in Fig. 5.14. For this investigation, an open loop PQ controller designed in the *dq*-frame [107] is used to generate the reference currents $\mathbf{I}_{dq}^{*} = [I_d^* \; I_q^*]^T$. Then, a current controller based on a PI controller and also designed in the *dq*-frame [40], [107] is used to regulate the inverter current. It is to be noted that the current controller is enhanced with a harmonic compensation module [40] (Chapter 6) in order to minimize the distortion of the injected current. Further, the PQ controller is enhanced with FRT capabilities [41] in order to provide a proper voltage support under voltage sags, in terms of proper reactive current injection I_Q, according to I_Q=k(v_N-v_s), where k is set to 2 for the purposes of this investigation and v_N is the nominal grid voltage according to [41].

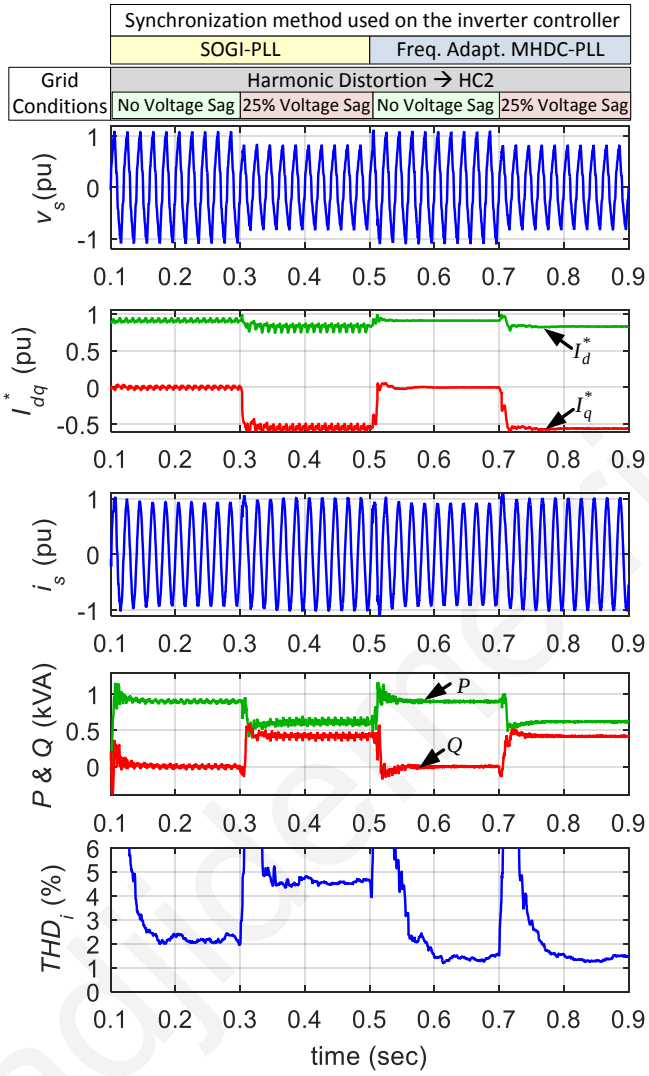

Fig. 5.14. Simulation results for the inverter operation when (a) a SOGI-PLL and (b) a frequency adaptive MHDC-PLL is used for the synchronization of the inverter under harmonic distorted voltage and a voltage sag event.

The simulation results of Fig. 5.14 present the inverter operation when: (a) a SOGI-PLL (t<0.5 s) and (b) when the proposed Frequency Adaptive MHDC-PLL (t>0.5s) are used for the grid synchronization of the inverter. It should be noted that the SOGI-PLL [71], [107]-[110] does not present immunity against harmonic distortion in contrast with the new PLL which presents a great robustness against harmonics. The inverter operation

is demonstrated under highly harmonic distorted grid voltage (HC2 of TABLE 5.3) and under a 25% voltage sag. It is obvious that the accuracy of the new synchronization against harmonics enables the accurate generation of reference currents ($\mathbf{I}_{dq}^{*}$) while the inaccuracies of SOGI-PLL cause undesired oscillations on the reference currents. The oscillations on the reference currents cause an increased total harmonic distortion of the current (THD_i) in the case of the SOGI-PLL, with a THD_i=2.15% when there is no voltage sag and THD_i=4.5% when a voltage sag occurs. On the other hand, the accuracy of the proposed frequency adaptive MHDC-PLL enables an oscillation-free generation of the reference currents and thus, a high quality current injection is achieved, with a THD_i=1.5% under normal operation and voltage sag. Further, the dynamic response of the frequency adaptive MHDC-PLL enables a fast and a proper FRT operation of the inverter, where a reactive power support is properly injected into the grid within 15 ms, for enhancing the stability of the power system. During the FRT operation the injected active power is decreased to maintain the injected current within the inverter limits. Hence, the results of Fig. 5.14 demonstrate that the accurate and fast response of the frequency adaptive MHDC-PLL is particularly beneficial for the operation of the grid tied inverter, in terms of increasing the power quality and of enabling an appropriate dynamic and FRT operation of the inverter.

5.4.6 Conclusions

In this Section, a new synchronization method, named frequency adaptive MHDC-PLL, has been proposed that can achieve a fast dynamic response and presents a great immunity against low- and high-order harmonic distortion. The proposed frequency adaptive MHDC-PLL is the evolution of the initial MHDC-PLL (proposed in Section 5.3) in order to improve the performance of the initial MHDC-PLL in terms of accuracy against frequency change events and to decrease the required processing time of the synchronization. The accurate response of the new PLL under non-nominal frequency is achieved by proposing a novel frequency adaptive QSG while the decrease in complexity is realized by re-formulating the decoupling network and proposing the new improved MHDC. Hence, the new frequency adaptive MHDC-PLL presents fast dynamic response against grid faults, which is beneficially affecting the fault ride through operation of a grid tied PV system. Further, the new synchronization method offers a great immunity against harmonic distortion, which can enhance the power quality of the grid tied inverter. The only limitation of the proposed synchronization method is that its accuracy can be affected by the inter-harmonics (which may occur when more and more power electronic converters

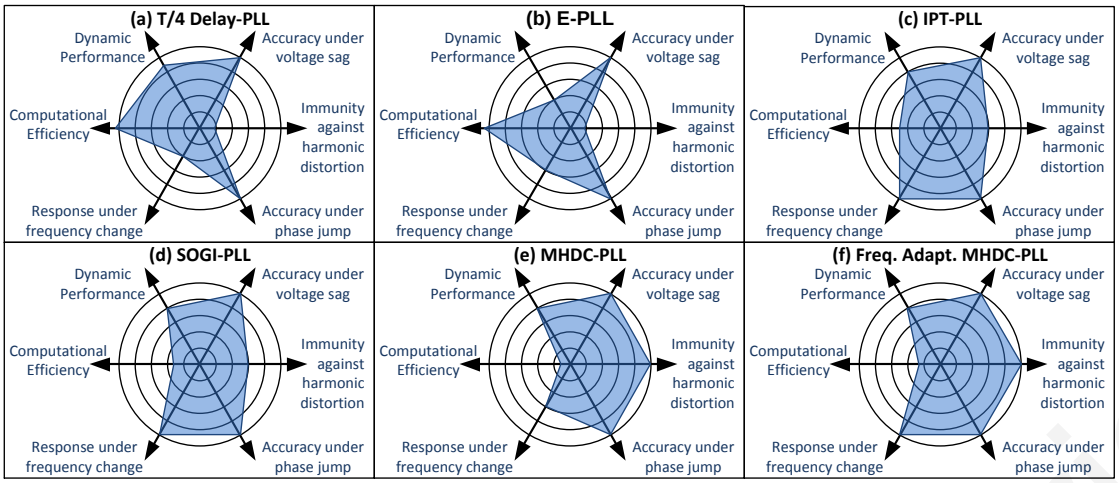

Fig. 5.15. Synopsis of the performance benchmarking between the six single-phase synchronization methods examined in this chapter: (a) the T/4 delay-PLL, (b) the E-PLL and (c) the IPT-PLL, (d) the SOGI-PLL, (e) the proposed MHDC-PLL and (f) the proposed frequency adaptive MHDC-PLL.

are added to the power system). The effect of the inter-harmonics can be minimized (but cannot be completely eliminated) by the band-pass filtering characteristics of the QSG.

5.5 Conclusions

In this Chapter, two new PLL based synchronization methods have been proposed for single-phase grid tied inverters. The first synchronization, named MHDC-PLL, is introduced in Section 5.3 and can present a fast and accurate response under grid faults and harmonic distortion. The only disadvantage of the MHDC-PLL is the inaccurate response under non-nominal frequencies and the increased complexity of the decoupling network. The second synchronization method, named frequency adaptive MHDC-PLL, is proposed in Section 5.4 to overcome the main disadvantages of MHDC-PLL. Thus, a new frequency adaptive QSG is proposed to enable the accurate synchronization under frequency changes and a new improved MHDC is developed to decrease the complexity and to still achieve a great immunity against harmonics. Hence, the proposed frequency adaptive MHDC-PLL can be considered as an outstanding synchronization method for single-phase inverter, since it presents fast dynamics under disturbances, great immunity against harmonics and requires a satisfactory processing time for real-time applications. A synopsis of the comparison between the proposed synchronization methods within this Chapter, some conventional synchronization methods, such as the T/4 delay-PLL [27], [107], [108] and the E-PLL [50], [70]-[72], [107], [108], and some advanced techniques from the literature, such as the IPT-PLL [71], [107]-[110] and the SOGI-PLL [71], [107]-[110], is presented in Fig. 5.15, where it is obvious that the proposed frequency adaptive MHDC-PLL is the most outstanding synchronization scheme, ideal to be used for the grid synchronization of

single-phase inverters. The outstanding synchronization of the proposed frequency adaptive MHDC-PLL can enable the proper FRT operation of grid tied PV systems and can beneficially affect the power quality of grid tied inverters.

CHAPTER 6
A NEW CURRENT CONTROLLER FOR ACCURATE OPERATION UNDER ABNORMAL CONDITIONS

6.1 Introduction

The power produced by the Renewable Energy Sources (RES) is injected to the power system by the Grid Side Converter (GSC). In the case of Wind Power Systems (WPS) and Photovoltaic (PV) technology systems with rated power above 5 kW, a three-phase GSC is required to enable the proper injection of the generated power into the grid. The appropriate operation of the GSC is ensured by the design of its controller in order to maintain the voltage at the DC bus, to regulate the injection of the produced active power into the grid in a synchronized way, and to provide reactive power into the grid if it is needed in order to support the voltage stability of the power system. The main topology and the corresponding controller diagram for such a three-phase GSC is described in [27], [43]-[47] and is presented in Fig. 6.1.

According to Fig. 6.1, the GSC controller is usually based on a synchronization method, on an active and reactive power (PQ) controller, on a current controller and on a Pulse Width Modulation (PWM) technique. Phase-Locked Loop (PLL) based synchronization techniques are already discussed in Chapters 2-5. The PQ controller generates the reference currents according to the active power produced by RES that affects the voltage at the DC-link and according to the required reactive power that affects the amplitude of the grid voltage as already discussed in Sections 2.4.2, 3.3.3 and 4.4.5. The output of the synchronization method and the PQ controller is fed into the current controller in order to regulate the injected currents by the GSC. It is obvious that there is a strong interaction between the response of the main units of the GSC controller, since an inaccurate synchronization can affect the accuracy and the quality of the injected currents by the current controller. Further, the massive penetration of RES into the grid requires that the modern RES should also be able to provide voltage and frequency support under grid faults in order to maintain the stability of the power grid. Moreover, a high quality power injection under harmonic distorted voltage and balanced or unbalanced low-voltage grid

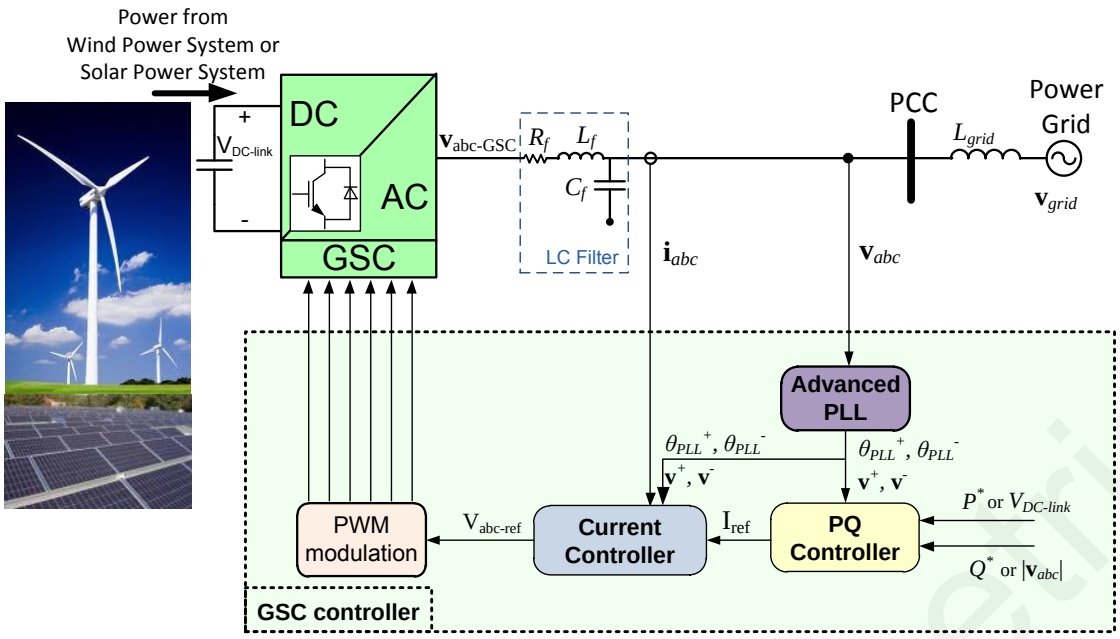

Fig. 6.1. Topology of a three-phase grid-connected RES though a GSC among with its controller structure.

faults is required, according to the international standards [5]-[10] and the recently issued grid regulations [11]-[27]. In light of the prior-mentioned issues, there is a need to advance the GSC controller in order to achieve the performance of the GSC and as a consequence the response of the entire RES.

In previous chapters (Chapter 2-Chapter 5), several PLL methods have been proposed to enable a fast and accurate synchronization under any grid conditions. The outstanding response of these synchronization methods can only affect the performance of the GSC if the advanced synchronization methods are properly combined with an improved current controller. Therefore, in this chapter an advanced current controller is proposed in order to ensure the proper operation of the GSC under any grid conditions. The developed current controller is modular and simplified in structure and can achieve the accurate injection of high quality sinusoidal (positive or negative sequence) currents under harmonic distorted conditions and under balanced and unbalanced faults. Hence, by utilizing the proposed current controller an outstanding performance can be achieved by the GSC to enable the RES to meet the grid regulations.

6.2 Literature review

The controller of the GSC is based on a synchronization unit, a PQ controller unit and the current controller unit as shown in Fig. 6.1. The advanced synchronization methods, proposed in Chapters 2-5 and in [28]-[39], can fast and accurately estimate the synchronization signals, such as the phase angle (θ') and the voltage vector ($\mathbf{v}_{dq}^{+1}$) of the

positive sequence of the fundamental grid voltage. Therefore, the proper synchronization can be achieved even under highly harmonic distorted conditions and under unbalanced low-voltage sag events. However, for achieving an appropriate operation of the GSC under any grid conditions the use of an advanced synchronization method is not enough. Hence, the output of the synchronization should be fed into an advanced current controller in order to enable an accurate and high quality current injection by the GSC operation under any grid conditions.

The current controller is responsible for generating the reference voltage vector ($\mathbf{v}^*_{abc}$) that will be fed to the PWM unit in order to produce the corresponding injected currents by the GSC ($\mathbf{i}_{abc}$) as demonstrated in Fig. 6.1. For a proper operation, the injected currents by the GSC should follow the reference currents that are generated by the PQ controller. The conventional current controller [27], [43] is designed in the Synchronous Reference Frame (SRF) of the fundamental component (dq^{+1}-frame) and uses two Proportional-Integral (PI) controllers in order to generate the reference voltage as shown in Fig. 6.2. The corresponding Clarke's [$T_{\alpha\beta}$] and Park's [$T_{dq}{}^{+1}$] transformation matrices are used in order to properly express the voltage and current vectors into the dq^{+1}-frame as explained in Appendix A. The voltage ($\mathbf{v}_{dq}$) and current ($\mathbf{i}_{dq}$) vectors expressed in the dq^{+1}-frame and are actually non oscillated vectors under ideal grid conditions and thus, the use of PI controller is allowed in order to properly regulate the current injection. The design of the conventional current controller is simplified and can achieve a sufficient performance under normal grid conditions; however, this controller is inadequate under unbalanced grid voltage and under a harmonic distorted grid. The unbalanced conditions cause unavoidable double frequency oscillations on the voltage and current vectors due to the existence of the negative sequence grid voltage. Similarly, higher frequency oscillations are also caused

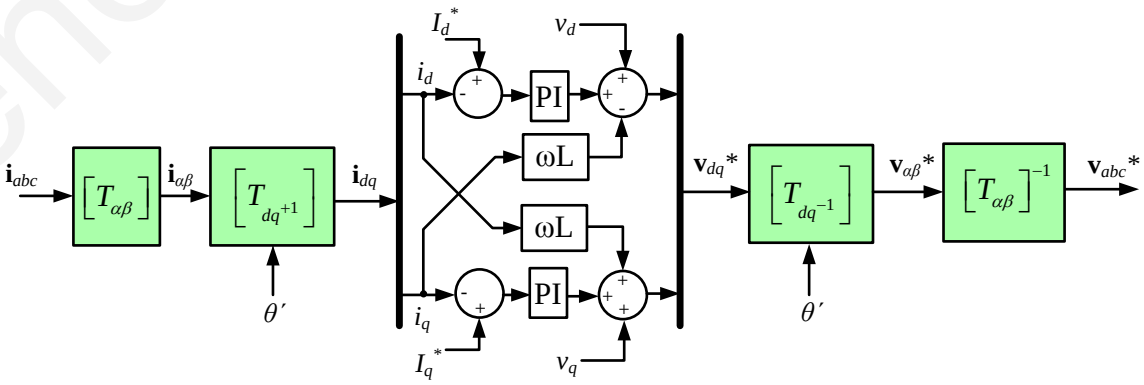

Fig. 6.2. The structure of the conventional current controller method designed in the synchronous reference frame.

due to the effect of the harmonic distortion. Hence, these oscillations affect the accuracy of the controller and the conventional current controller fails to inject high quality currents into the grid.

To overcome this problem caused by the undesired double frequency oscillations due to the unbalanced conditions, some dual SRF current controllers have been proposed [82], [83], where they are using certain filtering techniques to decouple the effect between the positive and the negative sequence. These techniques can achieve the accurate estimation of positive and negative voltage and current free of any oscillations. Unfortunately, the use of filtering techniques in the controller path causes the unwanted deceleration of its dynamic performance and thus the overall response of the current control techniques is affected. An enhanced dual SRF current controller is proposed in [84] for the accurate operation under unbalanced grid conditions. In this controller a decoupling network is used to enable the dynamic performance and the accurate control of both positive and negative sequence currents. The complexity of this current controller is an issue and the performance of the PI-controller is limited due to the high required control effort because the voltage feed-forward technique is not used in this control path. It is to be noted that the current control techniques mentioned in this paragraph do not consider the effect of harmonic distortion.

The current controller proposed in [118] uses a Proportional-Resonant (PR) controller, instead of a PI controller, and it is designed in the stationary reference frame ($\alpha\beta$-frame). This controller is equivalent to the conventional current controller and thus, it cannot operate accurately under abnormal conditions. Some interesting techniques are proposed in [85], [86] for achieving an accurate response under unbalanced conditions, where a combination of PI controllers and PR controllers is used. The PI controllers operate in the SRF to regulate the positive fundamental sequence current and in addition, the PR controllers are used to regulate the double frequency oscillations produced by the unbalanced condition. Further, a very interesting technique is proposed in [87] where a PI controller is combined with several multi resonant controllers in order to regulate the currents under unbalanced and harmonic distorted conditions. This technique can only inject pure sinusoidal positive sequence of currents. It is worth mentioning that the use of a resonant controller does not usually allow the use of the feed-forward technique which means that an undesired higher control effort is required by the current controller.

Furthermore, some other interesting and simplified current controllers have been proposed using harmonic compensation techniques as presented in [88]-[90]. These controllers are designed in multiple synchronous reference frames enabling the high quality current injection under harmonic distorted grid conditions; however, the effect of unbalanced conditions is not considered in this controller and thus, an accurate operation under an unbalanced grid fault is not enabled.

This chapter proposes an advanced current controller that can accurately operate under unbalanced and harmonic distorted grid conditions and can inject high quality pure sinusoidal positive or negative sequence currents. The structure of the proposed current controller is simplified and modularized and the outstanding performance is achieved by adding to the conventional current controller designed in the dq^{+1}-frame two compensation modules designed in multiple synchronous reference frames. The harmonic compensation module eliminates the effect of the harmonic distortion while the unbalanced compensation module enables the accurate operation under unbalanced conditions. Hence, the proposed current controller enables accurate and high quality full positive or full negative sequence current injection under any grid conditions as validated by the simulation and experimental results. Thus, the proper operation of the GSC is ensured under grid faults and the appropriate Fault Ride Through (FRT) operation can be achieved by the RES for supporting the stability of the grid. Moreover, the high quality current injection even under a harmonic distorted grid can enhance the power quality of the RES and of the entire power system. Further, the accurate operation of the current controller during unbalanced grid conditions can minimize the oscillations of the DC-link voltage, thus the size of the DC-link capacitor can be reduced.

6.3 Power analysis under abnormal conditions

The proposed current controller in this chapter aims to operate very accurately under unbalanced and harmonic distorted conditions. Thus, it is necessary to first analyze in depth the operation of the GSC under abnormal conditions before proposing the new current controller. According to the instantaneous power theory presented in [27], [119] and in Appendix A.6, the instantaneous active and reactive power supplied by the GSC of an interconnected RES can be calculated in any reference frame as shown in (6.1) and (6.2) respectively.

$$p = \mathbf{v}_{abc} \cdot \mathbf{i}_{abc} = \frac{3}{2}\left(\mathbf{v}_{\alpha\beta} \cdot \mathbf{i}_{\alpha\beta}\right) = \frac{3}{2}\left(\mathbf{v}_{dq} \cdot \mathbf{i}_{dq}\right) \tag{6.1}$$

$$q = \left|\mathbf{v}_{abc} \times \mathbf{i}_{abc}\right| = \frac{3}{2}\left|\mathbf{v}_{\alpha\beta} \times \mathbf{i}_{\alpha\beta}\right| = \frac{3}{2}\left|\mathbf{v}_{dq} \times \mathbf{i}_{dq}\right| \;\Leftrightarrow$$
$$q = \mathbf{v}_{abc\perp} \cdot \mathbf{i}_{abc} = \frac{3}{2}\left(\mathbf{v}_{\alpha\beta\perp} \cdot \mathbf{i}_{\alpha\beta}\right) = \frac{3}{2}\left(\mathbf{v}_{dq\perp} \cdot \mathbf{i}_{dq}\right) \tag{6.2}$$

Where **v** is the voltage vector at the Point of Common Coupling (PCC), **i** is the injected current vector by the RES, and $\mathbf{v}_{\perp}$ is an orthogonal version (90^{o} leading) of the original voltage vector **v**. All the equations presented in this chapter are valid for the all the voltage and current vectors expressed in any reference frame (e.g., natural *abc* reference frame, stationary $\alpha\beta$ reference frame, and synchronous *dq* reference frame rotating with the synchronous angular speed of the grid $+\omega$) as shown in (6.3).

$$\mathbf{v}_{abc} = \begin{bmatrix} v_a \\ v_b \\ v_c \end{bmatrix},\ \mathbf{v}_{\alpha\beta} = \begin{bmatrix} v_\alpha \\ v_\beta \end{bmatrix},\ \mathbf{v}_{dq} = \begin{bmatrix} v_d \\ v_q \end{bmatrix} \text{ and } \mathbf{i}_{abc} = \begin{bmatrix} i_a \\ i_b \\ i_c \end{bmatrix},\ \mathbf{i}_{\alpha\beta} = \begin{bmatrix} i_\alpha \\ i_\beta \end{bmatrix},\ \mathbf{i}_{dq} = \begin{bmatrix} i_d \\ i_q \end{bmatrix}$$
$$\mathbf{v}_{abc\perp} = \begin{bmatrix} 0 & 1 & -1 \\ -1 & 0 & 1 \\ 1 & -1 & 0 \end{bmatrix}\mathbf{v}_{abc},\ \mathbf{v}_{\alpha\beta\perp} = \begin{bmatrix} 0 & 1 \\ -1 & 0 \end{bmatrix}\mathbf{v}_{\alpha\beta},\ \mathbf{v}_{dq\perp} = \begin{bmatrix} 0 & 1 \\ -1 & 0 \end{bmatrix}\mathbf{v}_{dq} \tag{6.3}$$

Since the proposed current controller in this chapter is designed in synchronous reference frames, the further power analysis is presented based on vectors expressed in the *dq*-frame.

During unbalanced and harmonic distorted grid conditions the voltage and the current vectors, expressed in the *dq*-frame, could be expressed as a summation of the positive sequence, the negative sequence and the harmonic component as given by,

$$\mathbf{v}_{dq} = \mathbf{v}_{dq}^{+} + \mathbf{v}_{dq}^{-} + \mathbf{v}_{dq}^{h} \text{ and } \mathbf{i}_{dq} = \mathbf{i}_{dq}^{+} + \mathbf{i}_{dq}^{-} + \mathbf{i}_{dq}^{h} \tag{6.4}$$

Therefore, the equations for the active and reactive power of (6.1) and (6.2) can be re-written as,

$$p = \frac{3}{2}\left(\mathbf{v}_{dq} \cdot \mathbf{i}_{dq}\right) = \frac{3}{2}\left(\mathbf{v}_{dq}^{+} + \mathbf{v}_{dq}^{-} + \mathbf{v}_{dq}^{h}\right)\left(\mathbf{i}_{dq}^{+} + \mathbf{i}_{dq}^{-} + \mathbf{i}_{dq}^{h}\right) \;\Leftrightarrow$$
$$p = \frac{3}{2}\left\{\left[\mathbf{v}_{dq}^{+} \cdot \mathbf{i}_{dq}^{+} + \mathbf{v}_{dq}^{-} \cdot \mathbf{i}_{dq}^{-} + \mathbf{v}_{dq}^{h} \cdot \mathbf{i}_{dq}^{h}\right] + \left[\begin{array}{r} \left(\mathbf{v}_{dq}^{-} + \mathbf{v}_{dq}^{h}\right) \cdot \mathbf{i}_{dq}^{+} + \left(\mathbf{v}_{dq}^{+} + \mathbf{v}_{dq}^{h}\right) \cdot \mathbf{i}_{dq}^{-} + \\ \left(\mathbf{v}_{dq}^{+} + \mathbf{v}_{dq}^{-}\right) \cdot \mathbf{i}_{dq}^{h} \end{array}\right]\right\} \tag{6.5}$$
$$P \rightarrow \text{Non-oscillation terms} \qquad \tilde{p} \rightarrow \text{Oscillation terms}$$

$$q = \frac{3}{2}\left(\mathbf{v}_{dq\perp}\cdot\mathbf{i}_{dq}\right) = \frac{3}{2}\left(\mathbf{v}^{+}_{dq\perp}+\mathbf{v}^{-}_{dq\perp}+\mathbf{v}^{h}_{dq\perp}\right)\left(\mathbf{i}^{+}_{dq}+\mathbf{i}^{-}_{dq}+\mathbf{i}^{h}_{dq}\right) \;\Leftrightarrow$$

$$q = \frac{3}{2}\left\{\left[\begin{array}{r}\mathbf{v}^{+}_{dq\perp}\cdot\mathbf{i}^{+}_{dq}+\mathbf{v}^{-}_{dq\perp}\cdot\mathbf{i}^{-}_{dq}\\ +\mathbf{v}^{h}_{dq\perp}\cdot\mathbf{i}^{h}_{dq}\end{array}\right]+\left[\begin{array}{r}\left(\mathbf{v}^{-}_{dq\perp}+\mathbf{v}^{h}_{dq\perp}\right)\cdot\mathbf{i}^{+}_{dq}+\left(\mathbf{v}^{+}_{dq\perp}+\mathbf{v}^{h}_{dq\perp}\right)\cdot\mathbf{i}^{-}_{dq}+\\ \left(\mathbf{v}^{+}_{dq\perp}+\mathbf{v}^{-}_{dq\perp}\right)\cdot\mathbf{i}^{h}_{dq}\end{array}\right]\right\} \tag{6.6}$$

$Q \rightarrow$ Non-oscillation terms $\qquad\qquad \tilde{q} \rightarrow$ Oscillation terms

From (6.5) and (6.6) it is obvious that even if the harmonic distortion is considered as negligible, the existence of negative sequence voltage or current (unbalanced disturbances) could give a rise to oscillations in active and reactive power.

The oscillations in active and reactive power can cause oscillations on the generation of the reference currents by the PQ controller, which causes inaccuracies in the operation of the current controller. This chapter proposes a new current controller that can compensate the unbalanced and harmonic current injection and thus, a full positive or a full negative sequence pure sinusoidal current injection is enabled. It is worth mentioning that under grid faults, the positive sequence current injection can provide frequency and voltage support to the grid while the negative sequence currents can minimize the unbalances caused by the grid faults. Hence, in the case of full positive current injection, the current can be described only by the positive sequence component, so the active and reactive power of (6.5) and (6.6) are simplified as shown in (6.7).

$$\underset{P}{p = \frac{3}{2}\left\{\left[\mathbf{v}^{+}_{dq}\cdot\mathbf{i}^{+}_{dq}\right]\right.}+\underset{\tilde{p}}{\left.\left[\left(\mathbf{v}^{-}_{dq}+\mathbf{v}^{h}_{dq}\right)\cdot\mathbf{i}^{+}_{dq}\right]\right\}},\quad \underset{Q}{q = \frac{3}{2}\left\{\left[\mathbf{v}^{+}_{dq\perp}\cdot\mathbf{i}^{+}_{dq}\right]\right.}+\underset{\tilde{q}}{\left.\left[\left(\mathbf{v}^{-}_{dq\perp}+\mathbf{v}^{h}_{dq\perp}\right)\cdot\mathbf{i}^{+}_{dq}\right]\right\}} \tag{6.7}$$

Vice versa in the case of full negative current injection, the current is given by considering only the negative sequence component and the power equation is given by,

$$\underset{P}{p = \frac{3}{2}\left\{\left[\mathbf{v}^{-}_{dq}\cdot\mathbf{i}^{-}_{dq}\right]\right.}+\underset{\tilde{p}}{\left.\left[\left(\mathbf{v}^{+}_{dq}+\mathbf{v}^{h}_{dq}\right)\cdot\mathbf{i}^{-}_{dq}\right]\right\}},\quad \underset{Q}{q = \frac{3}{2}\left\{\left[\mathbf{v}^{-}_{dq\perp}\cdot\mathbf{i}^{-}_{dq}\right]\right.}+\underset{\tilde{q}}{\left.\left[\left(\mathbf{v}^{+}_{dq\perp}+\mathbf{v}^{h}_{dq\perp}\right)\cdot\mathbf{i}^{-}_{dq}\right]\right\}} \tag{6.8}$$

Thereby, the active and the reactive power oscillations are minimized and the useful for the control mean value of active and reactive power is given by P and Q as shown in (6.9) for the case of full positive sequence current injection and in (6.10) for the case of full negative sequence current injection.

$$P = \frac{3}{2}\mathbf{v}^{+}_{dq}\cdot\mathbf{i}^{+}_{dq},\; Q = \mathbf{v}^{+}_{dq\perp}\cdot\mathbf{i}^{+}_{dq} \tag{6.9}$$

$$P = \frac{3}{2}\mathbf{v}_{dq}^{-} \cdot \mathbf{i}_{dq}^{-},\ Q = \mathbf{v}_{dq\perp}^{-} \cdot \mathbf{i}_{dq}^{-} \tag{6.10}$$

The positive and negative sequence of the grid voltage and their orthogonal leading version can be accurately estimated by an advanced PLL based synchronization method, such as those that have already been proposed in Chapters 2-4. As a consequence, the PQ controller can easily generate the corresponding reference currents $\mathbf{I}_{dq}^{*}$ that enable the proper power injection according to the active P^{*} and reactive Q^{*} power set-points. Thus, in case of full positive sequence current injection, the reference currents can be generated by the PQ controller according to (6.11).

$$\mathbf{I}_{dq}^{*} = \begin{bmatrix} I_d^{+*} \\ I_q^{+*} \end{bmatrix} = \frac{2}{3} \cdot \frac{1}{\left|\mathbf{v}_{dq}^{+}\right|^2} \left(\mathbf{v}_{dq}^{+} \cdot P^{*} + \mathbf{v}_{dq\perp}^{+} \cdot Q^{*} \right) = \frac{2}{3} \cdot \frac{1}{\left(v_d^{+}\right)^2 + \left(v_d^{+}\right)^2} \begin{bmatrix} v_d^{+} & v_q^{+} \\ v_q^{+} & -v_d^{+} \end{bmatrix} \begin{bmatrix} P^{*} \\ Q^{*} \end{bmatrix} \tag{6.11}$$

Similarly, in the case of full negative sequence current injection the reference currents are given by (6.12).

$$\mathbf{I}_{dq}^{*} = \begin{bmatrix} I_d^{-*} \\ I_q^{-*} \end{bmatrix} = \frac{2}{3} \cdot \frac{1}{\left|\mathbf{v}_{dq}^{-}\right|^2} \left(\mathbf{v}_{dq}^{-} \cdot P^{*} + \mathbf{v}_{dq\perp}^{-} \cdot Q^{*} \right) = \frac{2}{3} \cdot \frac{1}{\left(v_d^{-}\right)^2 + \left(v_d^{-}\right)^2} \begin{bmatrix} v_d^{-} & v_q^{-} \\ v_q^{-} & -v_d^{-} \end{bmatrix} \begin{bmatrix} P^{*} \\ Q^{*} \end{bmatrix} \tag{6.12}$$

Hence, since the reference currents can be generated by the PQ controller according to (6.11) or (6.12) under unbalanced grid conditions, then a current controller needs to be designed in order to ensure that the injected currents by the GSC will follow these reference currents.

6.4 The proposed current controller

The proposed current controller enables fast and accurate injection of the full positive or full negative current injection under unbalanced grid faults and harmonic distorted grid. The proposed current controller is designed in multiple Synchronous Reference Frames (SRF), where the fundamental positive sequence SRF (dq^{+1}-frame) is used to regulate the main sinusoidal current injection and the rest of the SRFs are used to compensate the unbalanced and harmonic effects.

The structure of the proposed current controller is based on the conventional current controller designed in the dq^{+1}-frame and is enhanced with an Unbalanced Compensation Module (UCM) and a Harmonic Compensation Modules (HCM) as presented in Fig. 6.3. The proposed current controller requires the use of an accurate estimation of the positive $\mathbf{v}_{dq}^{+}$ or negative $\mathbf{v}_{dq}^{-}$ sequence of the grid voltage at the Point of Common Coupling (PCC), through an advanced PLL (such those proposed in Chapters 2-4).

The Clarke's and Park's transformation matrices (Appendix A) are used to enable the design of the current controller in multiple SRFs as given by (6.13) and (6.14) respectively.

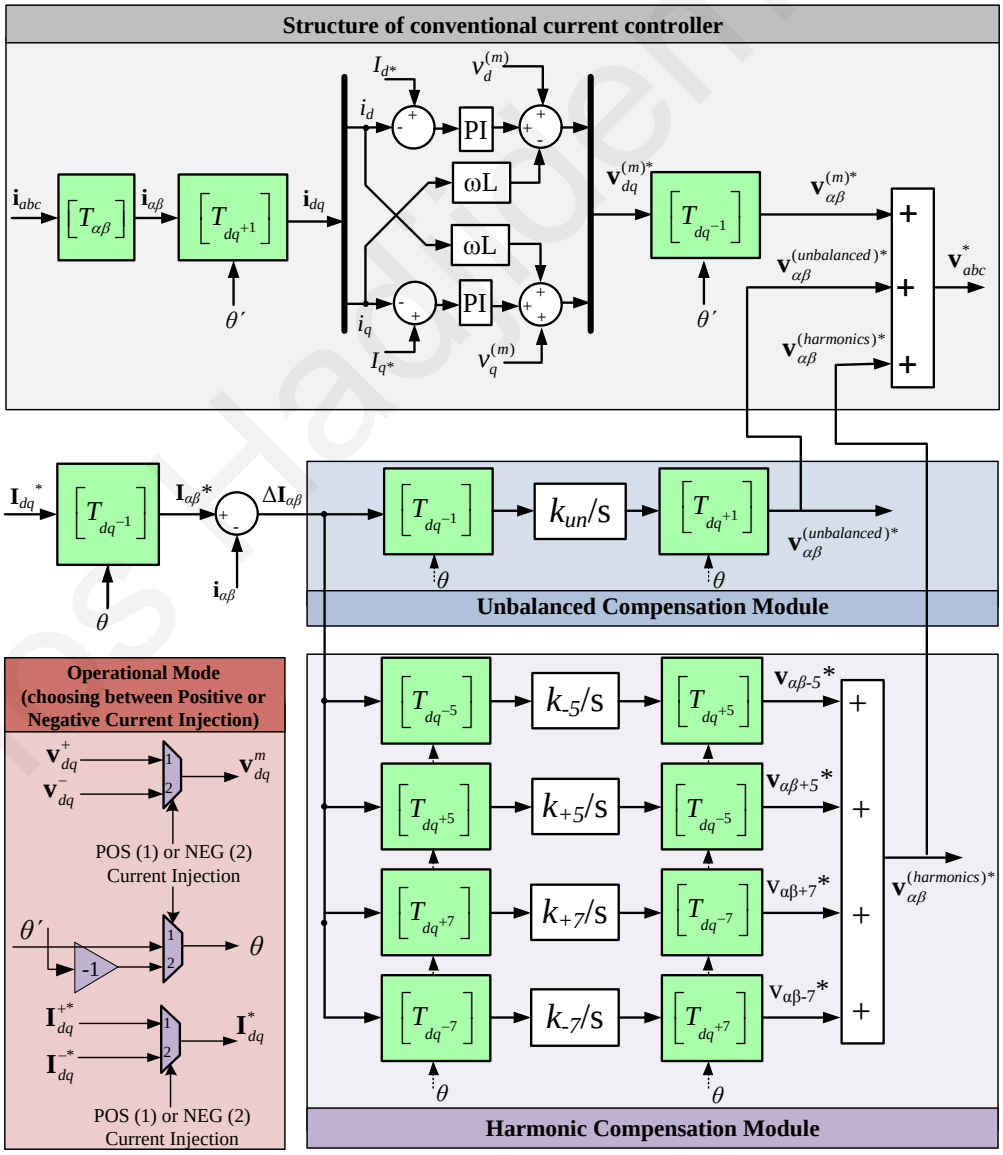

Fig. 6.3. The structure of the proposed current controller.

$$\left[T_{\alpha\beta}\right]=\frac{2}{3}\begin{bmatrix}1 & -1/2 & -1/2\\ 0 & \sqrt{3}/2 & -\sqrt{3}/2\end{bmatrix} \tag{6.13}$$

$$\left[T_{dq^{n}}\right]=\left[T_{dq^{-n}}\right]^{T}=\begin{bmatrix}\cos(n\omega t) & \sin(n\omega t)\\ -\sin(n\omega t) & \cos(n\omega t)\end{bmatrix} \tag{6.14}$$

The structure of the proposed current controller can be divided into the conventional current controller unit, the Unbalanced Compensation Module (UCM), the Harmonic Compensation Module and the unit for choosing the operational mode of the controller, as presented in Fig. 6.3. The higher layer unit is responsible for choosing between the two possible operational modes of the controller (full positive or full negative current injection). The only difference between the two modes is the accurate detection of the positive or negative sequence voltage vector and the phase angle of the fundamental voltage component from an advanced PLL. Obviously, the reference currents generated from the PQ controller in the case of positive current injection are different than in the case of negative current injection according to (6.11) and (6.12) respectively, since they are dependent on the positive or negative voltage vector.

6.4.1 Structure and tuning of the conventional current controller unit

The main structure of the current controller is inherited from the conventional current controller [27], [43] designed in the *dq*-frame and uses two PI controllers in order to generate the reference voltage vector $\mathbf{v}_{abc}^{*}$. The vector $\mathbf{v}_{abc}^{*}$ will be fed into the Pulse Width Modulation (PWM) unit of the GSC controller in order to enable the proper generation of the corresponding GSC voltage vector $\mathbf{v}_{abc-GSC}$, as shown in Fig. 6.1. The produced voltage $\mathbf{v}_{abc-GSC}$ by the GSC will force the injection of current $\mathbf{i}_{abc}$, as a result of the voltage drop among the resistor R_f and the inductor L_f of the LC filter according to,

$$\mathbf{i}_{abc}=\frac{\mathbf{v}_{abc-GSC}-\mathbf{v}_{abc}}{R_f+j\omega L_f} \tag{6.15}$$

where $\mathbf{v}_{abc}$ is the grid voltage at the PCC and ω is the grid frequency. Equation (6.15) can be equivalently expressed in the *dq*-frame as shown in (6.16).

$$\mathbf{i}_{dq}=\frac{\mathbf{v}_{dq-GSC}-\mathbf{v}_{dq}}{R_f+j\omega L_f} \quad \Leftrightarrow \quad (i_d+j\cdot i_q)=\frac{(v_{d-GSC}+j\cdot v_{q-GSC})-(v_d+j\cdot v_q)}{R_f+j\omega L_f} \tag{6.16}$$

By analyzing this equation into the real (*d*-axis) and the imaginary (*q*-axis), (6.16) can be re-written as,

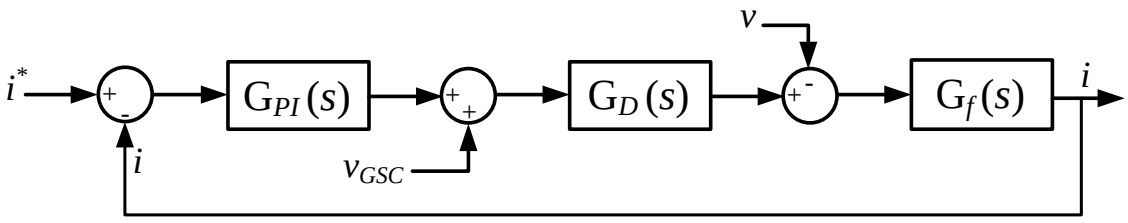

Fig. 6.4. The closed-loop control system of a current controller.

$$\begin{aligned} d-axis &\rightarrow v_{d-GSC} = v_d + i_d \cdot R_f - i_q \cdot \omega L_f \\ q-axis &\rightarrow v_{q-GSC} = v_q + i_q \cdot R_f + i_d \cdot \omega L_f \end{aligned} \tag{6.17}$$

These terms can be used as feed-forward terms into the current controller (in the structure of the conventional current controller) as shown in Fig. 6.3 and Fig. 6.4 in order to minimize the control effort of the controller and improve its performance. It is to be noted that usually the R_f is negligible and thus this term is ignored in the feed-forward voltage.

Another important aspect regarding the design of the conventional current controller is the tuning of the PI controller. For the tuning of the current controller, it is necessary to express the current controller as a closed-loop control system based on the transfer function $G_{PI}(s)$ of the PI controller, the transfer function $G_D(s)$ of all the delays of the control path and the transfer function $G_f(s)$ of the LC filter as shown in the closed-loop system of Fig. 6.4. The transfer function of the PI controller is given as,

$$G_{PI}(s) = k_P + \frac{1}{T_i}\frac{1}{s} \tag{6.18}$$

where k_p and T_i are the tuning parameters of the PI controller.

The transfer function $G_D(s)$ is given in (6.19) and represents all the delays that may occur on the control path of the current controller.

$$G_D(s) = \frac{1}{1+T_d s} \tag{6.19}$$

T_d is the total time delay of the control path as mentioned in [120], which is given as the summation of the delay due to the PWM unit (usually $0.5T_s$), the delay due to the sampling rate (T_s) and any other delays ($T_{other} \approx (3-5)Ts$) may be caused by the synchronization unit, the sensors, and the filters. It is to be noted that $T_s = 1/f_s$ represents the sampling period of the GSC controller.

The transfer function of the LC filter is given by (6.20), where R_f and L_f represent the resistor and inductor of the filter.

$$G_f(s) = \frac{1}{R_f + L_f s} \tag{6.20}$$

By combining the transfer function of (6.18)-(6.20) as a closed-loop system (Fig. 6.4), the transfer function of the current controller $H(s)$ is extracted as shown in [27] and given by,

$$H(s) = \frac{i}{i^*} = \frac{G_{PI}(s)G_D(s)G_f(s)}{1+G_{PI}(s)G_D(s)G_f(s)} \tag{6.21}$$

where i^* represents the reference currents generated by the PQ controller and i the injected currents by the GSC. By replacing the transfer functions (6.18)-(6.20) into (6.21) the following equation is derived,

$$H(s) = \frac{\left(k_p + \frac{1}{T_i s}\right)\left(\frac{1}{1+T_d s}\right)\left(\frac{1}{R_f + L_f s}\right)}{1+\left(k_p + \frac{1}{T_i s}\right)\left(\frac{1}{1+T_d s}\right)\left(\frac{1}{R_f + L_f s}\right)} \Leftrightarrow$$

$$H(s) = \frac{\left(\frac{k_p T_i s + 1}{T_i s}\right)\left(\frac{1}{1+T_d s}\right)\left(\frac{\frac{1}{R_f}}{1+\frac{L_f}{R_f}s}\right)}{1+\left(\frac{k_p T_i s + 1}{T_i s}\right)\left(\frac{1}{1+T_d s}\right)\left(\frac{\frac{1}{R_f}}{1+\frac{L_f}{R_f}s}\right)} \tag{6.22}$$

By setting the product of the tuning parameters equal to the time constant of the filter ($k_p \cdot T_i = L_f/R_f$), (6.22) can be simplified into (6.23).

$$H(s) = \frac{\left(\frac{1}{R_f T_i s}\right)\left(\frac{1}{1+T_d s}\right)}{1+\left(\frac{1}{R_f T_i s}\right)\left(\frac{1}{1+T_d s}\right)} = \frac{1}{R_f T_i T_d s^2 + R_f T_i s + 1} \tag{6.23}$$

It is to be noted that (6.23) can be re-written in the form of a typical second-order transfer function as given by,

$$H(s)=\frac{\left(\frac{1}{T_i T_d R_f}\right)}{s^2+\left(\frac{1}{T_d}\right)s+\left(\frac{1}{T_i T_d R_f}\right)};\quad \omega_n=\sqrt{\frac{1}{T_i T_d R_f}}\ \text{and}\ \zeta\omega_n=\frac{1}{2T_d} \tag{6.24}$$

where ω_n is the natural frequency of the system and ζ is the damping coefficient. For an optimally damped response of the current controller, the damping coefficient ζ should be set to $1/\sqrt{2}$ and thus, the tuning parameters of the PI controller should be set according to (6.25).

$$k_p=\frac{L_f}{2T_d}\ \text{ and }\ T_i=\frac{2T_d}{R_f} \tag{6.25}$$

6.4.2 Unbalanced and harmonic compensation modules

The main improvement of the proposed current controller is the addition of the unbalanced and harmonic compensation modules. The Harmonic Compensation Module (HCM) according to [27], [88]-[90] uses multiple SRFs in order to compensate the effect of the harmonics distortion and deliver purely sinusoidal currents under harmonic distorted voltage conditions. Further, the main contribution of this chapter is the implementation of the novel Unbalanced Compensation Module (UCM) in order to compensate the effect of the unbalanced grid voltage condition on the injected currents.

The UCM is responsible to regulate the reference voltage of the GSC in a way to allow the injection of symmetrical currents despite the unbalanced grid voltage at the PCC. In case of balanced grid voltage conditions, the synchronization method and the PQ controller can accurately estimate the synchronization signals and generate the reference currents respectively and thus, the conventional current controller can appropriately operate and produce a balanced reference voltage $\mathbf{v}^*_{abc}$. Now, in the case of unbalanced grid faults, the grid voltage at the PCC, $\mathbf{v}_{abc}$, will be unbalanced and so if the produced voltage by the GSC ($\mathbf{v}_{abc\text{-}GSC}$) is balanced, then the injected currents will be enforced to be unbalanced too. The unbalanced injected currents are resulting as a consequence of the unbalanced voltage drop among the R_f and L_f $\mathbf{i}_{abc}=(\mathbf{v}_{abc\text{-}GSC}-\mathbf{v}_{abc})/(R_f+j\omega L_f)$, as shown in Fig. 6.1. Therefore, the conventional current controller will not be able to deliver symmetrical currents.

To overcome this problem, a novel UCM is proposed and implemented here in order to observe any disturbances on the injected currents ($\Delta\mathbf{I}_{\alpha\beta}$) due to the effect of the

unbalanced conditions (negative sequence) and enforce the appropriate regulation to the control signal $\mathbf{v}_{abc}^{*}$ in order to achieve a symmetrical current injection. To implement the UCM as shown in Fig. 6.3, the disturbances $\Delta\mathbf{I}_{\alpha\beta}$ of the injected currents are transformed to the negative SRF (dq^{-1}-frame), rotating with a negative synchronous angular speed $-\omega$, in order to isolate the disturbances caused by the unbalanced grid conditions. An Integral (I) controller is then used (also operating as a low pass filter in order to clear any disturbances caused by other harmonics), to regulate the unbalanced voltage compensation $\mathbf{v}_{\alpha\beta}^{(unbalanced)*}$ in a way that the injected currents will be purely symmetrical as the reference currents.

Similar logic is used in the HCM, but the disturbances on the injected current ($\Delta\mathbf{I}_{\alpha\beta}$) are transformed each time to the corresponding harmonic reference frame (dq^{h}-frame), rotating with an angular speed of $h\cdot\omega$, in order to regulate the effect caused by each harmonic. It is worth to mention that usually the main harmonics appearing on the grid are the -5^{th} and $+7^{th}$ but in the proposed current controller (Fig. 6.3) the harmonic compensation is also used for $+5^{th}$ and -7^{th} harmonic orders, because they are likely to appear in the case of unbalanced faults. This is happening because the -5^{th} voltage harmonic will appear as unbalanced -5^{th} harmonic when an unbalanced low-voltage fault occurs and this will introduce the $+5^{th}$ harmonic in the same way that the negative sequence appears in the case of unbalanced fundamental voltage. Then, an I controller is used (also operating as a low pass filter in order to clear any disturbances caused by the negative sequence and by the other harmonics), to regulate the harmonic voltage compensation $\mathbf{v}_{\alpha\beta}^{(harmonics)*}$ in order to enable that the injected currents will be purely sinusoidal and free of any low order harmonics.

The tuning of the proposed current controller is very convenient since the dynamic part of the conventional current controller (PI-controller) is not affected by the added UCM and HCM. Therefore, the PI-controller can be tuned in the same way with the conventional current controller as already analyzed in Section 6.4.1. The I-controllers that are used on the UCM and HCM ensure the stability of these modules and can easily be tuned. The gain of the I-controller of UCM should be tuned relatively high (5000) due to the fast dynamics of the unbalanced faults and the gains of the I-controller of the HCM can be tuned lower (1000) due to the slow dynamics of the grid voltage harmonics.

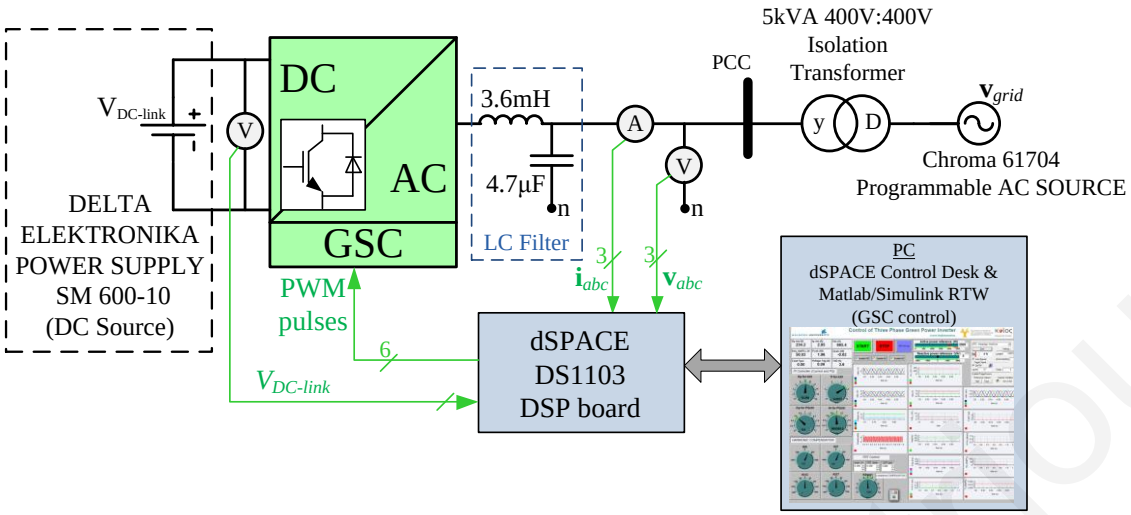

Fig. 6.5. Schematic of the experimental setup.

Therefore, the proposed current controller with unbalanced and harmonic compensation is a simplified and modular controller that achieves accurate injection of full positive or negative currents under unbalanced grid faults and harmonic distorted voltage. The tuning of the proposed current controller is easy due to the independency between the modules. Another advantage of the proposed current controller is the improved performance of the PI controller due to the ability of the voltage feed-forward technique, which cannot be used in the case of the current controller proposed in [82]-[84].

6.5 Simulation and experimental results

The advanced response of the proposed current controller under any grid conditions requires verification through simulation and experimental results. An experimental setup is implemented, as shown in Fig. 6.5, using a Chroma 61704 programmable AC source, a Delta Elektronika SM600-10 DC source power supply and a Danfoss FC302 (2.2kW) inverter as the GSC. The proposed GSC controller has been developed using the MATLAB/Simulink Real Time Workshop and the dSPACE DS 1103 DSP board. For the simulation results a dynamic model has been implemented in MATLAB/Simulink based on the topology of the experimental setup that is shown in Fig. 6.5. It is to be noted that a sampling rate of 10 kHz is used in both simulation and experimental setup.

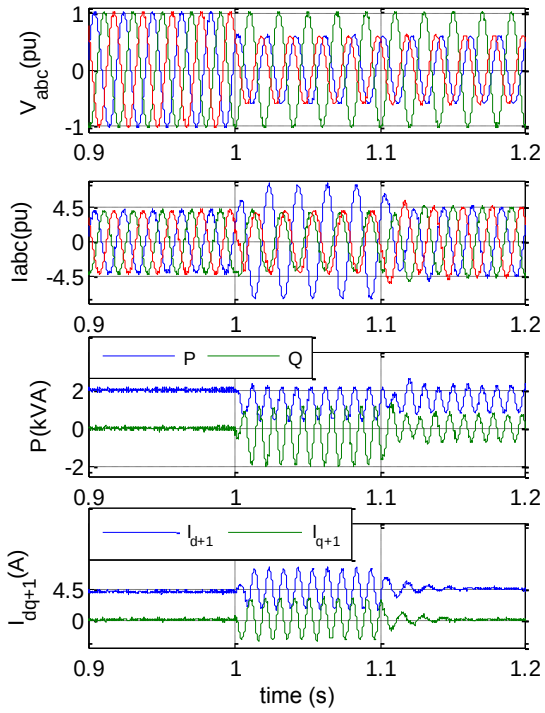

Fig. 6.6. Simulation results for the operation of the proposed current controller in full positive current injection mode.

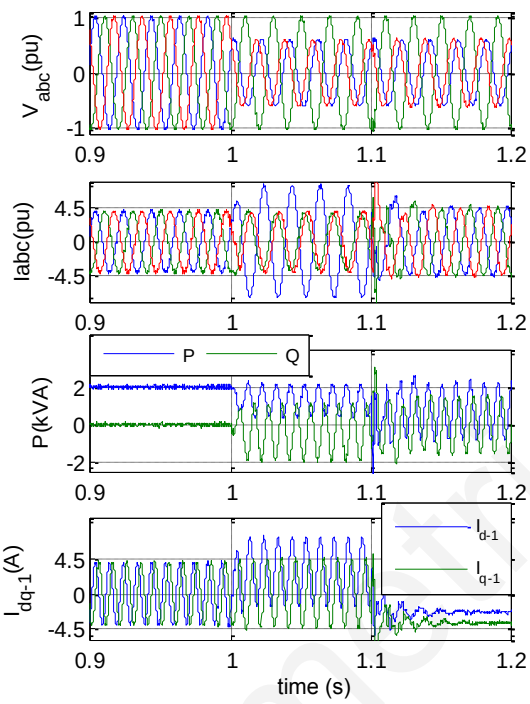

Fig. 6.7. Simulation results for the operation of the proposed current controller in full negative current injection mode.

6.5.1 Simulation results

Simulation results are required to observe the performance of the proposed current controller under harmonic distorted voltages and unbalanced grid faults. First, the operation of the current controller in full positive current injection mode is presented. During the simulation, the grid voltage presents harmonic distortion with -5th and + 7th harmonics ($|V_5|$=0.02 pu and $|V_7|$=0.01 pu) and the HCM is activated. The GSC ratings are 4.5 A peak and prior to the fault the RES is operating at the rated value (2 kW). At 1 s an unbalanced Type C (2-phase with no ground) fault occurs at the PCC with 65% voltage sag. The current controller continues to operate with the UCM deactivated until 1.1 s. At 1.1 s the UCM is activated and the results are presented in Fig. 6.6. It is obvious from Fig. 6.6 that the current controller without the UCM cannot inject symmetrical sinusoidal currents due to the effect of the unbalanced grid voltage and the converter ratings are violated. The proposed UCM enables the fast and accurate injection of full positive sequence symmetrical currents without violating the inverter limits in less than 10 ms. Further, the HCM enables the high quality pure sinusoidal current injection since it can compensate the effect of voltage harmonic distortion. Therefore, the proper operation of the proposed current controller is obtained under unbalanced grid faults and harmonic distorted conditions.

The operation of the proposed current controller in full negative current injection mode is demonstrated through simulation results in Fig. 6.7. The grid condition is the same as the previous case study and the same unbalanced fault occurs at 1 s. In this case study the current controller continues to operate in positive sequence current injection mode until 1.1 s with the UCM deactivated. Then, at 1.1 s the UCM is activated and the mode of the current controller is changed to full negative current injection. The results are presented in Fig. 6.7, where the proper fast and accurate injection of symmetrical negative sequence currents is ensured by the proposed current controller during unbalanced grid conditions.

6.5.2 Experimental results

This first case study of the experimental investigation aims at observing the steady state performance of the current controller under unbalanced grid fault and harmonic distorted conditions. The unbalanced fault is generated as a two-phase to ground (Type E) fault from the programmable AC source, which is propagated to the PCC as a Type F [27], [91] fault with a voltage sag (d=47%) through the yD isolation transformer (see Fig. 6.5). The grid voltage presents also a low harmonic distortion ($|V_5|$=0.013 pu and $|V_7|$=0.007 pu). Fig. 6.8 shows the results of the GSC control using the proposed current controller in positive sequence current injection mode. The proposed current controller is able to inject full positive sequence symmetrical currents with a total harmonic distortion lower than 3 %. The UCM and HCM enable the proposed current controller to inject high quality and symmetrical sinusoidal currents under unbalanced and harmonic distorted grid voltage conditions.

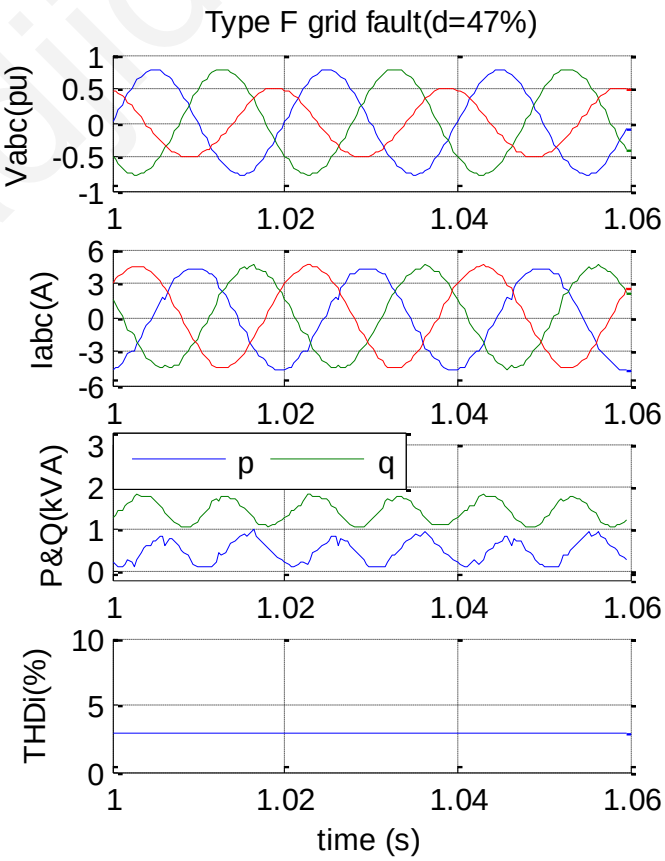

Fig. 6.8. Experimental results for the steady state operation of the proposed current controller (in positive sequence current injection mode) under a Type F (voltage dip of d=47%) grid fault.

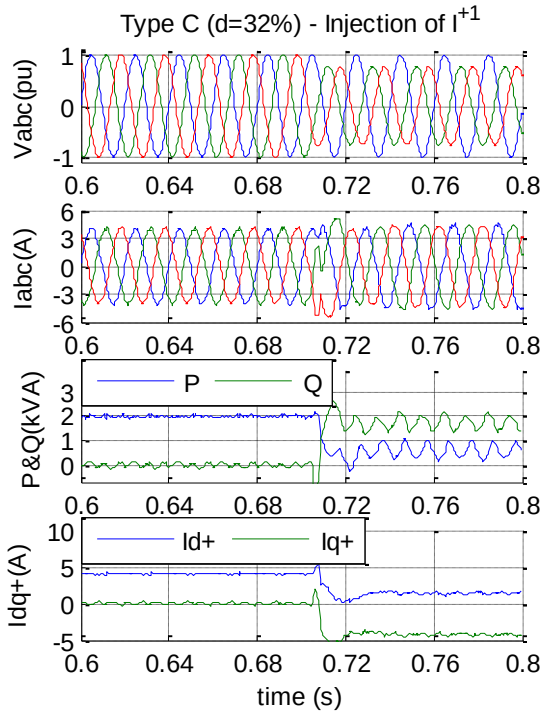

Fig. 6.9. Experimental results for the transient operation of the proposed current controller (in positive sequence current injection mode and enhanced with FRT strategy) when a Type C (voltage dip of d=32%) grid fault occurs.

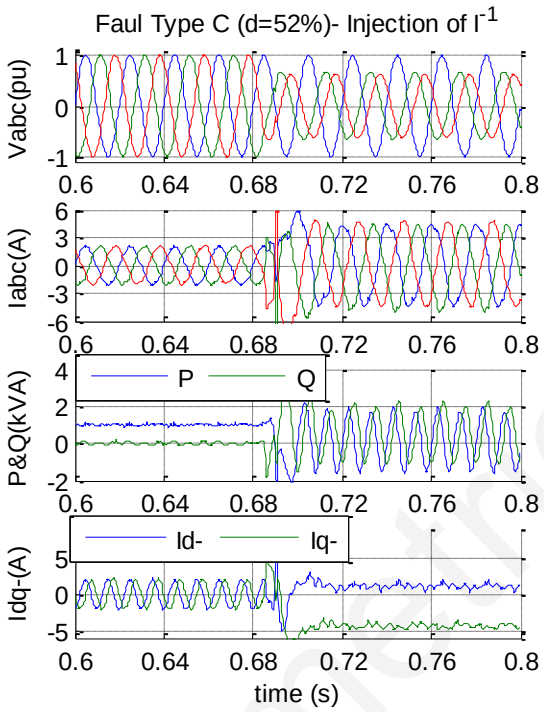

Fig. 6.10. Experimental results for the transient operation of the proposed current controller (in negative sequence current injection mode and enhanced with FRT strategy) when a Type C (voltage dip of d=52%) grid fault occurs.

The second case study was conducted to observe the transient response of the proposed current controller (in full positive sequence current injection mode and enhanced with FRT capabilities) when an unbalanced fault occurs. At 0.705 s a type C fault (2-phase with no ground) with voltage sag d=32% occurs at the PCC, as a consequence of the propagation of one phase to ground fault through the isolation transformer. The grid voltage presents the same low harmonic distortion as in the previous experimental case. Before the fault, the GSC is injecting 2 kW active and 0 kVAr reactive power and the converter rating is assumed to be 4.5 A peak. During the fault the RES should support the grid by injecting full positive sequence symmetrical and sinusoidal currents with a ratio Q:P=3 and within the GSC current ratings (4.5 A) in order to protect the converter components. Therefore, during the grid fault, the GSC delivers 1896 VAr reactive power and 632 W active power and the currents are within the converter limits as presented in Fig. 6.9. The dynamic response of the proposed current controller under FRT operation proves that the proposed current controller can achieve a fast and accurate performance since it enables the proper current injection in less than 10 ms after the fault occurs.

The last experimental case study presented in Fig. 6.10 shows the operation of the proposed current controller, when it is operating in the full negative sequence current

injection mode. A dip type C fault occurs at 0.685 s at the PCC with a 52% voltage sag. The grid voltage presents the same low harmonic distortion as all the previous experimental cases. The converter rating is assumed to be 4.5 A peak and before the grid fault occurs the GSC is injecting 1 kW active and 0 kVAr reactive power. During the fault the RES will support the grid by injecting full negative sequence sinusoidal currents with a ratio Q:P=3 and without violating the converter current ratings. The dynamic response of the current controller in full negative sequence symmetrical current injection is presented in Fig. 6.10 where the current controller achieves to inject high quality negative sequence currents within 10 ms after the fault occurs. The injection of negative sequence reactive power enables the support of the negative sequence of the grid voltage, which can allow the minimization of the unbalances of the grid voltage during the fault.

6.6 Conclusions

This chapter presents an advanced current controller with robustness against unbalanced grid conditions and harmonic distorted voltage. The proposed current controller achieves an outstanding performance, since it can enable the injection of high quality purely sinusoidal positive or negative sequence currents under unbalanced grid faults with harmonic distortion voltage conditions. The only limitation of the proposed current controller is that it can not inject unbalanced currents on purpose (e.g., injection of both positive and negative sequence currents). The advanced performance of the proposed current controller has been verified through simulations and experimental results. Therefore, the proposed current controller can be used in the controller of the GSC for enabling the FRT operation and improving the power quality of a grid connected RES. Thus, the proposed current controller can ensure the safe operation of the GSC and can enable the appropriate operation of the RES according to the modern grid regulations. Moreover, beneficial effects are expected for the entire power system by utilizing the proposed current controller, since a further penetration of RES can be promoted enable without risking the quality and stability of the power system.

CHAPTER 7
INVESTIGATION OF DIFFERENT FAULT RIDE THROUGH STRATEGIES FOR RENEWABLES

7.1 Introduction

The increasing price and the environmental impact of fossil fuels have grown the international attention on Renewable Energy Sources (RES). The worldwide installation of modern RESs, such as Wind Power Systems (WPS) and solar photovoltaic (PV) systems, presents a continuous growing trend. At the European level, RES have recently reached 14% of the total energy generation. Furthermore, according to the 2020 and 2030 frameworks of climate and energy of the European commission, the RES penetration should reach 20% and 27% respectively in the European Union.

Such an increased penetration of RES can have a significant impact on the operation of the power system. Therefore, several grid regulations have been issued in order to ensure the proper Fault Ride Through (FRT) operation of RES for enhancing the stability of the power system. It is worth mentioning that one of the main objectives of this dissertation is to improve the RES performance with regards to the FRT operation by improving the main synchronization and control units of the GSC as already shown in Chapters 2-6. This chapter aims to investigate the operation of RES, according to the proposed synchronization and control techniques, under different FRT strategies as defined by the grid regulations. Thus, the investigation performed within this chapter aims to consider the impact on the entire power system by the proper FRT operation of RES.

For enabling an even more increased penetration of RES, the grid interconnection of RES should be improved in order to support the grid under grid disturbances. The need for advancing the RES controllers for the proper grid interconnection is demonstrated through the evolution of grid regulations in the recent years. International standards [5]-[10] for the performance of distributed generation systems have been derived.

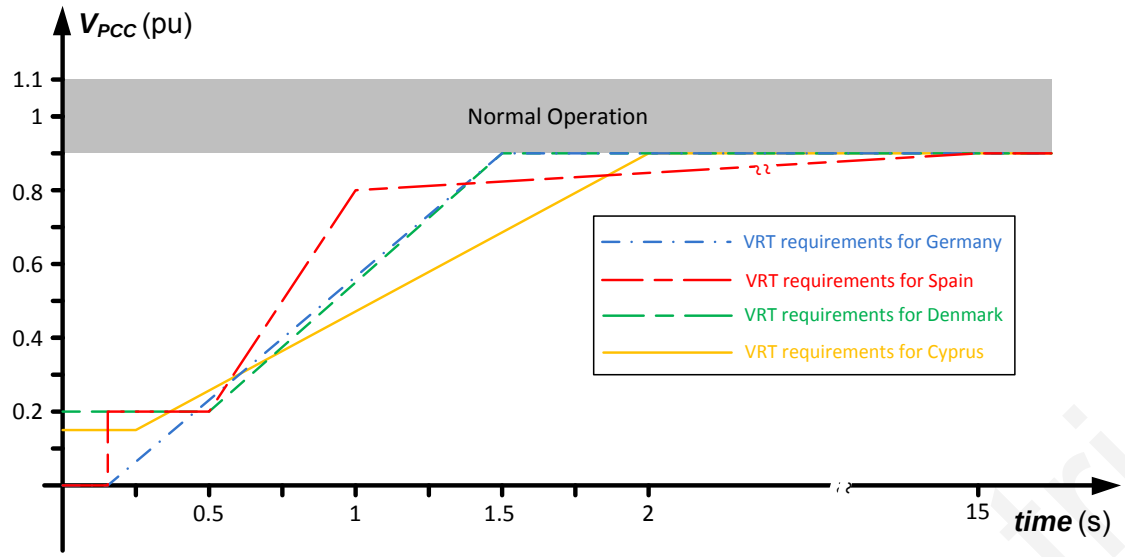

Fig. 7.1. Grid-connected RES should remain interconnected when the voltage at the PCC is above the line defined by the corresponding grid regulations.

Furthermore, local grid codes [11]-[27] have been issued in each country in order to guarantee the appropriate performance of grid-connected RES. These regulations define the desired RES operation under normal and abnormal grid conditions. According to these grid codes, an interconnected RES at the medium or high voltage level of the power system should be enhanced with FRT capabilities in order to ensure a proper operation under grid faults. An example of such FRT regulations for RES is demonstrated in Fig. 7.1, for four different countries; Germany [11], [12], Spain [13], [14], Denmark [15], [16] and Cyprus [17]. According to these regulations, interconnected RESs should keep their synchronization and remain grid-connected, when the voltage at the Point of Common Coupling (PCC) is above the characteristic line set by the regulations of each country, as presented in Fig. 7.1. It is to be noted that according to grid codes of Germany and Spain, RES should remain interconnected for 150 ms even under zero voltage conditions. Similar FRT regulations are expected to be issued for the interconnection of RES at the low-voltage level distribution network due to the significant amount of residential rooftop PV installations. So far, only Italy [20] and Japan [22] have issued such FRT regulations for residential RES.

Furthermore, when the voltage at the PCC is not within the normal operation window, the corresponding Low-Voltage Ride Through (LVRT) or High-Voltage Ride Through (HVRT) operation of RES should be activated. The LVRT and HVRT regulations are described in Fig. 7.2 for the case of Germany and Cyprus. According to these regulations for FRT operation, RES should inject or absorb respectively a proper reactive

current (I_Q) within 20 ms after the occurrence of the voltage fault. The proper reactive power injection is defined by the ratio k and the voltage sag $\Delta V=V_N-V_{PCC}$, where V_N is the nominal voltage and V_{PCC} is the voltage measurement at the PCC. The ratio k is given according to the grid regulations as,

$$k = \frac{I_Q}{\Delta V} \tag{7.1}$$

The value of ratio k should be greater or equal to two in order to provide a proper voltage support under grid faults according to [11], [12], [17]. Hence, the grid regulations specify that the grid-connected RESs should keep their synchronization under grid faults and additionally should operate fast and properly in order to provide support to the power system under grid disturbances. In that way, the stability of the power system in enhanced and undesired cascading events, which may lead to blackouts are avoided.

Hence, grid regulations determine, besides others, the desired operation of RES regarding the voltage and frequency normal operation window, the active/reactive power operation window according to grid frequency/voltage variations, the FRT capability, the reactive current support under LVRT or HVRT conditions, and the power quality specifications for limiting the injection of harmonic currents for the proper electromagnetic compatibility according to [9].

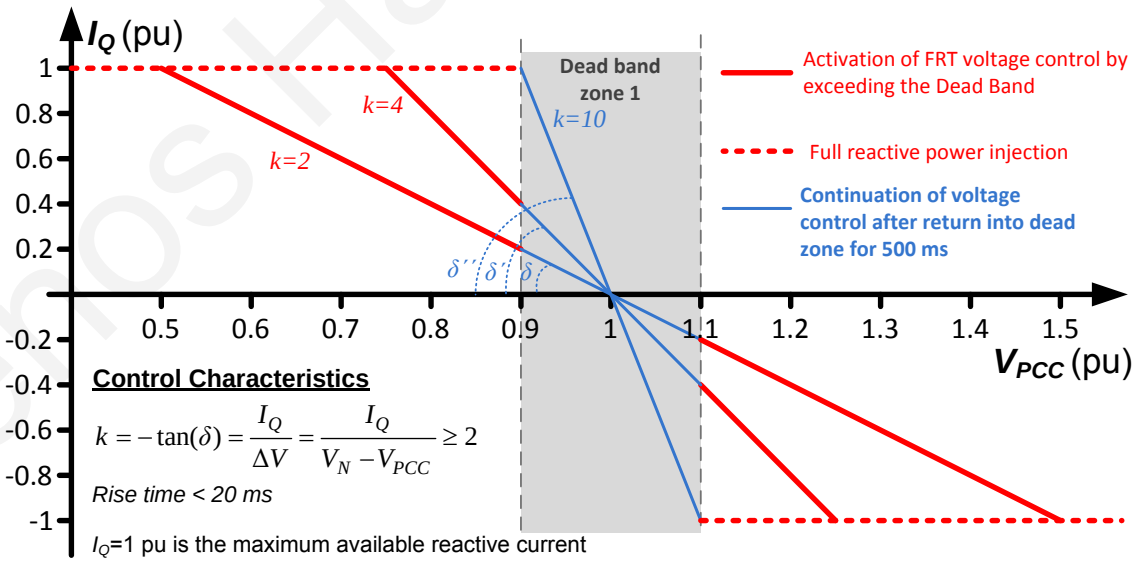

Fig. 7.2. Required reactive current support under LVRT and HVRT operation according to the grid regulations of Germany and Cyprus.

In the literature, several studies have been undertaken for investigating the FRT operation of RES. In general, these investigations are performed from two different perspectives. On one hand, researchers who focus their studies on the RES side are using advanced dynamic renewable models (based on switching power electronic devices) on the RES side, but they consider weak power systems with no dynamics on the grid side, such as the studies presented in [31], [33], [35], [92]-[96], [121]. In this case, the investigation of FRT operation of RES is based on ElectroMagnetic-Transient (EMT) simulations, providing instantaneous values of voltages and currents in the grid. On the other hand, researchers who focus their studies on the grid side consider full dynamic models for the power system components but they use simplified models for the renewables, as presented in [122], [123]. In this case, the analysis is usually based on Root Mean Square (RMS) simulations. The advantage of using RMS simulations is that the simulation speed can be significantly increased allowing the simulation of large scale power systems, but the simulations omit the fast electromagnetic transient phenomena and the switching effect of the power electronic devices. Thus, an exact realistic response, especially for the RES, is not possible by RMS simulations.

In this chapter, the FRT investigation is based on EMT simulations for the IEEE 14-bus test system implemented in PSCAD software, where a 20 MVA RES has been integrated at bus 13. Detailed and advanced EMT models have been used for both the synchronous machines and the power electronic Grid Side Converter (GSC) of the RES, allowing an analytical and transient study for the interactions between the power electronics based RES and the dynamic power system. Furthermore, this implemented simulation model allows an in depth investigation of the current FRT strategies according to the grid regulations. The investigation indicates some issues on the current regulations that were not considered previously. Slight modifications of the current grid codes are therefore suggested for overcoming these problems. These modifications include the addition of a critical dead band zone for a smoother fault recovery and the introduction of an adjustable parameter $k_1(f_{gr})$ for a fair compromise of voltage and frequency support.

7.2 Dynamic system model

The impact of the FRT strategies of RES on the operation of the power system requires the implementation of a dynamic power system model with integrated RES within the same simulation framework, as shown in Fig. 7.3. Thus, the IEEE 14-bus system has been implemented in PSCAD using detailed EMT models for each machine as shown in

Fig. 7.3. The network parameters for the IEEE 14-bus test system and the initial power flows of the system have been set according to [124]. The synchronous generators and condensers of the dynamic power system are modelled based on the sixth order machine model. The generator model is equipped with an associated exciter, turbine and governor while the condenser model is only equipped with an exciter as demonstrated in Fig. 7.3. The machine, turbine, governor and exciter parameters are set according to the typical parameters given in [125], [126].

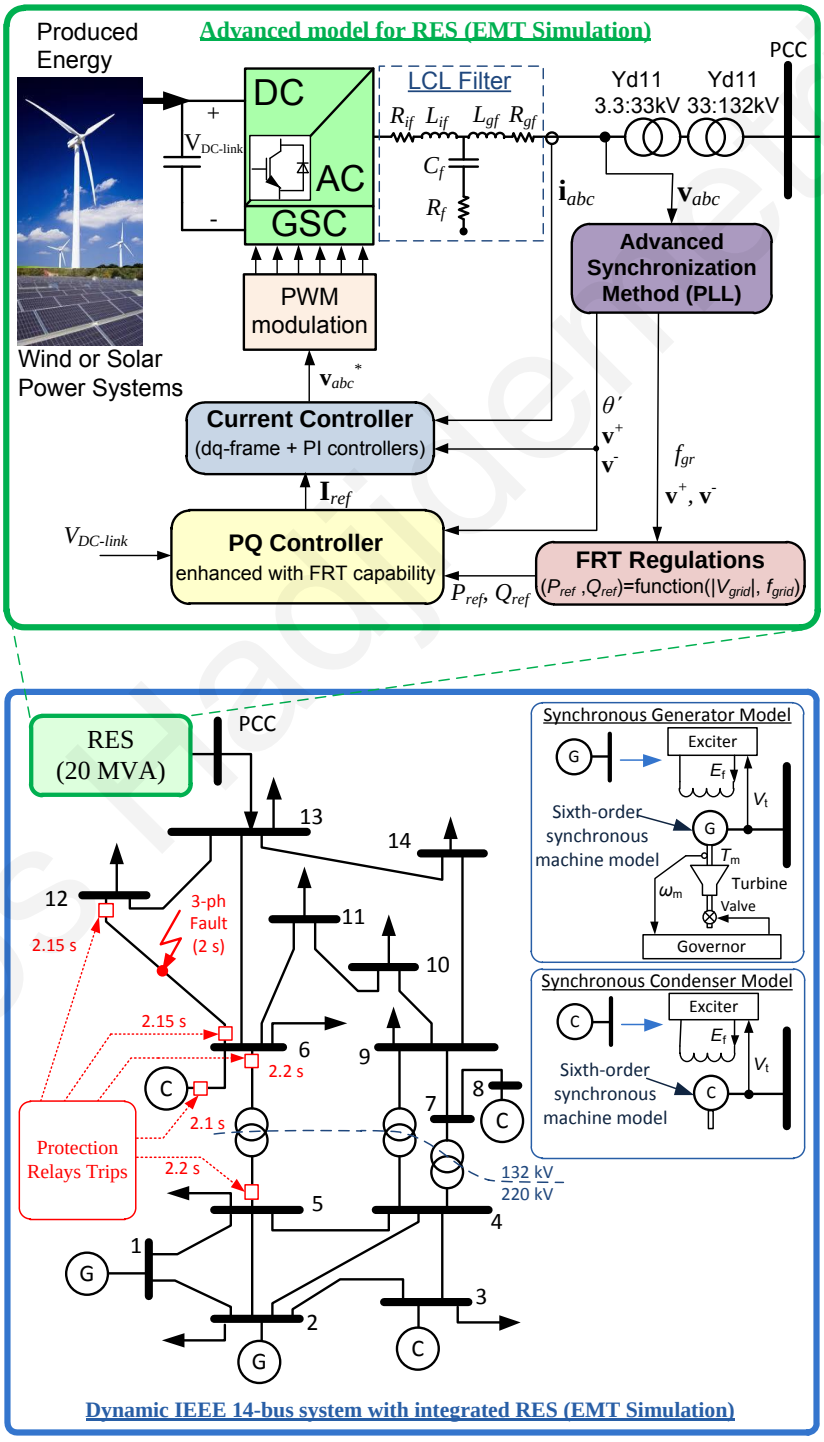

Fig. 7.3. The dynamic system model setup that allows the evaluation of the impact of different RES FRT strategies on the power system operation.

TABLE 7.1: RES DYNAMIC MODEL - DESIGN PARAMETERS FOR THE CENTRAL GSC

GSC nominal values	V_N=3.3. kV, f_N=50 Hz, S_N=20 MVA, $V_{DC\text{-}link}$=10.6 kV
LCL filter	L_{if}=1.5 mH, C_f= 292 μF, L_{gf}= 86 μH R_{if}=45.8 mΩ, R_f= 176.3 mΩ, R_{gf}= 2.7 mΩ
Sampling and PWM	$f_{SAMPLING}$ = f_{PWM} =4.9 kHz
PLL (tuning parameters)	k_P=92, T_I=0.000235
Current controller (tuning parameters)	k_P=1.3499, T_I=0.0229

Additionally to the dynamic power system simulation, a full detailed EMT model for a RES (based on a 20 MVA central power electronic GSC) has also been developed in the same PSCAD model. The RES is interconnected at bus 13 of the IEEE 14-bus system (Fig. 7.3). Bus 13 is considered as the Point of Common Coupling (PCC). The GSC of the RES is actually a typical three-phase two-level Pulse Width Modulation (PWM) Voltage Source Converter (VSC) based on six switching Insulated-Gate Bipolar Transistors (IGBT). The GSC injects high quality currents into the grid through an LCL filter and two step-up transformers (Fig. 7.3). The LCL filter has been designed according to [127]. The design parameters of the RES hardware are summarized in TABLE 7.1.

The GSC controller is implemented in the synchronous reference frame (*dq*-frame) using Proportional-Integral (PI) controllers and includes a synchronization method, a current controller and an active and reactive power controller (PQ Controller) enhanced with FRT capabilities as already explained in Chapters 2-6. The sampling and switching frequency of the controller is set to 4.9 kHz. The synchronization of the GSC controller is achieved by an advanced phase-locked loop (PLL) algorithm [29], [31], [35] (Chapters 2-4) that tracks fast and accurately the voltage phase angle under any grid conditions. The use of an advanced PLL method is necessary in order to achieve an appropriate and fast performance by the GSC as it is required by the grid regulations. Further, the use of an advanced synchronization method is also compulsory in order to allow the FRT investigation under unbalanced grid faults. The current controller of [40] (Chapter 6) is used to ensure the high quality current injection under normal and abnormal operation. The use of such advanced current controller is also essential for evaluating the performance of RES and of the entire power system under any kind of balanced and unbalanced grid disturbances. TABLE 7.1 provides the tuning parameters used in the development of the PLL and the current controller. An advanced PQ controller enhanced with FRT capabilities

has been developed according to [31], [33], [35] (Sections 2.4.2, 3.3.3, 4.4.5 and 6.3). The PQ controller regulates the active and reactive power injection by considering the produced energy of RES (DC-link voltage controller), and the amplitude and frequency of the grid voltage at the PCC (based on the FRT regulations presented in Fig. 7.2). Hence, the implemented dynamic model in the same simulation tool for both the RES and the power system enables the investigation performed in this chapter.

7.3 Investigation of fault ride through (FRT) operation

The implemented dynamic EMT model described in Section 7.2 (IEEE 14-bus system with integrated 20 MVA RES in PSCAD) allows a deeper evaluation of the RES FRT strategies on the operation of power systems. Due to the full analytical EMT models that have been used for both the RES and the power system model, this investigation considers all the transient phenomena of the power system due to the dynamic response of the machine and the fast dynamics and switching operation of the RES. In this benchmarking study, the power system operation when the RES operates according to current FRT regulations is demonstrated. However, under specific circumstances, the operation based on current FRT regulations highlights some problems. Modifications for overcoming these problems are suggested in Section 7.3.2.

7.3.1 FRT operation based on current regulations

According to the modern grid codes [11]-[27], when a RES senses a low-voltage grid fault at the PCC it should ensure its synchronization, remain interconnected, and provide reactive FRT support to the power system as already demonstrated in Fig. 7.1 and Fig. 7.2. The injection of reactive power (Q) is beneficial for the voltage (V) of the power system and correspondingly the injection of active power (P) for the frequency (f) of the system. The proper voltage support is defined by Fig. 7.2 according to [11], [12], [17]. The amount of reactive current (I_Q) that should be injected by the RES within less than 20 ms is defined by the grid codes as,

$$I_Q = k(V_N - V_{PCC}) = k\Delta V \tag{7.2}$$

where V_N is the nominal voltage (1 pu) and V_{PCC} is the voltage at the PCC. The parameter k determines the FRT type between voltage and frequency support. Regulations define this parameter as $k \geq 2$. Thus, for k=2, the FRT support is a compromise between Q and P. On the other hand, for k=10, when the V_{PCC} exits the Dead Band (DB) zone 1 (defined as $90<V_N<110\%$) the FRT operation provides only Q.

Since the reactive current is defined by regulations, the active current injection (I_P) by the RES should also be adjusted accordingly. In case where the GSC current ratings ($I_{GSC\text{-}ratings}$) are not violated due to the increased reactive current injection, then the instant active current should keep delivering all the produced energy by the RES to the grid. Otherwise, in case where there is a violation on the GSC current ratings, then the active current should immediately decrease for maintaining the converter operation within the GSC ratings as given by,

$$I_P = \sqrt{{I_{GSC-ratings}}^2 - {I_Q}^2} \tag{7.3}$$

As a result, the delivery of the produced energy by the RES will also be decreased accordingly in order to protect the GSC.

An investigation is performed to study the impact of the FRT operation of RES on the power system and the results are summarized in TABLE 7.2. The investigation examines a three-phase short-circuit event that occurs at the middle of line 6-12. The three-phase fault causes the tripping of the protection relays of: the line 6-12; the condenser at bus 6; and the transformer 5-6 within 200 ms in order to clear the fault as presented in Fig. 7.3. It is to be noted that the RES is generating 18 MW and 0 MVAr before the grid fault occurs and that the primary energy production capability of RES is considered as constant during the simulation.

TABLE 7.2: SUMMARY OF THE RESULTS FOR DIFFERENT FRT STRATEGIES

RES operation under low-voltage grid fault		Lower V_{Bus} (pu)	Number of buses out of limits	Comments
Disconnection of RES		0.73	6	-Deeper voltage sag -Causes further disturbances (loss of active power production)
FRT according to current grid regulations	k=0	0.81	5	-V and f support -For k=0: only frequency support -For k=5, 8, 10: Undesired repetitive small voltage dips (5-10%) due to the discontinuous character of DB 1 -For k=10: High P and Q variations can negatively affect the dynamic behavior of the machines
	k=2	0.84	5	
	k=5	0.86	3	
	k=8	0.87	3	
	k=10	0.88	3	
Critical DB zone modification	k=2	0.83	5	-V and f support -Avoid the repetitive voltage dips near DB1 due to the insertion of critical DB2 -Smooth fault recovery
	k=5	0.85	3	
	k=8	0.86	3	
	k=10	0.87	3	
Adjustable $k_1(f_{gr})$ + Critical DB modification	$k_1(f_{gr})$	0.87	3	-V and f support -Smooth fault recovery (DB2) -Fair compromise between voltage and frequency support, especially during under-frequency conditions

The first case study of TABLE 7.2 presents the results when the RES loses the synchronization and is disconnected from the grid when the event occurs. This is the worst-case scenario (since it causes further disturbance to the system by disconnecting a distributed generation unit from the grid) which forces six buses of the system to be outside the regulation limits with the lower operating voltage at 0.73 pu.

The second case study of TABLE 7.2 focuses on the FRT operation according to the current grid codes (for k=0, 2, 5, 8, 10). The results show that, in general, by increasing the value of parameter k, the provided voltage support is increased and thus, fewer buses are violating the voltage limits (the lower operating voltage of the system is also increased). The second case study begins with k = 0, even if this is not a current practice (since regulations define $k \geq 2$). This case represents an operation where the RES remains interconnected and synchronized with the grid, and provides only frequency support by injecting active power (P) to the power system. However, the results in TABLE 7.2 (five buses outside the voltage limits, lower bus voltage at 0.81 pu) show that this is a more desirable solution rather than disconnecting the RES during a grid fault. By increasing the value of k to 2 (current practice), a more compromising voltage and frequency support is applied, as presented in Fig. 7.4 and TABLE 7.2 (five buses outside the voltage limits, lower bus voltage at 0.84 pu). It is to be noted that all the results presented in this Section demonstrate only the voltages at all 132 kV buses of the IEEE 14-bus test system, since the voltage at all 220 kV buses always lies within the limits during fault recovery. Further improvement on voltage stability can be achieved by increasing the value of parameter k as shown in TABLE 7.2.

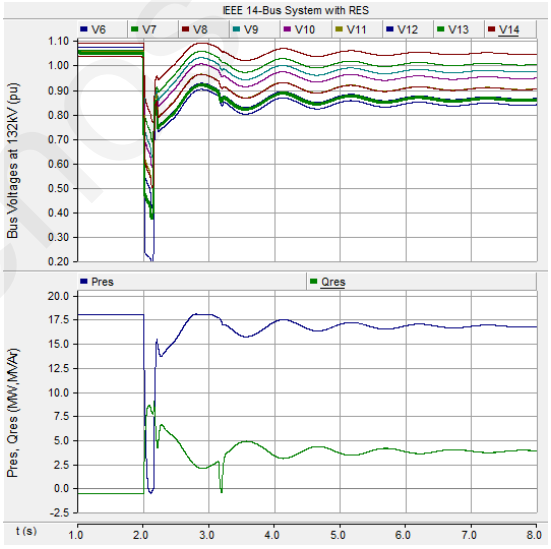

Fig. 7.4. IEEE 14-bus test system response when the RES operates according to the current grid regulations with k=2.

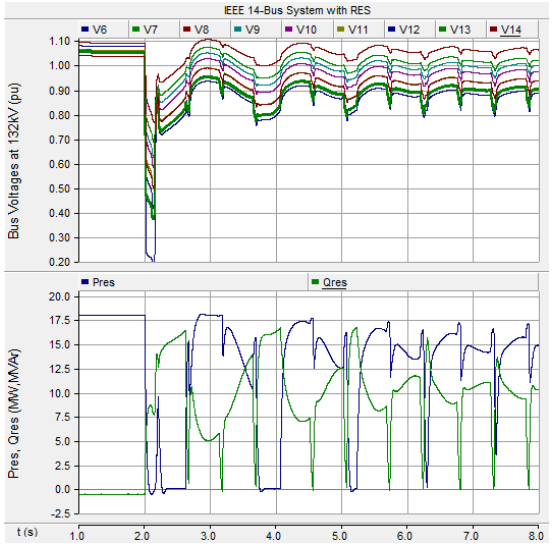

Fig. 7.5. IEEE 14-bus test system response (under specific circumstances) when the RES operates according to the current grid regulations with k=8.

However, under specific circumstances where the RES FRT support is sufficient to maintain the voltage at PCC within the limits, serious problems may be caused, especially as the value of *k* is increasing. These problems occur due to the fact that the reactive power support continues only for 500 ms after the voltage return within the DB zone 1. After 500 ms, the reactive power support by the FRT is stopped, imposing a discontinuity that causes intense reactive power fluctuation. The above-mentioned phenomena are observed in this case study when *k* is set to 5, 8, and 10. Power system operation according to Fig. 7.5, where RES operates according to the current FRT regulation (with *k*=8), indicates repeated voltage sags (3-10%) every 500 ms due to this discontinuity effect of the FRT. Hence, at the moment when the reactive power support stops (500 ms within DB zone 1), the voltage drops below the limits, forcing the RES to operate again according to the FRT regulations. This phenomenon is repeated as long as the voltage stability at the PCC is dependent on the reactive support by the RES. As *k* is increased, the discontinuity impact of the DB zone is more intense (due to higher *P* and *Q* fluctuation of RES). In some occasions (as the one presented in Fig. 7.6), such intense power fluctuations of RES can cause undamped oscillations on the synchronous machines operation, and as a result, the stability of the whole power system is also affected. These phenomena can be observed by the developed simulation model of both the dynamic power system and the RES due to the fact that full detailed and dynamic EMT models have been used to simulate the performance of the entire system.

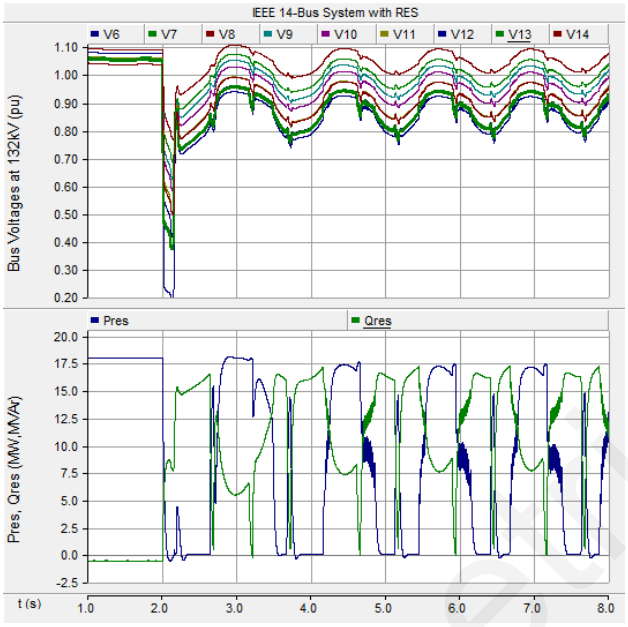

Fig. 7.6. IEEE 14-bus test system response (under specific circumstances) when the RES operates according to the current grid regulations with *k* =10.

7.3.2 Proposed modifications

The investigation of Section 7.3.1, highlights two issues; the undesired power fluctuations due to the discontinuity of DB zone 1, and the trade-off between voltage and frequency support of the FRT according to parameter *k*. This Section proposes two modifications on the FRT regulations for improving the power system operation.

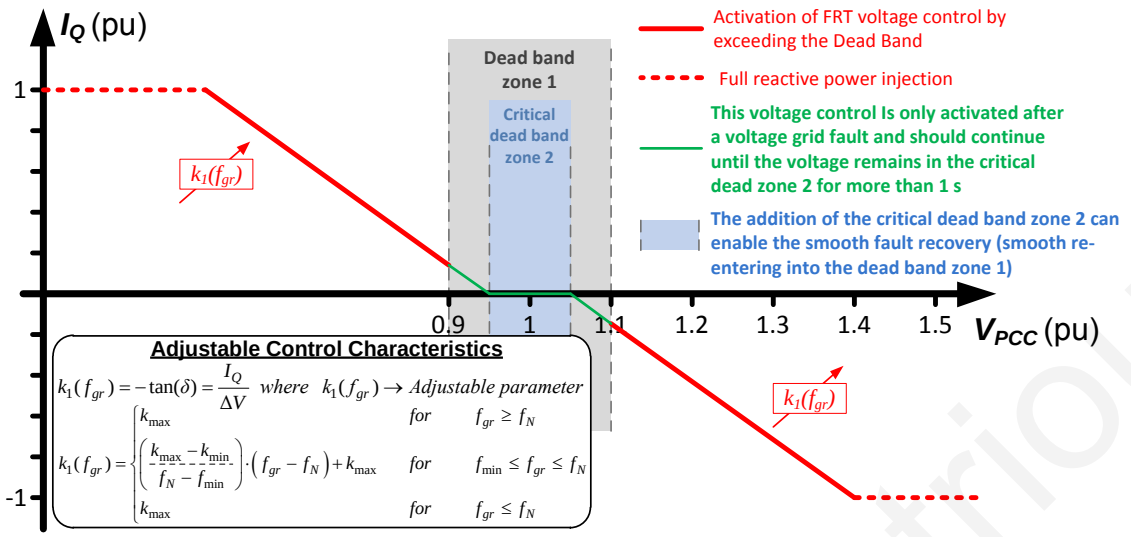

Fig. 7.8. Proposed modifications on the FRT voltage control strategy.

The discontinuity of DB zone 1 can cause undesired repeated power fluctuations of the RES when the voltage recovery at the PCC is achieved only with the contribution of RES. To overcome this undesired repetitive phenomena, a slight modification of current FRT regulations is proposed as shown in Fig. 7.8. The modification adds a new critical DB zone 2 (defined as $95<V_N<105\%$), which is only activated after a voltage sag event. The new voltage control as presented in Fig. 7.8 avoids the discontinuities effect on the fault recovery, since the termination of the voltage control is only achieved after the voltage returns smoothly (without discontinuities) into the critical DB zone 2 for more than 1 s. The results for this modification are presented in the third case study of TABLE 7.2. The results show that the FRT properly supports the system for various values of k without imposing repetitive voltage sags (and power fluctuations). The proposed modification causes a 1% lower voltage compared to the second case study (due to the offset added in the proposed FRT support), but it eliminates undesired phenomena. The improved operation of power system (avoiding undesired repetitive voltage sags) is demonstrated in Fig. 7.7, where

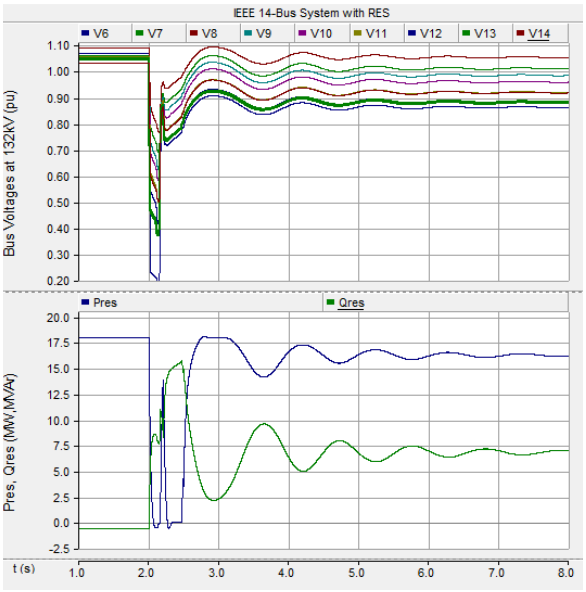

Fig. 7.7. IEEE 14 bus system response when the RES operates according to the suggested FRT strategy with the additional DB zone 2 and constant k =8.

the RES operates according to the proposed FRT modification (with the additional critical DB zone 2) with k=8.

The second modification tries to compromise the FRT between voltage and frequency support. Higher values of k enhance the voltage but can inversely affect the frequency support. It is worth mentioning that when a grid fault occurs, it usually affects both the voltage and the frequency of the system. Especially during under-frequency operation, a high value of k can cause cascading events in the system. Hence, a modification in FRT regulations is proposed for balancing the trade-off between voltage and frequency support. In this modification, parameter $k_1(f_{gr})$ of (7.4) is adjusted during an event according to the grid operating frequency (f_{gr}). Therefore, the new I_Q and I_P will be real-time adjusted (according to both the voltage and the frequency of the grid) providing a more properly FRT operation (better compromise between V and f support).

$$k_1(f_{gr}) = \begin{cases} k_{\max} & , f_{gr} \geq f_N \\ \left(\dfrac{k_{\max} - k_{\min}}{f_N - f_{\min}} \right) \cdot \left(f_{gr} - f_N \right) + k_{\max} & , f_{\min} \leq f_{gr} \leq f_N \\ k_{\min} & , f_{gr} \leq f_N \end{cases} \quad (7.4)$$

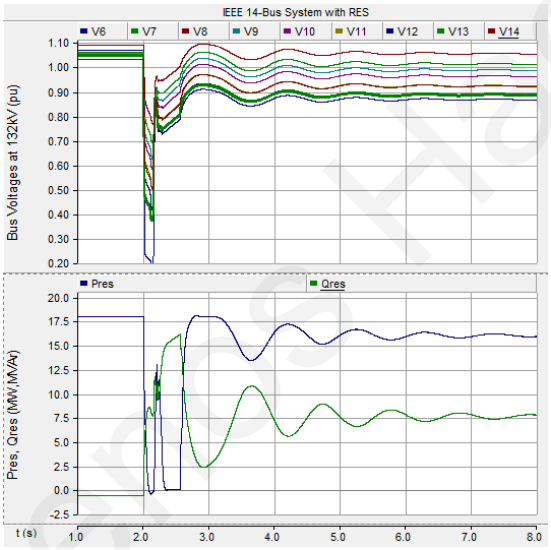

Fig. 7.9. IEEE 14 bus system response when the RES operates according to the suggested FRT strategy with the additional DB zone 2 and the adjustable $k_1(f_{gr})$.

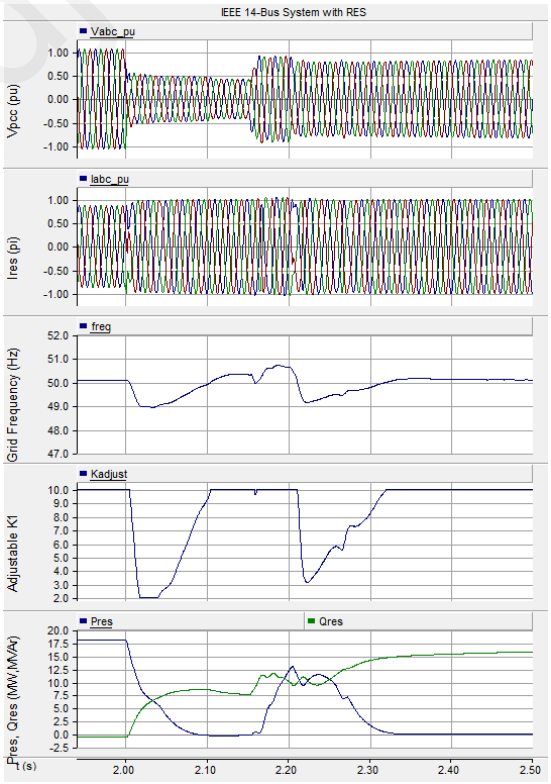

Fig. 7.10. The RES response when it operates according to the suggested FRT strategy with the additional DB zone 2 and the adjustable $k_1(f_{gr})$.

Fig. 7.9 presents the power system operation with the adjustable $k_1(f_{gr})$ modification. The last case study of TABLE 7.2 summarizes the evaluation of the above modification for k_{max}=10, k_{min}=2, f_N =50 Hz, and f_{min}=49 Hz. Additionally, Fig. 7.10 presents EMT simulation for the RES response according to the adjustable $k_1(f_{gr})$. It is clear that a proper voltage support is still provided during low-voltage events. In the meantime, when the RES also senses an under-frequency operation, it adjusts its support (by adapting $k_1(f_{gr})$) to fairly mitigate both voltage and frequency disturbances.

7.4 Conclusions

This chapter investigates the FRT operation of RES according to current grid regulations for providing support to the power system under grid faults. This investigation is necessary since one of the main objectives of this dissertation is to improve the RES performance with regards to the FRT operation by improving the main synchronization and control units of the GSC. The FRT operation of RES according to the current grid codes can enhance the stability of the power system. However, the investigation performed in this chapter highlights two issues of the current FRT regulations on the power system response that were not considered previously. Firstly, undesired power fluctuations imposed by the RES due to the discontinuity of DB zone may repeatedly cause small voltage sags and undamped machine oscillations. Secondly, the trade-off between voltage and frequency support of the FRT is required to be fairly balanced. Hence, a critical DB zone modification and an adjustable $k_1(f_{gr})$ modification are proposed to address these problems. Novel EMT simulations on the IEEE 14-bus system with integrated RES are used to investigate both current and proposed FRT strategies in order to properly capture all the transient dynamics phenomena of the power system and the switching operation of the power electronic based RES. The RES operation is based on the advanced synchronization and current control techniques that have been proposed within this dissertation. The simulation results demonstrate the beneficial effect of the proposed modifications in the operation of the power system.

CHAPTER 8
ENHANCING THE VOLTAGE STABILITY OF THE POWER SYSTEM THROUGH A CENTRALIZED CONTROL OF RENEWABLES

8.1 Introduction

In recent years the power systems infrastructure has experienced rapid changes. The large penetration of Renewable Energy Sources (RES), the use of electric vehicles as an alternative transportation means, and the distributed generation in the distribution level of the power systems are some of the factors that make the operation of the power systems different from the standard practices used in the past decades. Additionally, power systems are being operated close to their physical limits in an attempt of the electric utilities to remain competitive in the deregulated electricity market and to satisfy the ever increasing electricity demand. Consequently, power systems are more vulnerable to severe contingencies whose propagation to a large portion of the power system may cause a total system blackout.

The integration of modern RES, such as wind power systems and solar photovoltaic systems, has steadily increased in the recent years in the vision of significantly decreasing the carbon emissions produced by the conventional power plants. Although the incorporation of the RES in the power system network is environmentally beneficial, at the same time it poses some challenges regarding their smooth operation and control. In this sense, the RES should be considered not only as passive elements in the power system network, but, if possible, as ancillary services for the mitigation of evolving contingencies. In this chapter, a methodology is proposed to preserve the voltage stability of the power system after the occurrence of a contingency utilizing the RES capabilities.

An example of a power system contingency is the voltage drop below the nominal level of a particular bus or of several buses in an area of the power grid. This may lead to power system voltage instability unless it is prevented timely. In general, voltage instability in power systems occurs due to the load dynamics to preserve power

consumption beyond the power capacity of the power system [128]. There are several methodologies in the literature that deal with the timely detection of the voltage instability and which can be classified to local and wide area methods [129]. In [130], a constrained optimal power flow approach based on static line voltage stability indices to overcome voltage instability is proposed. A load shedding scheme for controlling the voltage stability of the power system is proposed in [131], while in [132] a controlled load shedding approach based on the reactive power of the generators is developed.

In order to limit the effects of the potential power system voltage instability to a large portion of the system, enhanced monitoring applications accommodated in the control center should be used. For instance, the power system state estimator is a key-element of the control center providing the power system states (i.e., bus voltage magnitudes and angles) in consecutive intervals of 5 seconds to 5 minutes. It is to be noted that for estimating the power system states in consecutive interval of less than a minute, the power system should be fully or partially observable by synchronized Phasor Measurement Units (PMUs). Thus, given that the long-term voltage instability is a relatively slow process [128], a voltage drop in a particular area of the power grid can be detected timely by observing the voltage magnitudes of the buses provided by the state estimator.

In this chapter, a voltage drop is detected by examining the states that are provided by an accurate state estimation scheme [133] within the control center of the Transmission System Operator (TSO). Further, the RES can provide ancillary services for maintaining the power system voltage stability. More specifically, the reactive power compensation for raising the bus voltage magnitude to the appropriate level can be given by the RES that is geographically close to the area of the voltage drop. It is to be noted that the voltage instability may not be observed at the Point of Common Coupling (PCC), where the RES is interconnected. In this case the local controller of the RES is not able to support the voltage of the power grid with the same way suggested in [31], [33], [35], [92]-[94], [121], since it is not aware about the voltage limit violation occurs at its neighborhood. The proposed real-time control methodology is applied at the control center of the TSO and decides the proper active and reactive power set-points for the RES that are installed geographically near the area where the voltage instability occurs. In this scheme, the voltage support by the RES can be achieved even if the voltage violation is not observed by the RES at the PCC. The exact amount of reactive power that is required for recovering the bus voltage to the appropriate voltage level is provided by iterative executions of power flow routines at the control center according to the new power set-points of the RES. It is

to be noted that the proposed control methodology can also be applied for regulating the reactive power of STAtic synchronous COMpensators (STATCOM) and Static VAR Compensators (SVC) [94] that are installed in the transmission system. The proposed methodology has been tested using the IEEE 14-bus test system with integrated RES and the results show that the voltage stability of the system can be significantly enhanced.

8.2 Proposed methodology

This chapter proposes a new algorithm for enhancing the voltage stability of the power system by utilizing the RES that are integrated within the power grid. It is important to mention that the proposed method can be executed directly from the control center of the TSO. The proposed methodology consists of two stages: the Violation detection stage and the Decision for the set-point of the RES stage, as illustrated in Fig. 8.1. In this Section, both stages will be described in detail.

8.2.1 Violation detection

In the first stage of the methodology, the voltage limit violation is detected through the observation of the power system states (i.e., bus voltage magnitudes and voltage angles), provided by an accurate hybrid state estimation scheme [133]. In general, the state estimator tool constitutes the cornerstone of the control center, since it essentially provides in consecutive time intervals the power system operating condition, using available measurements from dispersed substations. The output of the state estimator, called the state vector, contains the estimations of the voltage magnitude and angle of the power system buses, and is used in several tools for assessing and controlling power system operation.

The measurement model that the state estimator is based on is formulated as,

$$\mathbf{z} = \mathbf{h}(\mathbf{x}) + \mathbf{e}, \tag{8.1}$$

where, **z** is the measurement vector, **h**(**x**) is the vector containing the equations that relate the measurements to the system states, **x** is the state vector containing the power system states (i.e., bus voltage magnitudes and bus voltage angles) and **e** is the Gaussian noise introduced in the measurements.

Most of the state estimation schemes accommodated today in the control center are formulated based on the Weighted Least Squares (WLS) framework as,

$$Min\ J(\mathbf{x}) = [\mathbf{z} - \mathbf{h(x)}]\mathbf{R}^{-1}[\mathbf{z} - \mathbf{h(x)}], \tag{8.2}$$

where **R** is the measurement error covariance matrix, which acts as a weighting matrix for the measurements used in the state estimator.

Based on the WLS approach, the state vector **x** can be found by setting the derivative of (8.2) to zero. By expanding the derivative using the Taylor series and neglecting the higher order terms, the state vector can be obtained iteratively according to [134] and is given by,

$$\mathbf{x}^{k+1} = \mathbf{x}^{k} + [\mathbf{G}(\mathbf{x}^{k})]^{-1}\mathbf{H}^{T}(\mathbf{x}^{k})\mathbf{R}^{-1}[\mathbf{z} - \mathbf{h}(\mathbf{x}^{k})], \tag{8.3}$$

where $\mathbf{H}(\mathbf{x})$ is the Jacobian matrix and is equal to $\frac{\partial \mathbf{h}(\mathbf{x})}{\partial \mathbf{x}}$ and $\mathbf{G}(\mathbf{x})$ is the gain matrix and is equal to $\mathbf{H}^{T}(\mathbf{x})\mathbf{R}^{-1}\mathbf{H}(\mathbf{x})$.

The types of measurements used in a contemporary state estimator are the real/reactive power flows, real/reactive power injections, and voltage magnitudes. In the recent years, as Phasor Measurement Units (PMUs) are rapidly deployed in the transmission level of the power systems, there is a trend to introduce the PMU measurements to the conventional measurement vector in order to improve the accuracy of the conventional state estimator.

The type of PMU measurements are the voltage phasor of the bus that the PMU is installed, and the current phasors of the branches emanating from the PMU bus. Such a state estimation scheme that uses both conventional and PMU measurements is called hybrid (since it uses both conventional and PMU measurements) and exhibits improved accuracy in comparison to the contemporary state estimation scheme [133]. In this methodology, the hybrid state estimation scheme that was developed in [133] is utilized.

Without loss of generality, in this methodology it is assumed that the measurements arrive to the control center every 5 s, and consequently the execution rate of the hybrid state estimator is 5 s. At each 5 s interval, the voltage stability of the system is verified by checking if the estimated voltage magnitude $|V_n|$ of each bus is within the proper operating voltage window according to the grid regulations [27], which is defined as ±10% deviation of the nominal value. In case of a voltage limit violation, the methodology proceeds to the second stage for determining the reactive power set-point of the RES for maintaining power system voltage stability, as shown in Fig. 8.1. If there is no voltage limit violation, the algorithm waits for checking the next estimated states.

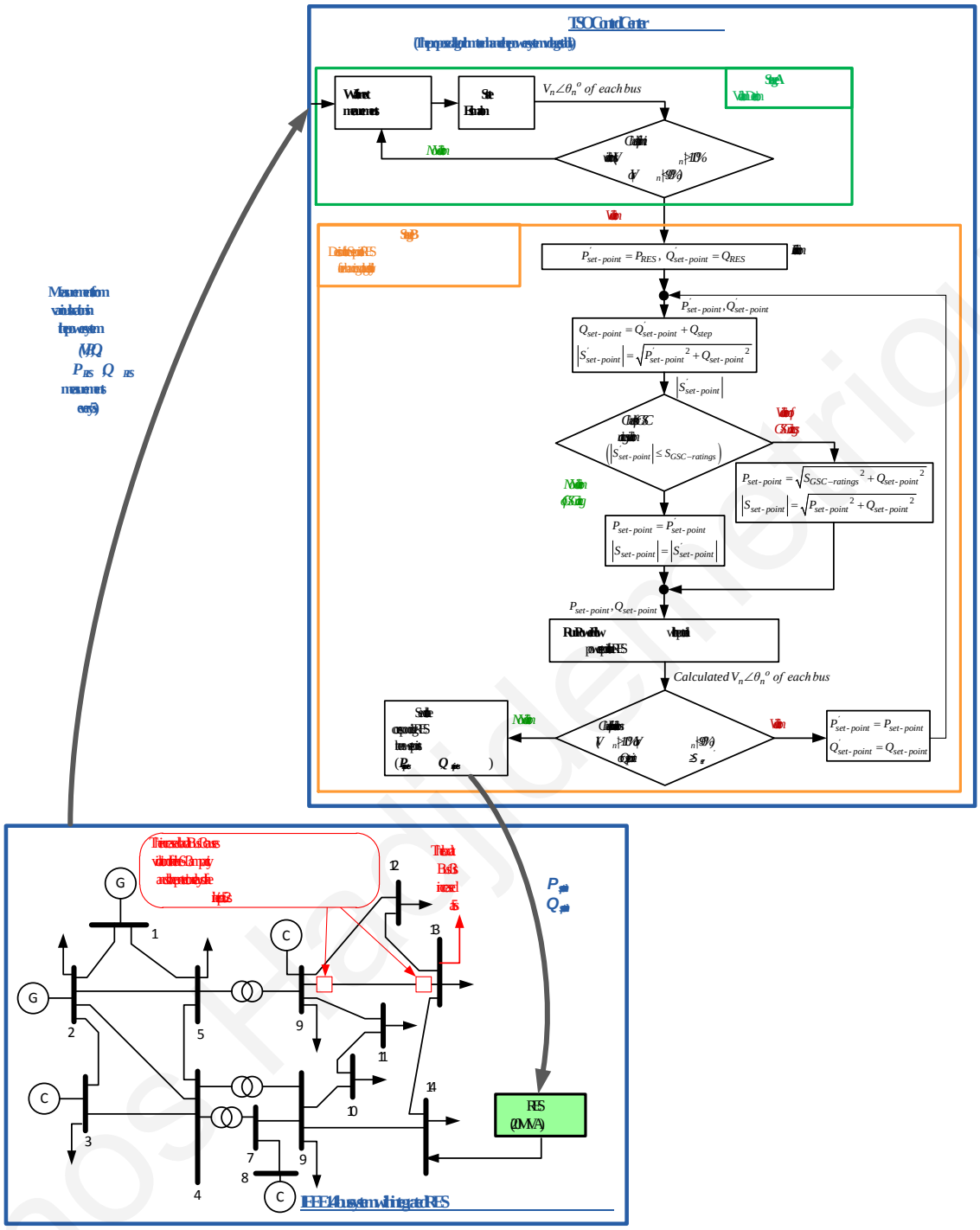

Fig. 8.1. The proposed control methodology to enhance the voltage stability of the system by utilizing the integrated RESs.

8.2.2 Decision for set-points of RES

As illustrated in Fig. 8.1, the second stage of the methodology for the proper RES set-points calculation begins with the initialization of the active and reactive power set-point. The initial values of the power set-points ($P'_{set-point}$, $Q'_{set-point}$) are assumed constant during the algorithm steps and equal to the generation of the RES (P_{RES} , Q_{RES}) according to the last set of measurements. For providing a proper voltage support to the grid, the

reactive generation set-point ($Q_{set\text{-}point}$) of the RES is changed by a certain MVAr step (Q_{step}); Q_{step} is either positive in the case that the voltage magnitude is below 0.91 p.u or negative in the case that the voltage magnitude is above 1.09 p.u. At the same time the initial amplitude of the complex power of the RES ($|S'_{set\text{-}point}|$) is calculated using the initial active power set-point ($P'_{set\text{-}point}$) and the new reactive power set-point ($Q_{set\text{-}point}$). Since the RES is connected to the grid through a Grid Side Converter (GSC) with certain MVA ratings ($S_{GSC\text{-}ratings}$) and current ratings, a check has to be performed for ensuring that the GSC power MVA ratings are not violated before applying the new power set-points to the RES. In case of GSC MVA ratings violation, the real power of the RES is adjusted to a new set point ($P_{set\text{-}point}$) as,

$$P_{set-point} = \sqrt{S^2_{GSC-ratings} - Q^2_{set-point}}, \tag{8.4}$$

while the new amplitude of the complex power set-point ($|S_{set\text{-}point}|$) which does not violate the GSC ratings is calculated as given by,

$$\left|S_{set\text{-}point}\right| = \sqrt{P_{set\text{-}point}{}^2 + Q_{set\text{-}point}{}^2} \tag{8.5}$$

Otherwise, in the case of no GSC MVA ratings violation, the real power generation of the RES remains unchanged, and the $S_{set\text{-}point}$ remains as calculated when the MVAr generation is increased.

As the new set points of the RES are determined following the aforementioned procedure, they are inserted in a power flow analysis for obtaining the voltage magnitudes in the case where the RES will provide the amount of the active and reactive power according to the new set-points ($P'_{set\text{-}point}$, $Q'_{set\text{-}point}$). It is to be noted that the power flow routine is executed in the control center for assessing the power system operating conditions and perform contingency analysis. The power flow analysis takes as input the real power generation and the voltage magnitudes of the PV buses, and the real and reactive power injection of the PQ buses. These quantities can be calculated through the latest estimated states provided by the state estimator. Further, the power flow analysis will take into consideration the new active and reactive power generation set-points of RES ($P_{set\text{-}point}$, $Q_{set\text{-}point}$). Executing the power flow analysis under these conditions the voltage magnitude values for all the buses can be updated based on the new set-points of the RES.

When the voltage limits are still violated, the reactive power provided by the RES should be set to a new set point. The procedure in the second stage of the proposed methodology is followed iteratively until all voltage magnitudes are in the permissible

limits. The final set-points ($P_{set\text{-}point}$ and $Q_{set\text{-}point}$) that are intended to restore the voltage stability of the system are sent to the RES plant to be directly applied to the RES operation.

It is to be noted that the $Q_{set\text{-}point}$ is likely to reach the GSC MVA rating during the iterative procedure, without managing to restore the voltage stability of the system (i.e., some bus voltages will still violate the limits). In such case, the maximum available $Q_{set\text{-}point}$ will be send to the RES plant, to at least improve the voltage profile of the system.

8.3 Simulation results

The effectiveness of the proposed methodology will be demonstrated within this Section through simulation results. A dynamic Electro-Magnetic Transient (EMT) simulation model has been implemented for this purpose, where a dynamic power system model and an analytical RES model have been combined under the same simulation framework of PSCAD. Then, the operation of the proposed control methodology is demonstrated for two different case studies in order to prove its effectiveness.

8.3.1 Dynamic EMT model of a power system with integrated RES

The IEEE 14-bus system has been developed in PSCAD using detailed EMT models for each machine. The transmission lines, transformers parameters and the initial power flows of the IEEE 14 bus system have been selected according to the available data in [124]. A sixth-order synchronous machine model along with its associated exciter, turbine and governor models have been used as shown in Fig. 8.2 for developing a dynamic power system model. The machine, turbine, governor and exciter parameters are set according to [125], [126] for each synchronous generator and condenser.

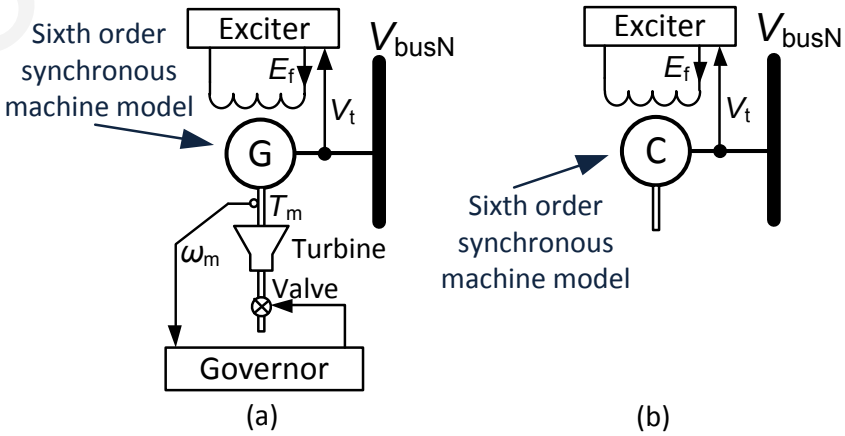

Fig. 8.2. EMT dynamic models (a) for each synchronous generator and (b) for each condenser of the IEEE 14-bus test system.

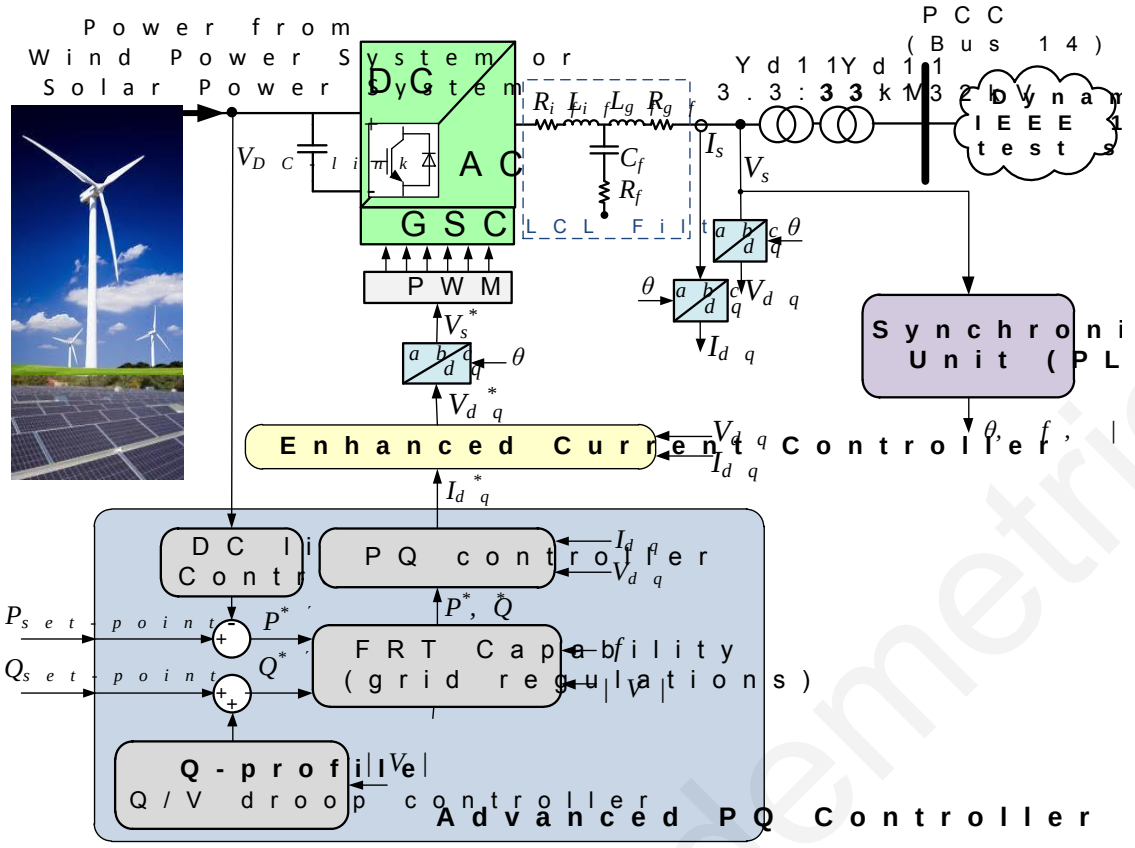

Fig. 8.3. Dynamic model of the GSC of a RES among with its controller. The RES is connected to the IEEE 14-bus system at bus 14.

Additionally to the dynamic power system simulation, a RES with a 20 MVA central GSC has been integrated at bus 14 as shown in Fig. 8.1, by using a full detailed EMT model for the power electronic GSC of the RES. The GSC of the RES has also been modeled within the same model of PSCAD based on the schematic of Fig. 8.3 with its nominal values presented in TABLE 8.1. The GSC is actually a typical three-phase two-level Pulse Width Modulation (PWM) bidirectional Voltage Source Converter (VSC) based on six switching Insulated-Gate Bipolar Transistor (IGBT). The injection of high quality currents by the GSC is enabled by designing an LCL according to [127].

The controller of the GSC is designed in the synchronous reference frame (*dq*-frame) using Proportional-Integral (PI) controllers. The controller includes a synchronization unit, an active and reactive power controller (PQ Controller) and a current controller. The synchronization method of the GSC controller is actually a phase-locked loop (PLL) algorithm and it is responsible for tracking the grid phase angle, frequency and amplitude. The synchronization method of algorithm [35] (Chapter 4) has been used allowing a fast response with immunity against balanced or unbalanced grid faults and harmonic distorted voltage. The tuning parameters of the PLL are presented in TABLE 8.1.

TABLE 8.1: RES DYNAMIC MODEL - DESIGN PARAMETERS FOR THE CENTRAL GSC

GSC nominal values	V_N=3.3. kV, f_N=50 Hz, S_N=20 MVA, $V_{DC\text{-}link}$=10.6 kV
Sampling and PWM	$f_{SAMPLING} = f_{PWM}$ =4.9 kHz
PLL (tuning parameters)	k_P=92, T_I=0.000235
Current controller (tuning parameters)	k_P=1.3499 , T_I=0.0229
LCL filter	L_{if}=1.5 mH, C_f= 292 μF, L_{gf}= 86 μH R_{if}=45.8 mΩ, R_f= 176.3 mΩ, R_{gf}= 2.7 mΩ

An advanced PQ controller has been developed according to [35] and Section 4.4.5. It regulates the active power injection (*P*) by considering the produced energy by the RES (DC-link controller) and the reactive power (*Q*) by considering the voltage at the PCC (Q-profile controller according to grid regulations as shown in Chapter 7). In the model implemented for the purpose of this chapter, the PQ controller can also adjust the GSC power according to external set-points sent by the TSO. Moreover, the PQ controller is enhanced with Fault Ride Through (FRT) capability in order to be able to support the grid when abnormal conditions are sensed at the PCC. Finally, an enhanced current controller has been developed according to [40] and Chapter 6 and has been tuned according to [120] (tuning parameters are presented in TABLE 8.1) for ensuring an accurate and high quality current injection by the GSC under any grid conditions.

The effectiveness of the proposed algorithm is tested based on the dynamic model for the IEEE 14-bus system and the RES that are developed within the same simulation framework of PSCAD. The simulation results for two case studies will be presented in the following sub-sections. Case study 1 investigates the effectiveness of the proposed algorithm when the RES initially generates 60% of its nominal power (12 MW), and case study 2 when the RES initially generates its nominal power (20 MW).

8.3.2 Case study 1

For both case studies, the simulations start with the initial power flows according to the values given in [124]. Thus, the load at bus 14, where the RES is installed, is increased correspondingly to the initial active power production of the RES in order to maintain the initial power flows. Measurements arrive at the TSO control center every 5 s (e.g., at t =2.5 s, 7.5 s, 12.5 s, ...). At t =5 s, the load at bus 13 suddenly increases by 27 MW and 11.6 MVAr, which causes the tripping of line 6-13 after 200 ms. Hence, in the next set of

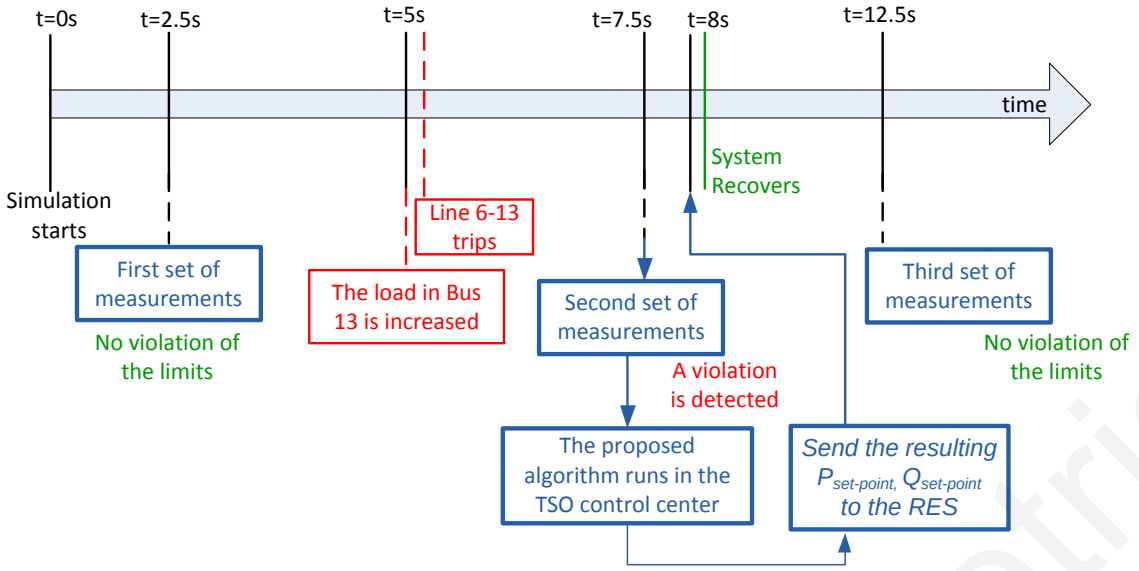

Fig. 8.4. Time sequence of the investigation with the simulation results for the two case studies.

measurements (t=7.5 s), the TSO control center will detect the voltage violation. As a result, the proposed algorithm will run for calculating the RES power set-points in order to support the voltage stability of the system. After 0.5 s, the proper power set-points will be sent to the RES and the RES will adjust its active and reactive power injection for supporting the power system and for enhancing the system voltage stability. It is to be noted that a 500 ms delay has been considered for the execution of the proposed algorithm and the communication delay for sending the set-points to the RES. Furthermore, an established communication between the control center and the RES is implicitly assumed in this chapter. The time sequence of the case studies is analytically presented in Fig. 8.4.

For case study 1, the RES initially operates at 60% of its nominal power (12 MW) and delivers only active power to the grid. At t =5 s, the load of bus 13 is increased causing a violation of the power rating of the line 6-13, which is finally tripped at 5.2 s by the protection relays (Fig. 8.1 and Fig. 8.4). Hence, after these events, the voltage at bus 13 is dropped below the permissible limits as presented in Fig. 8.5. It is to be noted that the voltage at bus 14, where the RES is integrated, is within the limits. Thus, the RES cannot detect the low-voltage conditions locally and provide FRT support to the grid.

The state estimation according to the measurements taken at 7.5 s by the TSO control center, detects the voltage violation at bus 13 ($|V_{13}|$=0.875 p.u.). Then, the proposed algorithm executes iterative power flow solutions to determine the required $Q_{set\text{-point}}$. The results for the iterative power flow solutions are summarized in TABLE 8.2. The proposed algorithm suggests that the RES should adjust their generation by increasing the reactive

power to 8 MVAr to maintain the system voltage stability (all the bus voltages above the desirable limit of 0.91 pu). Since the initial active power generation in combination with the new $Q_{set\text{-}point}$ does not violate the MVA ratings of the GSC, the active power by the RES will not change. The resulted set-points ($P_{set\text{-}point}$=12 MW, $Q_{set\text{-}point}$=8 MVAr) are sent from the TSO to the RES at t = 8 s. The simulation results of Fig. 8.6 present the dynamic response of the RES according to the new power set-points. The results of Fig. 8.6, show that the GSC adjusts the power injection of the RES according to the new set-points within less than 80 ms. As a result, the voltage stability of the system is enhanced and the violated voltage magnitude of bus 13 returns within the voltage limits. Therefore, the calculated set-points for the RES at bus 14, force the voltage at bus 13 to be equal to 0.91 pu as it is expected by the proposed methodology.

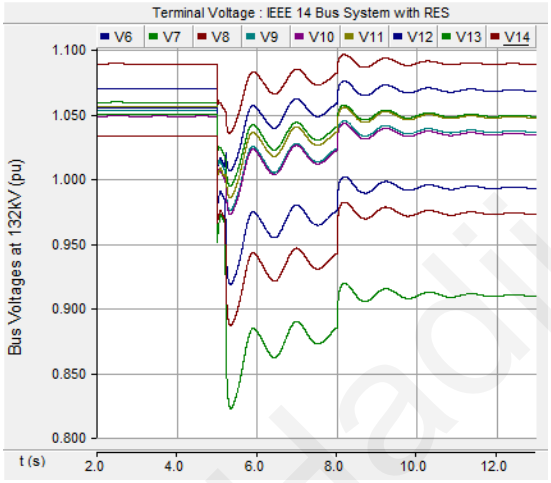

Fig. 8.5. Bus voltages for the 132 kV buses of IEEE 14-bus system for the case study 1. The RES is initially injecting 12 MW and two events occur at 5 s and 5.2 s. Measurements are taken by the TSO at t =2.5 and 7.5 s and the set-points of the proposed methodology are sent to the RES at t = 8 s.

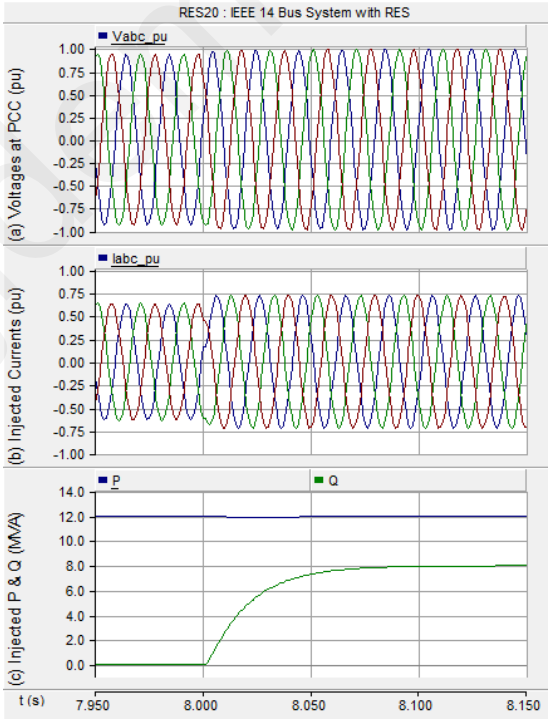

Fig. 8.6. RES response (integrated at bus 14) according to the power set-points sent by the system operator at t = 8 s for case study 1

TABLE 8.2: ITERATIVE POWER FLOW SOLUTION RESULTS FOR CASE STUDY 1
(PRESENTED RESULTS EVERY 1 MVAR FOR THE REACTIVE SET-POINT)

$Q_{set\text{-}point}$ (MVAr)	$P_{set\text{-}point}$ (MW)	V_{13} (p.u.)	$Q_{set\text{-}point}$ (MVAr)	$P_{set\text{-}point}$ (MW)	V_{13} (p.u.)
0.00	12.00	0.875	5.00	12.00	0.899
1.00	12.00	0.880	6.00	12.00	0.903
2.00	12.00	0.885	7.00	12.00	0.907
3.00	12.00	0.890	8.00	12.00	0.911
4.00	12.00	0.894			

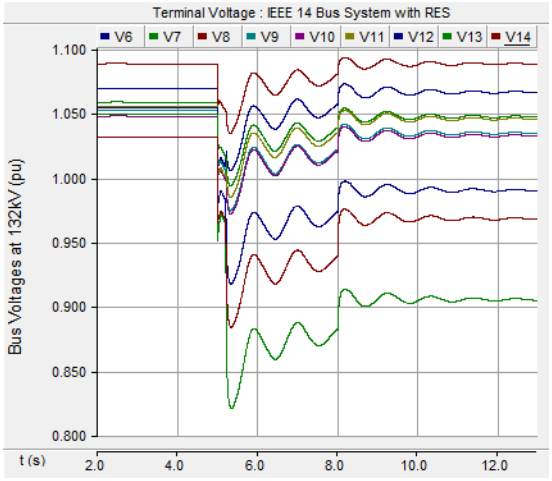

Fig. 8.7. Bus voltages for the 132 kV busses of IEEE 14-bus system for the case study 2. The RES is initially injecting 20 MW and two events occur at 5 s and 5.2 s. Measurements are taken by the TSO at t =2.5 and 7.5 s and the set-points of the proposed methodology are sent to the RES at t = 8 s.

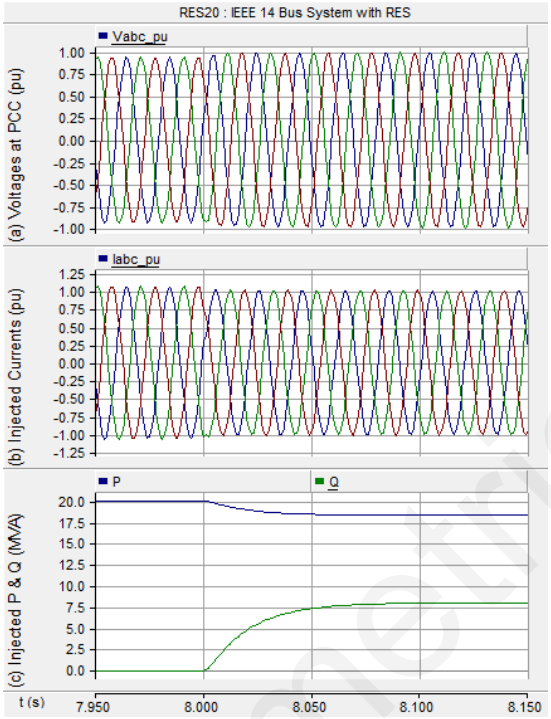

Fig. 8.8. RES response (integrated at bus 14) according to the power set-points sent by the system operator at t = 8 s for the case study 2.

TABLE 8.3: ITERATIVE POWER FLOW SOLUTION RESULTS FOR CASE STUDY 2
(PRESENTED RESULTS EVERY 1 MVAR FOR THE REACTIVE SET-POINT)

$Q_{set\text{-}point}$ (MVAr)	$P_{set\text{-}point}$ (MW)	V_{13} (p.u.)	$Q_{set\text{-}point}$ (MVAr)	$P_{set\text{-}point}$ (MW)	V_{13} (p.u.)
0.00	20.00	0.880	5.00	19.36	0.901
1.00	19.97	0.885	6.00	19.08	0.905
2.00	19.90	0.889	7.00	18.73	0.908
3.00	19.77	0.894	8.00	18.33	0.911
4.00	19.60	0.898			

8.3.3 Case study 2

A similar simulation scenario is presented in case study 2. The only difference here is that the RES initially operates at its nominal power (20 MW). The same events occur at t =5 s and t =5.2 s, which cause a violation of the voltage limits at bus 13 as shown in Fig. 8.7. The TSO control center detects this violation and the proposed algorithm runs to calculate the new power set-points for the RES. The results of the proposed methodology are presented in TABLE 8.3. The methodology depicts that for maintaining the voltage stability (all the voltages to be above 0.91 pu) the RES should adjust its power injection to $P_{set\text{-}point}$=18.33 MW, and $Q_{set\text{-}point}$=8 MVAr. The decrease of the active power is to ensure the operation of the GSC without any violation of the converter ratings. Fig. 8.7 presents the bus voltages of the 132 kV buses of IEEE 14-bus system during this case study and the

performance of the RES according to the set-points calculated by the proposed methodology is shown in Fig. 8.8. The proper response of the RES according to the calculated set-points ensures that the voltage stability is maintained, since all the bus voltages return within the permissible limits.

8.4 Conclusions

This chapter proposes a real-time control methodology for power system operators to utilize the installed renewable energy sources at the transmission level in order to enhance the power system voltage stability. The control center of the TSO monitors the state of the power system (according to a state estimation technique) and in case of limit violation on the bus voltages, calculates the required support by the RES in order to maintain the voltage stability of the system. The proper reactive power support is calculated through iterative power flow solutions in order to estimate the reactive power that needs to be injected by the RES. The resulting power set-points are sent to the RES that are installed in the power system to enhance the system stability. The simulation results demonstrate the beneficial effect of the proposed method in the operation of the power system. It is further illustrated through the case studies that it is possible to use the renewable energy sources as ancillary services in the power systems in case of contingencies.

CHAPTER 9
CONCLUSIONS

9.1 Conclusions and impact

The Grid Side Converter (GSC) based on power electronic technology is the cornerstone for the grid interconnection of RES. This Ph.D. dissertation focuses on advancing the operation of the GSC, and consequently the operation of the whole RES, by proposing novel synchronization and control methods (six new synchronization methods for three-phase GSC, two new synchronization scheme for single-phase GSC, a new current controller and an advanced PQ controller) that are applied on the controller of the GSC. The proposed methodologies for the GSC controller enhance the performance of the GSC in terms of dynamic response (especially under Fault Ride Through (FRT) operation) and in terms of robustness against harmonic distortion. An enhanced FRT operation can improve the power system support by the RES, when faults and disturbances occur on the power grid and thus the power system stability is beneficially affected. Further, the robustness against harmonic distortion can enhance the power quality of RES and of the whole power system. Hence, this Ph.D. dissertation significantly contributes to the advancement of grid interconnection of RES with an impact on the performance of the RES and on the operation of the whole power system. The contributions and impact of this Ph.D. dissertation can pave the way for an even higher penetration of RES in the electricity generation, providing great environmental and economic benefits.

This Ph.D. dissertation begins with a benchmarking between three-phase synchronization methods under several grid conditions and under voltage sag events (Section 2.3). The results of this benchmarking inspire the development of a new hybrid Phase Locked Loop (PLL) based synchronization method (Section 2.4), named dαβ-PLL, which inherits the advantages of two different PLLs. The proposed dαβ-PLL presents an outstanding response in terms of accuracy under unbalanced voltage sags and in terms of fast dynamic response. The accurate and fast performance of dαβ-PLL can enable the proper FRT operation of the GSC under grid faults and thus the RES can provide an appropriate support to the grid as specified by the modern grid regulations (Section 2.4.2 and Section 2.4.3).

The fast performance of the synchronization can positively affect the control of the GSC and consequently can affect the operation of the whole RES, especially under grid disturbances. Therefore, this Ph.D. dissertation aims to further accelerate the response of synchronization methods by proposing adaptive tuning mechanisms for PLLs in Chapter 3. The first adaptive tuning mechanism proposes a novel online adaptation of the PLL tuning parameters according to the type and the voltage characteristics of the grid fault. This adaptive tuning mechanism has been applied in the structure of the dαβ-PLL, and thus the adaptive dαβ-PLL has been proposed (Section 3.3). The adaptive dαβ-PLL can achieve a faster response compared to the dαβ-PLL as it has been proved through simulation and experimental results (Section 3.3.3 and Section 3.3.4). An investigation shows that the fast synchronization achieved by the adaptive dαβ-PLL can beneficially affect the performance of the GSC and the whole RES (especially under FRT operation). The second tuning mechanism is based on the decoupling between the frequency and the phase estimation loop in combination with the adaptation of the integral parameter of the PLL. The Frequency-Phase Decoupling (FPD) mechanism has also been applied in the structure of the dαβ-PLL and therefore, the FPD-dαβ-PLL is proposed (Section 3.4.1). The FPD-dαβ-PLL also presents a faster dynamic response under grid faults compared to the initial dαβ-PLL. It is worth to be mentioned that the adaptive tuning mechanism of the adaptive dαβ-PLL and of the FPD-dαβ-PLL can accelerate the time response of the synchronization; however, the reason of improvement in each case is different. Hence, the two adaptive mechanisms have been combined and the adaptive FPD-dαβ-PLL has been proposed in Section 3.4.2, which outperforms the other PLLs in terms of dynamic response under grid faults.

Another important aspect is the robustness of synchronization methods against voltage harmonic distortion. The inaccuracies on the synchronization due to the grid harmonic distortion can negatively affect the operation of the GSC with undesired effects on the power quality of the RES and on the power quality of the entire power system. Methods found in the literature for enhancing the robustness of the synchronization against harmonics can cause undesired deceleration of the dynamic response of the synchronization, which consequently affect the FRT capability of RES. This Ph.D. dissertation proposes two novel three-phase synchronization methods that achieve an accurate response under harmonic distortion without any compromises in their dynamic performance. The first synchronization method (MSHDC-PLL) is proposed in Section 4.3 and is based on a novel decoupling cell that enables the fast and accurate estimation of the

positive sequence of the grid voltage. The only disadvantage of this method is the increased computational complexity. Thus, a second synchronization method (DNαβ-PLL) is proposed in Section 4.4 by reformulating the decoupling network of the MSHDC-PLL. The new decoupling network is developed in the stationary reference frame using an advanced space vector transformation theory. The new decoupling network can achieve exact equivalent performance with the MSHDC, but it requires significantly less computational process (so the DNαβ-PLL can easily be applied on conventional microcontrollers that are embedded within the GSC). Therefore, the proposed DNαβ-PLL is an ideal synchronization solution for RES under a highly distorted grid environment. The effect of the robustness of the synchronization method is also investigated within this Ph.D. dissertation. This investigation shows that the utilization of the proposed DNαβ-PLL (with robustness against harmonics), can beneficially affect the power quality of the RES and consequently of the whole power system. Further, the fact that the robustness against harmonics is achieved without compromising the dynamic response of the synchronization can enable the proper FRT operation of the RES according to the modern grid regulations.

The penetration of single-phase rooftop PV system into the grid has reached a considerable percentage of the total electricity generation. Thus, it is necessary to also improve the interconnection of the single-phase PV systems in order to enable their FRT support and to ensure a high quality current injection under any grid conditions. This Ph.D. dissertation proposes two new single-phase synchronization methods that can achieve a very accurate response under harmonic distorted conditions without any compromise on the dynamic response of the synchronization under grid faults. The MHDC-PLL is proposed in Section 5.3 and is based on a novel decoupling network for the fast decoupling of the harmonic effect. The MHDC-PLL presents a very fast response under grid disturbances and a great immunity against harmonic distortion. The only disadvantage of the MHDC-PLL is the high complexity of the algorithm and the inaccurate performance under non-nominal frequency conditions. The second synchronization method, named frequency adaptive MHDC-PLL, is proposed in Section 5.4 and overcomes these issues. Thus, a novel frequency adaptive technique is applied to achieve an accurate response under frequency change events, while the decoupling network of MHDC-PLL is re-designed in a more computational efficient way. Thus, the new frequency adaptive MHDC-PLL presents a fast response under any grid disturbances, is very accurate under the worst case harmonic distortion and its complexity is significantly decreased compared to the initial MHDC-PLL. Hence, the frequency adaptive MHDC-PLL is an ideal solution

for the synchronization of single-phase PV systems under any condition, it can enhance the dynamic response of PV systems in terms of FRT operation under grid faults and it can significantly improve the power quality of the PV system and as a consequence the power quality of the whole grid.

Another important contribution of this dissertation is the proposition of an advanced current controller in Chapter 6 that will enable the accurate injection of full positive or full negative sequence symmetrical and high quality currents under unbalanced and harmonic distorted grid conditions. The proposed current controller is a preferable solution compared to other advanced current controllers that can be found in the literature due to its dynamic response (other methods are based on filtering techniques that can decelerate their response), its simplified and modular structure and its low control effort (enabled by the use of the voltage feed-forward technique). The design of the current controller is based on a novel and simplified unbalanced compensation module which regulates the reference voltage for compensating the inaccuracies due to the unbalanced conditions. Further, the proposed current controller is also enhanced in a way to achieve an accurate performance under harmonic distortion. Such a simplified and advanced current controller is essential for the proper FRT operation of the GSC under unbalanced grid faults and for the injection of high quality currents into the grid. Therefore, the combination of the proposed current controller in Chapter 6 with the synchronization techniques proposed in Chapters 2-5 can advance the operation of the whole GSC in terms of fast dynamic response under grid faults and in terms of increased power quality.

A very important task of this Ph.D. dissertation is to investigate how the proper FRT operation of RES, enabled by the advanced synchronization and control techniques proposed in Chapters 2-6, can affect the overall power system performance. The proper support of the grid by the RES under grid disturbances is required by the modern grid regulations in order to enhance the stability of the power system. An investigation of the impact on the power system, when the RESs operate according to different FRT strategies (according to the grid regulations) is performed in Chapter 7. The investigation shows the beneficial effect of a proper FRT operation by RES; however, the investigation depicts some issues that have not previously been reported. These issues are: the unfair support of the grid when both voltage sag and under-frequency events occur and the possibility of undesired repeated power oscillations due to the discontinuities of the dead-band zone of the FRT strategies. Hence, in this Ph.D. dissertation some modifications on the current grid codes are proposed in order to overcome these issues.

Finally, in Chapter 8, an application is proposed for enhancing the voltage stability of the power system though a centralized control of the installed large RES farms. This application is enabled when installed RESs in the power grid are equipped with advanced synchronization and control methods for the GSC, as the methods suggested within this Ph.D. dissertation. According to this control application, the RESs should be able to communicate with the control center of the power system operator, and should be able to regulate their operation according to the specific power set-point defined by the control center. In the proposed application, the control center monitors the power system operation through the state estimation algorithm for possible voltage violation at any bus of the system. In case of violation, the control center should define in real-time the required set-points for the RES that are installed in a location near the violation in order to provide the proper voltage support and maintain the stability of the grid. The required set-points for RES are calculated by repeated power flow solutions where the reactive power set-points for RES are increased in each iteration until the voltage stability of the system is maintained. The proposed application combines advanced RES with the power systems in the framework of smart grids and can be used to enhance the voltage stability of the power system.

As a conclusion, this Ph.D. dissertation significantly contributes to advance the GSC operation and thus, to improve the grid-connection of RES. The synchronization and

TABLE 9.1: SUMMARY OF THE CONTRIBUTIONS AND IMPACTS OF THIS Ph.D. DISSERTATION

Contribution of this Ph.D. dissertation	**Impact on RES performance**	**Impact on power system operation**	**Enviromental impact**
-Proposes eight new synchronization methods for single- and three-phase RES that can achieve a very fast and accurate response under grid faults and harmonic distorted voltage -Proposes a new simplified current controller that can achieve an outstanding performance under any grid conditions -Investigates the effect of the new synchronization and control methods for RES in terms of FRT operation and in terms of power quality -Investigates the effect of different FRT strategies by RES on the operation of the power system and proposes modifications to improve current grid codes -Proposes a control application for the TSO control center that improves voltage stability by utilizing the capabilities of large RES	-Improves the overall RES performance under any grid conditions -Advances the power quality of RES -Enhances the dynamic FRT response of RES -Enables new ancillary services by RES -RES can meet the new grid codes	-Paves the way for a seamless and increased RES penetration -Enhances the stability of the power system -Improves the power quality of the entire system	-Paves the way for an even more increased penetration of green energy -Minimizes carbon dioxide emissions

control methods presented here improve the performance of the GSC under any grid disturbances and under harmonic distorted grid voltage. The improvements on the GSC operation have an essential impact on the performance of the RES and on the operation of the entire power system in terms of stability and power quality. Hence, methods proposed within this Ph.D. dissertation, can be used to pave the way for an even higher penetration of RES with great environmental impact. The contributions and impacts of this Ph.D. dissertation are summarized in TABLE 9.1.

9.2 Application Guide for the synchronization method

This Ph.D. dissertation mainly focuses on advancing the synchronization and control techniques for the GSC, which can improve the grid interconnection of RES with obvious benefits for the RES performance and for the operation of the entire power system. Since the synchronization method is the most important aspect regarding the grid interconnection of RES, this Ph.D. dissertation has proposed several new advanced Phase-Locked Loop (PLL) based synchronization method for single- and three-phase RES. This section provides an application guide for single- and three-phase synchronization methods to aid the inverter manufacturers, the regulatory authorities and transmission/distribution system operators to choose the appropriate synchronization method based on their requirements and of the grid codes for each country.

9.2.1 Application guide for three-phase synchronization methods

Six novel PLL based synchronization methods for three-phase RES have been proposed and developed in Chapters 2-4. A performance comparison is synopsized in Fig. 9.1 for conventional, state-of-the-art, and proposed three-phase synchronization methods. It is obvious from Fig. 9.1 that the conventional PLLs, such as the dq-PLL and the αβ-PLL, present a high computational efficiency and a satisfactory dynamic response. However, the performance of these techniques is inadequate under grid faults (especially under unbalanced voltage sag events) and under harmonic distorted voltage conditions. Hence, such methods cannot ensure the proper operation of RES according to the new grid regulations.

A state-of-the-art synchronization solution for three-phase systems that can be found in the literature is the ddsrf-PLL as presented in Section 2.2.2. This solution achieves a very accurate response under unbalanced grid faults without any compromise in its dynamic performance. The accuracy against unbalanced conditions is achieved by

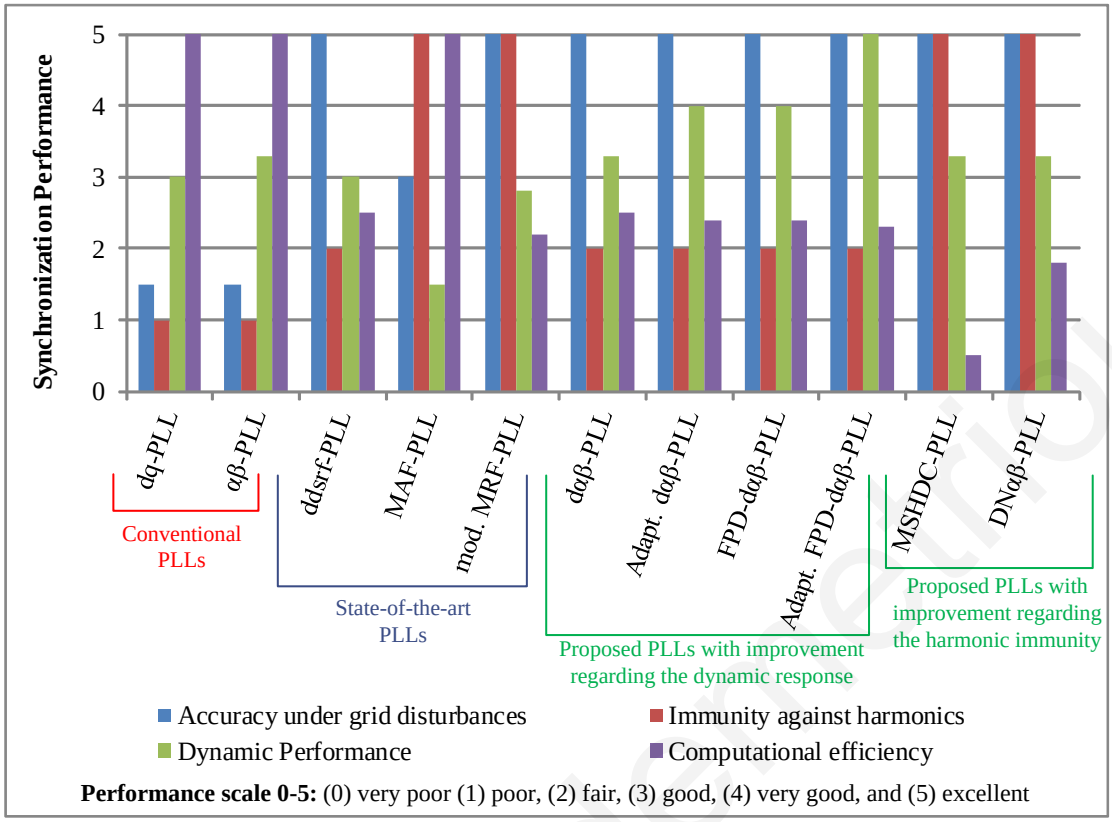

Fig. 9.1. Synopsis of the performance of conventional, state-of-the-art and proposed synchronization methods for three-phase RES.

increasing the complexity of the method while this method does not present any robustness against low-order harmonic distortion. The ddsrf-PLL can be used by RES in order to meet the grid regulations for the Fault Ride Through operation in case of strong grids with negligible harmonic distortion.

In case of weak grids and in case of high penetration of green energy, the fast and appropriate FRT performance of RES is very important in order to maintain the stability of the entire power system. Thus, this Ph.D. dissertation proposes four new synchronization methods for advancing the RES performance regarding their dynamic response against grid faults with a minimum complexity increment. The dαβ-PLL (Section 2.4) can slightly improve the dynamic response of the synchronization under grid faults compared to the ddsrf-PLL. Moreover, the adaptive mechanisms proposed in Chapter 3 are used for further improving the dynamic response of the dαβ-PLL. Hence, the adaptive dαβ-PLL and the FPD-dαβPLL (Section 3.3 and Section 3.4.1 respectively) accelerate the dynamic response of the synchronization under grid faults. More particularly, the combination of the two prior mentioned PLLs in the new adaptive FPD-dαβ-PLL (Section 3.4.2) enables the most outstanding synchronization performance in terms of dynamic response under low-voltage grid faults as shown in Fig. 9.1. Such an advanced synchronization method enables the fast

and proper dynamic response of a RES when a grid fault occurs. This is particularly useful in case of weak grids or of power systems with high RES penetration where the fast FRT operation of RES is vital for maintaining the stability of the system. Hence, in case where a RES is connected to a weak power grid with negligible harmonics (i.e., when the RES is connected to the medium or high voltage level where usually the harmonics are negligible), is highly recommended to use the adaptive FPD-dαβ-PLL for its synchronization.

In case where the RES is connected to a weak grid with a significant harmonic distortion due to the non-linear loads, the use of robust synchronization with accuracy against harmonics is necessary. Such solutions can be found in the literature based on moving average filters, such as the MAF-PLL and the modified MRF-PLL presented in Section 4.2. These solutions can achieve an accurate response against unbalanced and harmonic distorted conditions; however, their dynamic response is seriously affected with undesired impact on their FRT operation. Thus, these solutions may not be appropriate in case of weak systems with high RES penetration because they may raise stability issues for the entire power system. Therefore, two new synchronization methods have been proposed in Chapter 4, the MSHDC-PLL and the DNαβ-PLL, which can present a very accurate operation under any harmonic distortion and ensure a fast dynamic response under grid faults. The DNαβ-PLL is a preferable solution compared to MSHDC-PLL due to its higher computational efficiency. Hence, the DNαβ-PLL presents an outstanding response under harmonic distorted conditions and under any grid faults. Thus, it is an ideal synchronization solution for weak grids with non-negligible harmonic distortion (i.e., when the RES is connected to the low voltage distribution network), since it can enable the high power quality and the appropriate FRT operation of RES. Further, in case of very weak grids, the DNαβ-PLL can be combined with the adaptive tuning mechanism of Chapter 3 in order to achieve an even faster response without any compromise in its accuracy against harmonics.

The application guide for the synchronization methods presented in this section can be applied for the case of Cyprus. The Cyprus power system is a small and autonomous system and can be considered as a weak power grid. Furthermore, according to the 2020 frameworks of climate and energy of European commission the RES penetration in Cyprus should reach 13%. Therefore, in order to maintain the stability of a weak power grid with high penetration of RES it is necessary to use fast synchronization methods for interconnecting RES in order to ensure their proper FRT operation. The voltage harmonic distortion at the Point of Common Coupling (PCC) is also an important aspect in order to

choose a proper synchronization method. Thus, in case of small RESs that are connected to a low-voltage feeder of the distribution network, it is highly recommended to use the DNαβ-PLL which presents fast dynamic response under grid faults and great immunity against harmonics. It is to be noted, that highly harmonic distortion condition is more likely to exist in a low-voltage distribution network since the network is affected by the non-linear loads that are installed in the low-voltage feeders. The harmonic distortion is usually restricted in medium- or high-voltage networks and thus, for large wind power or PV system installed at the medium- or high voltage-network, it is highly recommended to use the adaptive FPD-dαβ-PLL for their synchronization which presents very fast dynamics and very accurate response under grid faults and under limited harmonic distortion. Furthermore, in case where a non-negligible harmonic distortion occurs at the medium- or high-voltage network according to field measurements, it is then necessary to combine the DNαβ-PLL with the adaptive tuning mechanism of Chapter 3 in order to achieve an even faster response without any compromise in its accuracy against harmonics. It is worth mentioning that the fast FRT response is more important in large RES since can directly affect the stability of the entire power system.

9.2.2 Application guide for the proposed single-phase synchronization methods

Chapter 5 proposes two new PLLs for single-phase PV systems. A performance comparison is summarized in Fig. 9.2 for conventional, state-of-the-art and proposed single-phase synchronization methods. The conventional PLLs, such as the T/4 delayed-PLL and the E-PLL, present adequate performance only under ideal grid conditions. The T/4 delayed-PLL is fast but it is inaccurate under harmonic distorted conditions and under non-nominal frequencies, while the E-PLL presents slow dynamics and it is inaccurate under harmonics. The state-of-the-art solutions that can be found in the literature are the IPT-PLL and the SOGI-PLL. These PLLs present an adequate dynamic response, are accurate under any grid frequencies, but they can accurately operate only under high-order harmonics. It is worth mentioning that the fast operation of PLLs is very important for the stability of the systems, especially as the installation of single-phase PV systems is increased. Further, the robustness against harmonics is crucial, since the single-phase PV systems are connected to low-voltage distribution networks where a significant amount of non-linear loads are connected. Therefore, synchronization methods are needed with fast dynamic response and robustness against harmonics. The MHDC-PLL is proposed in Section 5.3 and overcomes the effect of low-order harmonics, but its complexity is too high and it is inaccurate under frequency changes. Hence, the frequency adaptive MHDC-

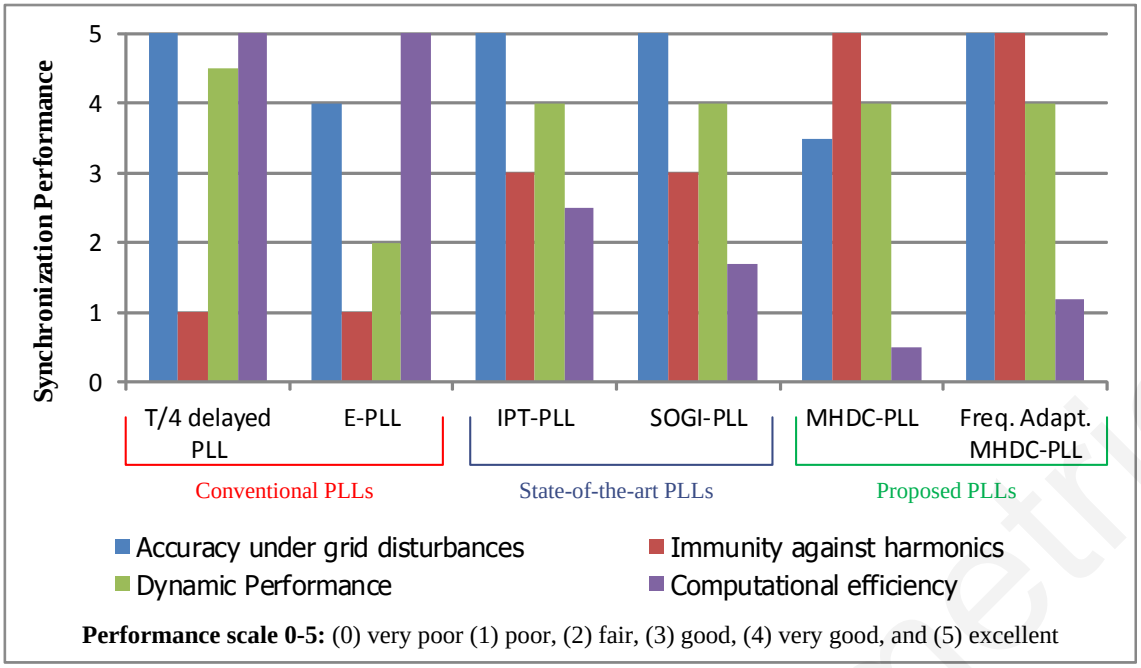

Fig. 9.2. Synopsis of the performance of conventional, state-of-the-art and proposed synchronization methods for single-phase PV systems.

PLL is proposed in Section 5.4, which presents great immunity against the worst case harmonic distortion, accurate and fast response under any grid disturbances and its complexity is sufficiently less compared to the initial MHDC-PLL. Thus, the proposed frequency adaptive MHDC-PLL is an ideal solution to be used for the synchronization of single-phase PV systems, since it is fast and accurate under any grid conditions and can enable a proper FRT operation and a high power quality for interconnected PV systems.

9.3 Future work

This Ph.D. dissertation focuses on advancing the interconnection of RES by improving the GSC operation. Thus, several synchronization and control techniques have been proposed for the GSC controller to enable an advanced operation under any grid conditions. As a result, the performance of the GSC has significantly improved in terms of fast dynamic response under FRT operation and in terms of power quality, especially when it operates under harmonic distorted grid conditions. Furthermore, the impact of advancing the controller of GSC on the overall operation of the RES and of the entire power system has been investigated through this Ph.D. dissertation. However, there are still some improvements that can be performed in this area. An obvious future work is to apply the proposed synchronization and control methodologies to similar systems (not only in RES applications) in order to improve their performance as well. Such systems may be the

controllable rectifiers (such as the chargers of electric vehicles), the uninterruptable power supply systems, High Voltage DC (HVDC) transmission systems, and static synchronous compensators.

This Ph.D. dissertation mainly focuses on improving the synchronization methods that are used in single- and in three-phase RES. Several novel solutions have been proposed that can achieve an outstanding synchronization under any grid conditions. Further, an interesting work is to combine a PLL with robustness against harmonics, such as the three-phase DNαβ-PLL or the single-phase MHDC-PLL, with the adaptive tuning mechanism of Chapter 3 in order to develop a new PLL with very fast dynamics and great immunity against harmonics. Moreover, an interesting aspect is also to develop PLL methods that can achieve an outstanding response under any grid conditions, but with significantly less computational complexity.

The only limitation of the proposed three-phase synchronization (DNαβ-PLL) and the single-phase synchronization (frequency adaptive MHDC-PLL) is the vulnerability against inter-harmonics. The inter-harmonics are generated by the interaction of a high number of power electronic converters (that are installed in close proximity). The interaction between these converters may result to harmonics that are non-integer multiples of the grid frequency. The decoupling networks proposed for the single- and three-phase synchronization methods are not able to completely eliminate the effect of inter-harmonics. Thus, the design of the proposed decoupling networks should be extended in order to consider the effect of the most significant inter-harmonics. It is to be noted that the decoupling network extention will adaptively consider the most significant inter-harmonics. Very interesting future work can be performed in the area of current controllers. Some simplified current control techniques can be designed that will enable a symmetrical and purely sinusoidal current injection. This controller can use the estimated negative sequence and harmonic component of the grid voltage by the advanced PLL proposed in this dissertation, in order to design open loop compensation modules that will enable the injection of high quality symmetrical currents under abnormal conditions. Further, the design of another current controller that will be able to intentionally inject regulated asymmetrical and harmonic distorted currents is of high interest. Such a current controller can be used in a way to compensate the unbalances and the distortion of other loads that are connected near RES. Therefore, the distribution network can benefit from such operation since the overall power quality of the grid will be improved and the power losses will be minimized by symmetrizing the load of the grid.

The investigation of Chapter 7 shows the beneficial impact of the FRT operation of RES on the stability of the power system. However, the investigation indicates some issues on the current grid regulations that may lead to an unfair support of the grid when both voltage sag and under-frequency events occur and to undesired repeated power oscillations under specific circumstances. It is to be noted that these issues have been highlighted in the IEEE 14-bus system. As further steps, it is important to investigate if these issues can also be occurred in the case of Cyprus power system with the corresponding installed RES. Thus, if the investigation indicates that the stability of the Cyprus power system can be affected by the current grid regulation for interconnecting RES, then a technical report will be send to the Cyprus Energy Regulatory (CERA) and the Cyprus Transmission System Operator (TSO - Cyprus) mentioning these issues and proposing proper modification on the current grid regulations in order to ensure the stability of the system.

Some research work can also be done for extending the control application suggested in Chapter 8. In this application, only one RES farm is considered for enhancing the power system stability. Therefore, it is necessary to investigate the case where several RES are installed in an area and how each RES will contribute, under a contingency in order to maintain the system stability.

Another task for future work is to enhance the reliability of the grid side power electronic converters. The reliability and the life-time of the inverter can be directly affected by the operating temperature, which is affected by the power exchange through the inverter. Especially in case where there is an available storage device on the DC-link of the GSC, the power exchange can be regulated in a more appropriate manner in order to extend the GSC lifetime. Therefore, it is very interesting to develop active and reactive power controllers that will manage the power exchange and the charging and discharging of the storage in a way to extend the power electronic inverter lifetime and to maximize the economic outcome from the whole system (RES and storage system). An available storage on the DC-link can also enable new opportunities regarding a more appropriate FRT support by RES. Hence, it is necessary to investigate possible modification on the grid regulations for RES that are equipped with storage devices.

Another way to improve the reliability of the inverter is to develop Fault Detection, Isolation and Accommodation (FDIA) techniques for the GSC. These model based FDIA techniques will applied on the controller of the GSC in order to detect sensor faults (e.g., current sensors, voltage sensors) or actuator faults (e.g., IGBT failures), to isolate this fault

and to enable the ride through such faults. In this way, the reliability of the GSC and of the whole RES will increase, undesired failures and loss of energy will be avoided and the maintenance procedure will be accelerated.

In general, this Ph.D. dissertation proposes several new synchronization and control methods that can improve the performance of the GSC under abnormal grid conditions. An important further step for disseminating the results of this Ph.D. dissertation is to communicate the results to inverter manufacturers to investigate the possibility of using the proposed techniques and methodologies in order to improve their products.

REFERENCES

[1] REN 21, "The first decade: 2004-2014, 10 years of renewable energy progress," [Online]. Available: http://www.ren21.net/, 2014.

[2] REN 21, "Renewables 2014: Global Status Report (GSR)," [Online]. Available: http://www.ren21.net/, June 2014.

[3] European Photovoltaic Industrial Association, "Global market outlook for photovoltaics 2014-2018," [Online]. Available: http://www.epia.org/, 2014.

[4] A. Izadian, N. Girrens and P. Khayyer, "Renewable energy policies: A brief review of the latest U.S. and E.U. policies," *IEEE Magazine Industrial Electronics*, vol. 7, no. 3, pp. 21-34, Sep. 2013.

[5] IEEE Std 1547-2003, "Standard for interconnecting distributed resources with electric power systems," IEEE, 2003.

[6] International Electrotechnical Commision, "IEC 61727 - Photovoltaic (PV) systems – Characteristics of the utility interface," 2004.

[7] EN 50438, "Requirements for the connection of micro-generators in parallel with public low-voltage distribution networks," 2008.

[8] VDE-AR-N 4105, "Technical requirements for the connection to and parallel operation with low-voltage distribution networks," 2011.

[9] International Electrotechnical Commision, "IEC 61000 Ed. 3.0, Electromagnetic Compatibility (EMC)," 2005.

[10] Standard EN 50160, "Voltage characteristics of public distribution system," CENELEC: European Committee for Electrotechnical Standardization, Brussels, Belgium 1999.

[11] TransmissionCode 2007, "Networks and system rules of the German transmission system pperators," VDN-e.v.beim VDEW, Aug. 2007, www.vdn-berlin.de.

[12] E.ON, "Requirements for offshore grid connections in the E.ON Netz network," E.ON, 2008, www.eon-netz.com.

[13] Annex of O.P. 12.2, "Restricted to the technical requirements of wind power and photovoltaic facilities," Red Electrica Oct. 2008, www.ree.es (translated into English by Spanish Wind Association AEE in www.aeolica.es).

[14] A. Morales, X. Robe, M. Sala, P. Prats, C. Aguerri and E. Torres, "Advanced grid requirements for the integration of wind farms into the spanish transmission system," *IET Renewable Power Generation*, vol. 2, no. 1, pp. 47-59, Mar. 2008.

[15] Technical Regulation TF 3.2.5, "Technical regulations for the properties and the regulation of wind turbines. Wind turbines connected to grids with voltages above 100 kV," Eltra and Elkraft System, Dec. 2004, www.energinet.dk.

[16] Technical Regulation TF 3.2.5, "Technical regulation 3.2.5 for wind power plants with a power output greater than 11 kW," ENERGINET.DK, 2010, www.energinet.dk.

[17] TSO Cyprus, "Transmission and distribution rules - Issue 4.0.0," Transmission System Operator - Cyprus, July 2013 (in Greek), http://www.dsm.org.cy/.

[18] NGET, "The Grid Code," Issue 5, Revision 13, National Grid Electricity Transmission plc, Jan. 2015.

[19] The EirGrid, "Grid Code," version 3.1, Apr. 2008.

[20] CEI, "CEI 0-21: Reference technical rules for connecting users to the active and passive LV distribution companies of electricity," Comitato Elettrotecnico Italiano 2012.

[21] Order 661, "Interconnection with wind energy," issued by Federal Energy Regulatory Commission (FERC) of United States June 2005.

[22] H. Kobayashi, "Fault ride through requirements and measures of distributed PV systems in Japan," in *Proc. IEEE-PES General Meeting*, San Diego (CA), USA, 2012, pp. 1-6.

[23] I. Erlich, W. Winter and A. Dittrich, "Advanced grid requirements for the integration of wind turbines into the German transmission system," in *Proc. IEEE-PES Genaral Meeting*, Montreal, Canada, 2006, pp. 1253-1257.

[24] F. Iov, A.D. Hansen, P.E. Soersensen and N.A. Cutululis, "Mapping of grid faults and grid codes," Risø Nat. Lab., Tech. Univ. Denmark, Roskilde, Denmark 2007.

[25] B. Craciun, T. Kerekes, D. Sera and R. Teodorescu, "Overview of recent grid codes for PV power integration," in *Proc. OPTIM*, Brasov, Romania, 2012, pp. 959-965.

[26] M. Tsili and S. Papathanasiou, "A review of grid code technical requirements for wind farms," *IET Renewable Power Generation*, vol. 3, no. 3, pp. 308-332, Sep. 2009.

[27] R. Teodorescu, M. Liserre and P. Rodriguez, *Grid converters for photovoltaic and wind power systems*, John Wiley & Sons, 2011.

[28] L. Hadjidemetriou, E. Kyriakides and F. Blaabjerg, "A new hybrid PLL for interconnecting Renewable Energy Systems to the grid," in *Proc. IEEE ECCE*, Raleigh (NC), USA, 2012, pp. 2075-2082.

[29] L. Hadjidemetriou, E. Kyriakides and F. Blaabjerg, "A new hybrid PLL for interconnecting renewable energy systems to the grid," *IEEE Trans. Industry Applications*, vol. 49, no. 6, pp. 2709-2719, 2013.

[30] L. Hadjidemetriou, E. Kyriakides and F. Blaabjerg, "An adaptive Phase-Locked Loop algorithm for faster fault ride through performance of interconnected renewable energy sources," in *Proc. IEEE ECCE*, Denver (CO), USA, 2013, pp. 2619-2626.

[31] L. Hadjidemetriou, E. Kyriakides and F. Blaabjerg, "An adaptive tuning mechanism for phase-locked loop algorithms for faster time performance of interconnected renewable energy sources," *IEEE Trans. Industry Applications*, vol. 51, no. 2, pp. 1792-1804, Apr. 2015.

[32] L. Hadjidemetriou and E. Kyriakides, "The performance of a new hybrid PLL in an interconnected renewable energy system under fault ride through operation," in *Proc. POEM*, Limassol, Cyprus, 2012, pp. 1-7.

[33] L. Hadjidemetriou and E. Kyriakides, "The performance of a new hybrid PLL in an interconnected renewable energy system under fault ride through operation," *Hindawi Publishing Corporation/CPIE*, vol. 2013, no. Article ID 168054, pp. 1-10, Mar. 2013.

[34] L. Hadjidemetriou, E. Kyriakides and F. Blaabjerg, "Synchronization of grid-connected renewable energy sources under highly distorted voltages and unbalanced grid faults," in *Proc. IEEE IECON*, Vienna, Austria, 2013, pp. 1887-1892.

[35] L. Hadjidemetriou, E. Kyriakides and F. Blaabjerg, "A robust synchronization to enhance the power quality of renewable energy systems," *IEEE Trans. Industrial Electronics*, vol. 62, no. 8, pp. 4858-4868, Aug. 2015.

[36] L. Hadjidemetriou, E. Kyriakides, Y. Yang and F. Blaabjerg, "Power quality improvement of single-phase photovoltaic systems through a robust synchronization method," in *Proc. IEEE ECCE*, Pittsburgh (PA), USA, 2014, pp. 2625-2632.

[37] L. Hadjidemetriou, E. Kyriakides, Y. Yang and F. Blaabjerg, "A synchronization method for single-phase grid-tied inverters," *IEEE Trans. Power Electronics*, vol. 31, no. 3, pp. 2139-2149, Mar. 2016.

[38] Y. Yang, L. Hadjidemetriou, F. Blaabjerg and E. Kyriakides, "Benchmarking of phase locked loop based synchronization techniques for grid-connected inverter systems," in *Proc. ICPE ECCE Asia*, Seoul, Korea, 2015, pp. 2517-2524.

[39] L. Hadjidemetriou, Y. Yang, E. Kyriakides and F. Blaabjerg, "A synchronization scheme for single-phase grid-tied inverters under harmonic distortions and grid disturbances," in *Proc. IEEE APEC 2016*, Long Beach (CA), USA, 2016, pp. 1-8.

[40] L. Hadjidemetriou, E. Kyriakides and F. Blaabjerg, "A grid side converter current controller for accurate current injection under normal and fault ride through operation," in *Proc. IEEE IECON*, Vienna, Austria, 2013, pp. 1454-1459.

[41] L. Hadjidemetriou, P. Demetriou and E. Kyriakides, "Investigation of different fault ride through strategies for renewable energy sources," in *Proc. IEEE POWERTECH*, Eindhoven, Netherlands, 2015, pp. 1-6.

[42] L. Hadjidemetriou, M. Asprou, P. Demetriou and E. Kyriakides, "Enhancing power system voltage stability through a centralized control of renewable energy sources," in *Proc. IEEE POWERTECH*, Eindhoven, Netherlands, 2015, pp. 1-6.

[43] F. Blaabjerg, R. Teodorescu, M. Liserre and A. Timbus, "Overview of control and grid synchronization for distributed power generation systems," *IEEE Trans. Industrial Electronics*, vol. 53, no. 5, pp. 1398-1409, Oct. 2006.

[44] F. Blaabjerg and K. Ma, "Future on power electronics for wind turbine systems," *IEEE Journal of Emerging and Selected Topics in Power Electronics*, vol. 1, no. 3, pp. 139-152, Sep. 2013.

[45] Z. Chen, J.M. Guerrero and F. Blaabjerg, "A review of the state of the art of power electronics for wind turbines," *IEEE Trans. Power Electronics*, vol. 24, no. 8, pp. 1859-1875, Aug. 2009.

[46] J. Rocabert, A. Luna, F. Bllabjerg and P. Rodriguez, "Control of power converters in AC microgrids," *IEEE Trans. Power Electronics*, vol. 27, no. 11, pp. 4734-4749, Nov. 2012.

[47] P. Rodriquez, I. Candela, C. Citro, J. Rocabert and A. Luna, "Control of grid-connected power converters based on a virtual admittance control loop," in *Proc. IEEE EPE*, Lille, France, 2013, pp. 1-10.

[48] B. Bahrani, A. Rufer, S. Kenzelmann and L.A.C. Lopes, "Vector control of single-phase voltage-source converters based on fictive-axis emulation," *IEEE Trans. Industry Applications*, vol. 47, no. 2, pp. 831-840, Apr. 2011.

[49] H. Hu, S. Harb, N. Kutkut, I. Batarseh and Z.J. Shen, "A review of power decoupling techniques for microinverters with three different decoupling capacitor locations in PV systems," *IEEE Trans. Power Electronics*, vol. 28, no. 6, pp. 2711-2726, June 2013.

[50] S.A. Khajehoddin, M. Karimi-Ghartemani, A. Bakhshai and P. Jain, "A power control method with simple structure and fast dynamic response for single-phase grid-connected DG systems," *IEEE Trans. Power Electronics*, vol. 28, no. 1, pp. 221-233, Jan. 2013.

[51] Y. Yang, H. Wang and F. Blaabjerg, "Reactive power injection strategies for single-phase photovoltaic systems considering grid requirements," *IEEE Trans. Industry Applications*, vol. 50, no. 6, pp. 4065-4076, Dec. 2014.

[52] L. Zhang, K. Sun, H. Hu and Y. Xing, "A system-level control strategy of photovoltaic grid-tied generation systems for european efficiency enhancement," *IEEE Trans. Power Electronics*, vol. 29, no. 7, pp. 3445-53, Jul. 2014.

[53] R.A. Mastromauro, M. Liserre and A. Dell'Aquila, "Control issues in single-stage photovoltaic systems: MPPT, current and voltage control," *IEEE Trans. Industrial Informatics*, vol. 8, no. 2, pp. 241-254, May 2012.

[54] P. Rodriquez, A. Luna, J.I. Candela, R. Rosa, R. Teodorescu and F. Blaabjerg, "Multi-resonant frequency-locked loop for grid synchronization of power

converters under distorted grid conditions," *IEEE Trans. Industrial Electronics*, vol. 58, no. 1, pp. 127-138, Jan. 2011.

[55] P. Rodriquez, A. Luna, R.S.I. Monoz-Aguilar, I. Etxaberria-Otadui, R. Teodorescu and F. Blaabjerg, "A stationary reference frame grid synchronization system for three-phase grid-connected power converters under adverse grid conditions," *IEEE Trans. Power Electronics*, vol. 27, no. 1, pp. 99-111, Jan. 2012.

[56] S. Vasquez, J.A. Sanchez, M.R. Reyes, J.I. Leon and J.M. Carrasco, "Adaptive vectorial filter for grid synchronization of power converters under unbalanced and/or distorted grid conditions," *IEEE Trans. Industrial Electronics*, vol. 61, no. 3, pp. 1355-1367, March 2014.

[57] F. Baradarani, M.R. Dadash Zadeh and M.A. Zamani, "A phase-angle estimation method for synchronization of grid-connected power electronic converters," *IEEE Trans. Power Delivery*, vol. 30, no. 2, pp. 827-835, Apr. 2015.

[58] S. Mishra, D. Das, R. Kumar and P. Sumathi, "A power-line interference canceler based on sliding DFT phase locking scheme for ECG signals," *IEEE Trans. Instrumentation and Measurement*, vol. 64, no. 1, pp. 132-142, Jan. 2015.

[59] V. Kaura and V. Blasko, "Operation of a phase locked loop system under distorted utility conditions," *IEEE Trans. Industry Applications*, vol. 33, no. 1, pp. 58-63, Jan./Feb. 1997.

[60] G.C. Hsich and J.C. Hung, "Phase-locked loop techniques—A survey," *IEEE Trans. Industrial Electronics*, vol. 43, no. 6, pp. 609-615, Dec. 1996.

[61] S.K. Chung, "Phase-locked loop for grid-connected three-phase power conversion systems," *Proc. IEE Electric Power Applications*, vol. 147, no. 3, pp. 213-219, Aug. 2002.

[62] R. Teodorescu and F. Blaabjerg, "Flexible control of small wind turbines with grid failure detection operating in stand-alone and grid-connected mode," *IEEE Trans. Power Electronics*, vol. 19, no. 5, pp. 1323-1332, Sep. 2004.

[63] S. Golestan, M. Monfared and F.D. Freijedo, "Design-oriented study of advanced synchronous reference frame PLL," *IEEE Trans. Power Electronics*, vol. 28, no. 2, pp. 765-778, Feb. 2013.

[64] R. Teodorescu, I. Candela, A.V. Timbus, M. Liserre and F. Blaabjerg, "New positive-sequence voltage detector for grid synchronization of power converters under faulty grid conditions," in *Proc. IEEE PESC*, 2006, pp. 1-7.

[65] I. Carugati, S. Maestri, P.G. Donato, D. Carrica and M. Benedetti, "Variable sampling period filter PLL for distorted three-phase systems," *IEEE Trans. Power Electronics*, vol. 27, no. 1, pp. 321-330, Jan. 2012.

[66] F. Gonzalez-Espin, G. Garcera, I. Patrao and E. Figueres, "An adaptive control system for three-phase photovoltaic inverters working in a polluted and variable frequency electric grid," *IEEE Trans. Power Electronics*, vol. 27, no. 10, pp. 4248-4261, Oct. 2012.

[67] F. Gonzalez-Espin, E. Figueres and G. Garcera, "An adaptive synchronous-reference-frame phase-locked loop for power quality improvement in a polluted utility grid," *IEEE Magazine Industrial Electronics*, vol. 59, no. 6, pp. 2718-2731, June 2012.

[68] K.J. Lee, J.P. Lee, D. Shin, D.W. Yoo and H.J. Kim, "A novel grid synchronization PLL method based on adaptive low-pass notch filter for grid-connected PCS," *IEEE Trans. Industrial Electronics*, vol. 61, no. 1, pp. 282-301, Jan. 2014.

[69] M. Karimi-Ghartemani and M.R. Iravani, "A method for synchronization of power electronic converters in polluted and variable-frequency environments," *IEEE Trans. Power Systems*, vol. 19, no. 3, pp. 1263-1270, Aug. 2004.

[70] M. Karimi-Ghartemani and M.R. Iravani, "A nonlinear adaptive filter for online signal analysis in power systems: Applications," *IEEE Trans. Power Delivery*, vol. 17, no. 2, pp. 617-622, Apr. 2002.

[71] M.K. Ghartemani, S.A. Khajehoddin, P.K. Jain and A. Bakhshai, "Problems of startup and phase jumps in PLL systems," *IEEE Trans. Power Electronics*, vol. 27, no. 4, pp. 1830-1838, Apr. 2012.

[72] M. Karimi-Ghartemani, S.A. Khajehoddin, P.K. Jain and A. Bakhshai, "Derivation and design of in-loop filters in phase-locked loop systems," *IEEE Trans. Instrumentation and Measurement*, vol. 61, no. 4, pp. 930-940, Apr. 2012.

[73] S. Golestan, M. Ramezani, J.M. Guerrero, F.D. Freijedo and M. Monfared, "Moving average filter based phase-locked loops: Performance analysis and design

guidelines," *IEEE Trans. Power Electronics*, vol. 29, no. 6, pp. 2750-2763, June 2014.

[74] L. Shi and M.L. Crow, "A novel phase-locked-loop and its application in STATCOM system," in *Proc. North American Power Symposium (NAPS)*, Arlington (TX), USA, 2010, pp. 1-5.

[75] F.D. Freijedo, J. Doval-Gandoy, O. Lopez and E. Acha, "Tuning of phase-locked loops for power converters under distorted utility conditions," *IEEE Trans. Industry Applications*, vol. 45, no. 6, pp. 2039-2047, Nov. 2009.

[76] Liang Wang, Qirong Jiang, Lucheng Hong, Chunpeng Zhang and Yingdong Wei, "A novel phase-locked loop based on frequency detector and initial phase angle detector," *IEEE Trans. Power Electronics*, vol. 28, no. 10, pp. 4538-4549, Oct. 2013.

[77] M.A. Perez, J.R. Espinoza, L.A. Moran, M.A. Torres and E.A. Araya, "A robust phase-locked loop algorithm to synchronize static-power converters with polluted AC systems," *IEEE Trans. Industrial Electronics*, vol. 55, no. 5, pp. 2185-2192, May 2008.

[78] H. Karimi, A. Yazdani and R. Iravani, "Negative-sequence current injection for fast islanding detection of a distributed resource unit," *IEEE Trans. Power Electronics*, vol. 23, no. 1, pp. 298-307, Jan. 2008.

[79] P. Rodriguez, J. Pou, J. Bergas, J.I. Candela, R.P. Burgos and D. Boroyevich, "Decoupled double synchronous reference frame PLL for power converters control," *IEEE Trans. Power Electronics*, vol. 22, no. 2, pp. 584-592, Mar. 2007.

[80] P. Xiao, L. Thermadyne N.H., K.A. Corzine and G.K. Venayagamoorthy, "Multiple reference frame-based control of three-phase PWM boost rectifiers under unbalanced and distorted input conditions," *IEEE Trans. Power Electronics*, vol. 23, no. 4, pp. 2006-20017, July 2008.

[81] F. Xiong, W. Yue, L. Ming, W. Ke and L. Wanjun, "A novel PLL for grid synchronization of power electronic converters in unbalanced and variable-frequency environment," in *Proc. IEEE PEDG*, Hefei, China, 2010, pp. 466-471.

[82] H.S. Song and K. Nam, "Dual current control scheme for PWM converter under unbalanced input voltage conditions," *IEEE Trans. Industrial Electronics*, vol. 46, no. 5, pp. 953-959, Oct. 1999.

[83] Y. Suh and T.A. Lipo, "Control scheme in hybrid synchronous stationary frame for PWM AC/DC converter under generalized unbalanced operating conditions," *IEEE Trans. Industry Applications*, vol. 42, no. 3, pp. 825-835, May 2006.

[84] M. Reyes, P. Rodriguez, S. Vazquez, A. Luna, R. Teodorescu and J.M. Carrasco, "Enhanced decoupled double synchronous reference frame current controller for unbalanced grid-voltage conditions," *IEEE Trans. Power Electronics*, vol. 27, no. 9, pp. 3934-3943, Sep. 2012.

[85] J. Hu, Y. He, L. Xu and B.W. Williams, "Improved control of DFIG systems during network unbalance using PI–R current regulators," *IEEE Trans. Industrial Electronics*, vol. 56, no. 2, pp. 439-451, Feb. 2009.

[86] C. Wessels, N. Hoffmann, M. Molinas and F.W. Fuchs, "StatCom control at wind farms with fixed-speed induction generators under asymmetrical grid faults," *IEEE Trans. Industrial Electronics*, vol. 60, no. 7, pp. 2864-2873, July 2013.

[87] M. Liserre, R. Teodorescu and F. Blaabjerg, "Multiple harmonics control for three-phase grid converter systems with the use of PI-RES current controller in a rotating frame," *IEEE Trans. Power Electronics*, vol. 21, no. 3, pp. 836-841, May 2006.

[88] V.T. Phan and H.H. Lee, "Control strategy for harmonic elimination in stand-alone DFIG applications with nonlinear loads," *IEEE Trans. Power Electronics*, vol. 26, no. 9, pp. 2662-2675, Sep. 2011.

[89] T.L. Lee and S.H. Hu, "Discrete frequency-tuning active filter to suppress harmonic resonances of closed-loop distribution power systems," *IEEE Trans. Power Electronics*, vol. 26, no. 1, pp. 137-148, Jan. 2011.

[90] M.J. Newman, D.N. Zmood and D.G. Holmes, "Stationary frame harmonic reference generation for active filter systems," *IEEE Trans. Industry Applications*, vol. 38, no. 6, pp. 1591-1599, Nov. 2002.

[91] M. Bollen, *Understanding power quality problems: Votlage sags and interruptions*, New York: Wiley-IEEE press, 2000.

[92] P. Rodriguez, A.V. Timbus, R. Teodorescu, M. Liserre and F. Blaabjerg, "Flexible active power control of distributed power generation systems during grid faults," *IEEE Trans. Industrial Electronics*, vol. 54, no. 5, pp. 2583-2592, Oct. 2007.

[93] P. Rodriguez, A. Timbus, R. Teodorescu, M. Liserre and F. Blaabjerg, "Reactive power control for improving wind turbine system behavior under grid faults," *IEEE Trans. Power Electronics*, vol. 24, no. 7, pp. 1798-1801, July 2009.

[94] P. Rodriguez, G. Medeiros, A. Luna, M.C. Cavalcanti and R. Teodorescu, "Safe current injection strategies for a STATCOM under asymmetrical grid faults," in *IEEE ECCE*, Atlanta (GA), USA, 2010, pp. 3929-3935.

[95] F. Wang, J.L. Duarte and M.A.M. Hendrix, "Pliant active and reactive power control for grid-interactive converters under unbalanced voltage dips," *IEEE Trans. Power Electronics*, vol. 26, no. 5, pp. 1511-1521, May 2011.

[96] A. Junyent-Ferré, O. Gomis-Bellmunt, T.C. Green and D.E. Soto-Sanchez, "Current control reference calculation issues for the operation of renewable source grid interface VSCs under unbalanced voltage sags," *IEEE Trans. Power Electronics*, vol. 26, no. 12, pp. 3744-3753, Dec. 2011.

[97] K.J. Astrom and T. Hagglund, "The future of PID control," *Control Engineering Practice*, vol. 9, no. 11, pp. 1163-1175, 2001.

[98] T. Thacker, D. Boroyevich, R. Burgos and F. Wang, "Phase-locked loop noise reduction via phase detector implementation for single-phase systems," *IEEE Trans. Industrial Electronics*, vol. 58, no. 6, pp. 2482-2490, June 2011.

[99] H.J. Choi, S.H. Song, S.G. Jeong, J.Y. Choi and I. Choy, "Enhanced dynamic response of SRF-PLL system for high dynamic performance during voltage disturbance," *Journal of Power Electronics*, vol. 11, no. 3, pp. 369-374, May 2011.

[100] X. Qiu, J. Xiao and C. Wu, "Research of variable gain nonlinear PI controller based three-phase phase-locked-loop system," in *Proc. ICECE*, Wuhan, China, 2010, pp. 4050-4053.

[101] M.H. Bollen and I. Gu, *Signal processing of power quality disturbances*, John Wiley & Sons, 2006.

[102] M.H.J. Bollen, "Algorithms for characterizing measured three-phase unbalanced voltage dips," *IEEE Trans. Power Delivery*, vol. 18, no. 3, pp. 937-944, July 2003.

[103] V. Ignatova, P. Granjon and S. Bacha, "Space vector method for voltage dips and swells analysis," *IEEE Trans. Power Delivery*, vol. 24, no. 4, pp. 2054-2061, Oct. 2009.

[104] A. Kulkarni and V. John, "Analysis of bandwidth-unit-vector-distortion tradeoff in PLL during abnormal grid conditions," *IEEE Trans. Industrial Electronics*, vol. 60, no. 12, pp. 5820-5829, Dec. 2013.

[105] S. Golestan, M. Monfared, F.D. Freijedo and J.M. Guerrero, "Design and tuning of a modified power-based PLL for single-phase grid-connected power conditioning systems," *IEEE Trans. Power Electronics*, vol. 27, no. 8, pp. 3639-3650, Aug. 2012.

[106] A. Nicastri and A. Nagliero, "Comparison and evaluation of the PLL techniques for the design of the grid-connected inverter systems," in *Proc. IEEE ISIE*, 2010, pp. 3865-3870.

[107] Y. Yang, F. Blaabjerg and Z. Zou, "Benchmarking of grid fault modes in single-phase grid-connected photovoltaic systems," *IEEE Trans. Industry Applications*, vol. 49, no. 5, pp. 2167-2176, Sep. 2013.

[108] Y. Yang and F. Blaabjerg, "Synchronization in single-phase grid-connected photovoltaic systems under grid faults," in *Proc. IEEE PEDG*, Aalborg, Denmark, 2012, pp. 476-482.

[109] M. Ciobotaru, R. Teodorescu and F. Blaabjerg, "A new single-phase PLL structure based on second order generalized integrator," in *Proc. IEEE PESC*, Jeju, Korea, June 2006, pp. 1-6.

[110] P. Rodríguez, A. Luna, R.S. Muñoz-Aguilar, I. Etxeberria-Otadui, R. Teodorescu and F. Blaabjerg, "A stationary reference frame grid synchronization system for three-phase grid-connected power converters under adverse grid conditions," *IEEE Trans. Power Electronics*, vol. 27, no. 1, pp. 99-112, Jan. 2012.

[111] M. Saitou, N. Matsui and T. Shimizu, "A control strategy of single-phase active filter using a novel d-q transformation," in *Proc. IAS Annual Meeting*, Salt Lake City (UT), USA, 2003, pp. 1222, vol. 2-1227.

[112] F. Gonzalez-Espin, G. Garcera, I. Patrao and E. Figueres, "An adaptive control system for three-phase photovoltaic inverters working in a polluted and variable frequency electric grid," *IEEE Trans. Power Electronics*, vol. 27, no. 10, pp. 4248-4261, Oct. 2012.

[113] K. Lee, J. Lee, D. Shin, D. Yoo and H. Kim, "A novel grid synchronization PLL method based on adaptive low-pass notch filter for grid-connected PCS," *IEEE Trans. Industrial Electronics*, vol. 61, no. 1, pp. 292-301, Jan. 2014.

[114] M. Rashed, C. Klumpner and G. Asher, "Repetitive and resonant control for a single-phase grid-connected hybrid cascaded multilevel converter," *IEEE Trans. Power Electronics*, vol. 28, no. 5, pp. 2224-34, May 2013.

[115] B. Zhang, K. Zhou and D. Wang, "Multirate repetitive control for PWM DC/AC converters," *IEEE Trans. Industrial Electronics*, vol. 61, no. 6, pp. 2883-2890, June 2014.

[116] Y. Han, M. Luo, X. Zhao, J. Guerrero and L. Xu, "Comparative performance evaluation of orthogonal-signal-generators based single-phase PLL algorithms-A survey," *IEEE Trans. Power Electronics*, vol. 31, no. 5, pp. 3932-3944, May 2016.

[117] Y. Yang, K. Zhou, H. Wang, F. Blaabjerg, D. Wang and B. Zhang, "Frequency adaptive selective harmonic control for grid-connected inverters," *IEEE Trans. Power Electronics*, vol. 30, no. 7, pp. 3912-3924, July 2015.

[118] D.N. Zmood and D.G. Holmes, "Stationary frame current regulation of PWM inverters with zero steady-state error," *IEEE Trans. Power Electronics*, vol. 18, no. 3, pp. 814-822, May 2003.

[119] H. Akagi, E.H. Watanabe and M. Aredes, *Instantaneous power theory and applications to power conditioning*. New Jersey, NJ, USA, John Wiley & Sons, 2007.

[120] B. Zigmund, A. Terlizzi, X. Garcia, R. Pavlanin and L. Salvatore, "Experimental evaluation of PI tuning techniques for field oriented control of permanent magnet synchronous motors," *Advances in Electrical and Electronic Engineering*, vol. 5, no. 1-2, pp. 114-119, June 2006.

[121] A. Camacho, M. Castilla, J. Miret, J.C. Vasquez and E. Alarcon-Gallo, "Flexible voltage support control for three-phase distributed generation inverters under grid fault," *IEEE Trans. Industrial Electronics*, vol. 60, no. 4, pp. 1429-1441, Apr. 2013.

[122] K. Daunghom and S. Premrudeepreechacharn, "Fault ride-through of fully enclosed squirrel-cage induction generators for wind farms in Thailand," in *Proc. IEEE TDCE*, New Orleans, 2010, pp. 1-6.

[123] J.H. Liu, C.C. Chu and Y.Z. Lin, "Applications of nonlinear control for fault ride-through enhancement of doubly fed induction generators," *IEEE Journal of Emerging and Selected Topics in Power Electronics*, vol. 2, no. 4, pp. 749-763, Dec. 2014.

[124] R. Christie. (1999). *Power system test archive* [Online]. available: https://www.ee.washington.edu/research/pstca/.

[125] P.M. Anderson and A.A. Fouad, *Power system control and stability*. New Delhi, John Wiley & Sons, 2002.

[126] P. Demetriou, M. Asprou, J. Quiros-Tortos and E. Kyriakides, "Dynamic IEEE test systems for transient analysis," *IEEE Systems Journal*, pp. 1-10, 2016 (in press).

[127] A. Reznik, M.G. Simoes, A. Al-Durra and S.M. Muyeen, "LCL filter design and performance analysis for grid-interconnected systems," *IEEE Trans. Industry Applications*, vol. 50, no. 2, pp. 1225-1232, Apr. 2014.

[128] T. Van Cutsem and C. Vournas, *Voltage stability of electric power systems*, Springer Science & Business Media, 1998.

[129] M. Glavic and T. Van Cutsem, "A short survey of methods for voltage instability detection," in *Proc. IEEE PES general meeting*, Detroit, USA, 2011, pp. 1-8.

[130] T. Zabaiou, L.-. Dessaint and I. Kamwa, "Preventive control approach for voltage stability improvement using voltage stability constrained optimal power flow based on static line voltage stability indices," *IET Generation, Transmission & Distribution*, vol. 8, no. 5, pp. 924-934, May 2014.

[131] L. Peng, W. Yuting, Y. Yubo and Z. Baohui, "Study on a novel load shedding strategy for voltage stability control," in *Proc. IEEE PES General Meeting*, Vancouver, Canada, 2013, pp. 1-5.

[132] F. XueXin, W. Gang, F. Lijun, Y. Hua and J. Feng, "Control strategy of voltage stability based on generator dynamic reactive power releasing," in *Proc. International Conf. on Advanced Power System Automation and Protection (APAP)*, Beijing, China, 2011, pp. 460-465.

[133] M. Asprou and E. Kyriakides, "Enhancement of hybrid state estimation using pseudo flow measurements," in *Proc. IEEE PES General Meeting*, Detroit (MI) USA, 2011, pp. 1-7.

[134] A.I. Abur and A.G. Exposito, *Power system state estimation: Theory and implementation*. New York: Basel, CRC Press, 2004.

[135] E. Clarke, *Circuit analysis of AC power systems*, New York: John Wiley & Sons Inc., 1943.

[136] R.H. Park, "Two-reaction theory of synchronous machines generalized method of analysis-part I," *Transaction of the AIEE*, vol. 48, no. 3, pp. 716-727 1929.

[137] C.L. Fortescue, "Method of symmetrical co-ordinates applied to the solution of polyphase networks," *Transactions of the AIEE*, vol. 37, no. 2, pp. 1027-1140, 1918.

[138] W.V. Lyon, *Applications of the method of symmetrical components*, New York: McGraw-Hill, 1937.

[139] G.F. Franklin, J.D. Powell and A. Emami-Naeini, *Feedback control of dynamic systems*, 4th ed., Prentice Hall: Englewood Cliffs, New Jersey, 2002.

LIST OF PUBLICATIONS

Refereed Archival Journal Publications

1. **L. Hadjidemetriou**, E. Kyriakides, Y. Yang and F. Blaabjerg, "A synchronization method for single-phase grid-tied inverters," *IEEE Trans. Power Electronics*, vol. 31, no. 3, pp. 2139-2149, Mar. 2016.
2. **L. Hadjidemetriou**, E. Kyriakides and F. Blaabjerg, "A robust synchronization to enhance the power quality of renewable energy systems," *IEEE Trans. Industrial Electronics*, vol. 62, no. 8, pp. 4858-4868, Aug. 2015.
3. **L. Hadjidemetriou**, E. Kyriakides and F. Blaabjerg, "An adaptive tuning mechanism for phase-locked loop algorithms for faster time performance of interconnected renewable energy sources," *IEEE Trans. Industry Applications*, vol. 51, no. 2, pp. 1792-1804, Apr. 2015.
4. **L. Hadjidemetriou**, E. Kyriakides and F. Blaabjerg, "A new hybrid PLL for interconnecting renewable energy systems to the grid," *IEEE Trans. Industry Applications*, vol. 49, no. 6, pp. 2709-2719, 2013.
5. **L. Hadjidemetriou** and E. Kyriakides, "The performance of a new hybrid PLL in an interconnected renewable energy system under fault ride through operation," *Hindawi Publishing Corporation/CPIE*, vol. 2013, no. Article ID 168054, pp. 1-10, Mar. 2013.

Refereed Archival Journal Publications (submitted)

1. **L. Hadjidemetriou**, Y. Yang, E. Kyriakides and F. Blaabjerg, "A synchronization scheme for single-phase grid-tied inverters under harmonic distortion and grid disturbances," *IEEE Trans. Power Electronics*, pp. 1-8 (under review).

Refereed Archival Conference Proceedings

1. **L. Hadjidemetriou**, Y. Yang, E. Kyriakides and F. Blaabjerg, "A synchronization scheme for single-phase grid-tied inverters under harmonic distortions and grid disturbances," in *Proc. IEEE APEC 2016*, Long Beach (CA), USA, 2016, pp. 1-8.
2. **L. Hadjidemetriou**, G. Nicolaou, D. Stavrou and E. Kyriakides, "Low-cost real-time monitoring of a laboratory scale power system," in *Proc. IEEE MELECON 2016*, Limassol, Cyprus, 2016, pp. 1-6.
3. A. Charalambous, **L. Hadjidemetriou**, P. Demetriou and E. Kyriakides, "Dynamic modeling of IEEE test systems including renewable energy sources," in *Proc. IEEE MELECON 2016*, Limassol, Cyprus, 2016, pp. 1-6.
4. **L. Hadjidemetriou**, P. Demetriou and E. Kyriakides, "Investigation of different fault ride through strategies for renewable energy sources," in *Proc. IEEE POWERTECH*, Eindhoven, Netherlands, 2015, pp. 1-6.
5. **L. Hadjidemetriou**, M. Asprou, P. Demetriou and E. Kyriakides, "Enhancing power system voltage stability through a centralized control of renewable energy sources," in *Proc. IEEE POWERTECH*, Eindhoven, Netherlands, 2015, pp. 1-6.
6. P. Demetriou, **L. Hadjidemetriou**, A. Kyriacou, E. Kyriakides and C. Panayiotou, "Real-time identification of coherent generator groups," in *Proc. IEEE POWERTECH*, Eindhoven, Netherlands, 2015, pp. 1-6.
7. Y. Yang, **L. Hadjidemetriou**, F. Blaabjerg and E. Kyriakides, "Benchmarking of phase locked loop based synchronization techniques for grid-connected inverter systems," in *Proc. ICPE ECCE Asia*, Seoul, Korea, 2015, pp. 2517-2524.
8. **L. Hadjidemetriou**, E. Kyriakides, Y. Yang and F. Blaabjerg, "Power quality improvement of single-phase photovoltaic systems through a robust synchronization method," in *Proc. IEEE ECCE*, Pittsburgh (PA), USA, 2014, pp. 2625-2632.
9. S. Vagropoulos, **L. Hadjidemetriou**, A. Bakirtzis and E. Kyriakides, "Assessment of electric losses minimization in commercial facilities through combined EV charging and PV generation operation," in *Proc. IEEE MEDPOWER*, Athens, Greece, 2014, pp. 1-6.
10. **L. Hadjidemetriou**, E. Kyriakides and F. Blaabjerg, "An adaptive Phase-Locked Loop algorithm for faster fault ride through performance of interconnected

renewable energy sources," in *Proc. IEEE ECCE*, Denver (CO), USA, 2013, pp. 2619-2626.

11. **L. Hadjidemetriou**, E. Kyriakides and F. Blaabjerg, "A grid side converter current controller for accurate current injection under normal and fault ride through operation," in *Proc. IEEE IECON*, Vienna, Austria, 2013, pp. 1454-1459.
12. **L. Hadjidemetriou**, E. Kyriakides and F. Blaabjerg, "Synchronization of grid-connected renewable energy sources under highly distorted voltages and unbalanced grid faults," in *Proc. IEEE IECON*, Vienna, Austria, 2013, pp. 1887-1892.
13. Y. Tofis, **L. Hadjidemetriou** and E. Kyriakides, "An intelligent load shedding mechanism for maintaining frequency stability," in *Proc. IEEE POWERTECH*, Grenoble, France, 2013, pp. 1-5.
14. D. Stavrou, **L. Hadjidemetriou**, E. Kyriakides and C. Panayiotou, "Low-cost interface platform for controlling a real-time system;" in *Proc. IEEE HSB*C, Nicosia, Cyprus, 2013, pp. 1-2.
15. **L. Hadjidemetriou**, E. Kyriakides and F. Blaabjerg, "A new hybrid PLL for interconnecting Renewable Energy Systems to the grid," in *Proc. IEEE ECCE*, Raleigh (NC), USA, 2012, pp. 2075-2082.
16. **L. Hadjidemetriou** and E. Kyriakides, "The performance of a new hybrid PLL in an interconnected renewable energy system under fault ride through operation," in *Proc. POEM*, Limassol, Cyprus, 2012, pp. 1-7.

APPENDIX A
SPACE VECTOR TRANSFORMATIONS AND THREE-PHASE SYSTEM ANALYSIS

A.1 Introduction

Several space vector transformations have been proposed in order to facilitate the analysis of three-phase power systems. The space vector transformation on symmetrical components is particularly useful for analyzing the operation of power systems, especially under non-symmetrical conditions. Furthermore, space vector transformations on stationary and synchronous reference frames are employed for simplifying the design of the controllers for power electronic converters. Especially, the transformation on the synchronous reference frame enables the decoupled control of active and reactive power from power electronic converters. This Appendix aims to briefly present the transformation theory that has been used in this Ph.D. dissertation.

A.2 Natural reference frame (*abc*-frame)

The operation of a three-phase power system is based on the interaction between three phase voltages and currents. The power system operation is analyzed on the natural reference frame (*abc*-frame) due to the nature and physics of three-phase power systems, and more especially of the three-phase synchronous machine. The *abc*-frame is actually a three-axis stationary plane (each axis represents a phase of the three-phase system) with a 120^{o} phase difference between each axis as presented in Fig. A.1.

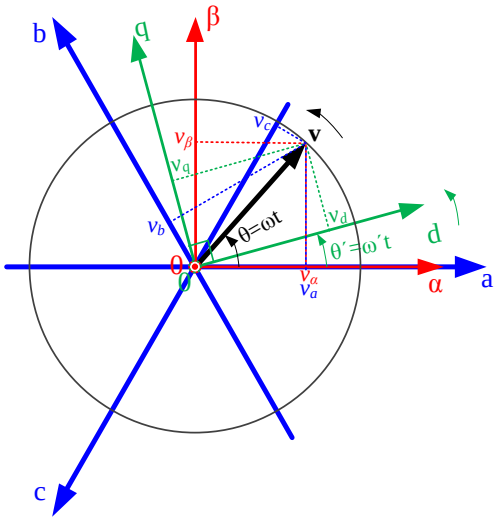

Fig. A.1. Graphical representation of abc-, αβ- and dq-frame.

In general, the three-phase voltage vector is defined by its phase voltages and the corresponding current vector is defined by the line current on each phase as,

$$\mathbf{v}_{abc} = \begin{bmatrix} v_a \\ v_b \\ v_c \end{bmatrix} \quad \text{and} \quad \mathbf{i}_{abc} = \begin{bmatrix} i_a \\ i_b \\ i_c \end{bmatrix} \tag{A.1}$$

The further analysis and transformations will be explained based only on the voltage vector. However, this analysis can be applied on both voltage and current vectors.

Under balanced and ideal three-phase voltage conditions, the voltage of each phase should be sinusoidal with the same rotational frequency (ω) and amplitude (V) and furthermore, should present a constant phase difference of $2\pi/3$ rad between phases as defined in (A.2) and presented in Fig. A.2(a).

$$\mathbf{v}_{abc} = \begin{bmatrix} v_a \\ v_b \\ v_c \end{bmatrix} = V \begin{bmatrix} \cos(\omega t + \varphi) \\ \cos(\omega t - 2\pi/3 + \varphi) \\ \cos(\omega t + 2\pi/3 + \varphi) \end{bmatrix} \tag{A.2}$$

Now, if the voltage vector $\mathbf{v_{abc}}$ is analyzed in the three-axis plane (*abc*-frame), then the voltage vector can be represented by a rotating vector with constant rotational speed (ω) and constant amplitude as shown in Fig. A.2(d).

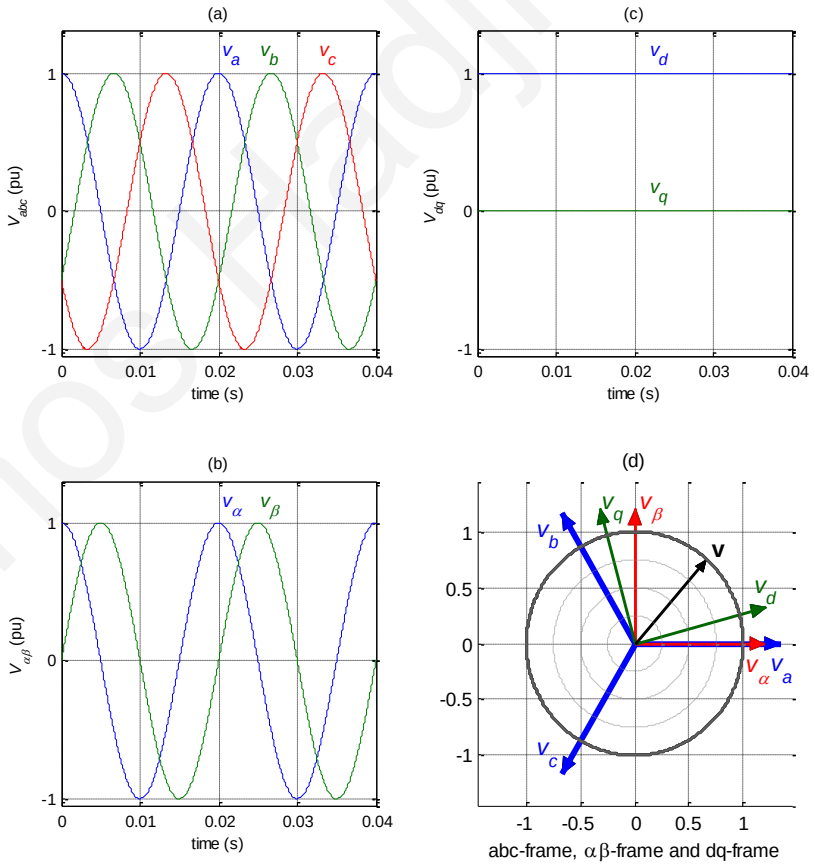

Fig. A.2. Three-phase voltage under ideal and balanced conditions: (a) Instantaneous voltage waveforms in natural abc-frame, (b) Instantaneous voltage waveforms in stationary αβ-frame, (c) Instantaneous voltage signals in synchronous dq-frame and (d) Three-phase voltage vector (**v**) representation in abc-, αβ-, and dq-frame.

A.3 Stationary reference frame (*αβ*-frame)

The power system analysis allows the transformation of the voltage and current vectors to other planes in order to simplify the analysis and the design of power electronic controllers. Such a Cartesian plane is the well-known stationary reference frame (*αβ0*-frame). The *αβ0*-frame is equivalent to the *abc*-frame and allows the analysis of the voltage and current vectors to a stationary and orthogonal system as shown in Fig. A.1. Therefore, the transformation of the voltage vector $\mathbf{v}_{abc}$ to the equivalent $\mathbf{v}_{\alpha\beta 0}$ and vice versa is achieved through the following transformation matrices in (A.3), based on the geometric analysis suggested by Clarke [135].

$$\mathbf{v}_{\alpha\beta 0} = \left[T_{\alpha\beta 0}\right]\mathbf{v}_{abc} \quad \text{and} \quad \mathbf{v}_{abc} = \left[T_{\alpha\beta 0}\right]^{-1}\mathbf{v}_{\alpha\beta 0}$$

where:
$$\mathbf{v}_{\alpha\beta 0} = \begin{bmatrix} v_\alpha \\ v_\beta \\ v_0 \end{bmatrix},\ \mathbf{v}_{abc} = \begin{bmatrix} v_a \\ v_b \\ v_c \end{bmatrix},$$

$$\left[T_{\alpha\beta 0}\right] = \frac{2}{3}\begin{bmatrix} 1 & -\frac{1}{2} & -\frac{1}{2} \\ 0 & \frac{\sqrt{3}}{2} & -\frac{\sqrt{3}}{2} \\ \frac{1}{\sqrt{2}} & \frac{1}{\sqrt{2}} & \frac{1}{\sqrt{2}} \end{bmatrix},\ \left[T_{\alpha\beta 0}\right]^{-1} = \begin{bmatrix} 1 & 0 & \frac{1}{\sqrt{2}} \\ -\frac{1}{2} & \frac{\sqrt{3}}{2} & \frac{1}{\sqrt{2}} \\ -\frac{1}{2} & -\frac{\sqrt{3}}{2} & \frac{1}{\sqrt{2}} \end{bmatrix} \tag{A.3}$$

It is worth to mention that the transformation matrix [$T_{\alpha\beta 0}$] of (A.3) has already been rescaled by $\sqrt{2/3}$ and thus, the amplitude of the sinusoidal signals that compose the voltage vector component in the *abc*- and the *αβ0*-frames are equal. This normalization affects the active (*p*) and reactive (*q*) power calculation of a three-phase system in each reference frame [27]. Therefore, the power calculations are given by,

$$p = \mathbf{v}_{abc}\cdot\mathbf{i}_{abc} = \frac{3}{2}\left(\mathbf{v}_{\alpha\beta 0}\cdot\mathbf{i}_{\alpha\beta 0}\right) \text{ and } q = \left|\mathbf{v}_{abc}\times\mathbf{i}_{abc}\right| = \frac{3}{2}\left|\mathbf{v}_{\alpha\beta 0}\times\mathbf{i}_{\alpha\beta 0}\right| \tag{A.4}$$

In general, the power electronic converters are connected to a three-phase power system through a three-wire connection and thus, the zero-sequence current is forced to be zero. Since the zero-sequence current is zero in such applications, there is no need to synchronize the zero-sequence voltage component to the corresponding current component and therefore, the analysis of the zero-sequence component of the vector can be intentionally ignored from the analysis presented in this Appendix. Hence, by ignoring the

last row of the $[T_{\alpha\beta 0}]$ and the last column of the $[T_{\alpha\beta 0}]^{-1}$ of (A.3), the same transformation matrices can be used for transforming $\mathbf{v}_{abc}$ to the equivalent $\mathbf{v}_{\alpha\beta}$ and vice versa as,

$$\mathbf{v}_{\alpha\beta} = \left[T_{\alpha\beta}\right]\mathbf{v}_{abc} \quad \text{and} \quad \mathbf{v}_{abc} = \left[T_{\alpha\beta}\right]^{-1}\mathbf{v}_{\alpha\beta}$$

where:

$$\mathbf{v}_{\alpha\beta} = \begin{bmatrix} v_\alpha \\ v_\beta \end{bmatrix},\ \mathbf{v}_{abc} = \begin{bmatrix} v_a \\ v_b \\ v_c \end{bmatrix},\ \left[T_{\alpha\beta}\right] = \frac{2}{3}\begin{bmatrix} 1 & -\frac{1}{2} & -\frac{1}{2} \\ 0 & \frac{\sqrt{3}}{2} & -\frac{\sqrt{3}}{2} \end{bmatrix},\ \left[T_{\alpha\beta}\right]^{-1} = \begin{bmatrix} 1 & 0 \\ -\frac{1}{2} & \frac{\sqrt{3}}{2} \\ -\frac{1}{2} & -\frac{\sqrt{3}}{2} \end{bmatrix} \quad \text{(A.5)}$$

If the transformation matrix of (A.5) is applied on the ideal and balanced voltage vector $\mathbf{v}_{abc}$ as defined by (A.2), then the voltage vector $\mathbf{v}_{\alpha\beta}$ under ideal voltage conditions is given by,

$$\mathbf{v}_{\alpha\beta} = \left[T_{\alpha\beta}\right]\mathbf{v}_{abc} = \frac{2}{3}\begin{bmatrix} 1 & -\frac{1}{2} & -\frac{1}{2} \\ 0 & \frac{\sqrt{3}}{2} & -\frac{\sqrt{3}}{2} \end{bmatrix} \cdot V\begin{bmatrix} \cos(\omega t + \varphi) \\ \cos(\omega t - 2\pi/3 + \varphi) \\ \cos(\omega t + 2\pi/3 + \varphi) \end{bmatrix} = V\begin{bmatrix} \cos(\omega t + \varphi) \\ \sin(\omega t + \varphi) \end{bmatrix} \quad \text{(A.6)}$$

It is to be noted that under ideal conditions the transformation into the $\alpha\beta$-frame results to a voltage vector $\mathbf{v}_{\alpha\beta}$, which consists of two sinusoidal signals (v_α and v_b) with a 90^o phase difference between the two components as shown in Fig. A.2(b). Further, the voltage vector $\mathbf{v}_{\alpha\beta}$ can be represented in the $\alpha\beta$-frame by a rotating voltage vector $\mathbf{v}$ with constant speed (ω) and constant amplitude (V) as shown in Fig. A.2(d).

A.4 Synchronous reference frame (*dq*-frame)

Another reference frame useful for the power electronic design is the synchronous reference frame (*dq0*-frame) that has been proposed by Park [136]. The *dq0*-frame is actually an orthogonal plane that rotates with the synchronous speed ω' (ω' is usually equal to the rotating speed of the voltage vector ω) as demonstrated in Fig. A.1. The transformation of the voltage vector to the *dq*-frame allows the representation of voltages as constant/DC quantities under ideal conditions. This is particularly useful for designing the controller of power electronic converters, since it simplifies the structure of the controller, allows a decoupled control of active and reactive power and enables the use of simple Proportional-Integral (PI) controllers for controlling the power electronic converters.

The transformation of the voltage vector between two different reference frames is achieved by projecting the equivalent three-phase voltage vector **v** on the corresponding axis of each reference frame as shown in Fig. A.1. The voltage vector **v** is equivalent in each reference frame as defined by,

$$\mathbf{v} = \mathbf{v}_{dq0} = \mathbf{v}_{\alpha\beta 0} = \sqrt{\frac{2}{3}}\mathbf{v}_{abc} \tag{A.7}$$

The voltage vector of the natural *abc*-frame ($\mathbf{v}_{abc}$) can be transformed to the equivalent vector ($\mathbf{v}_{dq0}$) expressed in the *dq*-frame and vise versa according to,

$$\mathbf{v}_{dq0} = \left[T_{\theta'}\right]\mathbf{v}_{abc} \quad \text{and} \quad \mathbf{v}_{abc} = \left[T_{\theta'}\right]^{-1}\mathbf{v}_{dq0}$$

where: $$\mathbf{v}_{dq0} = \begin{bmatrix} v_d \\ v_q \\ v_0 \end{bmatrix},\ \mathbf{v}_{abc} = \begin{bmatrix} v_a \\ v_b \\ v_c \end{bmatrix},$$

$$\left[T_{\theta'}\right] = \frac{2}{3}\begin{bmatrix} \cos(\theta') & \cos(\theta'-2\pi/3) & \cos(\theta'+2\pi/3) \\ -\sin(\theta') & -\sin(\theta'-2\pi/3) & -\sin(\theta'+2\pi/3) \\ 1/\sqrt{2} & 1/\sqrt{2} & 1/\sqrt{2} \end{bmatrix}, \tag{A.8}$$

$$\left[T_{\theta'}\right]^{-1} = \begin{bmatrix} \cos(\theta') & -\sin(\theta') & 1/\sqrt{2} \\ \cos(\theta'-2\pi/3) & -\sin(\theta'-2\pi/3) & 1/\sqrt{2} \\ \cos(\theta'+2\pi/3) & -\sin(\theta'+2\pi/3) & 1/\sqrt{2} \end{bmatrix}$$

It is to be noted that by setting θ'=0 to $[T_{\theta'}]$ of (A.8), the *dq*-frame is becoming stationary and identical with to *αβ*-frame and thus, the transformation matrix $[T_{\theta'}]$ should be equivalent to $[T_{\alpha\beta 0}]$.

The transformation matrix $[T_{\theta'}]$ has also been rescaled by $\sqrt{2/3}$ as shown in (A.7). The normalization of the transformation matrices of this Appendix is performed considering that the voltage amplitude of the components in each reference frame should be equal. This normalization affects the amplitude of the voltage vector as shown in (A.9).

$$\begin{aligned} \left|\mathbf{v}_{dq0}\right| &= \left|\mathbf{v}_{\alpha\beta 0}\right| = \sqrt{\frac{2}{3}}\left|\mathbf{v}_{abc}\right| = V \\ \sqrt{v_d^2 + v_q^2 + v_0^2} &= \sqrt{v_\alpha^2 + v_\beta^2 + v_0^2} = \sqrt{\frac{2}{3}}\sqrt{v_a^2 + v_b^2 + v_c^2} = V \end{aligned} \tag{A.9}$$

The normalization affects the amplitude of the voltage and current vectors in each reference frame and therefore, it should be considered on the three-phase power calculations given in (A.10).

$$\begin{aligned} p &= \mathbf{v}_{abc} \cdot \mathbf{i}_{abc} = \frac{3}{2}\left(\mathbf{v}_{\alpha\beta 0} \cdot \mathbf{i}_{\alpha\beta 0}\right) = \frac{3}{2}\left(\mathbf{v}_{dq0} \cdot \mathbf{i}_{dq0}\right) \\ q &= \left|\mathbf{v}_{abc} \times \mathbf{i}_{abc}\right| = \frac{3}{2}\left|\mathbf{v}_{\alpha\beta 0} \times \mathbf{i}_{\alpha\beta 0}\right| = \frac{3}{2}\left|\mathbf{v}_{dq0} \times \mathbf{i}_{dq0}\right| \end{aligned} \tag{A.10}$$

Another important transformation is the transformation matrix that achieves to translate the voltage vector from the *αβ0*-frame to the *dq0*-frame and vice versa. This transformation matrix is given by,

$$\mathbf{v}_{dq0} = \left[T_{dq0}\right]\mathbf{v}_{\alpha\beta 0} \quad \text{and} \quad \mathbf{v}_{\alpha\beta 0} = \left[T_{dq0}\right]^{-1}\mathbf{v}_{dq0}$$

where:

$$\mathbf{v}_{dq0} = \begin{bmatrix} v_d \\ v_q \\ v_0 \end{bmatrix}, \quad \mathbf{v}_{\alpha\beta 0} = \begin{bmatrix} v_\alpha \\ v_\beta \\ v_0 \end{bmatrix}, \quad \left[T_{dq0}\right] = \sqrt{\frac{2}{3}}\begin{bmatrix} \cos(\theta') & \sin(\theta') & 0 \\ -\sin(\theta') & \cos(\theta') & 0 \\ 0 & 0 & 1 \end{bmatrix} \tag{A.11}$$

As already mentioned in the previous subSection, the power electronic converters are connected to a three-phase power system through a three-wire connection and thus, the zero-sequence voltage and current can be intentionally ignored. Consequently, by ignoring the last row of the $[T_{\theta'}]$ and the last column of the $[T_{\theta'}]^{-1}$ of (A.8), the resulted transformation matrices can be used for transforming the $\mathbf{v}_{abc}$ to the equivalent $\mathbf{v}_{dq}$ and vice versa as presented in (A.12),

$$\mathbf{v}_{dq} = \left[T_{\theta'}\right]\mathbf{v}_{abc} \quad \text{and} \quad \mathbf{v}_{abc} = \left[T_{\theta'}\right]^{-1}\mathbf{v}_{dq}$$

$$\mathbf{v}_{abc} = \begin{bmatrix} v_a \\ v_b \\ v_c \end{bmatrix}, \mathbf{v}_{dq} = \begin{bmatrix} v_d \\ v_q \end{bmatrix}, \left[T_{\theta'}\right] = \frac{2}{3}\begin{bmatrix} \cos(\theta') & \cos(\theta' - 2\pi/3) & \cos(\theta' + 2\pi/3) \\ -\sin(\theta') & -\sin(\theta' - 2\pi/3) & -\sin(\theta' + 2\pi/3) \end{bmatrix}, \tag{A.12}$$

$$\left[T_{\theta'}\right]^{-1} = \begin{bmatrix} \cos(\theta') & -\sin(\theta') \\ \cos(\theta' - 2\pi/3) & -\sin(\theta' - 2\pi/3) \\ \cos(\theta' + 2\pi/3) & -\sin(\theta' + 2\pi/3) \end{bmatrix}$$

Similarly, the transformation from $\mathbf{v}_{\alpha\beta}$ to $\mathbf{v}_{dq}$ can be achieved by ignoring the last row and last column of $[T_{dq0}]$ as given by (A.13).

$$\mathbf{v}_{dq} = \left[T_{dq}\right]\mathbf{v}_{\alpha\beta} \quad \text{and} \quad \mathbf{v}_{\alpha\beta} = \left[T_{dq}\right]^{-1}\mathbf{v}_{dq}$$

where:

$$\mathbf{v}_{dq} = \begin{bmatrix} v_d \\ v_q \end{bmatrix}, \mathbf{v}_{\alpha\beta} = \begin{bmatrix} v_\alpha \\ v_\beta \end{bmatrix}, \left[T_{dq}\right] = \begin{bmatrix} \cos(\theta') & \sin(\theta') \\ -\sin(\theta') & \cos(\theta') \end{bmatrix}, \left[T_{dq}\right]^{-1} = \begin{bmatrix} \cos(\theta') & -\sin(\theta') \\ \sin(\theta') & \cos(\theta') \end{bmatrix} \tag{A.13}$$

Now, if the transformation matrix $[T_{\theta'}]_{|\theta'=\omega t}$ of (A.12) is applied on the ideal voltage vector $\mathbf{v}_{abc}$ as defined by (A.2) or if the transformation matrix $[T_{dq}]_{|\theta'=\omega t}$ of (A.13) is applied on the resulted $\mathbf{v}_{\alpha\beta}$ of (A.6), then the voltage vector $\mathbf{v}_{dq}$ under ideal voltage conditions will be generated as shown in (A.14).

$$\begin{aligned} & \mathbf{v}_{dq} = \left[T_{\theta'}\right]\mathbf{v}_{abc} = \left[T_{dq}\right]\mathbf{v}_{\alpha\beta} \\ \Leftrightarrow\ & \mathbf{v}_{dq} = \begin{bmatrix} \cos(\theta') & \sin(\theta') \\ -\sin(\theta') & \cos(\theta') \end{bmatrix} \cdot V \begin{bmatrix} \cos(\omega t + \varphi) \\ \sin(\omega t + \varphi) \end{bmatrix} \\ \Leftrightarrow\ & \mathbf{v}_{dq} = V \begin{bmatrix} \cos(\theta')\cos(\omega t + \varphi) + \sin(\theta')\sin(\omega t + \varphi) \\ -\sin(\theta')\cos(\omega t + \varphi) + \cos(\theta')\sin(\omega t + \varphi) \end{bmatrix} \\ \Leftrightarrow\ & \mathbf{v}_{dq} = V \begin{bmatrix} \cos(\theta' - \omega t - \varphi) \\ \sin(\omega t + \varphi - \theta') \end{bmatrix} = V \begin{bmatrix} \cos(\varphi) \\ \sin(\varphi) \end{bmatrix} \end{aligned} \tag{A.14}$$

It is remarkable that under ideal conditions the transformation into the *dq*-frame results to a voltage vector $\mathbf{v}_{dq}$, which consists of constant/DC quantities as represented in Fig. A.2(c). The transformation of the component of the voltage and current vectors from sinusoidal signals to DC signals simplifies the controller structure and enables the use of PI controllers in the controller design of such power electronic applications. Further, if the v_q component is forced to be zero, the v_d represents the amplitude of the voltage vector and more importantly, the decoupled control of active and reactive power can be ensured. The decoupled power control is enabled when v_q=0, since by controlling the i_d or i_q components of the current vector $\mathbf{i}_{dq}$, then the corresponding active or reactive power can be regulated as can be observed by (A.10).

A.5 Voltage analysis under abnormal conditions

A.5.1 Space vector transformation on symmetrical components

The analysis presented in the previous sections considers the three-phase voltage under ideal and balanced conditions. In case of unbalanced voltage and/or current conditions, the well-known transformations on symmetrical components [137], [138] are used in order to allow a more elegant analysis of the power system operation. The

transformations on symmetrical components can be used to express any unbalanced voltage vector $\mathbf{v}_{abc}$ into a summation of three symmetrical voltage vectors, the positive-sequence ($\mathbf{v}^{+}_{abc}$), the negative-sequence ($\mathbf{v}^{-}_{abc}$) and the zero-sequence ($\mathbf{v}^{0}_{abc}$) voltage vector as given in (A.15).

$$\mathbf{v}_{abc} = \begin{bmatrix} v_a \\ v_b \\ v_c \end{bmatrix} = \mathbf{v}^{+}_{abc} + \mathbf{v}^{-}_{abc} + \mathbf{v}^{0}_{abc}$$

where:

$$\mathbf{v}^{+}_{abc} = V^{+}\begin{bmatrix} \cos(+\omega t + \varphi^{+}) \\ \cos(+\omega t - 2\pi/3 + \varphi^{+}) \\ \cos(+\omega t + 2\pi/3 + \varphi^{+}) \end{bmatrix},\ \mathbf{v}^{-}_{abc} = V^{-}\begin{bmatrix} \cos(\omega t + \varphi^{-}) \\ \cos(\omega t + 2\pi/3 + \varphi^{-}) \\ \cos(\omega t - 2\pi/3 + \varphi^{-}) \end{bmatrix}, \quad \text{(A.15)}$$

$$\mathbf{v}^{0}_{abc} = V^{0}\begin{bmatrix} \cos(\omega t + \varphi^{0}) \\ \cos(\omega t + \varphi^{0}) \\ \cos(\omega t + \varphi^{0}) \end{bmatrix}$$

Thereafter, the three symmetrical vectors ($\mathbf{v}^{+}_{abc}$, $\mathbf{v}^{-}_{abc}$, $\mathbf{v}^{0}_{abc}$) can be used to enable an elegant analysis of an unbalanced power system according to the conventional theory that is valid for symmetrical systems. The transformation matrices of (A.16), (A.17) and (A.18) can be used in order to calculate the corresponding positive- negative- and zero-sequence symmetrical voltage vectors from an unbalanced voltage vector $\mathbf{v}_{abc}$.

$$\mathbf{v}^{+}_{abc} = [T_{+}]\mathbf{v}_{abc} \quad \Leftrightarrow \quad \begin{bmatrix} v^{+}_a \\ v^{+}_b \\ v^{+}_c \end{bmatrix} = \frac{1}{3}\begin{bmatrix} 1 & a & a^2 \\ a^2 & 1 & a \\ a & a^2 & 1 \end{bmatrix}\begin{bmatrix} v_a \\ v_b \\ v_c \end{bmatrix} \quad \text{(A.16)}$$

$$\mathbf{v}^{-}_{abc} = [T_{-}]\mathbf{v}_{abc} \quad \Leftrightarrow \quad \begin{bmatrix} v^{-}_a \\ v^{-}_b \\ v^{-}_c \end{bmatrix} = \frac{1}{3}\begin{bmatrix} 1 & a^2 & a \\ a & 1 & a^2 \\ a^2 & a & 1 \end{bmatrix}\begin{bmatrix} v_a \\ v_b \\ v_c \end{bmatrix} \quad \text{(A.17)}$$

$$\mathbf{v}^{0}_{abc} = [T_{0}]\mathbf{v}_{abc} \quad \Leftrightarrow \quad \begin{bmatrix} v^{0}_a \\ v^{0}_b \\ v^{0}_c \end{bmatrix} = \frac{1}{3}\begin{bmatrix} 1 & 1 & 1 \\ 1 & 1 & 1 \\ 1 & 1 & 1 \end{bmatrix}\begin{bmatrix} v_a \\ v_b \\ v_c \end{bmatrix} \quad \text{(A.18)}$$

In the equations above, the operator $\alpha = 1\angle 120^{o} = e^{j2\pi/3}$ represents the Fortescue operator.

A.5.2 Voltage analysis under abnormal and harmonic distorted conditions

The transformation analysis presented in A.5.1 considers the voltage analysis under unbalanced conditions. The harmonic distortion of the voltage vector has been intentionally ignored in the previous analysis. Therefore, in the general case of unbalanced and harmonic distorted voltage the voltage vector can be expressed as a summation of positive (+*n*), negative (-*n*) and zero (0_n) sequence voltage vectors of the fundamental (*n*=1) and all the existence harmonic components (*n*=2, 3, 4, 5,…) [27] as given by,

$$\mathbf{v}_{abc} = \begin{bmatrix} v_a \\ v_b \\ v_c \end{bmatrix} = \sum_{n=1}^{\infty} \left(\mathbf{v}_{abc}^{+n} + \mathbf{v}_{abc}^{-n} + \mathbf{v}_{abc}^{0_n} \right)$$

where:

$$\begin{aligned} \mathbf{v}_{abc}^{+n} &= V^{+n} \begin{bmatrix} \cos(+n\omega t + \varphi^{+n}) \\ \cos(+n\omega t - 2\pi/3 + \varphi^{+n}) \\ \cos(+n\omega t + 2\pi/3 + \varphi^{+n}) \end{bmatrix} \\ \mathbf{v}_{abc}^{-n} &= V^{-n} \begin{bmatrix} \cos(n\omega t + \varphi^{-n}) \\ \cos(n\omega t + 2\pi/3 + \varphi^{-n}) \\ \cos(n\omega t - 2\pi/3 + \varphi^{-n}) \end{bmatrix} = V^{-n} \begin{bmatrix} \cos(-n\omega t - \varphi^{-n}) \\ \cos(-n\omega t - 2\pi/3 - \varphi^{-n}) \\ \cos(-n\omega t + 2\pi/3 - \varphi^{-n}) \end{bmatrix} \\ \mathbf{v}_{abc}^{0_n} &= V^{0n} \begin{bmatrix} \cos(n\omega t + \varphi^{0n}) \\ \cos(n\omega t + \varphi^{0n}) \\ \cos(n\omega t + \varphi^{0n}) \end{bmatrix} \end{aligned} \tag{A.19}$$

Therefore, in case of unbalanced voltage conditions, the three-phase voltage vector $\mathbf{v}_{abc}$ can be express as a summation of the positive-sequence (+1), negative-sequence (-1) and zero-sequence (0_1) of the fundamental voltage component. For example, if a Type C [91] unbalanced phase-to-phase grid fault occurs, the voltage vector can be describe by the individual symmetrical vectors of (A.19) with amplitudes ($V^{+1} = 0.8\,pu,\ V^{-1} = 0.2\,pu,\ V^{0_1} = 0\,pu$) and initial phase angles ($\varphi^{+1} = \varphi^{-1} = \varphi^{0_1} = 0^o$). Fig. A.3(a)-(c) presents the instantaneous waveforms of the components of the unbalanced voltage vector $\mathbf{v}_{abc}$ of this example expressed in the corresponding natural *abc*-frame, stationary αβ-frame and synchronous *dq*-frame. Fig. A.3(d) presents the rotating voltage vector $\mathbf{v}=\mathbf{v}_{abc}$ in each reference frame. It is to be noted that under unbalanced conditions, the root locus of the rotating voltage vector **v** can be described by an eclipse. This means that the amplitude and the rotating speed of the three-phase voltage vector is not constant any more (as happen under ideal conditions). Furthermore, it is remarkable that the existence of the negative-

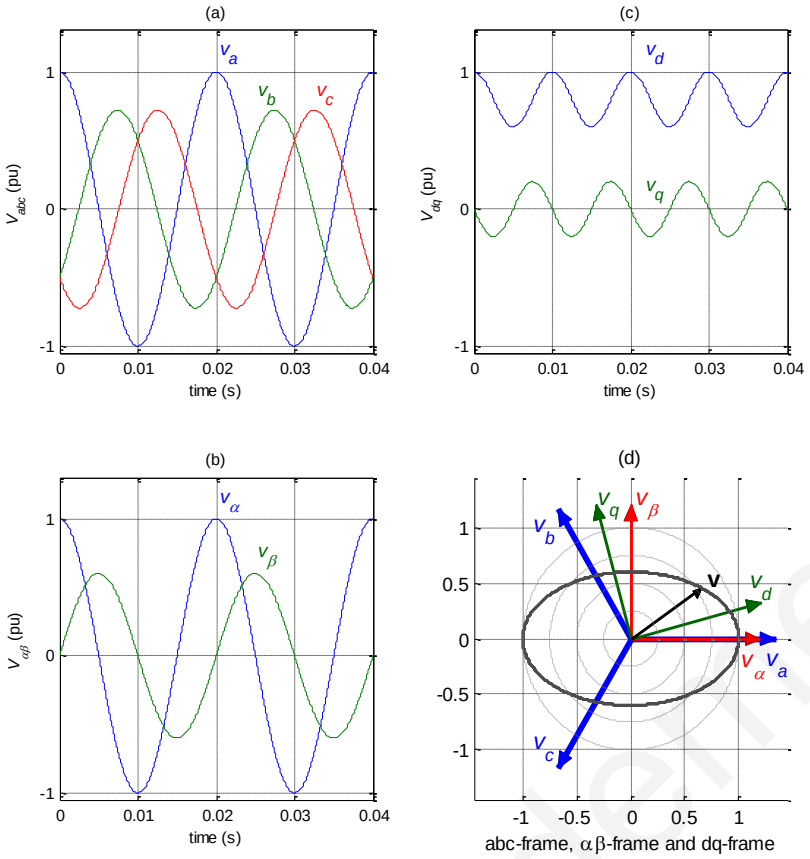

Fig. A.3. Three-phase voltage under unbalanced (Type C) fault with V+1=0.8 pu and V-1=0.2 pu: (a) Instantaneous voltage waveforms in natural abc-frame, (b) Instantaneous voltage waveforms in stationary αβ-frame, (c) Instantaneous voltage signals in synchronous dq-frame and (d) Three-phase voltage vector (v) representation in abc- and αβ- and dq-frame.

sequence causes significant double-frequency oscillations on the voltage signals when those are expressed in the *dq*-frame. Therefore, the estimation of the phase angle and amplitude of the positive sequence component, which is particular useful for the synchronization and controller of power electronic devices, is not a trivial procedure any more. Furthermore, these undesirable oscillations under unbalanced conditions can affect the operation of the power electronic converters.

Now a more complex voltage example is described in Fig. A.4, where there is an unbalanced grid fault (Type C) [91] and the voltage is harmonic distorted (with minus fifth harmonic). The three-phase voltage vector $\mathbf{v}_{abc}$ can be express as a summation of the positive-sequence (+1), negative-sequence (-1) of the fundamental component and the negative-sequence of the fifth harmonic component (-5). For the example of Fig. A.4, the voltage vector can be describe by the individual symmetrical vectors of (A.19) with amplitudes $(V^{+1} = 0.8\,pu,\ V^{-1} = 0.2\,pu,\ V^{-5} = 0.1\,pu)$ and initial phase angles $(\varphi^{+1} = \varphi^{-1} = \varphi^{-5} = 0^o)$. Fig. A.4(a)-(c) presents the instantaneous waveforms of the components of the unbalanced and harmonic distorted voltage vector $\mathbf{v}_{abc}$ expressed in the corresponding natural abc-frame, stationary αβ-frame and synchronous dq-frame. Fig.

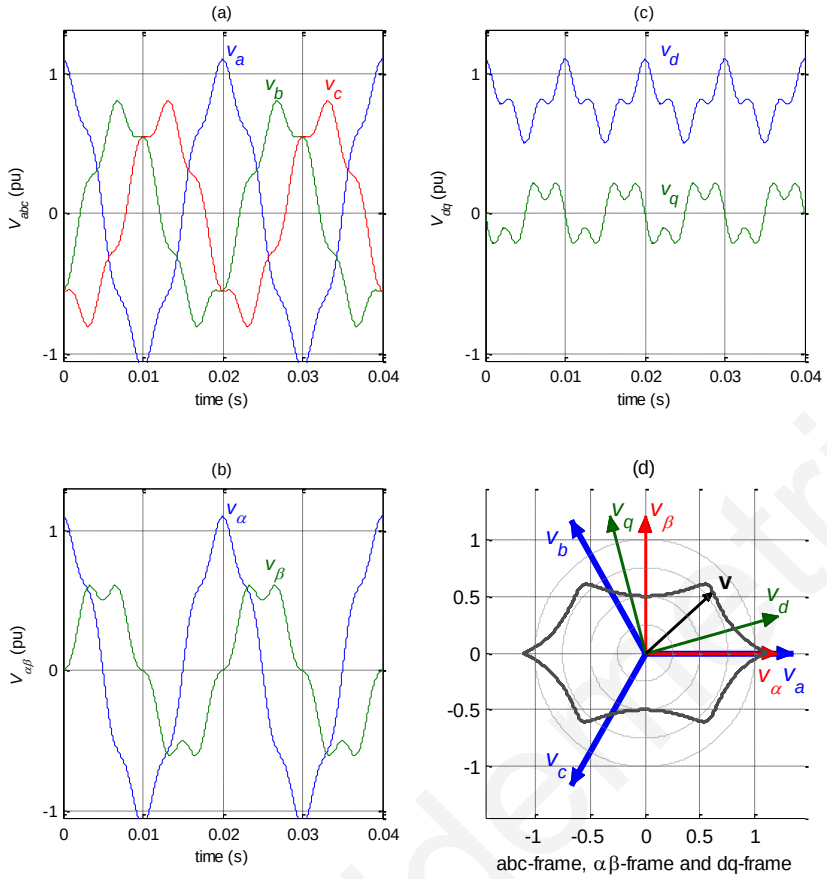

Fig. A.4. Three-phase voltage under unbalanced (Type C) fault and harmonic distortion with V+1=0.8 pu, V-1=0.2 pu and V-5=0.1 pu: (a) Instantaneous voltage waveforms in natural abc-frame, (b) Instantaneous voltage waveforms in stationary αβ-frame, (c) Instantaneous voltage signals in synchronous dq-frame and (d) Three-phase voltage vector (v) representation in abc- and αβ- and dq-frame.

A.4(d) presents the rotating voltage vector $\mathbf{v}=\mathbf{v}_{abc}$ in each reference frame. It is to be noted that under unbalanced and harmonic distorted conditions, the root locus of the rotating voltage vector **v** is become more complicate (something between an eclipse and an hexagon) due to the effect of the negative-sequence and the negative fifth harmonic. Therefore, the amplitude and the rotating speed of the three-phase voltage vector is not constant any more (as happen under ideal conditions). Furthermore, it is remarkable that the existence of the negative-sequence and the negative fifth harmonic causes significant double-frequency and sixfold-frequency oscillations on the voltage signals when those are expressed in the *dq*-frame. Therefore, the fast and accurate estimation of the phase angle and amplitude of the positive sequence component is particular difficult procedure.

A.6 Instantaneous power theory under unbalanced conditions

According to instantaneous power theory [27], [119] the instantaneous active (*p*) and reactive (*q*) power supplied by the GSC of an interconnected RES can be calculated according to (A.20) and (A.21) respectively.

$$p = \mathbf{v}_{abc} \cdot \mathbf{i}_{abc} = \frac{3}{2}\left(\mathbf{v}_{\alpha\beta} \cdot \mathbf{i}_{\alpha\beta}\right) = \frac{3}{2}\left(\mathbf{v}_{dq} \cdot \mathbf{i}_{dq}\right) \tag{A.20}$$

$$q = \left|\mathbf{v}_{abc} \times \mathbf{i}_{abc}\right| = \frac{3}{2}\left|\mathbf{v}_{\alpha\beta} \times \mathbf{i}_{\alpha\beta}\right| = \frac{3}{2}\left|\mathbf{v}_{dq} \times \mathbf{i}_{dq}\right| \tag{A.21}$$

For the further analysis, only the voltage and current vector expressed in the dq^{+1}-frame rotating with the positive fundamental angular frequency of the grid $+\omega$ it is considered. However, the exact same theory can be applied in any reference frame. Therefore, the active and reactive power can be re-written as,

$$p = \frac{3}{2}\left(\mathbf{v}_{dq^{+1}} \cdot \mathbf{i}_{dq^{+1}}\right) \tag{A.22}$$

$$q = \frac{3}{2}\left|\mathbf{v}_{dq^{+1}} \times \mathbf{i}_{dq^{+1}}\right| = \frac{3}{2}\left(\mathbf{v}_{dq^{+1}\perp} \cdot \mathbf{i}_{dq^{+1}}\right) \tag{A.23}$$

where each voltage and current vector of are defined as,

$$\mathbf{v}_{dq^{+1}} = \begin{bmatrix} v_{d^{+1}} \\ v_{q^{+1}} \end{bmatrix}, \quad \mathbf{v}_{dq^{+1}\perp} = \begin{bmatrix} 0 & 1 \\ -1 & 0 \end{bmatrix}\begin{bmatrix} v_{d^{+1}} \\ v_{q^{+1}} \end{bmatrix} = \begin{bmatrix} v_{q^{+1}} \\ -v_{d^{+1}} \end{bmatrix} \; and \; \mathbf{i}_{dq^{+1}} = \begin{bmatrix} i_{d^{+1}} \\ i_{q^{+1}} \end{bmatrix} \tag{A.24}$$

$\mathbf{v}_{dq^{+1}}$ represents the voltage vector at the point of common coupling (PCC), $\mathbf{i}_{dq^{+1}}$ is the injected current vector, and $\mathbf{v}_{dq^{+1}\perp}$ is an orthogonal version (90^o leading) from the original voltage vector $\mathbf{v}_{dq^{+1}}$**,** all expressed in the dq^{+1}-frame.

During unbalanced grid conditions the voltage and the current could be written as a summation of the positive and the negative sequence components, as given by (A.25).

$$\mathbf{v} = \mathbf{v}^{+}_{dq^{+1}} + \mathbf{v}^{-}_{dq^{+1}} \quad \text{and} \quad \mathbf{i} = \mathbf{i}^{+}_{dq^{+1}} + \mathbf{i}^{-}_{dq^{+1}} \tag{A.25}$$

It is to be noted that $\mathbf{v}^{+1}_{dq^{+1}}$ and $\mathbf{i}^{+1}_{dq^{+1}}$ are oscillation-free terms while the $\mathbf{v}^{-1}_{dq^{+1}}$ and $\mathbf{i}^{-1}_{dq^{+1}}$ are double-frequency oscillation term. Hence, the equations (A.22) and (A.23) for the active and reactive power of can be reformulated as presented in (A.26) and (A.27).

$$p = (\mathbf{v}^{+}_{dq^{+1}} + \mathbf{v}^{-}_{dq^{+1}}) \cdot (\mathbf{i}^{+}_{dq^{+1}} + \mathbf{i}^{-}_{dq^{+1}}) \quad \Leftrightarrow$$

$$p = \underbrace{\mathbf{v}^{+}_{dq^{+1}} \cdot \mathbf{i}^{+}_{dq^{+1}} + \mathbf{v}^{-}_{dq^{+1}} \cdot \mathbf{i}^{-}_{dq^{+1}}}_{P} + \underbrace{\mathbf{v}^{+}_{dq^{+1}} \cdot \mathbf{i}^{-}_{dq^{+1}} + \mathbf{v}^{-}_{dq^{+1}} \cdot \mathbf{i}^{+}_{dq^{+1}}}_{\tilde{p}} \tag{A.26}$$

$$q = (\mathbf{v}^{+}_{dq^{+1}\perp} + \mathbf{v}^{-}_{dq^{+1}\perp}) \cdot (\mathbf{i}^{+}_{dq^{+1}} + \mathbf{i}^{-}_{dq^{+1}}) \quad \Leftrightarrow$$

$$q = \underbrace{\mathbf{v}^{+}_{dq^{+1}\perp} \cdot \mathbf{i}^{+}_{dq^{+1}} + \mathbf{v}^{-}_{dq^{+1}\perp} \cdot \mathbf{i}^{-}_{dq^{+1}}}_{Q} + \underbrace{\mathbf{v}^{+}_{dq^{+1}\perp} \cdot \mathbf{i}^{-}_{dq^{+1}} + \mathbf{v}^{-}_{dq^{+1}\perp} \cdot \mathbf{i}^{+}_{dq^{+1}}}_{\tilde{q}} \tag{A.27}$$

The terms P and Q of (A.26) and (A.27) represent the oscillation-free part of active and reactive power, while the terms $\tilde{p}$ and $\tilde{q}$ represent the double-frequency oscillation terms of the power due to the unbalanced conditions. Therefore, it is obvious that the existence of negative sequence voltage or current (unbalanced disturbances) could give a rise to oscillations in active and reactive power.

At this point, it is to be noted that the oscillation-free terms of active and reactive power of (A.26) and (A.27) can be re-written in an equivalent way using only oscillation-free terms, such the $\mathbf{v}_{dq^{-1}}^{-1}$ and $\mathbf{i}_{dq^{-1}}^{-1}$, as presented in (A.28) and (A.29).

$$P = \mathbf{v}_{dq^{+1}}^{+} \cdot \mathbf{i}_{dq^{+1}}^{+} + \mathbf{v}_{dq^{+1}}^{-} \cdot \mathbf{i}_{dq^{-1}}^{-} \tag{A.28}$$

$$Q = \mathbf{v}_{dq^{+1}\perp}^{+} \cdot \mathbf{i}_{dq^{+1}}^{+} + \mathbf{v}_{dq^{-1}\perp}^{-} \cdot \mathbf{i}_{dq^{-1}}^{-} \tag{A.29}$$

According to the last expressions, an oscillation-free active and reactive power can only be generated by voltage and current vectors that are rotated with the same direction and speed.

A.7 Conclusions

As a conclusion, this appendix has briefly presents the main space vector transformation theory that has been used in this Ph.D. dissertation. Further, the voltage analysis under abnormal conditions has been presented and some problems caused under unbalanced and harmonic distorted conditions are highlighted. Finally, the basic instantaneous theory under unbalanced conditions is presented, where it is shown that unbalanced voltage and/or current condition can rise oscillations on the active and reactive power injection.

APPENDIX B
TUNING PROCEDURE FOR PLL ALGORITHMS

All Phase-Locked Loop (PPL) algorithms of this Ph.D. dissertation have been tuned according to the linearized small signal model analysis for a PLL, as explained in [27], [29], [139]. The block diagram of the small signal model of an elementary PLL is presented in Fig. B.1. For simplicity, it is considered that the parameter K_{PD} of the phase detector unit is equal to one. Furthermore, the transfer function of the loop filter $LF(s)$, which consists of a Proportional-Integral (PI) controller is given by (B.1), where k_p and T_i represents the tuning parameters of the PI controller.

$$LF(s) = \frac{V_{LF}}{\Delta\theta} = k_p + \frac{1}{T_i \cdot s} \tag{B.1}$$

Therefore, the closed-loop transfer function $H_\theta(s)$ of the small signal linearized model of a PLL is given by,

$$H_\theta(s) = \frac{\theta_{PLL}}{\theta_{grid}} = \frac{2\zeta\omega_n s + \omega_n^2}{s^2 + 2\zeta\omega_n s + \omega_n^2} = \frac{k_p \cdot s + \frac{1}{T_i}}{s^2 + k_p \cdot s + \frac{1}{T_i}} \tag{B.2}$$

The θ_{grid} represents the phase angle of the grid voltage and the θ_{PLL} represents the estimated phase angle by the PLL algorithm. (B.2) shows that the response of a small signal linearized PLL is approximated by a second-order transfer function, whose response has been studied in many books, including [139]. According to (B.2), the natural frequency of the second-order system $\omega_n = 1/\sqrt{T_i}$ and the damping coefficient $\zeta = \left(k_p\sqrt{T_i}\right)/2$. Thus, the proper tuning of a PLL can be achieved by setting the damping factor ζ of (B.2) equals to $1/\sqrt{2}$ in order to achieve an optimally damped response. In this case, the settling

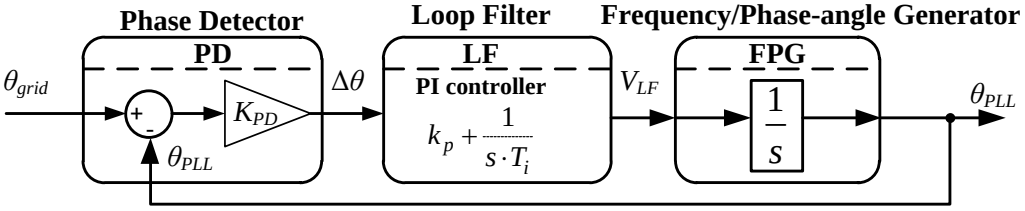

Fig. B.1. The block diagram of the linearized small signal model of an elementary PLL.

time (T_s) of the PLL, which represents the required time in which the system stays within 1% of its steady state response after a unitary step change of the input signal, can be regulated by the tuning parameters k_p and T_i of the PLL as shown in (B.3).

$$k_p = \frac{9.2}{T_s} \qquad \text{and} \qquad T_i = 0.047 \cdot \zeta^2 \cdot T_s^2 \tag{B.3}$$

It is to be noticed that the above-mentioned are valid for unitary (per unit) input signals. Further, it is worth mentioning that the second order transfer function of (B.2) depicts that PLLs based on a PI controller (for the loop filter stage) present low-pass filtering characteristics, therefore, the stability of PLLs is ensured and also the attenuation of the detection error caused by possible noise and high order harmonics in the input signal is proved.